Experimental and CFD investigations of the Megane multi-box bridge deck aerodynamic characteristics

by

Zhida Wang

A thesis submitted to the Faculty of Graduate and Postdoctoral Studies in partial fulfilment of the requirements for the degree of

Masters of Applied Science

In

Civil Engineering

Department of Civil Engineering

University of Ottawa

Ottawa, Canada

Jan. 2015

© Zhida Wang, Ottawa, Canada, 2015

Acknowledgements

I would like to express my gratitude to all those who helped me during the writing of this thesis.

First and foremost, my deepest thanks go to my Professor Elena Dragomirescu for her guidance, encouragement and teachings. She has walked me through all the stages from experiments to the writing of this thesis. This thesis is a better work thanks to her supervision and endless support.

I would like to acknowledge the generous help from National Research Council and Dr. Guy Larose who lend the equipment needed for the experiment. Thanks to Carleton University and Professor John Hayes who allowed us to perform experiments in their wind tunnel. Thanks to Alex Proctor, David Raude and all the staff of the Mechanical Workshop for the technical support during the experiments.

My deepest thanks go to Muslim Majid, Professor Tanaka, Ya Liu, Fan Feng, Xi Chen and all my friends for their great help and recommendations during this research project.

Finally, it is honor to say that I would like to dedicate this thesis to my beloved family, especially my parents without whom I would unlikely be able to finish this thesis. Their support and encouragement have been helping me unwavering throughout the journey. I am truly blessed to having them presence in my life.

Abstract

The shape of bridge deck sections used for long-span suspension bridges has evolved through the years, from the compact box deck girders, to twin box and multi-box decks sections, which proved to have better aerodynamic behaviour, and to bring economic advantages on the construction material usage side. This thesis presents a study of a new type of multi-box bridge deck for the Megane Bridge, consisting of two side decks for traffic lanes, and two middle decks for railway traffic, connected using stabilizing beams. Aerodynamic static force coefficient measurements were performed on a section model with a scale of 1:80, for Reynolds numbers up to 5.1×10^5 under angles of attack from -10 ° to 10 °. Also there-dimensional CFD simulations were performed by employing a Large Eddy Simulation (LES) algorithm with a standard Smagorinsky subgrid-scale model, for $Re = 9.3 \times 10^7$ and angles of attack α = -4 °, -2 °, 0 °, 2 ° and 4 °. The experimental and numerical results were compared with respect to accuracy, sensitivity, and practical suitability. Furthermore, the aerodynamic character for each individual decks including static coefficients, wind flow pattern and pressure distribution were studied through CFD simulation. ILS (Iterative Least Squares) method was applied to extract the flutter derivatives of Megane section model based on the results obtained from free vibration tests for evaluating the flutter stability. A comparison of the flutter derivatives was carried out between bridges with different deck configurations and the results are included in this thesis.

Contents

Acknowledgements ii

Abstract iii

Contents iv

List of Tables vii

List of Figures viii

Nomenclature xiii

Chapter 1 Introduction 1

1.1 Wind Load Effect on Long-span Bridge 1

1.2 Research motivation 2

1.3 Objectives 4

1.4 Scope of Research 5

1.5 Thesis Layout 7

Chapter 2 Literature review 9

2.1 Bridge Aeroelasticity Theory 9

2.1.1 Wake and Vortex formation around structures 9

2.1.2 Strouhal number and the Lock-in Phenomenon 12

2.1.3 Galloping aerodynamic instability 14

2.1.4 Flutter aerodynamic instability 17

2.1.5 Buffeting aerodynamic instability 23

2.2 Experimental Investigations of Different Bridge Section 24

2.2.1 Types of Wind Tunnel Tests for Long Span Bridges 24

2.2.2 Bridge deck section model and the Reynolds effect 25

2.2.3 Effects of deck shape on bridge aerodynamic 31

2.2.4 Double Slots decks and Messina Bridge 39

2.3 Computational fluid dynamics for bridge deck sections 46
2.3.1 Background on CFD simulations 46
2.3.2 Common CFD modelling approach for bridge engineering 47
Chapter 3 Experiment set-up and model configuration 56
3.1 Bridge Deck Model and wind tunnel description 56
3.1.1 Section model properties 56
3.1.2 Wind tunnel facility 61
3.2 The experimental set-up 63
3.2.1 Wind Force Coefficient Measurement 63
3.2.2 Free Vibration Spring System 65
3.2.3 The experiment procedure 71
Chapter 4 Experimental Results 73
4.1 Zero Wind Speed Free Vibration 73
4.2 Static aerodynamic force coefficients 75
4.3 Spring system results 80
4.3.1 Time displacement histories 80
4.3.2 Fast Fourier transform 102
Chapter 5 CFD Computational details and Results 115
5.1 Computational details 115
5.1.1 Numerical algorithms 115
5.1.2 Boundary conditions and mesh details 118
5.2 LES model validation with experimental results 120
5.3 Wind flow characteristics 123
5.4 Pressure distribution for the three-dimensional model 126
5.5 Aerodynamic force coefficients for the individual decks 130
Chapter 6 Flutter Derivatives Extraction 133
6.1 Flutter derivatives 133
6.2 Extraction of the flutter derivatives 134

6.3 Iterative least squares method 137
6.4 Comparison of the Flutter Derivatives 139
6.4.1 Comparison of the Theodorsen thin plate with Megane Bridge deck section 139
6.4.2 Comparison of the Megane Bridge Section with Other Deck Sections 143
6.5 Critical flutter velocity model and prototype prediction 147
Chapter 7 Conclusion and recommendations 149
7.1 Conclusions 149
7.2 Recommendations and Future work 152
References 154
Appendix A 159

List of Tables

Table 1-1 Critical flutter speed for bridge deck with without stabilizer or slot [3] 2
Table 2-1 Strouhal number for the Great Belt East Bridge [10] 13
Table 2-2 Critical flutter speed for girder with or without stabilizer [3] 35
Table 3-1 Calibration of the short spring 70
Table 3-2 Calibration of the short spring 70
Table 4-1 Summary of the maximum test wind speed for each angle cases 94
Table 6-1 Cut-off frequency for each wind speed cases 138
Table 6-2 Prediction of the critical flutter velocity 148

List of Figures

Figure 1.2.1 Wide slotted deck (Dorman Long Technology 2013) and narrow slotted deck with stabilizer (Ge & Xiang, 2009 [3]) 3
Figure 1.3.1 Flow-chart of the Megane Bridge deck aerodynamic stability evaluation 4
Figure 1.4.1 Geometrical dimensions of the Megane multi-deck prototype 6
Figure 2.1.1Flow past a two dimensional plate (Re<5) [2] 10
Figure 2.1.2 Flow past a two dimensional plate (Re>10) [2] 10
Figure 2.1.3 Flow past a two dimensional plate (Re > 250) [2] 11
Figure 2.1.4 Flow past a two dimensional plate (Re > 1,000) [2] 11
Figure 2.1.5 Karman vortex street behind a cylinder produced in a towing tank [6] 12
Figure 2.1.6 Relationship between Strouhal number and Reynolds number for circular cylinders [8] 13
Figure 2.1.7 Evolution of vortex shedding frequency with the wind velocity during the lock-in [2] 14
Figure 2.1.8 Aerodynamic forces induced by the wind flow [7] 15
Figure 2.1.9 Representation of the oscillatory motion of a body with appropriate notations [2]. 19
Figure 2.1.10 Real and imaginary parts of the Theodorsen circulatory function C (K) =F (K) + iG (K) [2] 20
Figure 2.2.1 Super long-span full bridge model with box girder [21] 24
Figure 2.2.2 Strouhal number St and drag coefficient CD as a function of Reynolds number Re [22] 29
Figure 2.2.3 Cross sections of deck models (dimensions for 1 : 10 scale model) [23] 30
Figure 2.2.4 Closed box girder section [25] 31
Figure 2.2.5 Plate girder section [25] 31
Figure 2.2.6 Static moment coefficients for different girder types [25] 32
Figure 2.2.7 13 Different Deck Types [26] 34
Figure 2.2.8 Relationships between the flutter speed and heaving degree [26] 34
Figure 2.2.9 Static coefficients comparison with angle of wind incidence for four cross-sections [27] 36

Figure 2.2.10 General layout and cross section at mid-span of the bridge twin-deck design configuration [28] 37
Figure 2.2.11Static Coefficients for different gap widths [25] 38
Figure 2.2.12 Geometric details and configuraitons for the basic deck models [30] 40
Figure 2.2.13Aerodynamic derivatives $A1*, H3*$ and $A2*$ of models 41
Figure 2.2.14 Configuration of the Messina Bridge [31] 42
Figure 2.2.15 Location of the sensors for the experiments of Messina Bridge deck [32] 42
Figure 2.2.16 Forced motion test rig. for the Messina Bridge deck [32] 43
Figure 2.2.17 Static coefficients of four famous bridges [32] 44
Figure 2.2.18 Variations of coefficients with angle of wind incidence for four cross-sections [27] 46
Figure 2.2.19 Geometry and boundary conditions for the CFD flow simulation around the flat section [35] 48
Figure 2.2.20 Comparison of the experimental results with the calculated results for the aerodynamic derivatives on the parallel rectangular section [35] 49
Figure 2.2.21 Flutter derivatives of the Great Belt East Bridge cross-section [36] 49
Figure 2.2.22 Section model and modeling of the permeable fence [37] 51
Figure 2.2.23 Three components of static aerodynamic wind forces (a) Cd (b) Cl and (c) Cm [37] 52
Figure 2.2.24 Bird's-eye view of instantaneous pressure contours [37] 53
Figure 2.2.25 Comparison of experimental and numerical aerodynamic coefficients of a box girder bridge section with and without handrails: (a) drag coefficient, (b) lift coefficient and (c) moment coefficient [38] 55
Figure 3.1.1 Prototype dimensions of the Megane Bridge deck with multiple gaps (m) 57
Figure 3.1.2 Dimensions of the four deck bridge model (mm) 58
Figure 3.1.3 Hollow shell of the Megane Bridge made by 3-D printing 59
Figure 3.1.4 3-D model created from Solidworks 59
Figure 3.1.5 Side deck foam core model 59
Figure 3.1.6 Middle deck foam core model 60
Figure 3.1.7 Final setting of the bridge section model in the wind tunnel 60
Figure 3.1.8 Upstream and downstream wind tunnel test sections 61

Figure 3.1.9 Inside view of the wind tunnel with floor roughness elements 62
Figure 3.1.10 Wind Tunnel Plan and Side View [39] 63
Figure 3.2.1 Force balance system measuring static wind force (One end) 64
Figure 3.2.2 Portable Strain Indicators 65
Figure 3.2.3 Laser sensor and ultrasonic sensor 65
Figure 3.2.4 Spring suspension system top view 66
Figure 3.2.5 Spring suspension system front view 67
Figure 3.2.6 Labview program detail 68
Figure 3.2.7 Final design of the spring system with laser sensors 69
Figure 3.2.8 Calibration for the force balance system 70
Figure 4.1.1Comparison of the displacements recorded under vertical motion only 74
Figure 4.1.2 Comparison of the displacements under torsional motion only 74
Figure 4.1.3 Vertical and torsional free vibration frequency 75
Figure 4.2.1 CL for the section model at 5 m/s and 10 m/s 77
Figure 4.2.2 CD for the section model at 5 m/s and 10 m/s 77
Figure 4.2.3 Lift coefficients obtained from the last three wind speed cases 79
Figure 4.2.4 Drag coefficients obtained from the last three wind speed cases 79
Figure 4.2.5 Galloping ratio for each attack angle under different wind speed 80
Figure 4.3.1 Sketch of the spring system [59] 81
Figure 4.3.2 Time displacement histories for the vertical and torsional modes at 3 m/s and 13 m/s wind speed under 0 ° attack angle 83
Figure 4.3.3 Time displacement histories for the vertical and torsional modes at 3 m/s and 12 m/s wind speed under 2 ° attack angle 86
Figure 4.3.4 Time displacement histories for the vertical and torsional modes at 3 m/s and 12 m/s wind speed under -2 ° attack angle 87
Figure 4.3.5 Time displacement histories for the vertical and torsional modes at 3 m/s and 10 m/s wind speed under 4 ° attack angle 89
Figure 4.3.6 Time displacement histories for the vertical and torsional modes at 3 m/s and 11 m/s wind speed under of -4 ° attack angle 90
Figure 4.3.7 Time displacement histories for the vertical and torsional modes at 3 m/s and 9 m/s wind speed under -6 ° attack angle 92

Figure 4.3.8 Time displacement history for vertical and torsional modes at minimum and maximum wind speed under attack angle of -8 °..... 94
Figure 4.3.9 Vibration amplitude at attack angle of 0 °, a) Vertical, b) Torsional 95
Figure 4.3.10 Vibration amplitude at attack angle of 2 °, a) Vertical, b) Torsional 96
Figure 4.3.11 Vibration amplitude at attack angle of -2 °, a) Vertical, b) Torsional..... 96
Figure 4.3.12 Vibration amplitude at attack angle of 4 °, a) Vertical, b) Torsional 97
Figure 4.3.13 Vibration amplitude at attack angle of -4 °, a) Vertical, b) Torsional..... 98
Figure 4.3.14 Vibration amplitude at attack angle of -6 °, a) Vertical, b) Torsional..... 99
Figure 4.3.15 Vibration amplitude at attack angle of -8 °, a) Vertical, b) Torsional..... 100
Figure 4.3.16 Vertical amplitudes variation for all wind test cases..... 101
Figure 4.3.17 Torsional amplitudes variation for all wind test cases 102
Figure 4.3.18 FFT before applying the low-pass filter 103
Figure 4.3.19 a) FFT of the bridge vibration under wind speed of 3 m/s and 13 m/s for attack angle of 0° 104
Figure 4.3.20 a) FFT of the bridge vibration under wind speed of 3 m/s and 12 m/s for attack angle of 2 °..... 106
Figure 4.3.21 a) FFT of the bridge vibration under wind speed of 3 m/s and 12 m/s for attack angle of -2 °..... 108
Figure 4.3.22 a) FFT of the bridge vibration under wind speed of 3 m/s and 10 m/s for attack angle of 4 °..... 109
Figure 4.3.23 a) FFT of the bridge vibration under wind speed of 3 m/s and 11 m/s for attack angle of -4 °..... 110
Figure 4.3.24 a) FFT of the bridge vibration under wind speed of 3 m/s and 9 m/s for attack angle of -6 °..... 112
Figure 4.3.25 a) FFT of the bridge vibration under wind speed of 3 m/s and 8 m/s for attack angle of -8 °..... 113
Figure 5.1.1 Geometry of the Bridge Deck model scaled 1:2 118
Figure 5.1.2 Mesh Detail for Simulation 119
Figure 5.2.1 Eddy viscosity distribution around the Megane deck for 50 m/s for a) RANS, b) LES 120
Figure 5.2.2 Instant pressure distribution around each deck with LES and RANS model..... 121

Figure 5.2.3 CFD lift coefficient vs. experiment lift coefficient 121
Figure 5.2.4 CFD drag coefficient vs. experiment drag coefficient 122
Figure 5.3.1 CFD simulation about the flow pattern around Megane Bridge deck for (a) α= 0 °, (b) α = 2 °, (c) α = 4 °, (d) α = -2 °, (e) α = -4 °..... 124
Figure 5.3.2 Three-dimensional flow patterns around the Megane Bridge deck for a) 0° front, (b) 0° back, (c) 2° front, (d) 2° back, (e) 4° front, (f) 4° back, (g) $-2°$ front, (h) $-2°$ back, (i) $-4°$ front, (j) $-4°$ back..... 125
Figure 5.4.1 Three-dimensional stress distributions for Megane Bridge Deck for a) 0° front, (b) 0° back, (c) 2° front, (d) 2° back, (e) 4° front, (f) 4° back, (g) $-2°$ front, (h) $-2°$ back, (i) $-4°$ front, (j) $-4°$ back..... 128
Figure 5.4.2 Pressure contours for the flow field around the Megane deck section, (a) α= 0 °, (b) α = 2 °, (c) α = 4 °, (d) α = -2 °, (e) α = -4 °..... 130
Figure 5.5.1 Drag coefficient for individual decks of the Megane Bridge..... 132
Figure 5.5.2 Lift coefficients for individual decks of the Megane Bridge 132
Figure 6.3.1 FFT before and after applying “Butterworth” filter 138
Figure 6.3.2 Algorithm for ILS used of the Matlab code 139
Figure 6.4.1 The experimentally extracted flutter derivatives vs. the theoretical thin plate results 142
Figure 6.4.2 Direct flutter derivatives comparison between four bridge decks..... 144
Figure 6.4.3 Cross flutter derivatives comparison between four bridge decks..... 146

Nomenclature

CFD	Computational fluid dynamics
ILS	Iterative least square
LES	Large eddy simulation
RANS	Reynolds Average Navier-Stokes
VIV	Vortex-induced vibration
ρ	Fluid density, kg/m^3
V	Mean velocity, m/s
L	Characteristic linear dimension of the structure, m
μ	Dynamic viscosity, $kg/(s \cdot m)$
Re	Reynolds number
F_i	Inertial forces, N
F_v	Viscous forces, N
St	Strouhal number
f	Frequency, Hz
B	Width of the cross-section, m
$C_L(\alpha)$	Aerodynamic lift coefficient respect to the angle of attack
$C_D(\alpha)$	Aerodynamic drag coefficient respect to the angle of attack
α	Angle of attack, °
V_r	Total relative velocity, m/s
ζ	Damping ratio
ω	Natural circular frequency, Hz
m	Mass, kg
I	Mass moment of inertia, $kg \cdot m^2$

r_g	The radius of gyration of the body, m
F (K)	Real part of Theodorsen circulatory function
G (K)	Imaginary part of Theodorsen circulatory function
H_i^*, A_i^*	Nondimentional parameters, flutter derivatives
L_h	Aerodynamic Lift force, N
M_α	Aerodynamic Moments, $N \cdot m$
E_{eff}	Effective modulus of elasticity
g	Gravitational acceleration, m/s^2
ABS	Acrylonitrile butadiene styrene plastic
ABL	Atmospheric boundary layer
k	Equivalent stiffness of the spring, N/m
C (t)	Vertical movement at the center of the bridge, m
$h(t)$	Net displacements, m
FFT	Fast Fourier Transform
$\underline{M}$	Mass matrix
$\underline{C}$	Damping matrix
$\underline{K}$	Stiffness matrix
$\underline{C^{eff}}$	System aeroelastically effective damping matrix
$\underline{K^{eff}}$	System aeroelastically effective stiffness matrix
U_{red}	Reduced wind speed

Chapter 1 Introduction

1.1 Wind Load Effect on Long-span Bridge

Before 1940, long-span bridges were predominantly designed to withstand static wind load only, until the collapse of the first Tacoma Narrow Bridge under the effect of less than half of its design wind speed [1]. The dramatic failure subverted the conventional designing concept and determined the appearance of a new type of investigation about the aerodynamic instability of long and slender structures, such as suspension bridges. The wind-induced load, which is also referred to the motion-induced or self-excited force, can modify the deformation as well as the induced dynamic response of the long-span bridge. However, in turn the deformation and the dynamic response can also affect the loads acting on the bridge. The interaction between the forces and the deformation leads to the negative dynamic damping, which means that the energy lost due to the structural damping is less than the energy induced by the wind loads. Under this circumstance, the long-span bridge can easily experience unexpected large vibrations, resulting in a dramatic disaster. With the increased span the bridges became more flexible and also the damping capabilities became lower, thus resulting in a higher vulnerability to wind induced vibrations.

Various methods have been adopted in analysing the wind load effects and the dynamic instability of long-span bridges, but still the prediction of aerodynamic loading is quite difficult without the assistance of wind tunnel tests [2]. Different types of bridge modelling are available for wind tunnel tests for capturing the wind flow evolution around a flexible bluff body. Among them, the most straightforward one is the full bridge model test, which requires an accurate bridge modelling and a large size facility. However, the section model test, which allows a relatively good understanding of bridge stability under wind loads, but at lower costs than the full bridge model became an important approach in the bridge design stage. Nowadays, due to the progress in understanding the aerodynamic phenomena and the mechanisms of the flow-

structure interaction, stability of suspension and cable-stayed bridges has greatly improved [Wardlaw, 1992, Larsen et al, 1995, Matsumoto et al, 2007, etc.].

1.2 Research motivation

The study performed by Ge and Xiang (2009) [3] mentioned that the limit of the span length due to aerodynamic stability is about 1,500 m for the traditional suspension bridges. In order to overpass the span limitation, new bridge deck geometries, which involve adopting several slots into the deck and connecting the multiple-decks by stabilizing beams have been proposed by wind engineers. Thus the construction of twin box deck bridges has been already blooming in recent years: Stonecutters Bridge finished in 2009 in Hong Kong [Hui et al, 2008] of 1,377m main span, Tsing Ma Bridge built in 1997 [Xu et al, 1997] with main span of 1,650 m, Xihoumen Bridge completed in 2008 [Ge and Xiang, 2009] of 1,410m main span, Great Belt Bridge in Denmark [Larsen, 1993] etc. Besides, several initiatives of designing multi-box decks have also been considered for long-span bridges such as 3,300m Messina Bridge [Diana et al, 1995], 5,000 m Gibraltar Strait Bridge [Lin and Chow, 1991] and Sunda Strait Bridge which is still under design, construction pending [Wangsadinata et al, 1992].

Table 1-1 Critical flutter speed for bridge deck with without stabilizer or slot [3]

CRITICAL FLUTTER SPEEDS OF THE ZHEJIANG XIHOUMEN BRIDGE

Deck Box Girder Configuration	Critical flutter speed (m/s)				Required (m/s)
	−3°	0°	+3°	Minimum	
Single box girder	50.7	46.2	48.7	46.2	78.4
Single box with a 1.2m stabilizer	>89.3	>89.3	37.7	37.7	78.4
Single box with a 1.7m stabilizer	88.0	>89.3	43.4	43.4	78.4
Single box with a 2.2m stabilizer	>89.3	>89.3	88.0	88.0	78.4
Twin box with a slot of 6m	88.4	>89.3	>89.3	88.4	78.4
Twin boxes with a slot of 10.6m	>89.3	>89.3	>89.3	>89.3	78.4

According to a study made by Ge and Xiang (2009) [3] a 5,000 m suspension bridge can be achieved either by employing a wide slotted deck, or a narrow slotted deck with vertical and horizontal stabilizers.

Figure 1.2.1 Wide slotted deck (Dorman Long Technology 2013) and narrow slotted deck with stabilizer (Ge & Xiang, 2009 [3])

These new deck configurations ensure the longer bridge span sought, and at the same time they have a better aerodynamic performance, such as higher critical flutter speed, which is an important aspect when designing super-long span bridges. The critical flutter speeds where effective damping equals to zero and the structure oscillation motion starts diverging represents the highest wind speed a bridge can withstand before encountering the most critical aerodynamic instability induced by the coupling of the torsional and vertical vibrations of the bridge and the continuous interaction with the varying aerodynamic loads. The critical flutter speeds for twin box bridge decks are much higher than those of the conventional single box as it can be noticed from Table 1-1 [3]. Besides, the flutter instability for the Messina multi-box deck, which occurred, during the experiments, beyond the design wind speed of 62 m/s, the reported static aerodynamic coefficients showed a smoother evolution than most of the conventional full-box girders and twin box girder decks [Diana et al, 2012, Diana et al, 1995]. However the resonant response for the vortex-induced vibrations (VIV) observed in the wind tunnel tests performed for the multiple-deck section proposed for Messina Bridge was significant [4].

Thus, in order to further improve the aerodynamic characteristics of multi-box deck sections, for both lower wind speeds where the VIV phenomena yields dominant resonant vibrations and for the high wind speeds where flutter instability might occur, a new bridge deck entitled Megane deck, with two side decks for traffic lanes, two middle railway decks and a total of 3 gaps separating them, is proposed during this research. A series of investigations of the aerodynamic properties have been carried out through wind tunnel tests on the Megane Bridge

deck section model scaled 1:80, for angles of attack between -10° and +10° and wind speeds up to 15 m/s. Most of the investigations focused on the flutter verification, aerodynamic coefficients and efficiency of various aerodynamic counter-measures, however did not detail the wind flow formations through the gaps and around the multiple decks, thus could not determine precisely the relationship between the wind flow pattern and the pressure release along the bridge decks. Computational Fluid Dynamics (CFD) simulations were conducted for this purpose and the accuracy of the results were also verified by comparison with the experimental results. Moreover, after the validation of the numerical model, the flow turbulence and wind speed data were extracted and were used for explaining the pressure and force coefficients obtained from the wind tunnel experiments.

1.3 Research objectives

This work focuses on the evaluation on the aerodynamic stability of the Megane Bridge with multi-deck configuration, by the means of three investigation procedures: the wind tunnel experiment, the CFD simulations and the numerical identification of the flutter derivatives. A simplified flowchart is presented in Figure 1.3.1 detailing the evaluation steps performed under each procedure as follows: the static wind tunnel tests were performed for measuring the

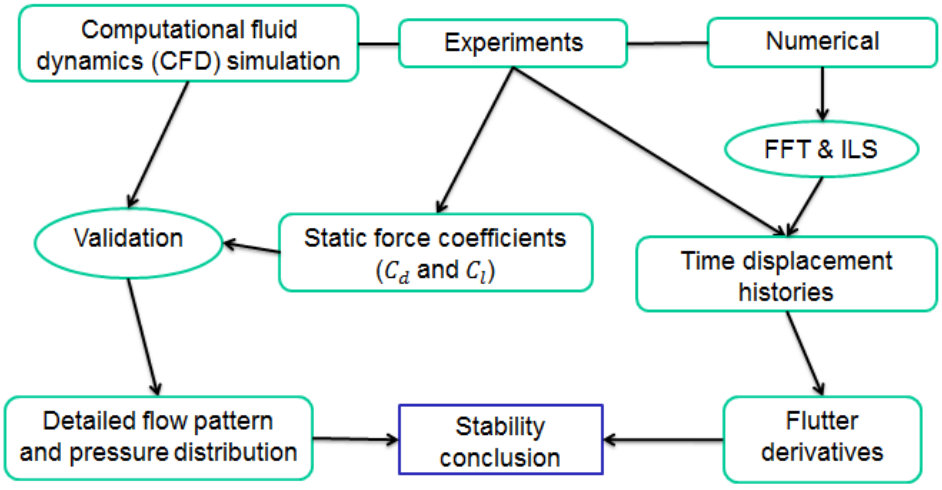

Figure 1.3.1 Flow-chart of the Megane Bridge deck aerodynamic stability evaluation

aerodynamic drag and lift force coefficients static C_L and C_D for several angles of attack; these coefficients were used for validating the Computational Fluid Dynamics (CFD) simulation, and thus the flow pattern and pressure distributions, which were not able to be obtained from the wind tunnel experiment, were determined from the CFD model for each individual deck composing the Megane multi-deck investigated. Based on the dynamic test, where the displacement time histories of the torsional and vertical vibrations of the Megane deck were measured, a frequency analysis was performed by the use of Fast Fourier Transform (FFT) and the flutter derivatives were obtained by applying the iterative least square (ILS) method, as part of the numerical procedure employed in this research. The flutter derivatives numerically extracted and a critical flutter speed of the Megane multi-deck prototype were estimated as a first stability recommendation for the aerodynamic instability. These recommendations were completed with the information regarding the critical wind-induced pressure and the turbulent flow formed around some of the individual decks of the Megane multi-deck.

1.4 Scope of Research

The prototype of the Megane multi-box deck has a total width of 62.0 m and a height of 5.0 m; each traffic deck (decks A and D) has 16.0 m width and a maximum height of 3.0 m, while the middle railway decks (decks B and C) have 10.0 m width and 2.0 m height each (Figure 1.4.1).The gaps between the decks are 3.6 m each and connecting beams of 3.0 m width and 5.0 m height were considered every 10.0 m along the decks.

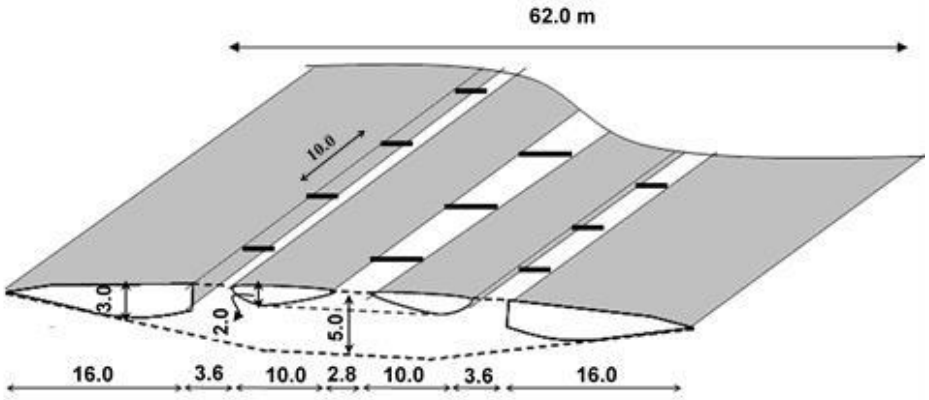

Figure 1.4.1 Geometrical dimensions of the Megane multi-deck prototype

- Static coefficients tests: A scaled 1:80 bridge section model was made through 3D printing and hot-wire cutting technique. Then the bridge deck section model was fixed during the tests and two force balances were used to measure the forces induced by flow to the bridge section, under different velocities and attack angles. 11 angles of attack were tested ranging from -10 °to 10 °varying every 2 °and the test wind speed in the wind tunnel started from 3.0 m/s and was increased up to the 10 m/s in steps of 1.0 m/s. Static force coefficients C_L and C_D corresponding to measured lift and drag aerodynamic forces were determined from the experiment and were plotted for comparison with other types of decks.
- Free vibration tests: The same Megane Bridge deck section model was mounted on a spring suspension system consisting of a total of 8 springs, 4 springs on each side of the model. Similar to the static tests, the vibration tests were performed under 9 attack angles with a maximum of 8 °and a minimum of -8 °. The test wind speeds started from 3 m/s; however the maximum test speed varied from case to case, depending on the observation of flutter instability occurrence. Free vibration displacement time histories were measured by two displacement sensors, one laser sensor and one ultrasonic sensor, and the data were recorded using the Labview program. Fast Fourier transforms were applied to all the displacement histories, for evaluating the vibration frequency from different flow cases. Flutter derivatives under an attack angle of 0°were also attempted using the iterative least square (ILS) method proposed by Sakar (2003) [5].
- CFD simulations: A detailed investigation of the wind flow evolution around the Megane Bridge multi-deck was performed employing the three-dimensional CFD – Large Eddy Simulation (LES), through the use of the Ansys Fluent commercial software. However to achieve convergence of the LES model, the Reynolds Average Navier-Stokes (RANS) algorithm was used. The drag and lift coefficients determined from the static wind tunnel test were used as a validation of the CFD-LES numerical model. Once the aerodynamic force coefficients were validated the flow patterns and the pressure distributions for the Megane deck section are discussed, based on the LES model. Thus

the results from the experimental tests were complemented by the outcomes of the CFD simulations.

- Numerical procedure: The experimentally obtained time displacement histories for the torsional and vertical vibrations were analysed in the frequency domain by the use of Fast Fourier Transformation (FFT), after which the ILS method recommended by Sarkar, (2003), [5] was applied to extract the flutter derivatives. The extracted flutter derivatives were compared with the Theodorsen's theoretical formulation for a flat plate [11] and also with the flutter derivatives obtained by similar investigation methods for other bridge decks of similar configurations.

1.5 Thesis Layout

The research motivation on the Megane Bridge is listed in Chapter 1 and in order to perform an accurate aerodynamic investigation of the Megane Bridge multi-deck, first it is required to understand the basic concepts of the wind-induced phenomena, which are presented in Chapter 2 along with the documents reporting the evaluation of the aerodynamic properties of various deck types, through experimental research which were also carefully detailed and interpreted. Moreover, since the CFD simulation for the flow around the deck is required, two major CFD flow models LES and RANS were reviewed and briefly discussed in Chapter 2.

The section Megane multi-deck model's dimensions and some dynamic characteristics were analyzed in Chapter 3. Chapter 3 also includes the detailed information about the deck model construction, instrument set-up, experimental techniques developed, and testing procedure for the static force coefficients as well as for the free vibration tests.

Chapter 4 and 5 are associated with the main part of this investigation, where the wind tunnel experiments and numerical analysis results are presented and analyzed, respectively. Lift and drag coefficients are presented and compared. Followed by demonstration of time displacements histories obtained from each flow case and the vibration frequency variations are also analyzed, case by case through the Fast Fourier transform in Chapter 4. Validation of the CFD-LES simulations, by comparing with the results from the experiment, was conducted in Chapter 5. Also, Chapter 5 concentrates on clarifying the flow patterns, pressure distributions

around the bridge multi-deck and also the effect of the different angles of attack. Related to the pressure distribution on the surface of the deck, static force coefficients for each separate deck were obtained through the CFD-LES simulation.

Chapter 6 describes the issues related to the flutter derivatives, together with the extraction techniques from the time displacement histories. The iterative least square (ILS) method proposed by the Sarkar (2003) is detailed and explained. The flutter derivatives are presented together with a comparison between the theoretical results and the reference values from other three different bridges, of similar deck configuration.

General discussions based on the results and the summary of the conclusions, which were derived from the current experimental and numerical investigations, along with the recommendations for the future research are presented in the Chapter 7.

Chapter 2 Literature review

2.1 Bridge Aeroelasticity Theory

2.1.1 Wake and Vortex formation around structures

The evolution of the air flow around a structure is dependent on many variables, such as flow velocity, cross sectional area of the structure, surface roughness and wind direction. The Reynolds number is a non-dimensional parameter that characterizes the flow effect on structures and helps distinguish flow types such as: laminar and turbulent [2]. The Reynolds number, Re, is defined as the ratio of kinetic force to inertial force, which is

$$Re = \frac{F_i}{F_v} = \frac{\rho LV}{\mu} \tag{2.1}$$

Where, ρ is the fluid density, V is the mean velocity, L is the characteristic linear dimension of the structure, and μ is the dynamic viscosity. When Re is smaller than 1 x 10^3, viscous forces dominate the flow characteristics. These forces keep the flow stream lines constant, so they can flow steadily in regard to each other and can form predictable paths. The inertial forces however will take a dominating role once Re is higher than 1 x 10^4. The fluid motion in this case becomes extremely irregular, each part of the flow mixing intensively and the particle trajectories becoming chaotic, which means that the flow field is very unstable. Simiu and Scanlan (1996) [2] provided a comprehensive classification for different types of flow separation, behind a slid body, represented by a two dimensional plate, in respect to the order of Reynolds number, as follows.

When the laminar flow hits a solid body, the separation of the flow occurs around its edges, at a very low Reynolds number, Re < 5.0 and the fluid flow bypasses the corners and follows the shape of the plate, as it can be noticed in Fig. 2.1.1.

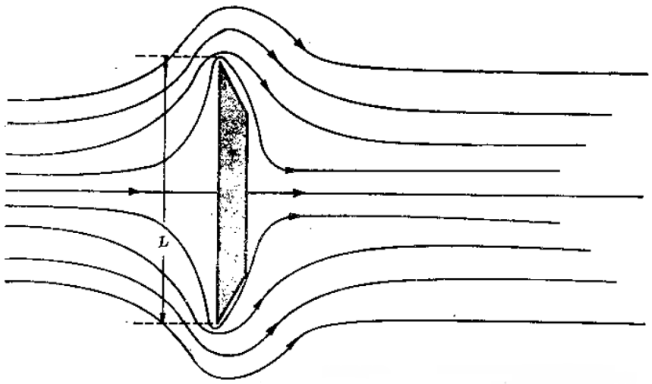

Figure 2.1.1Flow past a two dimensional plate (Re<5) [2]

When Re increases, for example over 10.0, the flow separates from the corners of the plate and forms a symmetrical pair of vortices attaching at the back of the plate (Fig 2.1.2).

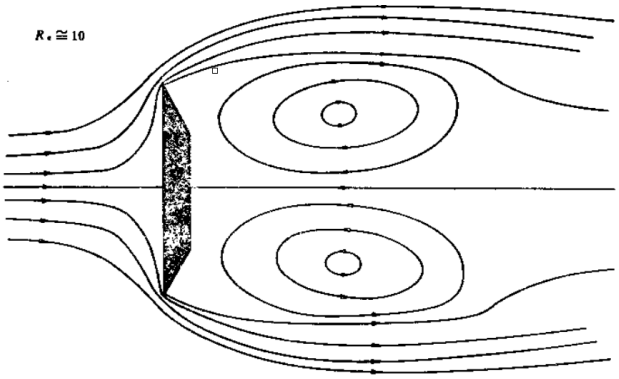

Figure 2.1.2 Flow past a two dimensional plate (Re>10) [2]

Since it is the same plate, the Reynolds number can increase simply by raising the wind velocity. Thus, at Re > 250, for higher wind speeds, two symmetrical vortices break away and are replaced by a periodic alternating vortices formed at the upper and lower edge of the plate (Fig. 2.1.3).

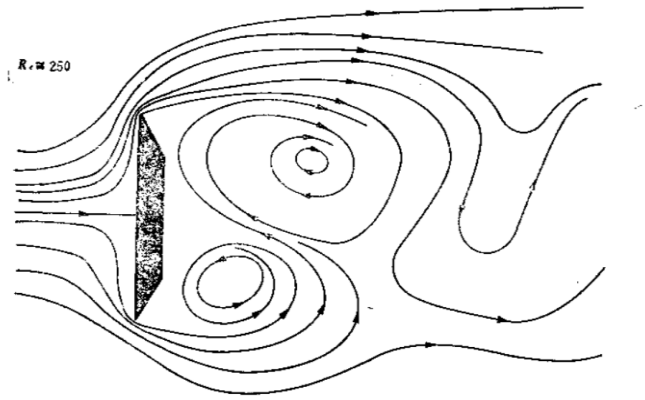

Figure 2.1.3 Flow past a two dimensional plate (Re > 250) [2]

As the Reynolds is further increased, Re > 1,000, the inertial forces start dominating the characteristics of the flow. At this stage, large vortices are unlikely to form behind the plate, instead a turbulent flow will form in the shear layers detaching from the corners of the plate. The shear layers are composed by a series of small vortices providing the turbulent flow with two clear boundaries which make the wake flow region and the adjacent smooth areas coexist together (Fig. 2.1.4.).

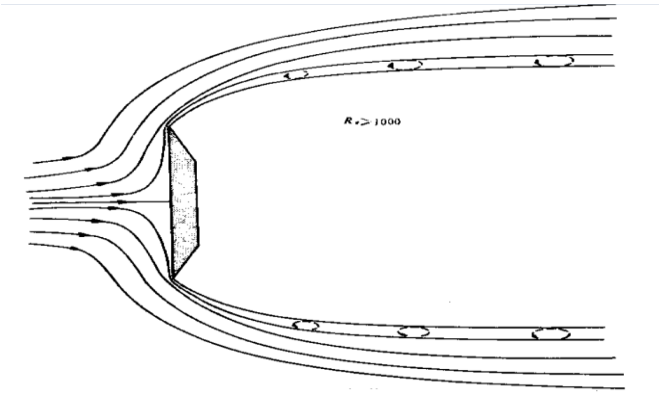

Figure 2.1.4 Flow past a two dimensional plate (Re > 1,000) [2]

For different shapes, rectangular plates, circular cylinders, etc., the flow evolution as a function of Re number would slightly change [2], however the current study focused on reviewing the flow patterns for structural shapes resembling bridge deck sections, such as the slid plate presented in Figure 2.1.1 to Figure 2.1.4.

2.1.2 Strouhal number and the Lock-in Phenomenon

For a certain range of Reynolds numbers, when flow past a bluff body, such as a square cylinder, a rectangular cylinder or any bridge deck shape, vortices are created behind the body, as depicted in the above pictures. Thus, a low pressure region is generated at the downstream side of the bluff body. These vortices are created due to the upper and the lower flow successive motion towards the low pressure region and these detach periodically from both sides of the body, phenomena known as the Karman vortex shedding [6].

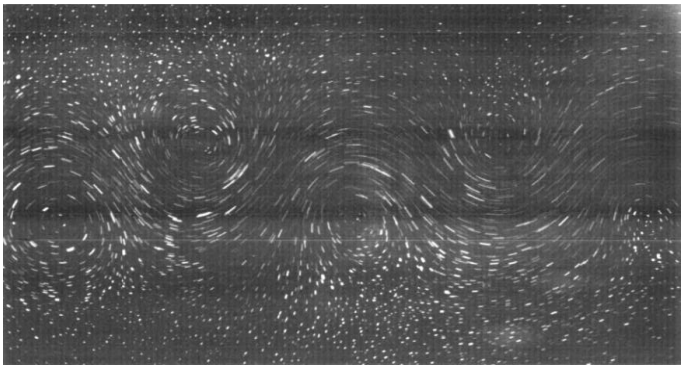

Figure 2.1.5 Karman vortex street behind a cylinder produced in a towing tank [6]

Vincent Strouhal, a Czech physicist found that there is a certain connection between the vortex shedding frequency, velocity of the flow and the diameter of the cylinder [7]. He expressed the relationship by the aid of Strouhal number (St) as follows:

$$St = \frac{fL}{V} \tag{2.2}$$

where f is the frequency of the vortex shedding, L is the characteristic length and V is the velocity of the fluid. Figure 2.1.5 shows the relationship between the St and the Re numbers for a smooth surface cylinder [8]. It can be noticed that, in the low Reynolds number region, St number increases parallel with the Re number. A stagnation is noticed when St number reaches 0.2, in spite of the fact that the Re number keeps increasing. At this stage, the vortices start shedding from the cylinder periodically. When the Reynolds number increases beyond 10^5, St number spikes up rapidly (upper line in Fig. 2.1.5.) and in this region random vortex shedding

appears. For a cylinder with rough surface, St does not change significantly staying at around 0.2 for the entire range of Re numbers, as the lower line in Fig. 2.1.5 shows. Basically, Strouhal number can be determined through wind tunnel experiments performed on circular cylinders, bridge deck models or other structures of interest. From the flow data measured in the wind tunnel, the Strouhal number for the full-scale bridge can be calculated by multiplying with the scale factor, usually ranging from 0.05 to 0.2 for bridge decks (Chen, 1990 [9]), such as Figure 2.1.6 made by Braun and Awruch (2003) [10]. Thus, as long as wind velocity is known, the frequency of a vortex can be easily obtained.

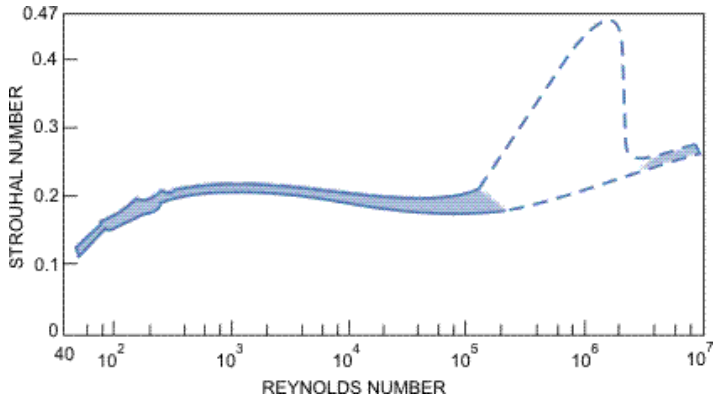

Figure 2.1.6 Relationship between Strouhal number and Reynolds number for circular cylinders [8]

Table 2-1 Strouhal number for the Great Belt East Bridge [10]

Reference	Strouhal number - Reynolds $3x10^5$
Present work	0.180
Larsen et al. (1998) (numer.)	0.170
Wind tunnel tests (from: Larsen et al. (1998))	0.160

Shear layers shedding from the corners of the body, cause the asymmetry of the vortices formed in the wake behind the structure, which in turn develop varying lift forces on each side of the bluff body. The bridge decks, which are flexible bluff bodies, and are mounted on elastic supports in experiments to simulate this flexibility, will experience an oscillating motion due to

the difference in lift forces. This kind of motion usually appears at low Reynolds numbers and at relatively moderate wind speed [5, 6, and 10]. At the beginning the motion amplitude is quite small and does no harm the bridge deck. Since the oscillation is driven by the lift forces caused by the vortex shedding, the alternative lift force frequency is equal to the shedding frequency, which can be determined by the Strouhal number. Thus, the shedding frequency is governed by the geometry of the bridge deck, wind speed and the angle of attack. When the shedding frequency coincides with the natural frequency of the body, resonant amplification will occur: the amplitude of oscillation grows with the increasing wind speed and starts to control the vortex frequency. Even the nominal frequency based on Strouhal number can deviate from the natural frequency with a few percentages, thus the shedding is still under control [2]. This resonant phenomenon of setting the flow frequency to the natural frequency of the structure is known as the "lock-in". During the stage of the "lock-in", the amplitude rarely exceeds half of the across wind dimension [2]. As a result, the bridge deck oscillation due to the vortex shedding is not decisive for the stability of the respective bluff body, but can cause fatigue of the structure's material and uncomfortable vibrations for the people and the vehicular traffic crossing the bridge.

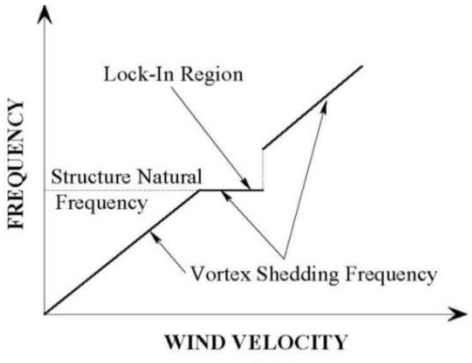

Figure 2.1.7 Evolution of vortex shedding frequency with the wind velocity during the lock-in [2]

2.1.3 Galloping aerodynamic instability

Galloping is an instability typically noticed for slender structures, as stated by Simiu and Scanlan, 1996 [2]. However this has become a potential threat to the stability of bridges due to the increasing length and flexibility of the bridge spans, thus a thorough verification is always

required prior to constructing a long-span bridge. Galloping instability, occurs usually at high wind speeds and has two major patterns, one of them is the bending oscillation that affects the bridge deck and the other is the across-wind horizontal oscillation, which affects the towers during the erection of suspension and cable-stayed bridges. For cases of galloping where the oscillation amplitude is quite large, on the order of several times the cross-sectional dimension of the bluff body, this can quickly lead to the failure of the oscillating structure. Basically, for the occurrence of galloping, the wind flow speed is much larger than the one reported for the "lock-in" and the frequency is much lower than the vortex shedding frequency found in Kármán Vortex Street. Another characteristic for galloping instability is that the flow reattachment which can be observed at vortex "lock-in" vanishes due to the high wind velocity. The flow is fully separated at the back of the bluff body and the vortex induced effects disappear. Because of this, the pressure distribution on the upper and the lower surface is almost the same in vibrating body and the body at rest. Thus, the quasi-steady theory is applied to the galloping analysis, that is the self-excited forces may be described by the forces acting on the body at rest [2].

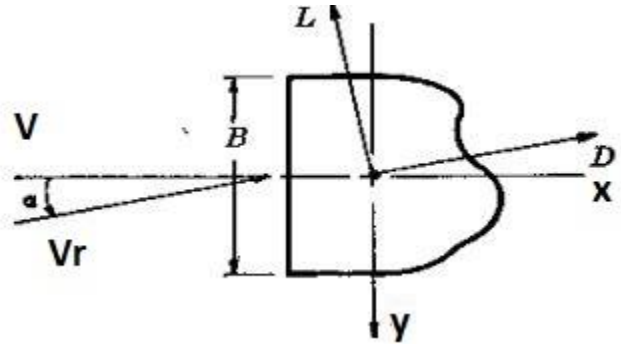

Figure 2.1.8 Aerodynamic forces induced by the wind flow [7]

Considering a body which is elastically restrained and mechanically damped in the direction normal to x-axis the body's motion is caused by the wind flow consisting of two parts, one is the motion induced by the flow velocity V, in the horizontal direction and the other is the motion $v = -\dot{y}$ moving up and down in the vertical direction (Fig. 2.1.8). The total relative velocity V_r becomes $V_r = \sqrt{v^2 + {V_r}^2}$ and the flow has an effective angle of attack with respect to the body of $\alpha \approx v/V_r$. The drag and lift aerodynamic forces in the along-wind and across-wind directions respectively can be written as [7]:

$$D(\alpha) = \frac{1}{2}\rho V_r^2 B C_D(\alpha) \tag{2.3}$$

$$L(\alpha) = \frac{1}{2}\rho V_r^2 B C_L(\alpha) \tag{2.4}$$

where B is the width of the cross-section, ρ is the air density and the $C_L(\alpha)$ and $C_D(\alpha)$ are the aerodynamic lift and drag coefficients for the oscillation body, respectively.

When the drag and lift forces are projected on the y and x directions, the total forces along these axes can be written as:

$$F_y(\alpha) = -D(\alpha)\sin(\alpha) - L(\alpha)\cos(\alpha) = \frac{1}{2}\rho V_x^2 B C_{F_y}(\alpha) \tag{2.5}$$

Since $V_x = V_r cos\alpha,$ then C_{F_y} can be rewritten as:

$$C_{F_y}(\alpha) = \frac{-[C_L(\alpha) + C_D(\alpha)\tan(\alpha)]}{\cos(\alpha)} \tag{2.6}$$

For small angles of attack, $\alpha = \frac{\dot{y}}{V} = 0,$ the equation turns to

$$\left.\frac{dC_{F_y}}{d\alpha}\right|_{\alpha=0} = -(\frac{dC_L}{d\alpha} + C_D)_{\alpha=0} \tag{2.7}$$

The body unit mass is m and its equation of motion is:

$$m[\ddot{y} + 2\zeta\omega_1\dot{y} + \omega_1^2 y] = F_y \tag{2.8}$$

where ζ is the damping ratio and ω_1 is the natural circular frequency. F_y represents the aerodynamic force acting on the body.

As a result the following equation of motion due to aerodynamic forces can be written:

$$m[\ddot{y} + 2\zeta\omega_1\dot{y} + \omega_1^2 y] = -\frac{1}{2}\rho V^2 B(\frac{dC_L}{d\alpha} + C_D)_{\alpha=0}\frac{\dot{y}}{V}$$

(2.9)

The sum of mechanical and aerodynamic damping affecting the system is therefore:

$$2\zeta\omega_1 m + \frac{1}{2}\rho V^2 B\left(\frac{dC_L}{d\alpha} + C_D\right)_{\alpha=0} = d$$

(2.10)

According to the theory used for estimating the possibility of encountering galloping, established by Den Hartog [2] the system damping should be negative (Eq. 2.10), while the mechanical damping is usually positive, which means that the aerodynamic damping must be negative during the galloping instability. In short, galloping is the phenomenon related to the flow pattern around the body, but for non-separated flow, galloping does not occur because the coefficient $\left(\frac{dC_L}{d\alpha} + C_D\right)_{\alpha=0}$ grows with the attack angle and makes the aerodynamic damping stay in the positive range. However if the angle of attack increases beyond a threshold value, the boundary layer separates and the lift coefficient, C_L starts to decrease. Therefore once the wake is fully separated, also the lift coefficient turns to negative values ($\left(\frac{dC_L}{d\alpha} + C_D\right)_\alpha < 0$), and the possibility of galloping oscillations appears, as stated by the Den Hartog criterion [2].

2.1.4 Flutter aerodynamic instability

Flutter is one type of self-excited aeroelastic phenomenon. Under a certain frequency and phase the oscillation can obtain energy from the wind force to offset the attenuation effect caused by the damping of the structure itself. Once the structure exposed to the wind force starts to vibrate, the amplitudes grow with time and wind speed and can quickly lead to a catastrophic failure of the structure. Usually there are two kinds of flutter in bridge aerodynamics. One is a classical flutter which is a two-degree of freedom oscillation. Usually this relies on aerodynamic coupling between two modes (first torsional modal and first vertical modal), thus it is also known as the coupled flutter. The frequencies of those two modes get closer to each other due to the increasing wind speed and thereafter two scenarios can be encountered: a) both the vertical and torsional frequencies change up to a certain value in between, and b) only the vertical frequency

might vary. For the first scenario, the vertical frequency increases with the aerodynamic stiffness while the torsional frequency decreases due to the increasing aerodynamic damping. For the latter scenario, the torsional frequency dominates and only the vertical frequency varies. But when both the frequencies match each other, resonance between the two motions will occur and the amplitudes of these self-excited oscillations will grow rapidly causing structure failure in a short period of time. Stall flutter or torsional flutter is the second kind of flutter which is a single-degree of freedom phenomenon. It has the feature that it doesn't rely on the coupling of two vibration modes and it is controlled by the nonlinear aerodynamic force. Flutter is always accompanied by vortex shedding, but it is distinct from the vortex induced vibration detailed in section 2.1.2 above. Vortex induced oscillation largely depends on the frequency and a large amplitude of oscillation occurs only when the vortex shedding frequency equals the natural frequency of the structure. Once the velocity is larger than the "lock-in" velocity, the oscillation becomes much weaker. For the flutter phenomenon, once this sets in, the strength of oscillation increases monotonically with the wind velocity and it never stabilizes again.

Researchers spent decades in trying to solve the flutter induced instability. From Theodorsen's theory [11] which was used to calculate flutter in a flat plate all the way to Scanlan's theory [2] which has become a standard procedure to obtain a good estimate of the flutter, numerous studies have been performed, but the expressions for self–excited forces still remain the main difficulty in estimating flutter induced oscillation. Theodorsen's theory works with aerodynamic shape bodies, such as airfoils, or thin plates, also assuming that the plate movement is an oscillatory motion in two dimensions.

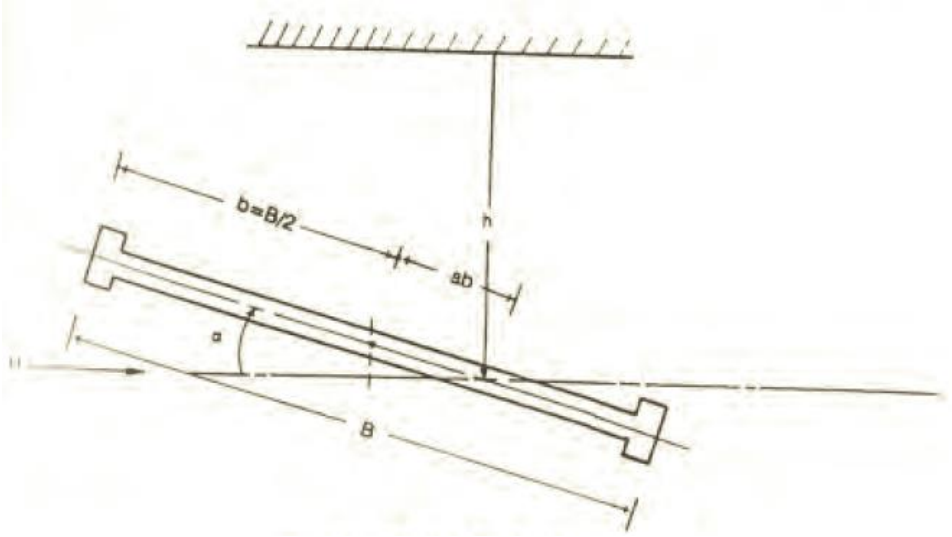

Figure 2.1.9 Representation of the oscillatory motion of a body with appropriate notations [2]

For such a two-degree-of-freedom linear dynamic system the equation of motion is usually defined as Simiu and Scanlan, 1996 [2]

$$m\left(\ddot{h} + a\ddot{\alpha} + 2\zeta_h\omega_h\dot{h} + \omega_h^2 h\right) = L_h \tag{2.12}$$

$$I\left(\frac{a}{r_g^2}\ddot{h} + \ddot{\alpha} + 2\zeta_\alpha\omega_\alpha\dot{\alpha} + \omega_\alpha^2\alpha\right) = M_\alpha \tag{2.13}$$

where m and I are the model mass and mass moment of inertia of the system, r_g is the radius of gyration of the body about the center of the rotation, ζ_h and ζ_α are the mechanical damping ratios-to-critical in bending and torsion, respectively. ω_h , ω_α are the natural and circular frequencies. Usually for bridge decks that are symmetrical, in which case a=0 and leaving $a\ddot{\alpha}$ and $\frac{a}{r_g^2}\ddot{h}$ equal to zero. The right hand side of the equations are the self-excited aerodynamic force and moment. Theodorsen developed a set of theoretical formulation to express the self-excited aerodynamic forces (lift and moment) for the aim of calculation [13].

$$L = 2\pi b\rho U^2\{(F+iG)\left[\alpha_0 + \frac{i}{b}kh_0 + \left(\frac{1}{2} - a\right)ik\alpha_0\right] - \frac{1}{2}k^2\left(\frac{h_0}{b} - a\alpha_0\right) + \frac{1}{2}ik\alpha_0\}e^{ik\tau} \tag{2.14}$$

$$M = 2\pi b^2 \rho U^2 \{\left(\frac{1}{2} + a\right)(F + iG)\left[\alpha_0 + \frac{i}{b}kh_0 + \left(\frac{1}{2} - a\right)ik\alpha_0\right] - \frac{1}{2}k^2 a\left(\frac{h_0}{b} - a\alpha_0\right) + \left(\frac{1}{2} - a\right)ik\alpha_0 + \frac{k^2}{8}\alpha_0\} e^{ik\tau}$$

(2.15)

where U is the average speed of the wind flow and ρ is the air density, b is the half width of the plate, and a is the distance from the midpoint of the plate to the point of rotation. The movement amplitude is expressed by $h = h_0 e^{i\omega t}$ and the phase angle with respect to the excitation force is $\alpha = \alpha_0 e^{i\omega t}$. Using the non-dimensional time variable $\tau = \omega t/U$, the displacement and the rotation can be rewritten as $h(\tau) = h_0 e^{ik\tau}$, $\alpha(\tau) = \alpha_0 e^{ik\tau}$, where $k = \omega b/U$ known as the reduced frequency response and b is the half chord of the airfoil. F and G are the real and imaginary parts of Theodorsen circulatory function $C(k) = F(k) + iG(K)$, respectively.

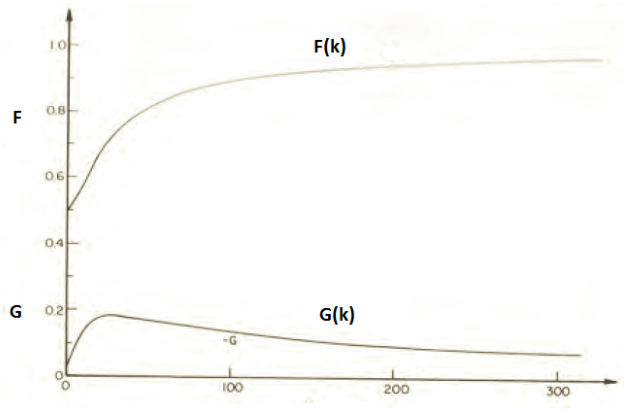

Figure 2.1.10 Real and imaginary parts of the Theodorsen circulatory function C (K) =F (K) + iG (K) [2]

Usually the value of $C\ (k)$ is not accurate and R. T. Jones (1955) [14] presented the approximate formulation as

$$C(k) = 1 - \frac{0.165}{1 - (0.445)/k \cdot i} - \frac{0.335}{1 - (0.3)/k \cdot i}$$

(2.16)

After Theodorsen's theory successfully simulated the wind induced force on an airfoil, Bleich (1948) [15] attempted to apply it directly to a bridge deck for calculating the flutter forces, but due to the geometry of the bridge deck section and the sensitivity of aerodynamic coefficients, the calculated forces didn't match well with the experimental results. Scanlan and Tomoko (1971) [16] established the flutter self-excited force formulae and developed the concept of flutter derivatives after considering the essential difference between aerodynamic shape bluff body and the deck section. Since the flutter forces can be expressed as a linear combination of the deck movement just as Theodorse considered in his theory, the lift force and the moments are defined as [11]:

$$L_{ae} = \frac{1}{2}\rho U^2 B(KH_1^*\frac{\dot{h}}{U} + KH_2^*\frac{B\dot{\alpha}}{U} + K^2H_3^*\alpha + K^2H_4^*\frac{h}{B}) \tag{2.17}$$

$$M_{ae} = \frac{1}{2}\rho U^2 B^2(KA_1^*\frac{\dot{h}}{U} + KA_2^*\frac{B\dot{\alpha}}{U} + K^2A_3^*\alpha + K^2A_4^*\frac{h}{B}) \tag{2.18}$$

where ρ is the air density, U is the wind velocity and the nondimensional parameters H_i^* & A_i^* are called the flutter derivatives, B is the deck width and K is reduced frequency

$$K = \omega B/U = B(2\pi n)/U \tag{2.19}$$

Those aerodynamic coefficients can be determined by means of special designed wind tunnel tests. By comparing the aeroelastic forces based on Theodorsen's theory with the formulation proposed by Scanlan [5], the theoretical values of the flutter derivatives of a thin plate section can be calculated.

$$L = \frac{1}{2}\rho U^2 B\left\{-2\pi F\cdot\frac{\dot{h}}{U} - \frac{\pi}{2}\left(1 + F + \frac{4G}{K}\right)\frac{B}{U}\dot{\alpha} - \pi\left(2F - \frac{GK}{2}\right)\alpha + \frac{\pi}{2}K^2(1+\frac{4G}{K})\frac{h}{B}\right\} \tag{2.20}$$

$$M = \frac{1}{2}\rho U^2 B^2\left\{\frac{\pi F}{2}\cdot\frac{\dot{h}}{U} - \frac{\pi}{2}\left(\frac{1}{4} - \frac{G}{K} + \frac{F}{4}\right)\frac{B}{U}\dot{\alpha} + \frac{\pi}{2}\left(\frac{K^2}{32} + F - \frac{GK}{4}\right)\alpha - \frac{\pi}{2}(KG)\frac{h}{B}\right\} \tag{2.21}$$

By identifying the coefficients of the variables α from the equations 2.17 and 2.18 with those from equations 2.20 and 2.21, it is easy to find the expressions for flutter derivatives,

$$KH_1^* = -2\pi F \tag{2.22}$$

$$KH_2^* = -\frac{\pi}{2}\left(1 + F + \frac{4G}{K}\right) \tag{2.23}$$

$$K^2H_3^* = -\pi\left(2F - \frac{GK}{2}\right) \tag{2.24}$$

$$K^2H_4^* = \frac{\pi}{2}(1 + \frac{4G}{K}) \tag{2.25}$$

$$KA_1^* = \frac{\pi F}{2} \tag{2.26}$$

$$KA_2^* = -\frac{\pi}{2}\left(\frac{1}{4} - \frac{G}{K} + \frac{F}{4}\right) \tag{2.27}$$

$$K^2A_3^* = \frac{\pi}{2}\left(\frac{K^2}{32} + F - \frac{GK}{4}\right) \tag{2.28}$$

$$K^2A_4^* = -\frac{\pi}{2}(KG) \tag{2.29}$$

Later, Sarkar (1992) [17] compared the theoretically calculated derivatives of an airfoil with the ones calculated based on the wind tunnel experiment for the same airfoil type by using the free vibration method [17]. The results showed good agreement between the airfoil theoretical and experimental estimations, which proves the reliability of the theoretical expression of flutter derivatives for airfoils or thin plate sections. The cable-stayed and suspension bridges became more flexible with increasing span, which increased the bridge tendency of vibrating in the horizontal direction. In 1996 Jain, with Jones and Scanlan [18] pushed this theory a step further by including a third degree of freedom corresponding to the movement in the horizontal direction, the same direction of the incoming wind. The formulations were written as [6]:

$$L_{ae} = \frac{1}{2}\rho U^2\left(BKH_1^*\frac{\dot{h}}{U} + KH_2^*\frac{B\dot{\alpha}}{U} + K^2H_3^*\alpha + K^2H_4^*\frac{h}{B} + KH_5^*\frac{\dot{p}}{U} + K^2H_6^*\frac{p}{B}\right) \tag{2.30}$$

$$D_{ae} = \frac{1}{2}\rho U^2 B\left(KP_1^*\frac{\dot{p}}{U} + KP_2^*\frac{B\dot{\alpha}}{U} + K^2P_3^*\alpha + K^2P_4^*\frac{p}{B} + KP_5^*\frac{\dot{h}}{U} + K^2P_6^*\frac{h}{B}\right) \tag{2.31}$$

$$M_{ae} = \frac{1}{2}\rho U^2 B^2 \left(K A_1^* \frac{\dot{h}}{U} + K A_2^* \frac{B\dot{\alpha}}{U} + K^2 A_3^* \alpha + K^2 A_4^* \frac{h}{B} + K A_5^* \frac{\dot{p}}{U} + K^2 A_6^* \frac{p}{B} \right) \quad (2.32)$$

Since the number of flutter derivatives increased from 8 to 16, it is much more difficult to obtain all the values through wind tunnel experiments. As a result the simplified theory of Scanlan it is still very popular for bridge wind tunnel experiments.

2.1.5 Buffeting aerodynamic instability

Buffeting aerodynamic instability is defined as a multi-mode random vibration of flexible structures, which occurs due to turbulent wind flow. As a result, the long-span slender bridges, under the effect of natural wind flow, are more likely to experience this critical phenomenon. In the aerodynamic analysis of buffeting, the quasi-steady theory is still employed, due to the small vibration amplitudes of the bridge motion and the low turbulence intensity registered in the wind data. Scanlan and Gade (1977) [19] developed a formulation to express the buffeting loads (D_b, L_b & M_b) as a linear combination of vertical (w) and along-wind (u) turbulence components. The buffeting-induced forces and moment per unit length can be written as follow [19]:

$$L_b = \frac{1}{2}\rho V^2 B[2C_L \frac{u(t)}{V} + (\frac{dC_L}{d\alpha} + C_D) \frac{w(t)}{V} \quad (2.33)$$

$$M_b = \frac{1}{2}\rho V^2 B[2C_M \frac{u(t)}{V} + \frac{dC_M}{d\alpha} \frac{w(t)}{V} \quad (2.34)$$

$$D_b = \frac{1}{2}\rho V^2 B[2C_D \frac{u(t)}{V}] \quad (2.35)$$

The theory proves to be effective, however since this is based on the assumption which requires the application of the quasi-steady theory, the formulations presented in equations 2.33 to 2.35, represent only an approximation of the buffeting forces acting on a bridge structure. Also when it comes to the problem of analyzing the aerodynamic instability of the entire long-span bridge, the wind effects acting along the span direction should be taken into consideration as well. Therefore, all the formulations presented for flutter and buffeting forces can be further modified and improved.

2.2 Experimental Investigations of Different Bridge Section

2.2.1 Types of Wind Tunnel Tests for Long Span Bridges

Some aeroelastic effects introduced by the wind flow to the bridge decks, such as flutter, buffeting, etc., are very difficult to determine only from theoretical formulations. Therefore, in order to predict the critical structural response of the bridge, the data collected from the wind tunnel tests become an important factor for investigating the aerodynamic characteristics of the bridge. In general, wind tunnel tests can be carried out not only for the bridge deck sections, but also for other structural parts of the bridge, such as cables, bridge towers etc. Moreover, the wind tunnel tests can be divided into three main types, according to the time limitation and the economic concern of the project. For flutter stability analysis, the section model wind tunnel test is the first and the most common wind tunnel test performed [20].

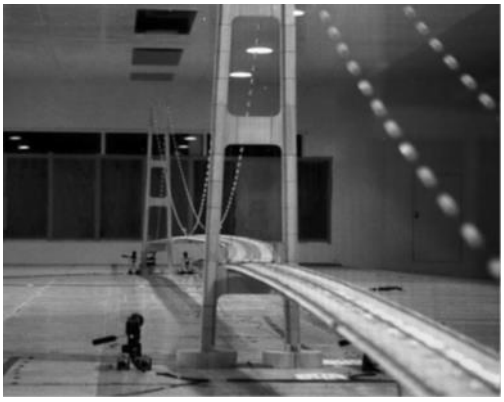

Figure 2.2.1 Super long-span full bridge model with box girder [21]

Full bridge models tests: Full bridge models tests are usually the most time consuming and economically costly type of experiments, due to the delicate and detailed construction of the bridge model, which should integrate all the bridge elements(Figure 2.2.1) Moreover, a series of strict scaling similarity requirements need to be satisfied to respect the full scale bridge (the prototype) properties, such as mass, mass of inertia, reduced frequency, mechanical damping and also the geometric dimensions. The full bridge aeroelastic models tests can simulate turbulence flow in the atmospheric boundary layer and more directly they can simulate the stability and

wind-induced vibrations response of the bridge structure under the turbulent wind action, especially for constructing important large long-span bridges such tests are generally required.

Three-dimensional partial bridge deck tests: This type of test is a simplified version of the full bridge tests models described above. Such tests can lead to reduced model construction cost, by employing only the model of the main span of the bridge into the wind tunnel, while keeping the same level of details.

Section model tests: Bridge section model is a scaled model which is mostly used in aerodynamic tests in wind engineering. The model represents a relatively short, but typical part of the bridge span, cable or tower, and usually the scale of the section model ranges between 1:10 to 1:100. The scaled model is mounted on a suspension system comprising of 8 springs, 4 springs at each extremity of the model, and thus allowing two-degrees of freedom vibrations (vertical and torsional). The tests conducted on section models provide information on the aerolastic stability, as well as aerodynamics parameters such as drag, lift, moment coefficients and the flutter derivatives, which can be further used in modelling or calculating the overall bridge deck motion under extreme wind loadings. The advantages of employing section models are their simplicity and the capability of using relatively large models, when compared to the full bridge tests models. More details of the real bridge can be included in the scaled model when using larger geometric scale and also a larger Reynolds number can be achieved during the tests. However the inability to examine the effects of wind fluctuation and the influence of the immediate surroundings, combined with the difficulty of simulating a representative wind flow, are sometimes the drawbacks of using section models tests. However, similar to the full bridge models tests, in order to ensure the accuracy of the test results, the deck geometry, inertia, and elastic properties of the bridge deck are dynamically scaled for the deck section model, based on strict similarity requirements [20].

2.2.2 Bridge deck section model and the Reynolds effect

In studying bridge aerodynamics, the first, and the most common procedure is to test the bridge deck section model in the wind tunnel. The model is usually built by a rigid material, and is relatively short in order to fit in the wind tunnel; also the model should respect the typical

cross-section of the bridge deck. It is usually mounted on springs so that the oscillations can be simulated in two degrees freedom. Generally speaking, the complete aerodynamic stability verification of long span bridges is evaluated based on the results of the scaled models section and full bridge models. Hence, not only the geometry, inertia and elastic properties of the model need to be similar with the prototype, but also the three principles related to aerodynamic properties also need to be respected as follows [20]:

1. Reynolds number similarity

As mentioned before, scaling of Reynolds number is generally not possible in wind tunnel tests. Hence, corrections for the difference between the Re number of the model and of the prototype are required especially for models with rounded shapes. Increasing the model surface roughness is a common way to simulate a higher Re number, so that the discrepancies between the response of the model and of the prototype could be minimised. The models with sharp edges however might be less sensitive to the Reynolds number similarity (Eq 2.35), but it is important to maintain a minimum model Re to decrease the fluid viscous effects. Once the Re drops below the range of 500 to 2,000, significant distortions will be caused.

$$\frac{\rho_m L_m V_m}{\mu_m} = \frac{\rho_p L_p V_p}{\mu_p} \tag{2.35}$$

where, ρ is the fluid density, V is the mean velocity, L is the characteristic linear dimension of the structure, μ is the dynamic viscosity.

2. Mass modelling and critical damping similarity

Keeping the inertia forces ratios for both structure and flow consistently scaled, is the main requirement for modelling the mass of the model. Similarity of inertia forces must maintain a constant ratio of the effective structure bulk density to the density of air. This similarity can be expressed as [20]:

$$\left(\frac{\rho_s}{\rho}\right)_m = \left(\frac{\rho_s}{\rho}\right)_p \tag{2.36}$$

in which ρ_s and ρ represent material density and air density, respectively. The m index stands for the model bridge deck and the p index stands for the prototype bridge deck. The generalized mass and the generalized mass moment of inertia for particular modes of vibration then become:

$$\frac{M_m}{M_p} = \frac{\rho_m}{\rho_p}\frac{L_m^3}{L_p^3} \tag{2.37}$$

$$\frac{I_{Mm}}{I_{Mp}} = \frac{\rho_m}{\rho_p}\frac{L_m^5}{L_p^5} \tag{2.38}$$

Damping similarity is maintained by keeping the model and the prototype with the same critical damping ratio for a particular mode of vibration.

3. Velocity similarity

The velocity scale is largely controlled by the scaling of stiffness properties of the bridge deck model. Based on the type of forces which cause the deformation of the structure, different formulations need to be applied. For the deformation mainly the result of the elastic forces and the velocity scale is determined by the Cauchy Number. Cauchy number is a non-dimensional parameter which represents the ratio of the elastic forces of a structure to the inertia forces of the flow [20]. The formulation of velocity scale can be written as:

$$\left(\frac{E_{eff}}{\rho V^2}\right) = constant \tag{2.39}$$

where, E_{eff} is the effective modulus of elasticity and is taken as E for the replica models and $E\tau/L$, EA/L^2 or EI/L^4 for various equivalent models, which represent the simulation of the member forces, axial forces and flexure or torsion. However this similarity condition is not usually employed for the bridge deck section models. For such section models, the above similarity becomes [20]:

$$\left(\frac{U}{Bf}\right)_m = \left(\frac{U}{Bf}\right)_p = \mathrm{U}_r \tag{2.40}$$

where f_m and f_p are the vibration frequency of the mode and the prototype, respectively. The U_r is also known as the reduced velocity. For the structures where the deformation is influenced by the gravity, especially for full suspension bridges or guyed structures, besides the Cauchy number similarity it is also required to respect the Froude number equality. Froude number is a non-dimensional parameter which represents the ratio between the inertia forces of the flow and the structure gravity forces. For the requirements of Froude equality we can write [20]:

$$\left(\frac{V^2}{gB}\right)_m = \left(\frac{V^2}{gB}\right)_p \tag{2.41}$$

where V is the velocity of wind, B is the deck width and g is the gravitational acceleration. Since the gravitational acceleration is the same for model and prototype, Eq. 2.41 can be rewritten as:

$$\frac{\lambda_V^2}{\lambda_L \lambda_g} = \frac{\lambda_L}{\lambda_t^2} = \lambda_L \lambda_f^2 = 1 \tag{2.42}$$

Hence the scale conditions of the vibration frequencies and the wind velocity becomes,

$$\lambda_f = \frac{1}{\sqrt{\lambda_L}} \tag{2.43}$$

$$\lambda_V = \sqrt{\lambda_L} \tag{2.44}$$

4. Scale Effect

In principle, the Reynolds number has to be the same, in order to achieve the similarity for aerodynamic phenomena of structures in general. However for the conventional wind tunnel tests, the Reynolds number for section models is always two to three orders of magnitude lower. Thus, the Reynolds number similarity is unavoidably violated, especially for the bodies with rounded shapes, when the flow pattern around the model is very sensitive to the change of Re, as showed above. Therefore, the flow separation points shift with changing of Re which correspondingly changes the wake width, the drag and lift forces, etc. Modifying the surface roughness and adding several devices to the body surface can reduced the effects of the Re violation [7]. For bluff bodies with sharp edges, in most of the cases of bridge decks, wind engineers believe that the flow around it has fixed separation points. These points do not shift and the flow pattern is less sensitive to the variation of Re. Flow reattachment, which relates to

the drag force as well as the frequency of vortices in the flow, may or may not occur. Even if it does, it might not be affected by the Reynolds number. Therefore the requirement for Reynolds number similarity could be relaxed.

The assumption that the Reynolds number effects are negligible for sharp-edged body is partially true. A big discrepancy was recorded between the wind tunnel results and the measurements at the site of the Great Belt East Bridge, in 1998 by Schewe and Larsen [22], who conducted an experiment using the section model of the bridge deck to measure the unsteady aerodynamic forces, the Strouhal number and other aerodynamic parameters. The Reynolds numbers employed in the wind tunnel test ranged from 3.0×10^4 to 4.0×10^6 and the results showed that, the Strouhal number displays a significant dependence on Re. For $Re < 8 \times 10^4$ the St was 0.18, which is in reasonable agreement with the low Re wind tunnel tests (St = 0.16). When Re number increased beyond 4.0×10^5 the St was 0.22 also similar to the prototype. As for the drag coefficient, it registered a sudden decrease from 0.7 to 0.6 as the Re number increased.

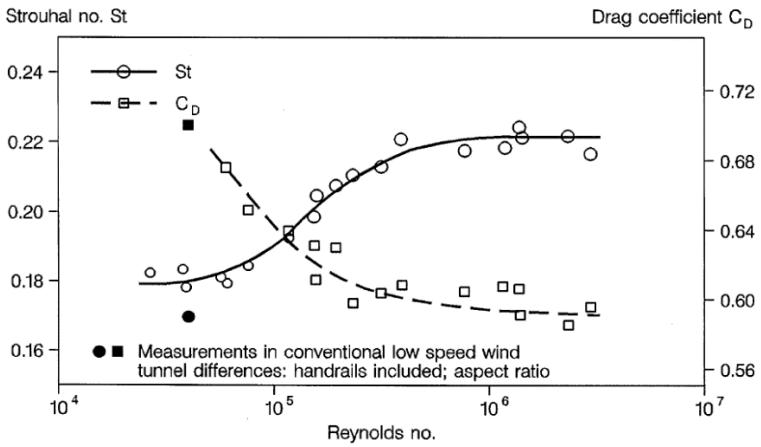

Figure 2.2.2 Strouhal number St and drag coefficient CD as a function of Reynolds number Re [22]

The conclusion he drew is that the aerodynamic characteristics of a slender body with sharp edges can be influenced by the Reynolds number effects, and the drag coefficient obtained from low Re numbers wind tunnel testing appears to be conservative. Matsuda (2001) [23] used section models of twin box decks (two parallel decks with a gap between them) with different gratings dimensions and configuration, to investigate the Reynolds number effects on the steady

and unsteady aerodynamic forces in the range of Re= 1.1×10^4 to 1.5×10^6. The models had three types of gratings 80 gratings, 80 closed and 40 gratings, as represented in Fig.2.2.2. [23].

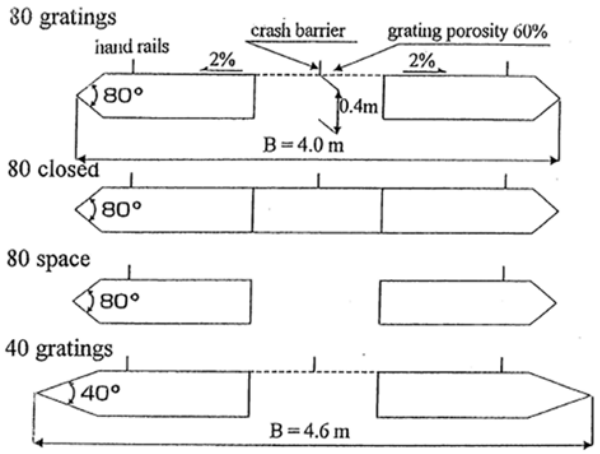

Figure 2.2.3 Cross sections of deck models (dimensions for 1 : 10 scale model) [23]

These models were tested at the National Research Council of Canada (NRCC) and Ishikawajima-Harima Heavy Industries (IHI) wind tunnels facing different angles of attack. The results concluded that, for the section bridge deck models used in their research, the wind-resistant design based on the conventional wind tunnel tests in low Reynolds numbers range, provides more conservative evaluation of the aerodynamic forces. Also, the critical flutter speeds calculated based on the low Reynolds number are slightly smaller than those obtained for high Reynolds numbers, which means that the Re number has almost no effect on flutter speed. For the bridge decks for which the steady aerodynamic force coefficients and the Strouhal number are affected by the Reynolds number variation, the unsteady force coefficients are also influenced. The Reynolds number effect was observed only for the bridge section with "80 gratings" and were not found for other bridge sections. Larose and Auteuil (2006) [24] carried out a review on the Reynolds number sensitivity of the aerodynamics of bluff bodies with sharp edges for different bridge deck models, including Storebelt East Birdge, the Ikara Bridge, the IHI bridge and also the Stonecutters Bridge. They pointed out that some bluff bodies with sharp edges are more sensitive to Re numbers effects than others. The Storebælt East Bridge, which has a more streamlined shape box girder, appeared to be less sensitive. In short, the study concluded that for wind tunnel tests, the Reynolds number effect is unavoildable, especially for the tests using large scale models, but some compromises can be made. The most common way

to account for Re number effect is by using a large deck section model and by studying the highest Re possible, to obtain the aerodynamic characteritics and then to adjust the geometry of smaller models to fit those chararcteritics. Also the same study recommended to use some less sensitive or streamlined deck shapes like Strait of Messina Bridge deck shape, to minimise the effect of the Reynolds number.

2.2.3 Effects of deck shape on bridge aerodynamic

Yuh-Yi Lin (2005) [25] investigated the influence of deck shape on the flutter and static coefficients through testing of a bridge deck section model in the boundary layer wind tunnel at Tamkang University, China which had a length of 18.7 m, 3.2 m in width and 2.0 m in height. The models for the tests were all 1.5 m long and were placed between two end plates. Two series of deck shapes were selected, one was box girder type and the other was plate girder type (Figure. 2.2.3. and 2.2.4.). The B/H ratio of the deck was one of the controlling parameters and four section models were included for each type of deck with B/H ratios from 4 to 20.

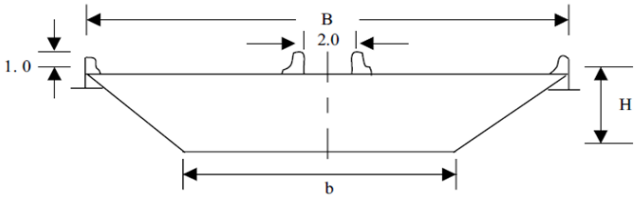

Model	1–1	1–2	1–3	1–4
H(cm)	1.75	2.4	3.2	5
b(cm)	27.7	25.4	21.8	15.4

(closed box girder)

Figure 2.2.4 Closed box girder section [25]

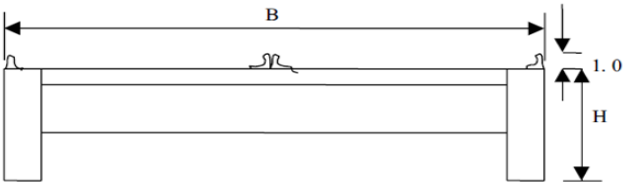

Model	2–1	2–2	2–3	2–4
H(cm)	1.5	2	3	5

(plate girder)

Figure 2.2.5 Plate girder section [25]

The wind force coefficients were measured for each test case when the bridge section model reached a stationary motion. From the results, they found that the drag coefficient in smooth flow both plate girder series and closed box girder series decreased with the increase of the B/H ratio. The ratio has only small effects on the lift coefficient for the closed box girder, while for the plate girder the absolute value of lift coefficient drops significantly with decreasing B/H ratio. They also found that in the case of the plate girder model with the biggest height H (model 2-4 in Fig. 2.2.4.), the lift coefficient and the attack angle had different relationship when compared with the other models. The coefficient of moment increases with the model's B/H ratio, for closed box girder section, while for the plate girder, the results showed that, the thicker the deck the smaller the moment coefficient becomes for negative wind attack angles; for positive attack angles however the moment coefficient registered higher values. Again, the torque moment for model 2-4 is significantly larger than those of the other three section models in the positive attack angles range (Fig. 2.2.6.).

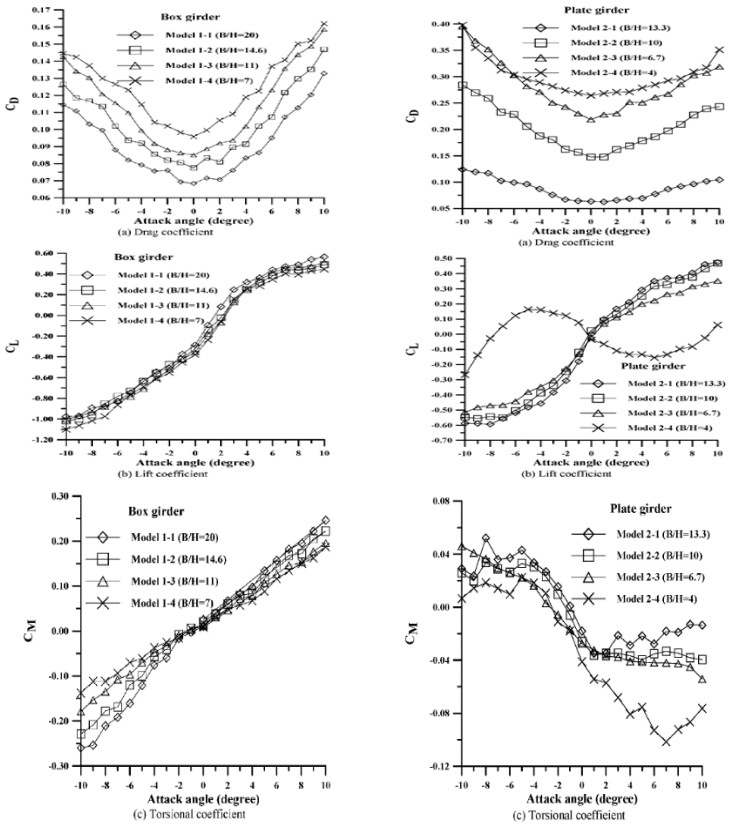

Figure 2.2.6 Static moment coefficients for different girder types [25]

The bridge deck shapes not only affect the static aerodynamic forces acting on the bridge, but also control the critical flutter speed. Ge, 2008 reviewed in a recent CFD investigation, the top ten longest suspension bridges [26] and he mentioned that due to aerodynamic stability condition, the maximum length for suspension bridges with a box or truss girder should not be over 1,400 m. With the advanced theoretical method and the full-mode flutter analysis approach Ge with his colleagues [3] made an estimation on the span length of suspension bridges with different cross-sections including single box, twin box, slotted box, etc. They concluded that the deep or shallow single box can provide up to 1,500 m span suspension bridge with about 56 m/s and 58 m/s flutter critical speed. For those with narrowly slotted twin box, the span length can reach up to the 1,500 m or 2,000 m with 70 m/s or 53 m/s flutter critical speed, and the widely slotted twin box along with the triple box can guarantee up to 5,000 m span suspension bridge having high enough flutter critical speeds of 86 m/s to withstand the wind load in the most typhoon prone areas worldwide.

Besides the predictions of the main span length, Ge et al also made an investigation on the flutter stability for deck cross-sections of up to 13 different types (Fig. 2.2.7.) [26]. Based on the results from the first two groups of cross-sections including streamlined thin plate, closed box, and bluff rectangular shapes, they concluded that the more streamlined the cross-section is, the more the heaving degree participates in the flutter onset velocity and accordingly higher flutter speed can be reached. Besides, the tests results from these deck sections with sharp edges also reflect a pattern that the participation of heaving degree in the flutter speed gradually increase with the sharpness of the edges (Fig. 2.2.8).

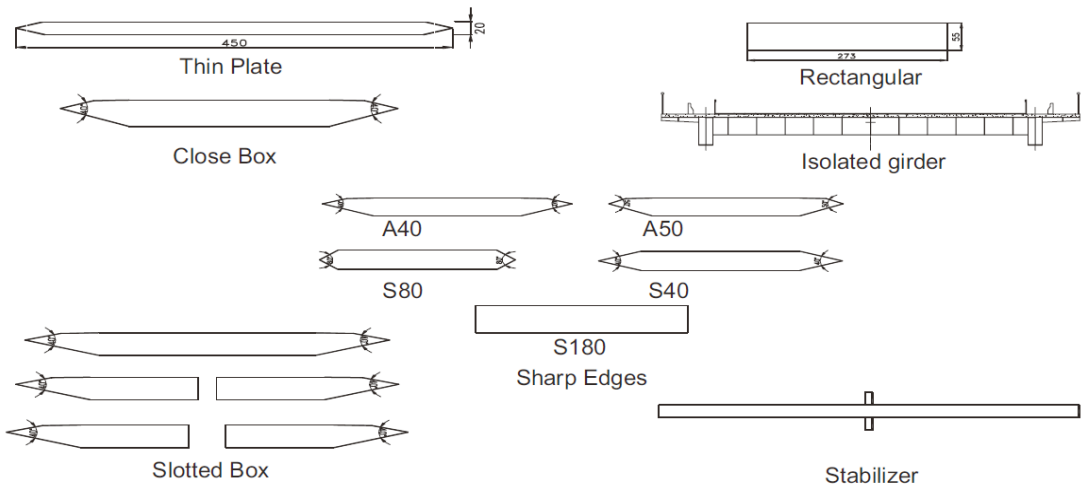

Figure 2.2.7 13 Different Deck Types [26]

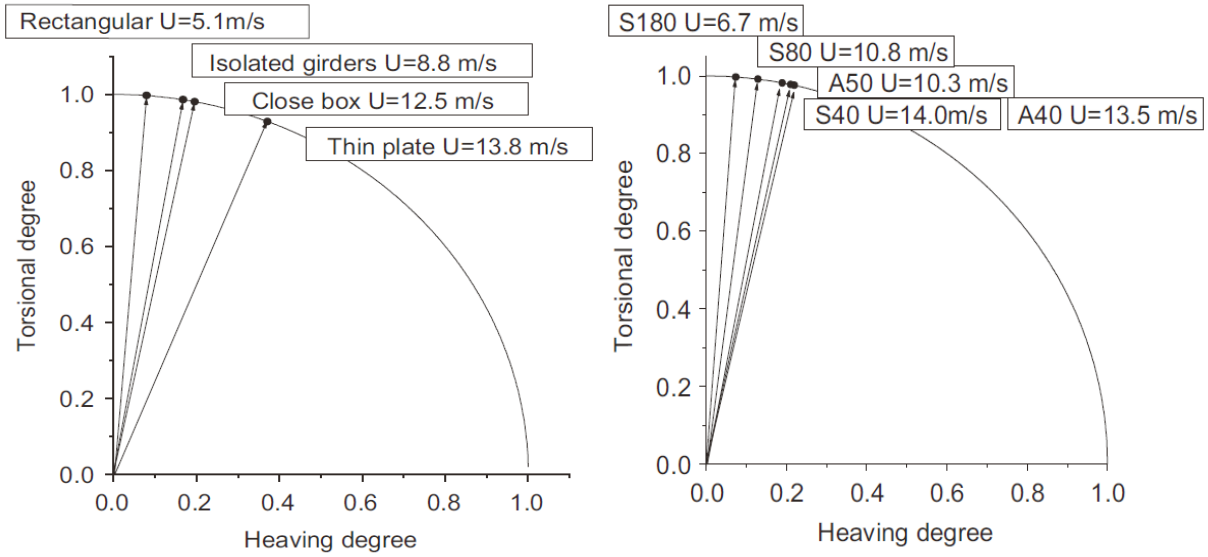

Figure 2.2.8 Relationships between the flutter speed and heaving degree [26]

The bridge deck sections with the lowest aerodynamic forces were the slotted deck and the deck with stabilizer. But the latter one has an optimum value of heaving degree participation for increasing the flutter wind speed and thus such deck section was used for the Jiangsu Runyang South Bridge. A wind tunnel experiment was carried out at Tongji University wind tunnel facility [3], to study the aerodynamic stability of the Jiangsu Runyang South Bridge using a 1:70 box girder section model without and with various width stabilizers. The results showed that the box girder with a stabilizer can increase the bridge deck flutter critical speed. They also conducted additional tests for a full aeroelastic bridge model to confirm that the results show good agreement with those from the section models tests (Table 2-2).

Table 2-2 Critical flutter speed for girder with or without stabilizer [3]

Box Girder Configuration	Critical flutter speed (m/s)				Required (m/s)
	SM at 0°	FM at 0°	SM at +3°	FM at +3°	
Original box girder	64.4	64.3	50.8	52.5	54
Box girder with a 0.65m stabilizer		69.5	58.1	53.8	54
Box girder with a 0.88m stabilizer		72.1	64.9	55.1	54
Box girder with a 1.1m stabilizer		>75	67.4	56.4	54

The Xihoumen Bridge is an example that shows the advantage of using a twin deck section with central slot. During the design phase, apart from the traditional single box, single box with stabilizer also the twin box with a slot were proposed [3]. After investigating each section's critical flutter speed, the twin box deck with a slot of 6.0 m was adopted and was further modified to become the final configuration of the bridge deck. The experimental results reflect that the twin box with a slot has a higher critical flutter speed than the single box with a stabilizer.

For shorter span bridges, the critical flutter speed of twin-box decks, would significantly increase, e.g.: the Xihoumen Bridge has a main span of 1,650 m and a critical flutter speed of U_{cr} = 89.3 m/s [Ge & Xiang (2008) [26]], and the Yi Sun-sin Bridge of 1,545 m main span has a very high flutter critical velocity of U_{cr} = 120 m/s [Gil (2012) [48]]. Numerous studies were performed as well for the deck cross-section proposed for the Messina Bridge [Diana et al, 2008, Diana et al, 1999, Larose et al, 1993], which has three decks connected by stabilizing beams, such that the wind flow can stream through the gaps between the decks and thus the wind-induced pressure is partially released. The experimental investigation performed by Larose and Livesey (1997) [27] confirmed the gradual release of the pressure along the bridge deck, by comparing the static pressure and force coefficients of the Messina Bridge with those of the Normandie Bridge (856 m main span), the Hoga Kusten Bridge (1,210 m main span) and a flat plate deck types (Figure 2.2.9). From these results, it is clear that the shape of the box deck is one major factor that affects the aerodynamic forces, while the gap-width is another factor which can't be ignored for the twin-box deck.

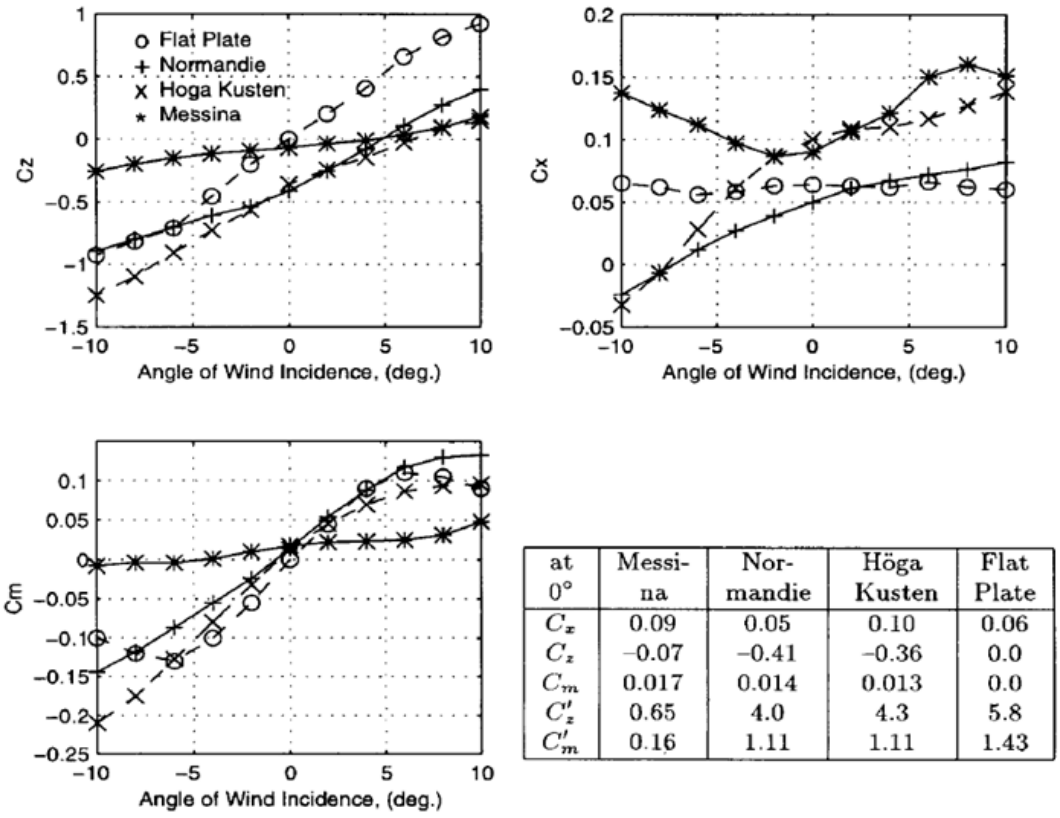

at 0°	Messi-na	Nor-mandie	Höga Kusten	Flat Plate
C_x	0.09	0.05	0.10	0.06
C_z	–0.07	–0.41	–0.36	0.0
C_m	0.017	0.014	0.013	0.0
C'_z	0.65	4.0	4.3	5.8
C'_m	0.16	1.11	1.11	1.43

Figure 2.2.9 Static coefficients comparison with angle of wind incidence for four cross-sections [27]

K.C.S. Kwok, X.R. Qin (2012) [28] carried out a series of wind tunnel experiments to determine the effects of gap-width on the aerodynamic forces and also the vortex shedding mechanisms (Fig.2.2.10). Tests were carried out at the CLP Power Wind/Wave Tunnel Facility at The Hong Kong University of Science and Technology, using a 3.0 m long section model with a length scaled of 1:80 from the prototype. The tests were conducted for five different twin-box decks based on gap-width, b to total chord, B ratio of 0%, 2.5%, 16%, 27% and 35%. All five configurations are denoted as Gap1, Gap 2, Gap 3, Gap 4 and Gap 5, in Figure 2.2.11.

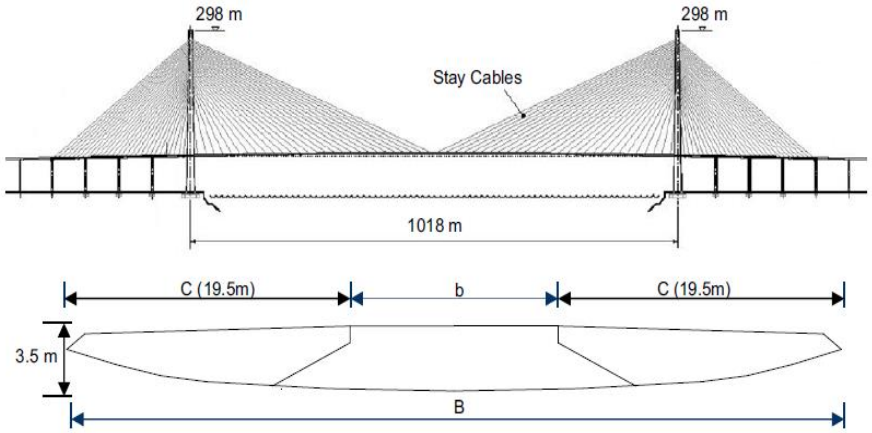

Figure 2.2.10 General layout and cross section at mid-span of the bridge twin-deck design configuration [28]

For the tests, the wind speed was set to over 15 m/s, in order to minimize the Reynolds number effect on the variation of the lift force. The equations used to express the static lift and drag forces and the moment coefficients are [28]:

$$C_L = \frac{\bar{L}}{\frac{1}{2}\rho_a \bar{U}^2 l}, \qquad C_D = \frac{\bar{D}}{\frac{1}{2}\rho_a \bar{U}^2 l}, \qquad C_M = \frac{\bar{M}}{\frac{1}{2}\rho_a \bar{U}^2 l^2} \tag{2.45}$$

where, $C_L, C_D \; and \; C_M$ are the aerodynamic coefficients of lift, drag and pitching moment of the bridge deck respectively; $\bar{L}$, $\bar{D}$ and $\bar{M}$ are the mean values of lift, drag forces and moment per unit length of the bridge deck; ρ_a is the air density; $\bar{U}$ is the mean wind speed and l is the length of the model section (sometimes considered as the single deck chord length, C or the total chord width, B) used to normalize the forces and the moment so that the tests results can be compared directly. The results obtained based on the single deck chord length, l = C are presented in the Fig. 2.2.11, a1), b1) and c1) and those obtained using l = B are showed in Fig. 2.2.11 a2), b2) and c2). From these results, it could be concluded that the effect of the gap width on the lift force and moment coefficients is negligible, since their magnitudes are similar for each of the tested configurations. However, when the force and moment coefficients are normalized with respect to the entire chord length B, the slope of both the lift and moment coefficients decreased with the increase of gap width. Besides, both coefficients show a high sensitivity to the wind attack angle during the experiments. As for the drag coefficient, it increased

significantly for the larger gap width deck, due to the large mean positive pressure on the windward side of the downstream deck. Besides the aerodynamic forces induced to the deck model, the vortex shedding mechanism downstream the deck, also reflects some influence by the gap width. Thus the Strouhal number increases together with the increasing gap width, and vortex shedding frequency experienced the same evolution. The same study [12] also pointed out that according to the pressure spectra, the wake excitation of the upstream deck and the turbulence buffeting induced by the vortex at the downstream deck are the main factors governing the vortex shedding phenomena of the entire bridge deck with twin-box configuration.

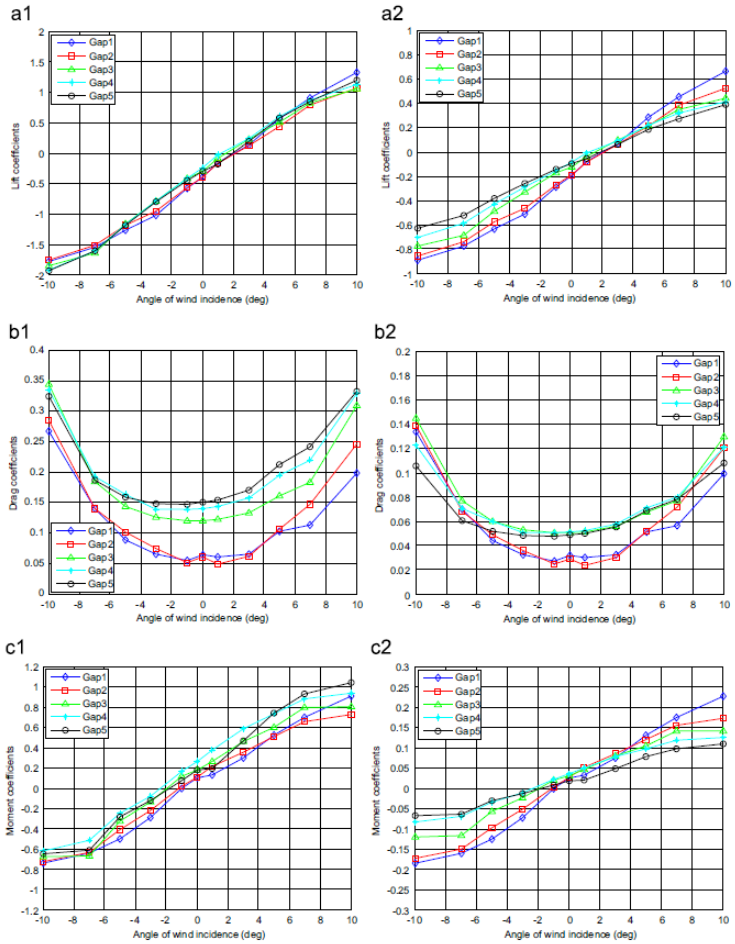

Figure 2.2.11Static Coefficients for different gap widths [25]

2.2.4 Double Slots decks and Messina Bridge

The main threat for the aerodynamic stability of a bridge deck is the problem of flutter which might occur at high wind speeds. In order to increase the aerodynamic stability of the modern super-long bridges, numerous deck sections have been proposed and tested, including the idea of introducing slots or gaps within the width of the bridge decks, such as the design of the Messina bridge deck which was based on this idea. Among the 8 flutter derivatives used to express the lift force and pitching moment in flutter analysis, A_1^* and H_3^* are the most important derivatives for coupled flutter instability, based on the SBS analysis method proposed by Matsumoto et al,(2007) [29]. The method explained the mechanism of flutter and pointed out that the torsional flutter, reducing the absolute value of A_1^* and H_3^*, can delay the excitation of the coupled flutter. Also for standard modern bridge decks the value of A_2^* is negative due to the streamlined and slender shape, so that torsional flutter is usually avoided. The value of flutter derivatives are basically determined by the shape of the deck which means the width and the position of the slots or gaps will affect the deck flutter instability. In this regard, Permata et al [30] performed several experiments to investigate the efficiency of bridge deck with double slots and its flutter stability property. The experiments were carried out in a wind tunnel with the size of 1.8 m height and 1.0 m width. The basic section was a rectangular prism with B / D = 20. The rectangular model consisted of 3 fixed blocks (at leading edge, center and trailing edge) and 12 removable blocks, so that double slots with varied width and position could be achieved (Fig. 2.2.12). The pressure and the fluctuating pressure were measured by the pressure taps for each model.

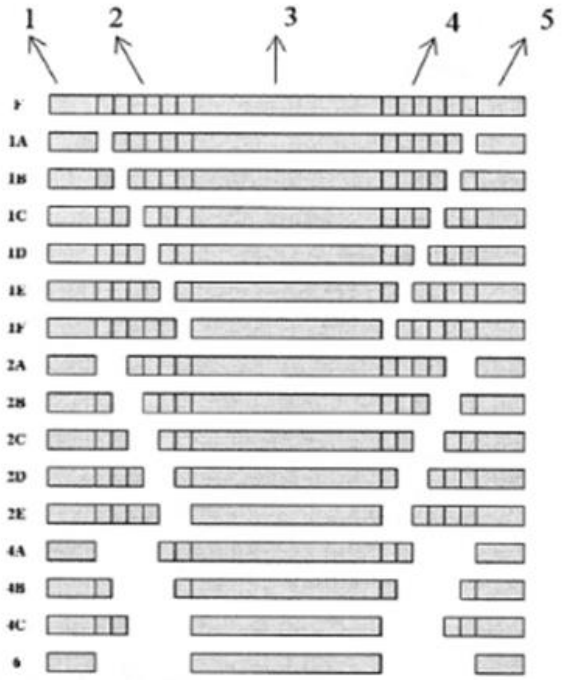

Figure 2.2.12 Geometric details and configuraitons for the basic deck models [30]

From the results, they found that among all the flutter derivatives, A_1^* and A_2^* were quite sensitive to the slot position. The derivative A_1^* can be reduced by moving the slot from the edge of the model towards the mid position, while A_2^* experienced the opposite trend. At low velocities, almost all the models were likely to encounter torsional flutter, due to the positive value of A_2^* they have. For the models which have narrow slots, the values of H_3^* flutter derivative were not significantly affected. However for the models with wide slots the values of H_3^* registered a reduction indicating the decrease of exciting coupling flutter force on the bridge sections.

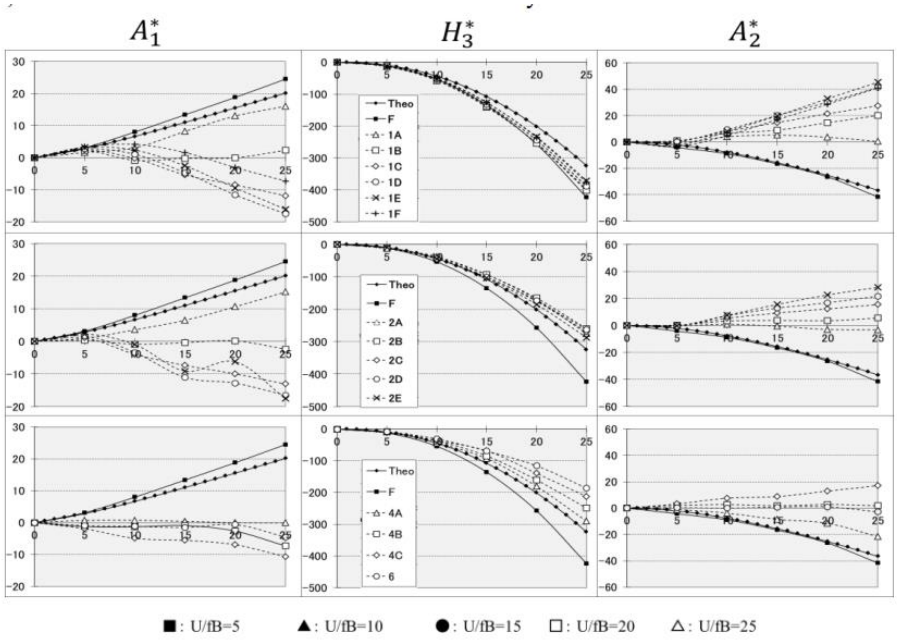

Figure 2.2.13Aerodynamic derivatives A_1^*, H_3^* and A_2^* of models

For bridge flutter instability, the combination of A_1^* and H_3^* plays the role of destabilizing while derivatives A_2^* and H_1^* brings the stabilizing effect for torsional and heaving branch, respectively. Thus, compared with other investigated models the model 4A, which has very low absolute values of A_1^* and negative A_2^* was the most stable section having a good flutter stability, low mass moment of inertia and the flutter stability index V_{rcr} over 3.3, but it has a higher frequency ratio which is an important parameter for flutter stability from structural dynamic properties point of view. In addition, the model 4A has the same economical concern just like the multi box girder section, being a bridge deck involving higher construction costs, however from the aerodynamic stability point of view this multi-deck type could provide another alternative for the bridge deck design.

The Strait of the Messina Bridge which links the Sicily to the mainland of Italy represents the most advanced aerodynamic bridge design in terms of deck geometry, showing a very good potential of using multi-deck for super long suspension bridges. Since the bridge main span has a length of 3,300 m, the longest known so far, the bridge is very sensitive to the wind action and the aerodynamic stability condition becomes the major problem dominating the entire design [31].

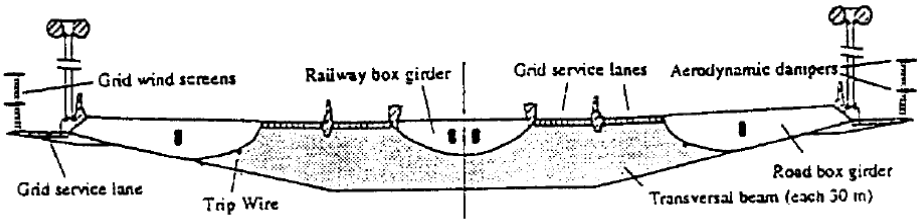

Figure 2.2.14 Configuration of the Messina Bridge [31]

Several numerical and wind tunnel tests have been carried out for investigating the aerodynamic characteristics of the Messina Bridge. In the paper of G. Diana (2004) [32], a 1:60 scaled section bridge deck model was tested for verifying the aerodynamic behaviour at reduced velocities (non-dimensional) U_r = 1.0 up to 70.0 were conducted in the wind tunnel facility at Politecnico di Milano (Fig.2.2.15). All six static aerodynamic coefficients including axial, drag, lift and pitching moment coefficients as a function of the angle of attack were measured, as well as the flutter derivatives as a function of the reduced velocity. The section model was 3.6 m long and 1.0 m wide and had seven dynamometers installed on the floating part of the model as indicated in Fig. 2.2.15 by white circles while the white squares represent the location where the drag force response was measured and the black circle indicates the position where axial force was measured.

From the results obtained from the "wind-off" and "wind-on" test conditions, it is worth to notice that the lift and moment coefficients registered positive values, very low in the whole range of attack angles investigated of -10 ° to 10 °, (Fig. 2.2.17) indicating a stable aerodynamic behaviour in terms of a single degree of freedom motion.

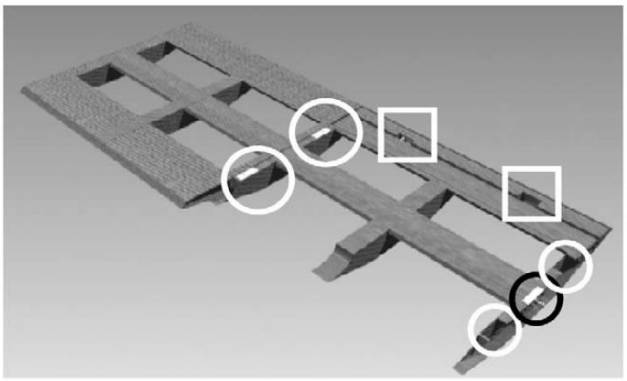

Figure 2.2.15 Location of the sensors for the experiments of Messina Bridge deck [32]

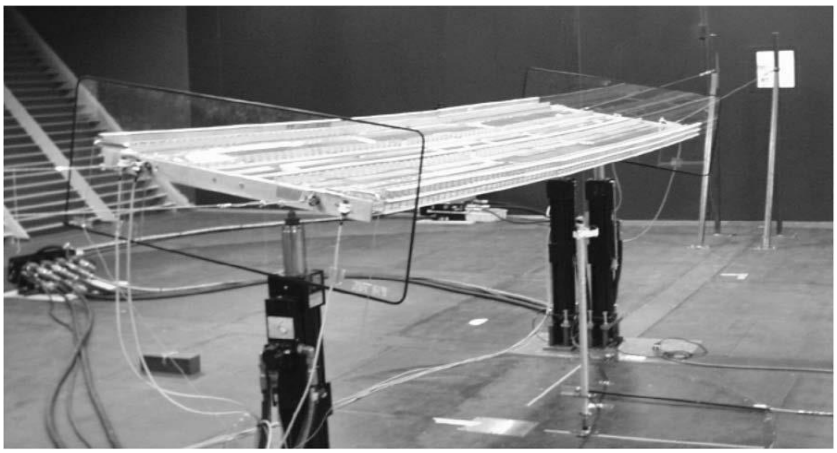

Figure 2.2.16 Forced motion test rig. for the Messina Bridge deck [32]

For the section model, both free motion and forced motion were conducted. In the free motion in the wind tunnel which was used to measure the admittance functions, the model was suspended by the means of steel-cables and the attack angle was controlled by the 13 m diameter supporting pneumatic turntable installed outside the wind tunnel. For the forced motion tests, three computer-controlled hydraulic actuators were employed for generating a multi-degree of freedom harmonic motion (Fig. 2.2.16). The static aerodynamic coefficients and 18 flutter derivatives were measure through forced motion under the different combination of six values of frequency and four wind velocities covering the reduced wind speed in the range of $1 \leq V^* \leq 70$. The validity of the quasi-steady theory for evaluating the flutter instability threshold was confirmed through the testing results. Besides, a comparison of the static forces coefficients obtained for the Messina Bridge, with other three famous suspension bridges, the Akashi Bridge (1,991 m span, steel-truss girder), the Humber Bridge (1410 m span, steel box girder) and the Tacoma New Bridge (853 m span, plate girder) performed by Diana shows a good aerodynamic property of the Messina Bridge, for which the lift coefficient is much smaller than those of conventional bridge deck like the Humber or Tacoma Bridges and the moment coefficient stays at a relatively lower value than the Akashi suspension bridge (Fig.2.2.18.).

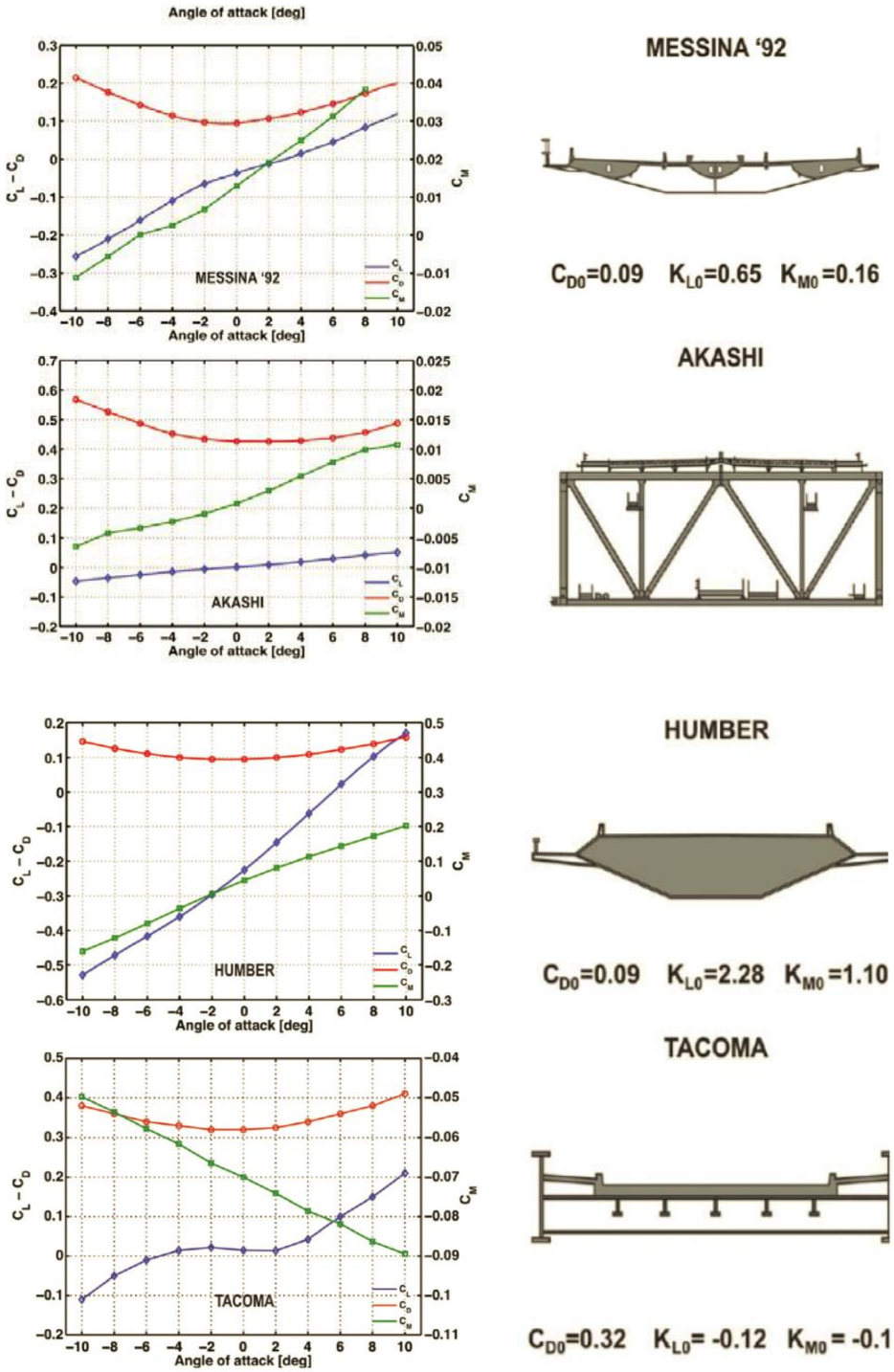

Figure 2.2.17 Static coefficients of four famous bridges [32]

Larose (1997) [27] also evaluated the aerodynamics of three different bridge decks by comparing them to a 16:1 flat plate. All three decks were selected to be streamlined shaped based on the proposed deck prototype of the Pont De Normandie, the Hoga Kusten Bridge and the

Messina Straits Bridge. The Pont de Normandie is a cable-stayed bridge which has a main span of 856 m and a width to depth (B/D) ratio of 7.5. The Hoga Kusten Bridge is a 1,210 m main span suspension bridge with a B/D ratio of 5.5 .The Messina Strait Bridge, has a main span of 3,300 m a deck with 60 m in width and a B/D ratio of 13, while the flat plate has a B/D of 16.The section model tests were carried out in the Danish Maritime Institute's 2.6 m-wide boundary layer wind tunnel and smooth and turbulent flow tests, with a vertical turbulence intensity of 6 %, were conducted for the section models except for the Messina bridge section which was tested in smooth flow only. The static force and moment coefficients were measured for all the models in each wind attack angle cases varied from -10 ° to 10 °. The results revealed that the lift and moment coefficients at the angle of attack around 0^o have positive rate of change which means they have a favourable effect on the aerodynamic damping. All three testing models have negative lift coefficients at 0^owhich indicates a downward force was pushing the deck, which increased the stability of the bridge. Both the Pont De Normandie and the Hoga Kusten section models have moment coefficients very close to the ones registered for a flat plate and smaller lift coefficients than those of the flat plate (Fig.2.2.19.). It is also worth to mention that, the Messina bridge section model has very favourable static coefficients, the changing rate of the lift and moment coefficients being almost a quarter of the other three bridge models. Besides, the fact that the lift and drag coefficients have very small values, ranging between -0.5 to 0.5 and -0.05 to 0.05, respectively, the overall aerodynamic behaviour of the multi-box girder deck of the Messina Bridge showed a great advantage when compared with other traditional bridge deck shapes.

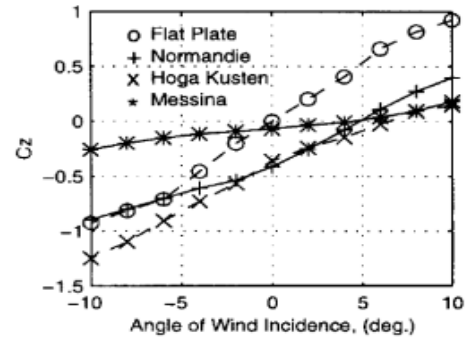

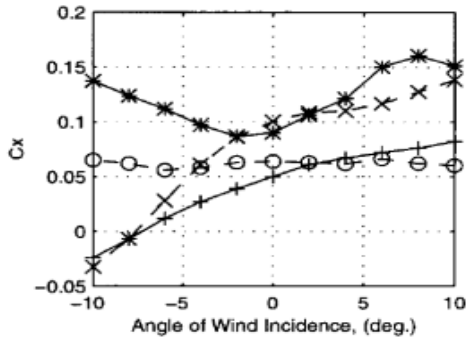

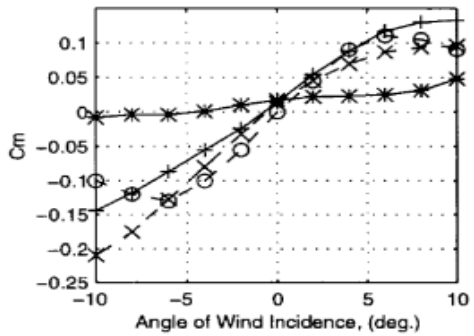

at 0°	Messi-na	Nor-mandie	Höga Kusten	Flat Plate
C_x	0.09	0.05	0.10	0.06
C_z	–0.07	–0.41	–0.36	0.0
C_m	0.017	0.014	0.013	0.0
C'_x	0.65	4.0	4.3	5.8
C'_m	0.16	1.11	1.11	1.43

Figure 2.2.18 Variations of coefficients with angle of wind incidence for four cross-sections [27]

2.3 Computational fluid dynamics for bridge deck sections

2.3.1 Background on CFD simulations

The computational fluid dynamics (CFD) is a numerical technique widely applied for simulating the wind flow around structures and to investigate the aerodynamic characteristics of structures of various geometries, before testing them in a wind tunnel. Any fluid flow is governed by the Newton's second law as well as the conservation of mass and energy. CFD uses the discretized algebraic formulations to replace the integrals or the partial derivatives contained in the governing equations and these equations are solved to obtain the required parameters for the flow field at discrete points in time and space [33]. With the given specific initial and boundary conditions, the interaction between the fluid flow and the surface of the investigated structure can be simulated through the application of numerical algorithms. Bridge engineers usually employ CFD simulation techniques as methods to enhance their understanding of the aerodynamic mechanisms in the wind-resistance design of bridge and also as a preliminary study useful for limiting the experimental work for the tests for which the similarity conditions show a

better compatibility with the full-scale or reduced-scale testing. Despite the economic advantage the CFD method has over the traditional wind-tunnel tests, it cannot replace entirely the measurements obtained from the wind tunnel tests in the wind engineering field. The CFD method is highly depended on how detailed the simulation domain and the boundary conditions are developed. The CFD methodology is more likely to be treated as a complementary wind study to the wind tunnel testing for bridge engineering, by providing relevant parameters regarding the entire wind-flow field, such as flow patterns, vortex shedding, Re stress intensity, etc., which can hardly be measured or visualized in the wind tunnel tests. It is noticeable that, in bridge engineering, numerous researchers have focused on verifying the accuracy of the CFD methods by comparing the results of the simulation with those obtained from the wind tunnel experiments.

2.3.2 Common CFD modelling approach for bridge engineering

The accurate modelling of the wind flow is a key factor in CFD simulations for wind engineering. Various numerical approaches with different level of phenomenological insight, mathematical complexity and also computational cost have been proposed through decades. The laminar approach [57] is the simplest and straight forward method which has very limited computational requirements. This method ignores the effect of the turbulent flow and will lose its accuracy with the increase of the Reynolds number as well as the level of flow instability, thus the application range of this method is very limited.

The Reynolds-averaged Navier-Stokes (RANS) approach represents today's most used method for simulating turbulence in bridge engineering which is based on the time-averaged of the Navier-Stokes equations for fluid flow. The basic idea behind this method is the decomposition of instantaneous turbulent flow quantity into its time-average quantity and an extra fluctuating component. Instead of solving the turbulent structure directly, adopting specific turbulence model based on the Boussinesque hypothesis [34] represent the fluctuating part, this method expands the application of RANS approach, relying on the tendency of using Reynolds stress transport models to replace the Boussinesque hypothesis, thus largely increasing the capability of this approach and decreasing the computational costs as well. In bridge engineering,

Shirai and Ueda (2003) [35] adopted the RANS method coupling with a nonlinear $k-\varepsilon$ model to investigate the aerodynamic behaviour of a flat box girder cross-section which is separated with the vertical and horizontal stabilizer installed. The computational region was generally 16 B × 7 B rectangular shape (Fig 2.3.1) with distances to the cross-section of 5B from the inlet, 10 B from the outlet and 3B from the upper and lower edges of the domain.

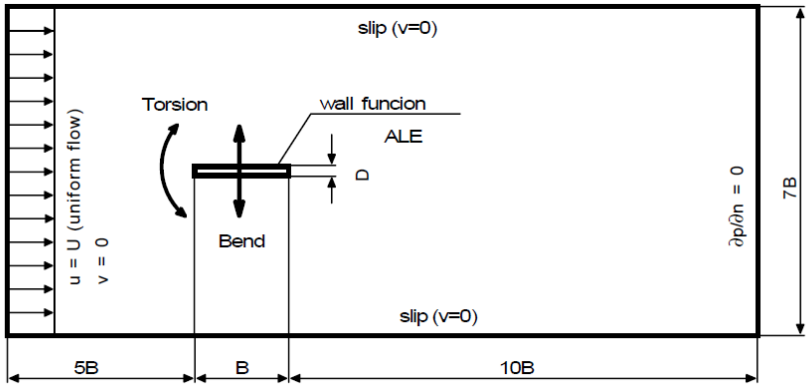

Figure 2.2.19 Geometry and boundary conditions for the CFD flow simulation around the flat section [35]

Initially, instead of using the flat box girder cross-section, they reproduced the flow around a parallel rectangular section with B/D=15 for the purpose of validating the applicability of the RANS approach together with the $k-\varepsilon$ model. The results for the aerodynamic derivatives and the unsteady pressure characteristics showed good agreements with the wind tunnel tests results reported by Matsumoto et al. [58]. Since the applicability has been confirmed, the method was applied to examine the aerodynamic behaviour of the box girder section with the stabilizers. Through the comparison between the flutter derivatives obtained from the experiment and the CFD simulation, they confirmed that the RANS model can predict aerodynamic behaviour accurately, in a weak irregular turbulent flow. However, as shown in Fig 2.3.2, in the strong irregular turbulent flow the accuracy of predicting flutter derivatives and also the phase lag of the fluctuating pressure, decreases. In addition, the function of the stabilizer is revealed through the analysis of the unsteady pressure characteristics around the bridge deck section. The stabilizers control the stream around the section as well as the generation of the vortex which decreased the amplitude of the fluctuating pressure and improved the aerodynamic stability [35].

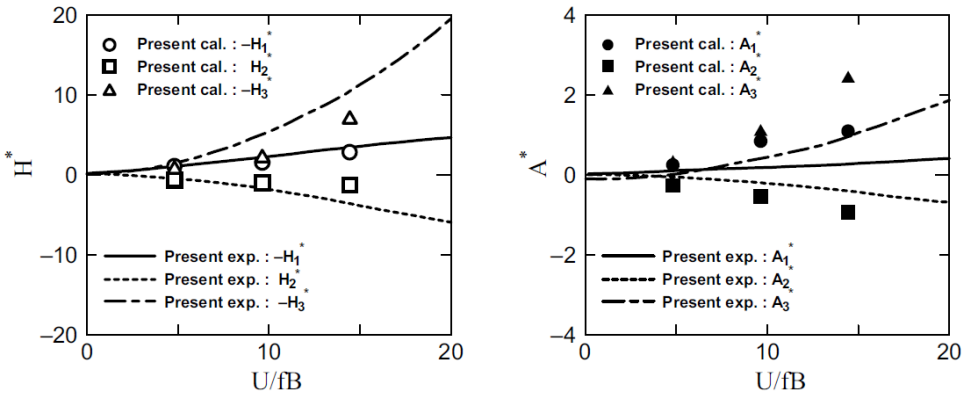

Figure 2.2.20 Comparison of the experimental results with the calculated results for the aerodynamic derivatives on the parallel rectangular section [35]

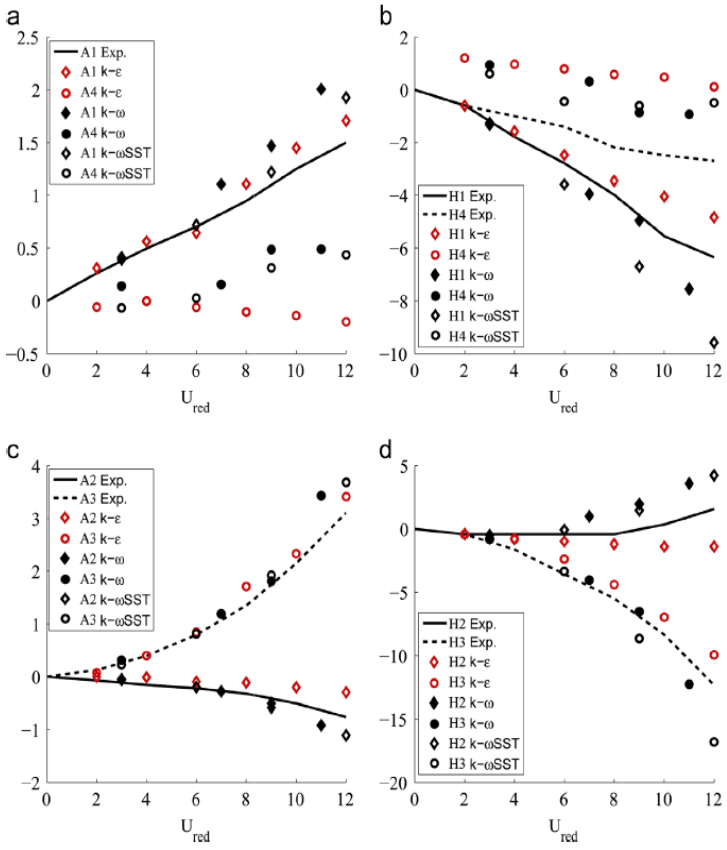

Figure 2.2.21 Flutter derivatives of the Great Belt East Bridge cross-section [36]

Similar experiments were conducted by Brusiani et, al (2013) [36] for evaluating the flutter derivatives of the Great Belt East Bridge using the RANS method, coupled with three different turbulent models ($k-\varepsilon, k-\omega$ and $k-\omega\ SST$). The trends of the flutter derivatives were well captured in both direct and indirect terms and the RANS method again proved its applicability and accuracy after comparing the results with those obtained from wind tunnel experiments (Fig 2.3.2). The results also showed that the knowledge from the experimental data is needed to tune the turbulence CFD models in order to reach more accurate results. They concluded that the $k-\omega\ SST$ model is preferable, especially when only a few experimental data are available.

The Large Eddy Simulation (LES) approach which is totally different from the RANS approach is also being accepted by bridge engineers. LES considers that the turbulent flow is composed of many eddies of different sizes and applies a filter to decompose the turbulent flow into large scale and small scale turbulent flows. Only the large scale eddies will be simulated directly, while the small scale eddies are modeled [37]. This approach is the most accurate one among the other methods, but at the same time it is unavoidable to not employ more computational costs than the RANS approach. Watanabe and Fumoto (2008) [37] conducted an aerodynamic study of a slotted box girder wind-resistance characteristics using a LES turbulence model with the Smagorinsky sub-grid scale model. The designed section was confirmed in the actual scale model to have enough resistance to the wind velocity of over 80 m/s, by the use of the proposed countermeasures. The slotted section was well modelled and contained permeable windshields installed at the edges of the deck model (Fig. 2.3.4). The analytical domain was 75D long by 5.07D wide by 25D high and the model for the CFD simulation had a B/D ratio of 5.84 including the slots axially at the center of the deck, with intervals of 2.54D. The experimental date were measured form the section model with windshield barriers mounted on the deck achieving a porosity ratio of 50%. In order to keep a good agreement between the experimental model and the CFD simulations, nine rectangular blocks at equal intervals are arranged for substitution of the permeable fence. The left end of the computational domain was set as the boundary of inflow U. Slip boundary was set on both the upper and lower boundaries while non-slip boundary was applied to the surface of the box girder section.

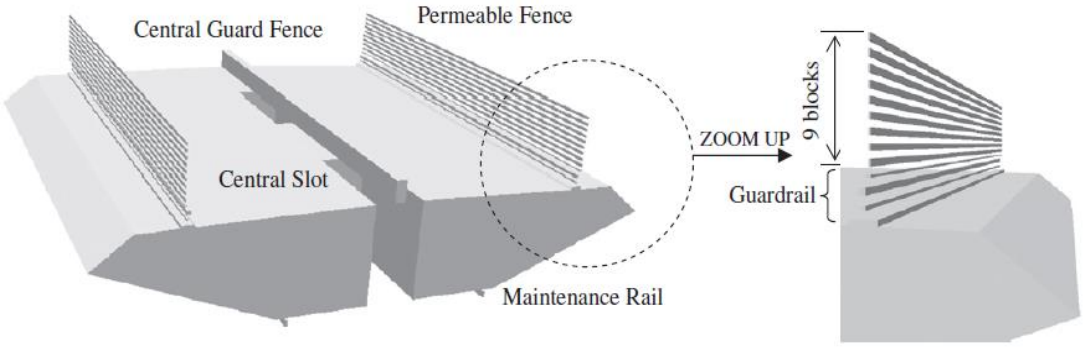

Figure 2.2.22 Section model and modeling of the permeable fence [37]

From the CFD simulation results they found that C_d increases steady at attack angles from -12° to 16° and both the trends and the values are in good agreement with the experimental data. For the C_l and C_m coefficients the gradient and the values are rather small and steady once the attack angle is more than -5° while they show rapid changes within the range from -16° to -5°(Fig 2.3.5.). The effect of the proposed countermeasures for the aerodynamic stability had been confirmed through a slightly increasing trend of the moment coefficient. Although, for the C_l values there were some deviations between the simulation ones and the experimental ones, generally the trends were not much different and thus the results were considered as acceptable.

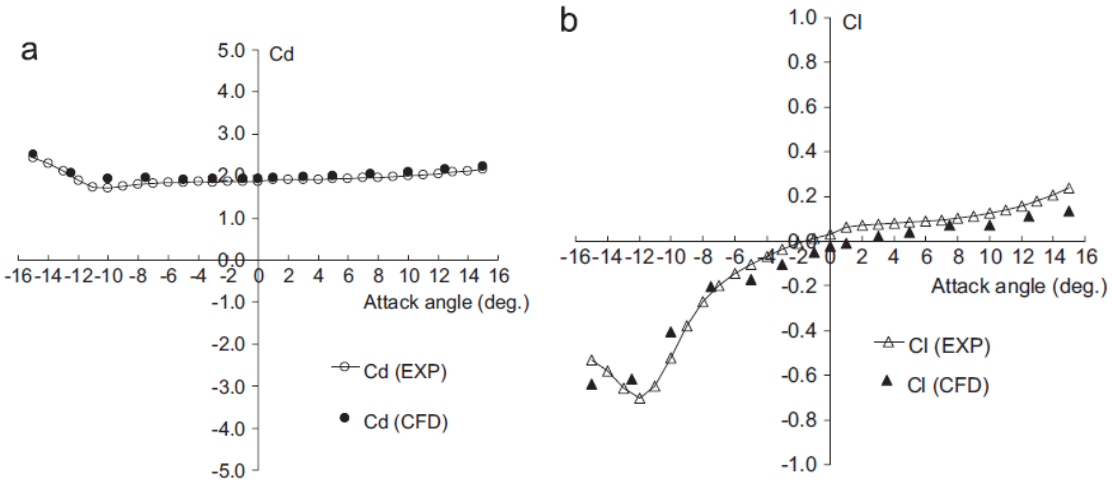

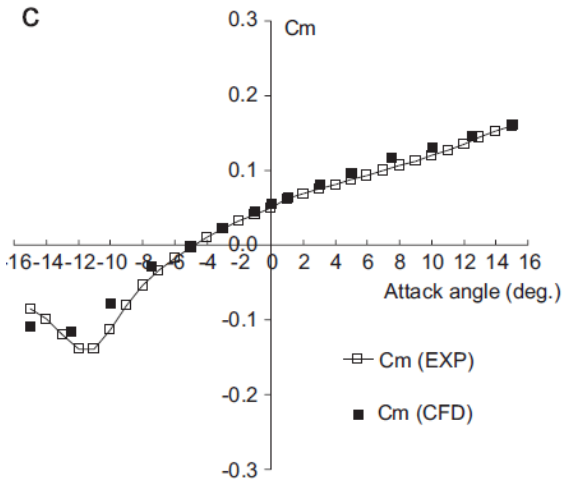

Figure 2.2.23 Three components of static aerodynamic wind forces (a) C_d (b) C_l and (c) C_m [37]

Also the same research [37] pointed out that only the static aerodynamic forces tendency cannot explain the generation of the aerodynamic forces, as well as the flow conditions around the deck. In consequence, the use of CFD simulations to visualize the flow conditions and to provide a comparison between the results for attack angles of -10° and 0°, was employed (Figure 2.3.6). Both instantaneous pressure distributions and the time - axial space averaged pressure data were analyzed. It is easier to notice that, at the attack angle of 0° the wind flow separation along the leading edge of the fairings only occurred in the upper area and reattached to the fairings immediately after. For lower area no separation was spotted and the flow moved smoothly along the surface of the bridge deck. For the case of -10°, the situation was different. Flow separations occurred at both upper and lower side of the fairings in the windward side. Especially, for the upper area of the fairings the flow reattached within the range of the maintenance rail location, which largely increased the downward C_l coefficient value and the counter clockwise of the C_m coefficient values as presented in Fig. 2.3.5. Time and axial space averaged pressure also confirmed these separation points and the reattached patterns.

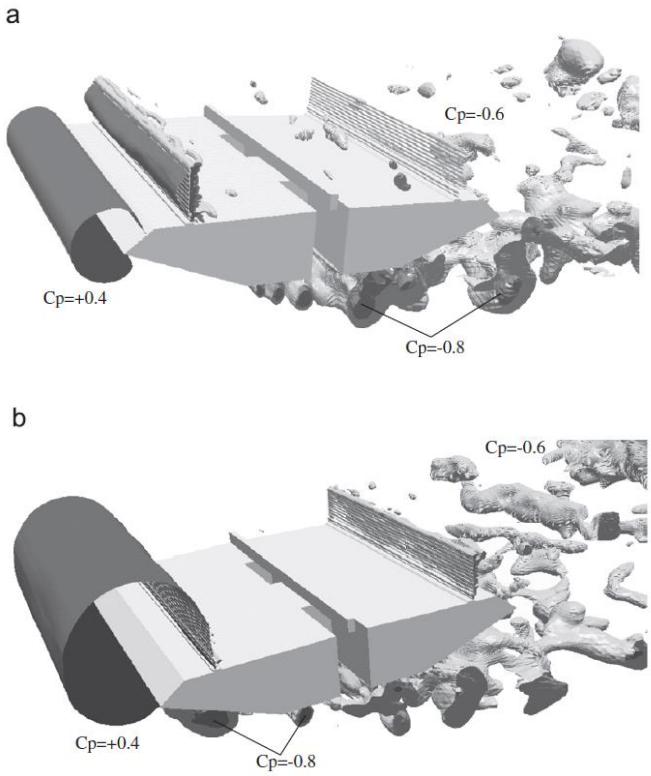

Figure 2.2.24 Bird's-eye view of instantaneous pressure contours [37]

Sarwara et, al (2008) [38] also conducted a three dimensional CFD analysis using the LES turbulence model to investigate the flow around a box girder bridge deck section. They analysed not only the accuracy of the LES-CFD model for the real bridge deck cross-section, by comparing the steady aerodynamic characteristics obtained by the LES with the experimental results, but also they made a comparison between two different simulation models which were LES and RANS using $k-\varepsilon$ models. The experimental results for both deck sections, with and without the attachments such as barriers or sidewalks were measured under the Reynolds number of $R_N = 3.5 \times 10^4$, however the CFD simulation was performed at a relatively low Reynolds number of $R_N = 1.0 \times 10^4$. The aerodynamic coefficients for the streamlined box deck girder with and without attachments were investigated under angles of attack from -15° to 15°. The results showed that the drag coefficients increase gradually in the range of -7° to 7° and reached the minimum value at 0°. Also, for both bridge deck sections, after the angles of attack over $\mp 7^\circ$ the drag coefficients increase rapidly. It was observed that the drag coefficients calculated using the 2-D standard RANS with $k-\varepsilon$ model were overall larger than the experimental ones which,

indicates overestimation of the drag force acting on the bridge section model. Meanwhile, the LES model results show good agreement with those of the experimental ones. The study analyzed the contribution of each component on the bridge deck section to the drag, lift force and moment, as well. They concluded that the use of fairings to modify the rectangular sections reduces the overall drag force acting on the bridge deck section. However, the drag force may increase instead if the size and density of these attachments are not designed appropriately. Overall, despite the higher computational costs, the effectiveness of the 3D LES model over the 2D RANS with k-ε model, in predicting the steady force coefficients and the flutter characteristics was proven.

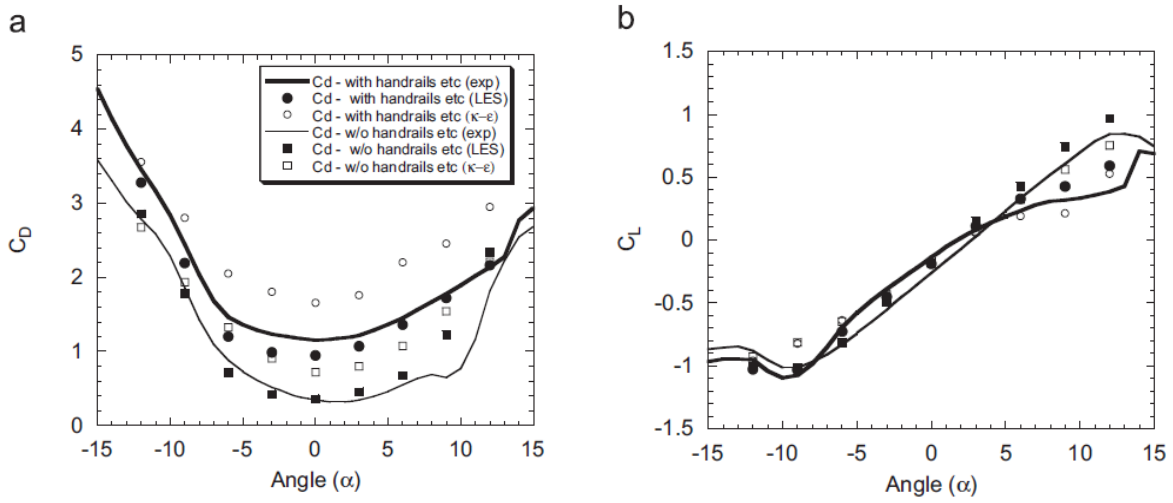

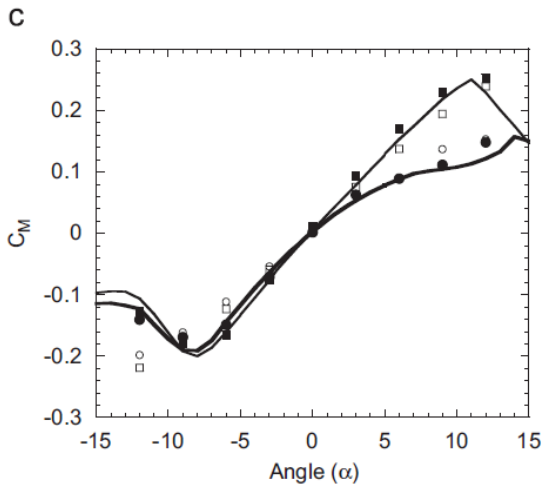

Figure 2.2.25 Comparison of experimental and numerical aerodynamic coefficients of a box girder bridge section with and without handrails: (a) drag coefficient, (b) lift coefficient and (c) moment coefficient [38]

Chapter 3 Experiment set-up and model configuration

Wind tunnel experiments is the most direct and practical approach to analyse the aerodynamic behaviour of bridges. In this chapter, the experiment details from the creating of the model to the size of wind tunnel and the instruments set-up are introduced. Both forced vibration tests using loading cells and free vibration tests with spring system procedures are also presented.

3.1 Bridge Deck Model and wind tunnel description

To improve the aerodynamic characteristics for long-span suspension bridges a new bridge deck model consisting of 4 separate decks connected by 3 stiffening beams was proposed in the current research. The numerical simulations (CFD) have shown promising results on lift and drag coefficients however the flutter derivatives can be determined only from wind tunnel test. Hence, the two degree of freedom vibration wind tunnel test was performed for a section of the Megane Bridge deck to validate the CFD results and to extract the flutter derivatives based on the time displacement histories, as detailed in the following sections.

3.1.1 Section model properties

The bridge deck sectional model used in the current experiment consisted of four individual airfoil shaped decks, with a total width dimension of the deck of 62.00 m and individual decks of 16.00 m and 10.00 m as shown in Figure 3.1.1 below, connected between them by three stabilizing beams with equal distances. The depth of the decks was 3.0 m for the side decks (traffic decks) and 2.0 m for the two middle decks (railway decks). The width of the gaps between the decks was of 3.6 m each, while the width of the stabilizing deck was 2.0 m. The configuration of this bridge deck prototype is an extension of the concept used for the design of the Strait of Messina Bridge, involving multiple decks, and is the first bridge deck with more than 2 gaps to be investigated.

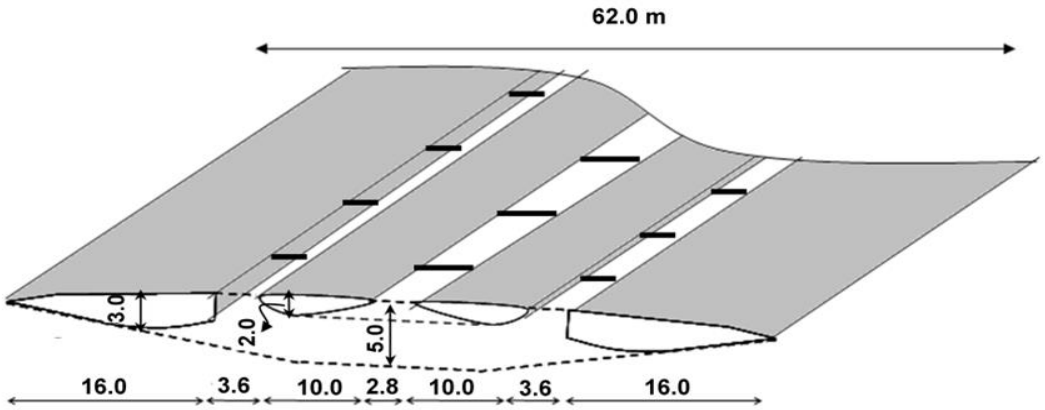

Figure 3.1.1 Prototype dimensions of the Megane Bridge deck with multiple gaps (m)

Thus, since the prototype did not reach the final design stage, no strict constrains are imposed for the mass, mass moment of inertia or the natural frequencies of the bridge deck. For the experiments a scale ratio for the model of 1:80 from the prototype was used, in order to fit the wind tunnel experimental section dimensions. Therefore the length of the sectional model was 1.00 m and the total width was 0.775 m. The gap distance between two 0.125 m middle decks was 0.035 m meanwhile for distance between the middle deck and the side deck which is 0.2 m wide became 0.045 m. Those four decks were all connected by three beams with a depth of 0.0625 m (Figure 3.1.2). The elastic constants of the springs used for the suspension system were chosen so that the estimated natural frequency was around 1.667 Hz, which is similar to the natural frequency of other deck models of long-span bridges [Larose et, al, 2006 [44]], Diana et,al (2010) [56]] and due to the limitation of the equipment, this model was tested in 2-DOF (Free vibration) and static test only. The maximum testing wind speed in the wind tunnel was 13.00 m/s; higher wind speeds of up to 17 m/s can be achieved in the wind tunnel, however the experiment was stopped whenever the vertical and torsional vibrations became too aggressive, in order to avoid any permanent damage to the bridge model or the mounting system. Also in order to construct a rigid bridge deck model and in the same time to achieve a relatively high natural frequency, the total mass of the section model was minimized to 5 kg. the streamlined shape of the individual decks was very difficult to construct using plywood, which is usually the most common material used for wind tunnel models, thus a 1:80 scaled external shell was created out of ABS plastic material, through 3-D printing techniques, to ensure an exact replication of the prototype curved cross-section (Fig 3.1.3). For printing a three-dimensional Autocad file was created for each of the decks and for the beams (Fig 3.1.4). Due to the dimension of the section

model the shell was printed in 4 parts and the manufacturing company connected them together. In order to maintain the homogeneity of the deck model, four low density foam cores with exactly the same geometry of the deck shells to be inserted inside each deck shell and also the same shape cross-beams connecting thee four decks were precisely shaped using a hot-wire cutting technique. In order to ensure the perfect curved shape during the cutting process, two cardboard papers were placed as end plates, which follow the shape of each individual bridge deck and were attached to both ends of the foam core as guidance. The same procedure was repeated several times until four pieces of the small middle deck core and four pieces of the large side deck cores could all fit perfectly in the plastic shell (Figure 3.1.5 and Figure 3.1.6). These finalized foam cores were inserted into the deck shells and were bonded to the internal surface of the shells with high performance glue. As the Acrylonitrile butadiene styrene (ABS) plastic is much more flexible than the wood material used for bridge deck models, four aircraft graded aluminum strips with 0.4 cm thick were glue to the top surface of the decks to increase the resistance to bending stiffness to improve the homogeneity and to eliminate the roughness along the deck model. Such improving technique is commonly used in wind tunnel testing.

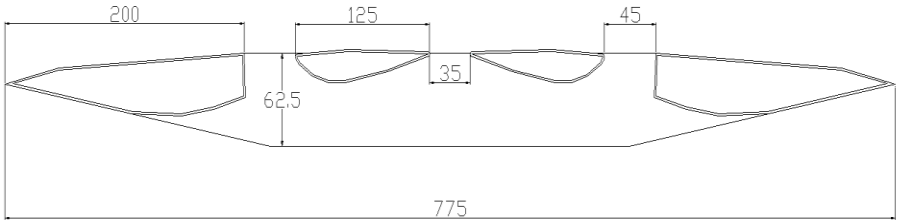

Figure 3.1.2 Dimensions of the four deck bridge model (mm)

Figure 3.1.3 Hollow shell of the Megane Bridge made by 3-D printing

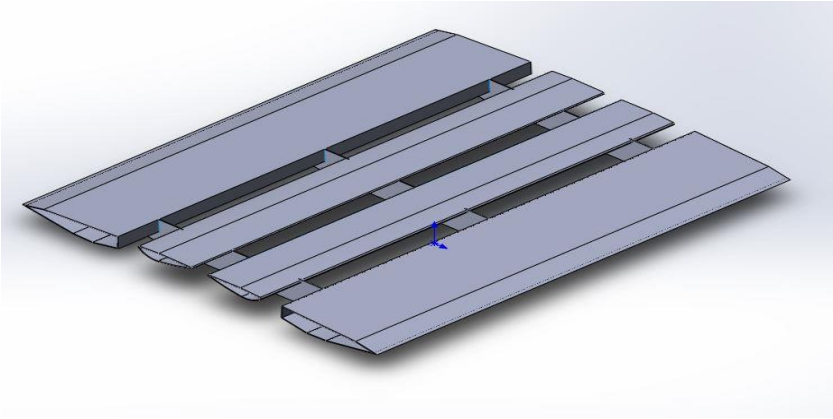

Figure 3.1.4 3-D model created from Solidworks

Figure 3.1.5 Side deck foam core model

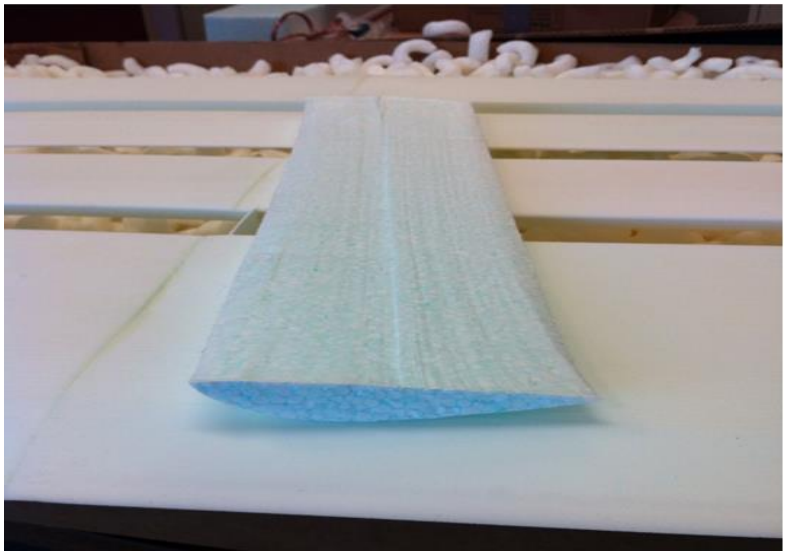

Figure 3.1.6 Middle deck foam core model

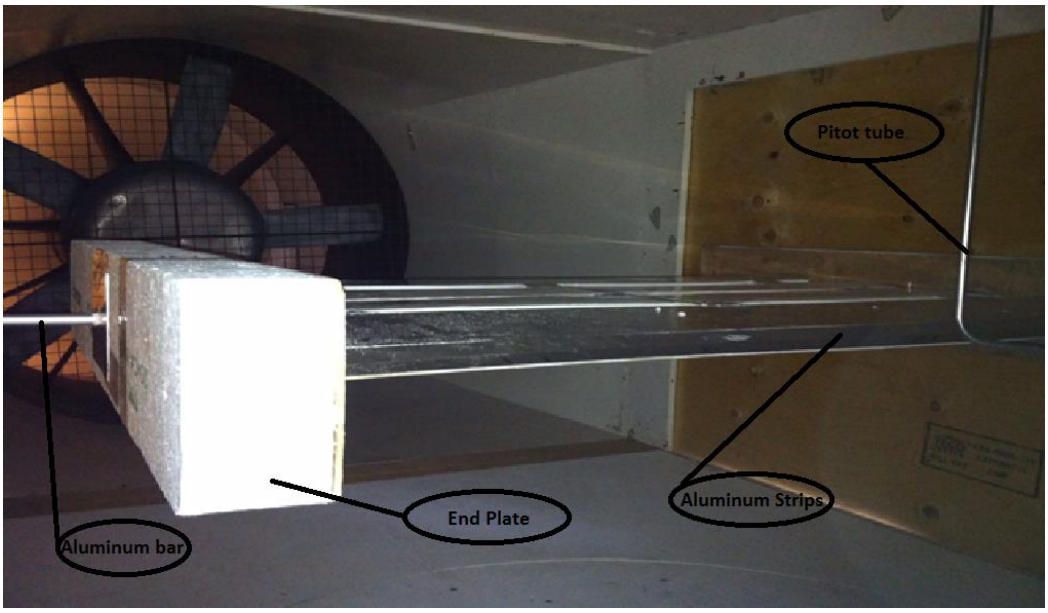

Figure 3.1.7 Final setting of the bridge section model in the wind tunnel

Two foam rectangular shape end plates were installed at the extremities of the bridge section model (Figure 3.1.7), in order to reduce the aerodynamic end effects (swirly flow formed because of the sudden termination of the model) and to ensure two dimensional-flows over the model during the tests. Reynolds number of the section model was estimated up to $Re = 5.2 \times$

10^5 with B = 0.775 m at the maximum test wind speed of 10 m/s during the static coefficients tests.

3.1.2 Wind tunnel facility

All the tests were conducted in the atmospheric boundary layer (ABL) wind tunnel at Carleton University located in 2140 ME building. The ABL wind tunnel is an open-circuit suction tunnel, with two test sections one upstream, connected to a pitot tube and allowing access to the model from both lateral sides of the tunnel and from underneath the wind tunnel, and the downstream section which allows access only from one side of the tunnel . Both sections have the height of 1.12 m, the width of 1.68 m and the length of 2.44 m. Four horizontally-hinged plexiglass windows were installed, which can provide access to each test section from both sides of the wind tunnel (Figure 3.1.8 and Figure 3.1.9).

Figure 3.1.8 Upstream and downstream wind tunnel test sections

Figure 3.1.9 Inside view of the wind tunnel with floor roughness elements

The five-blade fan has a diameter of 1.67 m and is powered by a 30 kW motor, which allows the wind tunnel to achieve wind speeds from 3.0 m/s to 17 m/s. The ABL wind tunnel has a contraction ration of 7.1:1 at the upstream and roughness elements on the floor inside the wind tunnel, to ensure low turbulence flow; uniform flow tests can also be performed by removing the roughness elements from the tunnel. The primary concern of the current study was determining the aerodynamic behaviour of the Megane Bridge deck section in smooth flow, therefore these elements were removed in the first place for achieving the smooth flow testing. Detailed plan view and side view of the ABL wind tunnel are adapted from Professor McTavish's notes, which was originally drawn by professor Kind [39] to reflect the dimensions of the ABL wind tunnel.

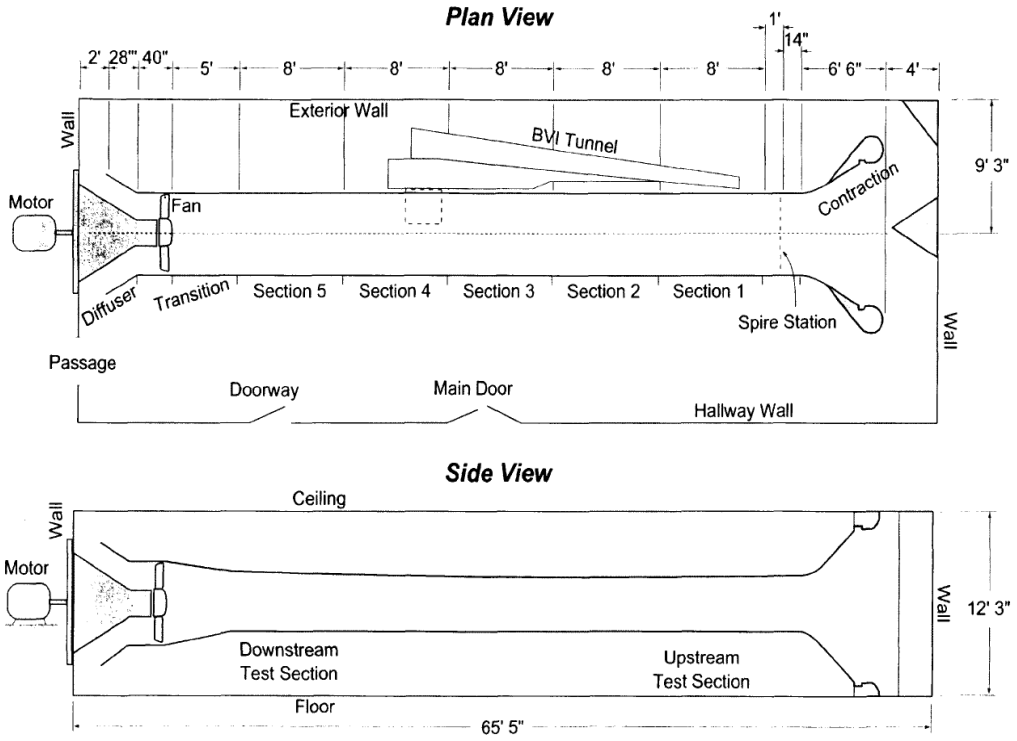

Figure 3.1.10 Wind Tunnel Plan and Side View [39]

3.2 The experimental set-up

3.2.1 Wind Force Coefficient Measurement

The experimental setup for the static wind load coefficients is shown in Figure 3.2.1. The testing system consists of a pair of steel frames of 1.9 m in height and almost the same size of the plexiglass window which is 1.7 m. The two frames were installed outside the wind tunnel test section and were robust enough to keep them steady during the test. Two aluminum bars reached out from the endplates of the bridge deck section model and were connected to the force balance devices which were used to measure the wind–induced force along the horizontal, x and vertical, z axis respectively. After several trials, wooden plates were mounted on each of the steel frames so that the load cells could be fixed to the plates to ensure the accuracy of the position and inclination when measuring the data. By adjusting the rotation angle of the wooden plates from the outside, the attack angle of the test model inside the wind tunnel could be easily changed. Due to the small magnitude of the voltage values read from the force balances the computer data

acquisition system of the wind tunnel couldn't record with accuracy the correct values. Thus, two P-3500, Portable Strain Indicators were used as an alternative to measure the changing voltage during the experiments (Figure 3.2.2). A static stainless steel pitot tube probe was mounted on the ceiling of the wind tunnel and was placed in front of the section test model to measure the incoming wind speed and to record it into the computer which controls the wind speed of the wind tunnel, thus ensuring that the desired wind speed is always achieved with accuracy. With the bridge deck model fixed in the wind tunnel as detailed above, only the static drag and lift force coefficients were measured for different angles of attack. For flutter test, the deck model must be allowed to vibrate, therefore a spring suspension system is required.

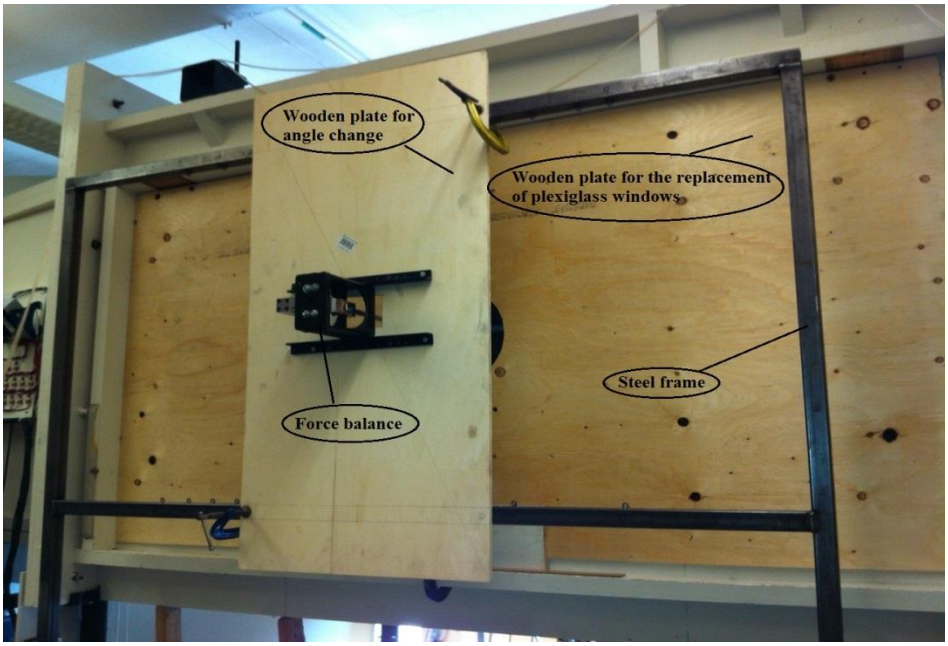

Figure 3.2.1 Force balance system measuring static wind force (One end)

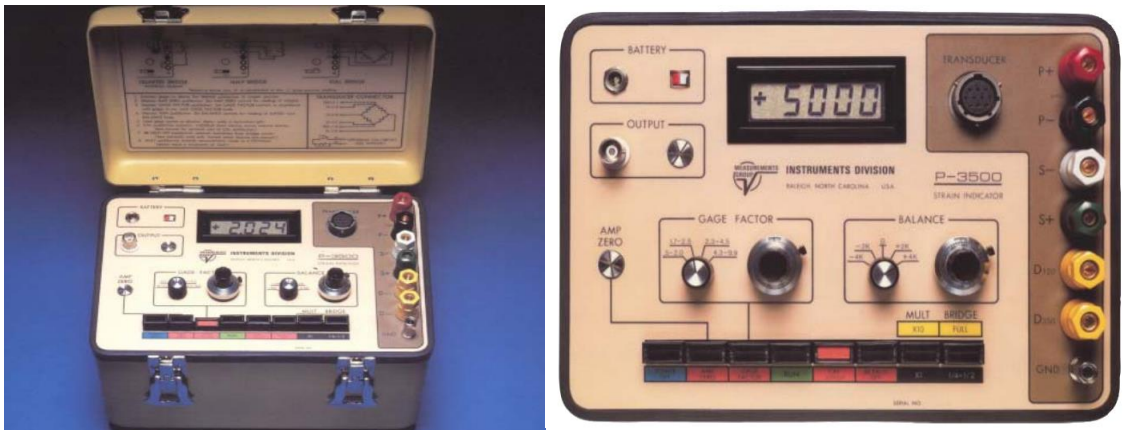

Figure 3.2.2 Portable Strain Indicators

Figure 3.2.3 Laser sensor and ultrasonic sensor

3.2.2 Free Vibration Spring System

The free vibration suspending spring system used for the flutter tests was developed by modifying the existing static wind force measurement system where the bridge deck model was fixed to the wooden plates and was not allowed to move (Figure 3.2.4 and Figure 3.2.5.) The spring system was required to enable simultaneous vertical and torsional motions of the section bridge model, at different wind speeds and different attack angles. The design of the suspending spring system included the same wooden plates, the steel frames which were used in the static force tests with load cells were removed and four springs were installed at each end of the model, two upper springs and two lower springs. Additionally one aluminum U-channel was fixed to each end of the aluminum bar which connects the deck model to the force balances. The eight

vertical springs were hung from the special connection on both top and bottom area of the wooden plate, to hold the model in position and to allow a harmonic motion around the equilibrium static position. The specific elastic constant of the springs was chosen so that it would satisfy the vibration frequency similarity requirement and also to ensure the reduced wind speed for which the model can reach the flutter instability is within the range of the tunnel's achievable wind speed. Similar to the static test, the wooden plates could be rotated to achieve different wind attack angles. The yellow collar twine which connected the lower springs could be adjusted so the U- channel bar could maintain the same angle with the plate.

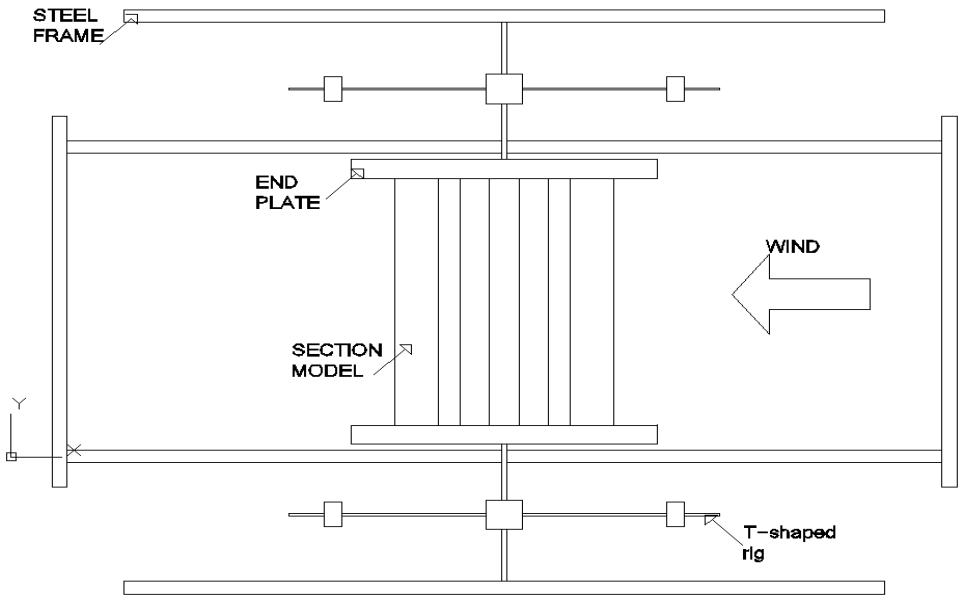

Figure 3.2.4 Spring suspension system top view

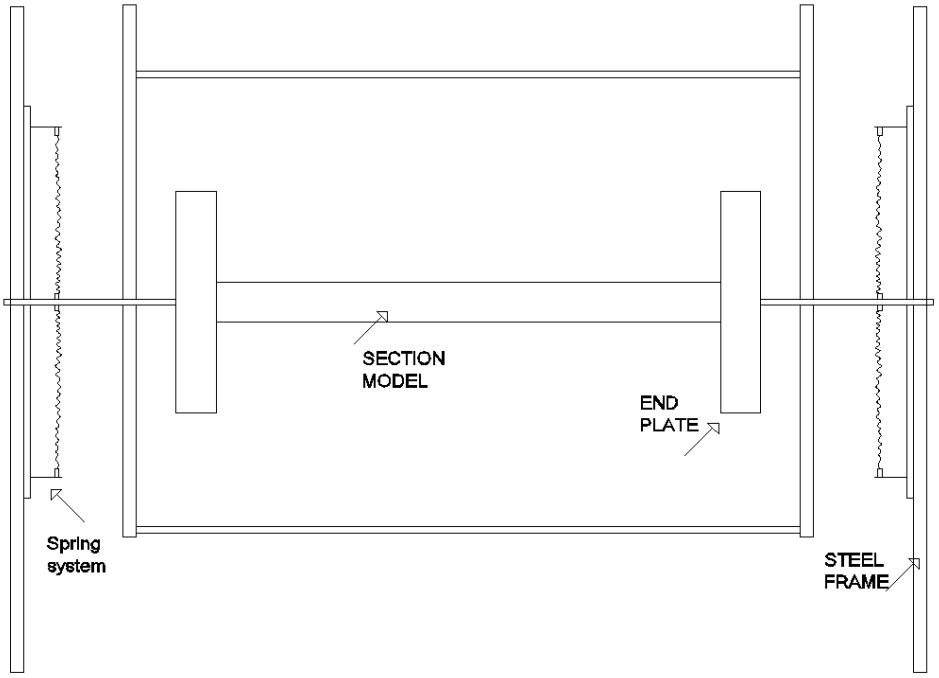

Figure 3.2.5 Spring suspension system front view

Because of the highly fluctuating vibration the wind aerodynamic forces cause for the bridge deck model, very sensitive laser sensors must be utilized. Thus one laser displacement sensor and one ultrasonic sensor (Figure 3.2.3) were attached to the top of the wooden plate to measure the vertical displacements at the extremities of the aluminum bar, corresponding to the upwind and downwind extremities of the model and based on the recorded values the rotational angular displacement was calculated. More exactly, one sensor was placed above the front edge of the U–channel bar and the second sensor was installed above the rear edge with a distance of 57.5 cm between each other (Figure 3.2.3). A computer data acquisition system was used for all experimental cases performed. The data logger was an 8-channel data acquisition system which converts the voltage signal to digital values recorded in a computer. The hardware was controlled by the Labview 2012 software which performed the task of recording and calculating the displacement based on the incoming digital signal. The specific program was designed for the data acquisition (Figure 3.2.6) for which the concept is to separate the output from the data acquisition system into two streams based on the source of the data. After that, the calibration results which were expressed from of equations (Equation 3.1 and 3.2) were written into the

block of formulas. By doing this, the voltage outputs can be transformed into displacement output and collected into .txt files. Based on the vertical displacements outcome at each end, the torsional motion $\alpha(t)$ can be determined through a simple calculation.

$$d_l = V_l * 4.33 + 6 \tag{3.1}$$

$$d_r = V_r * 3.024 + 4.73 \tag{3.2}$$

where d_l and d_r represent the left and right displacements calculated based on the voltage V_l and V_r measured by sensors.

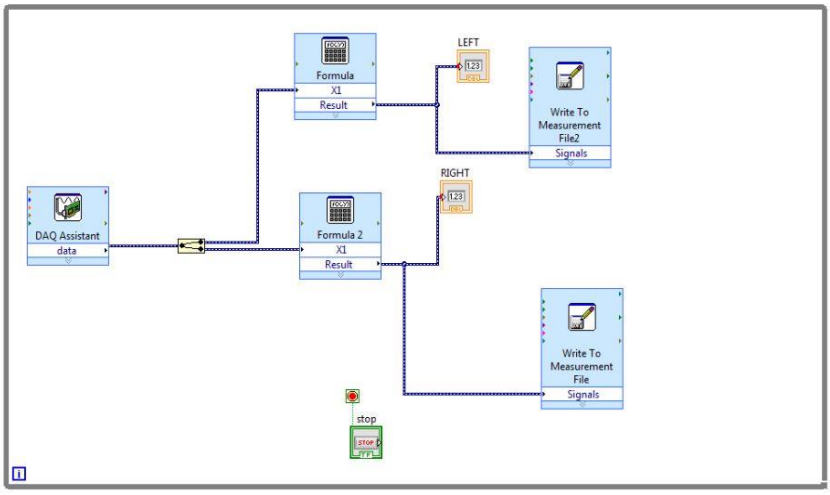

Figure 3.2.6 Labview program detail

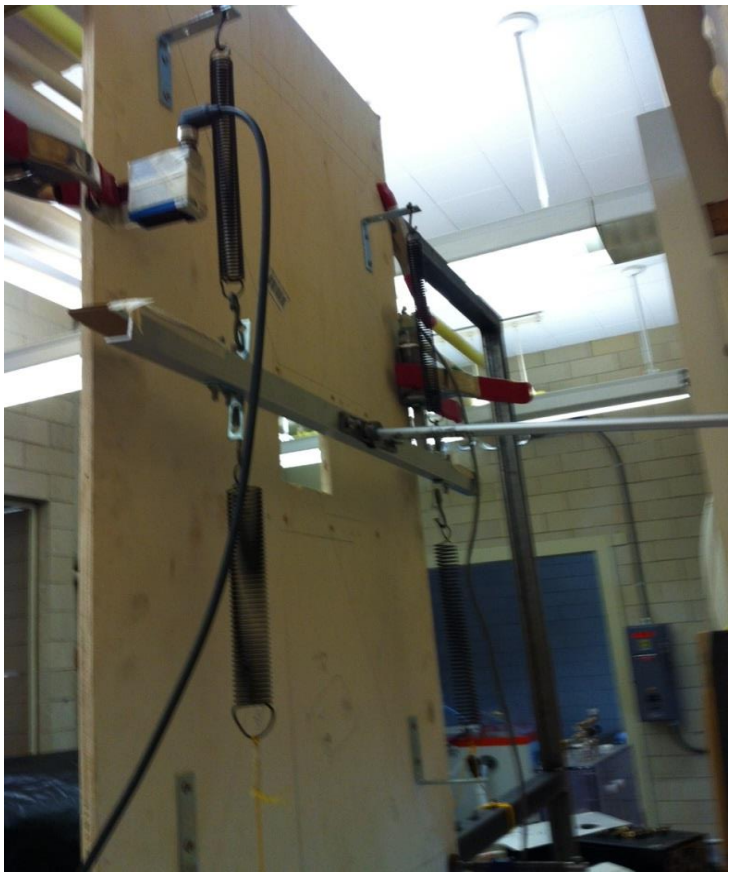

Figure 3.2.7 Final design of the spring system with laser sensors

The stiffness of two different types of spring was checked through Hooke's law by measuring the displacement with applied weight. A series of known weights from minimum of 914 gram to 4710 gram was used and the procedure was conducted twice and the average of the spring stiffness was picked (Table 3.2.1 & Table 3.2.2). Meanwhile, forces were applied to the bridge model vertically and horizontally separately for the calibration of the force balance system. The value corresponding to the applied force was reflected through strain indicator thus a linear equation was adopted (Figure 3.2.8). The calibration was repeated until no remarkable difference was noticed.

Table 3-1 Calibration of the short spring

Short Spring						
Set 1			Set 2			Average
Weight (N)	Displacement (m)	Stiffness (N/m)	Weight (N)	Displacement (m)	Stiffness (N/m)	
0.00	0.09		0.00	0.09		
18.29	0.11	1015.93	18.35	0.11	965.56	242.59
27.68	0.15	234.71	27.68	0.15	245.52	
36.58	0.18	262.01	37.25	0.18	245.50	
46.16	0.22	239.37	46.16	0.22	228.42	
Average		245.36			239.81	

Table 3-2 Calibration of the short spring

Long Spring						
Set 1			Set 2			Average
Weight (N)	Displacement (m)	Stiffness (N/m)	Weight (N)	Displacement (m)	Stiffness (N/m)	
0.00	0.12		0.00	0.12		
8.96	0.13	746.43	9.44	0.14	555.14	440.00
18.35	0.16	426.75	19.01	0.16	435.21	
27.25	0.18	468.85	28.34	0.18	424.07	
36.83	0.20	416.29	37.25	0.20	468.85	
Average		437.30			442.71	

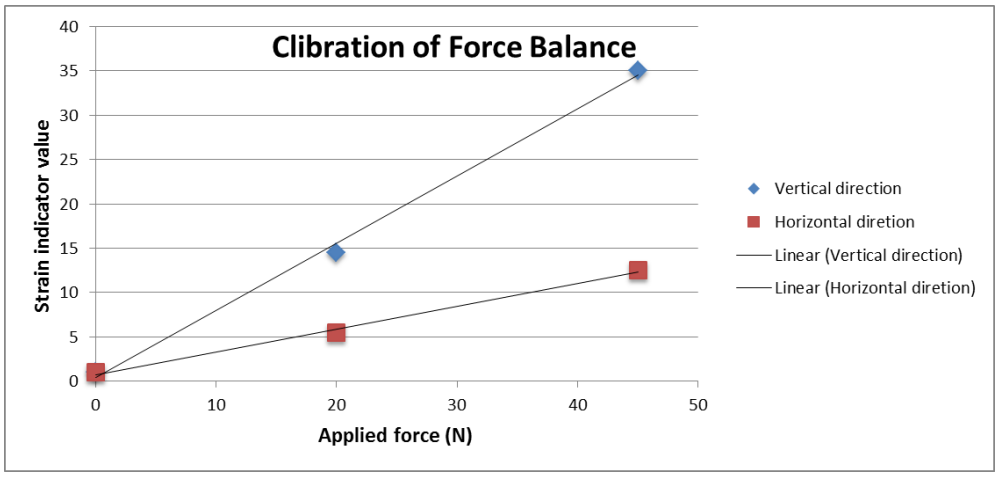

Figure 3.2.8 Calibration for the force balance system

3.2.3 The experiment procedure

- Static wind force experiment:

1) The frame system was setup; the model was installed into the wind tunnel.
2) The model was connected to the force balance which was fixed on the wooden plate from both sides and then the plates were mounted to the frame.
3) The initial mean attack angle was adjusted to 0^0.
4) The numbers showed on the Portable Strain Indicators for both vertical direction and horizontal direction were first recorded in wind-off situation.
5) The wind was applied and the average values showed on two indicators in 10 second were recorded.
6) The wind speed was increased by 1 m /s until the maximum of 14 m/s. In order to get reliable data at each stage, the wind speed were kept constant for 30 second. 10 samples were recorded during that time.
7) The wind tunnel was turned off and the system was adjusted to the next attack angle. Steps 4) to 6) were repeated. Until all the attack angles $-10^0 \sim +10^0$ were covered.

- Free vibration flutter test:

1) The force balances were removed from the wooden plate and the spring system was installed.
2) Free decaying vibration test was performed at first in wind-off situation by giving an initial displacement. The test was repeated 3 times and the displacement time history was recorded through laser sensors.
3) The angle of attack was set to 0^0 and then the wind speed was applied.
4) The wind speed was increased by 1 m/s and at each stage the wind speed lasted for few minutes.
5) During each stage, small external forces were applied to the model to check the vibration property. So the certain wind speed which cause VIV and Flutter could

be determined. At the same time, laser sensors were turned on and the displacement decay histories were recorded for 1 minute.

6) Once the bridge section model was performing a vibration with clear character of flutter the test was stopped.
7) The wind tunnel was turned off and the system was adjusted to the next attack angle. Steps 4) to 6) were repeated. Until all the attack angles $-8^0 \sim +8^0$ were covered.

Chapter 4 Experimental Results

4.1 Zero Wind Speed Free Vibration

The free vibration test was conducted with zero wind speed, wind-off conditions. The model was installed on the suspension spring system and an initial displacement was given to the model which was then released so it can vibrate freely. The decaying vibration amplitude was measured by the displacement sensor and thus the first natural frequency of the model was calculated as a function of elastic properties of the spring system with a first set of springs. The spring system for flutter tests, as mentioned earlier, was then modified based on the existing static wind force measurement system. The eight vertical springs which were designed to hold the model in position were located separately on the both top and bottom area of two wood plates as represented in Fig.3.2.5. The elastic constant k of the springs was 440 N/m for the top and 240 N/m for the bottom springs, leading to an equivalent elastic constant for the entire model of 680 N/m. Also the weight of the entire suspended model, including the four individual decks, the connecting beams, the end plates, and the springs and the connecting aluminum bars, was of 6 kg. Based on the equation of fundamental frequency the model had a natural frequency of 1.70 Hz along the vertical direction.

$$f_n = \frac{1}{2\pi}\sqrt{\frac{k}{m}} \tag{4.1}$$

where k is the equivalent stiffness of the spring and m is the total mass of the bridge system.

The wood plates installed on the supporting steel frames, can be rotated to achieve different wind attack angles and for the wind-off test these were adjusted to zero degree and only one sensor was used for the wind-off case. During the set-up phase, the aluminum bar reaching out from the model seemed to affect to the test results due to its flexibility. In order to eliminate possible errors, the displacements at two different points located at the middle and at the end of the model were recorded (Fig. 4.1.1. and Fig. 4.1.2.), for both the torsional and vertical vibration tests. For the accuracy of the results, each displacement was measured 4 times with a record period of 20 s and the average values were considered for the analysis.

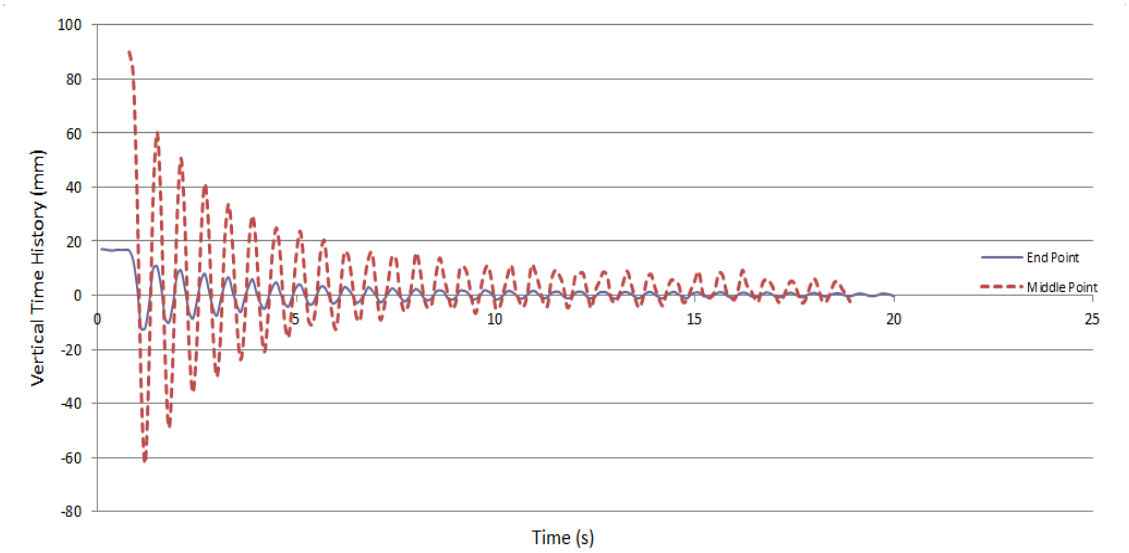

Figure 4.1.1Comparison of the displacements recorded under vertical motion only

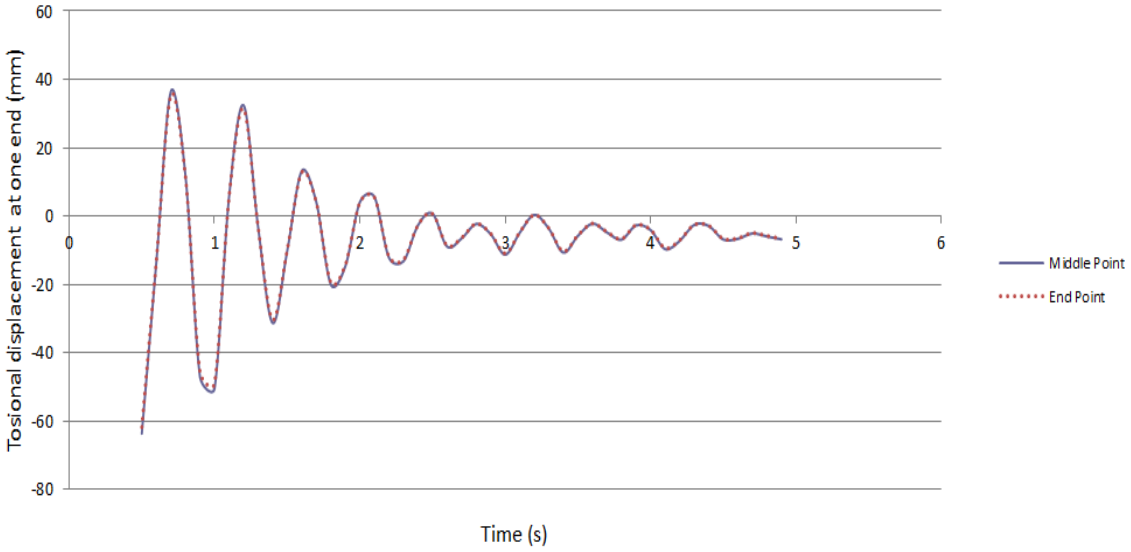

Figure 4.1.2 Comparison of the displacements under torsional motion only

By using fast Fourier transfer (FFT) the free vibration displacement time histories show that the model installed on the spring system has a frequency of 1.714 Hz in vertical vibration and around 2.4 Hz in torsional vibration(Fig 4.1.3). The vertical frequency is pretty close to the calculated result 1.7 Hz based on formula 4.1. The large difference between the two lines of the vertical displacement time history at the middle and end points of the deck (Figure 4.1.1), indicate the effect caused by the flexibility of the aluminum bars used to suspend the model to

the frames. Because of this, the recorded vertical displacement for all the wind-on cases would be averaged between the data from the laser sensors located at those two points. For the torsional direction (Figure 4.1.2), the displacements of the two points showed a good agreement, which means that the torsional displacement values do not need to be modified. After comparing the vibration amplitudes at the middle point and at the end point of the bridge model, for each cycle in vertical displacement time history, an amplification ratio of 5.2 was established and was applied to all the recorded vertical displacement time histories of the wind-on case to eliminate the error caused by the aluminium bars and the suspending spring system.

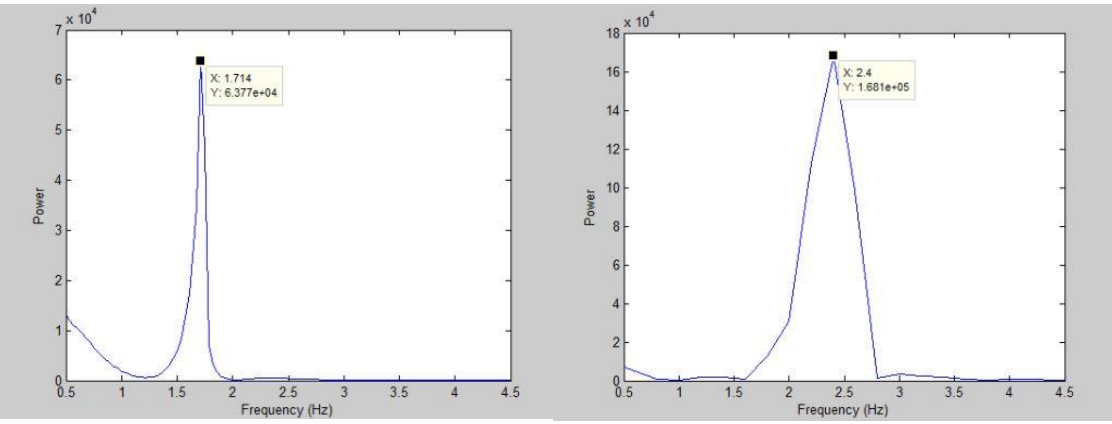

Figure 4.1.3 Vertical and torsional free vibration frequency

4.2 Static aerodynamic force coefficients

The static aerodynamic force coefficients can be determined from the results of two-dimensional experiments and these are presented below. As mentioned in Chapter 3 the experimental test results rely on the output data from the force balance equipment system. The force balances can only record the force changing situation in two directions which is vertical and horizontal, thus only the drag and lift forces were recorded. Under this condition the pitch moment acting on the bridge section model could not be monitored. Performing several initial tests, it was found out that the gage factor indicated by the two P-3500, Portable Strain Indicators, had a significant influence on the data output. If too large gage factors were used, even under the maximum wind speed, the strain values recorded didn't show big difference when compared

with those obtained under the minimum wind speed. While for the small gage factors the device became too sensitive and the output was changing becoming quite difficult for manually recording a stable value. At last, after a trial and error procedure, a gage factor of 1.0 was chosen for all the experiments.

The Reynolds number of the experiment was of the order of 1 to 5 x 10^5, based on the width of the deck and the wind speeds employed in the tests. The drag force coefficient and lift force coefficient are two non-dimensional parameters which are mainly controlled by the shape of the bridge deck model, as well as the angle of airflow reaching the deck surface (angle of attack). Thus, the static lift and drag forces induced on the model were obtained for angles of attack from -10 ° to 10 ° through the two-dimensional tests. Two separate equations were used to calculate the static drag and lift coefficients respectively, as recommended by Simiu and Scanlan, 1996 [2]:

$$D(\alpha) = \frac{1}{2}\rho U^2 B C_D(\alpha) \tag{4.1}$$

$$L(\alpha) = \frac{1}{2}\rho U^2 B C_L(\alpha) \tag{4.2}$$

where C_D and C_L are non-dimensional mean force coefficients, L is lift force, D is drag force, B is the model width, U is the wind speed and ρ is the air density. The calculation for each test case is provided in Table 4.1 for wind speeds of 5 m/s, 7 m/s and 10 m/s corresponding to Re numbers of 2.59 x 10^5, 3.64 x 10^5 and 5.19 x 10^5 respectively. The tests performed for 3 m/s wind speed yielded inaccurate estimation of the static coefficients, mainly because of the relatively small values of the static forces acting upon the bridge model, as well as the limitations of the strain gages measurement devices which were not able to capture very small force values. On the other hand, with the increase of the wind speed, the drag and lift coefficients changed and their evolution became stable after the wind speed reaches values of at least 7 - 8 m/s. The coefficients obtained for 5 m/s, 7 m/s and 10 m/s are represented for comparison purposes in order to demonstrate the difference in evolution of the static aerodynamic coefficients. The results at these three wind speeds are summarised in Figure 4.2.1 and 4.2.2.

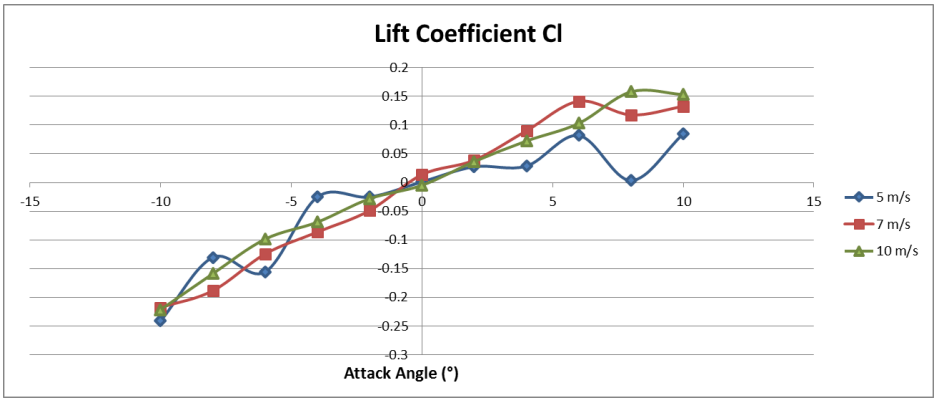

Figure 4.2.1 C_L for the section model at 5 m/s and 10 m/s

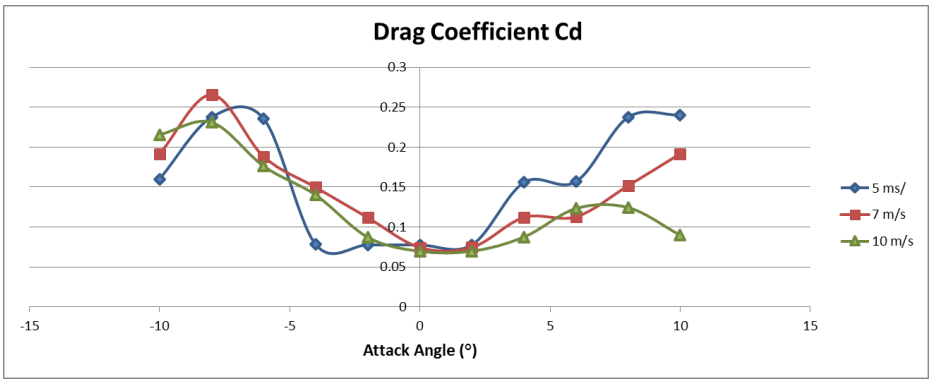

Figure 4.2.2 C_D for the section model at 5 m/s and 10 m/s

The lift coefficients presented a steady increase at 10 m/s from C_L = -0.222 up to C_L = 0.153 for the entire range of investigated attack angles, while the for the wind speed of 5 m/s, the lift coefficients fluctuated more. For small positive and negative attack angles, the minimum values of lift coefficients registered almost the same values for both wind speeds 5 m/s and 10 m/s. However, due to the higher wind speed, the magnitudes at 10 m/s are relatively larger than those of 5 m/s especially for attack angles from 4 ° to 10 ° and -4 ° to -10 ° (Figure 4.2.1) with C_L = 0.08572 to C_L = 0.153 and C_L = -0.069 to C_L = -0.222 , respectively. Despite the difference of the values caused by the wind speed the lift coefficients measured in all cases show similar increasing trends. For the drag coefficient, the results at 5 m/s and 10 m/s presented a relatively symmetric evolution in regard to the minimum drag coefficient occurring at the attack angle of 0 ° (Figure 4.2.2). However the comparison between 5 m/s and 10 m/s wind speeds show major differences for the drag coefficients especially in the range of -2 ° to 2 °angles of attack. For positive attack angles ranging from 4 ° to 10 ° and negative range from -4 ° to -10 °, the results

obtained under lower wind speeds are larger than those with high wind speeds, especially on the positive side. It is obvious that the static drag coefficients at negative attack angles are generally larger than those at positive angles. Both curves have a drop at the two ends of the graph which correspond to the attack angles of 10 ° and -10 ° respectively. The overall drag coefficient for the entire Megane deck section maintained relatively small values of C_D = 0.07 to 0.21.

As mentioned above, these static force coefficients will gradually become stable and thus will be independent of the Reynolds number after the wind speed reaching a certain value. In order to check if the calculated coefficients are no longer influenced by the magnitude of the Re number and of the wind speed respectively, the results obtained from 8 m/s to 10 m/s are collected and compared. (Figure 4.2.3 and Figure 4.2.4). It was noticed that the lift coefficients start at C_L = -0.212, C_L = -0.239 and C_L = -0.222 under wind speeds of 8 m/s, 9 m/s and 10 m/s, respectively and are increasing up to C_L =0.120, C_L =0.161 and C_L =0.155 for the high positive angle of 10 °. Therefore it can be ascertained that the critical wind speed which influences the variation of the lift coefficient was overpassed and the values would not change significantly with a further increase of the wind speed. The drag coefficients measured for 8 m/s, 9 m/s and 10 m/s have a very similar evolution namely the curves from three wind speed cases are in good agreement with each other, except for the side of the positive attack angles for the case of 10 °, they yield values of C_D = 0.173, C_D = 0.121 and C_D = 0.090 for 8 m/s, 9 m/s and 10 m/s respectively. To determine whether the drag and lift coefficients values beyond this angles of attack range will keep decreasing or not, a further study needs to be performed. However the slope of the aerodynamic static coefficients graph, between -10 ° to 0 ° and 0 ° to -10 ° is very important in determining the aerodynamic instability as it will be shown in the later sections.

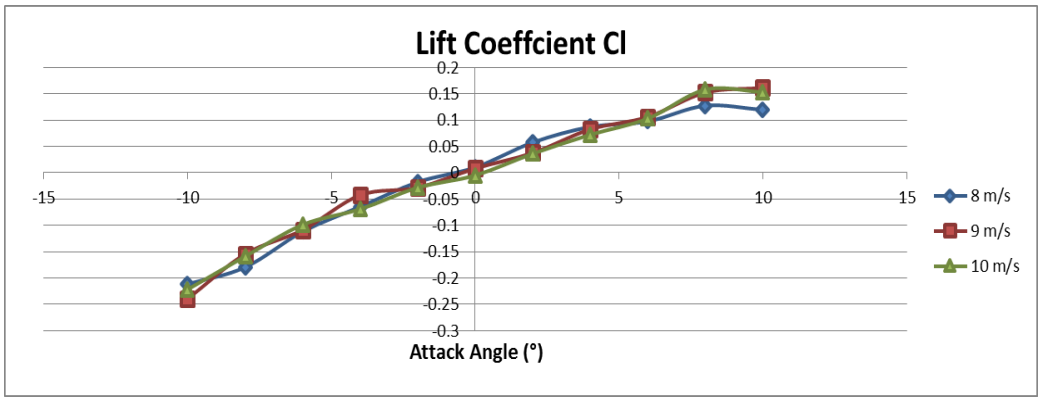

Figure 4.2.3 Lift coefficients obtained from the last three wind speed cases

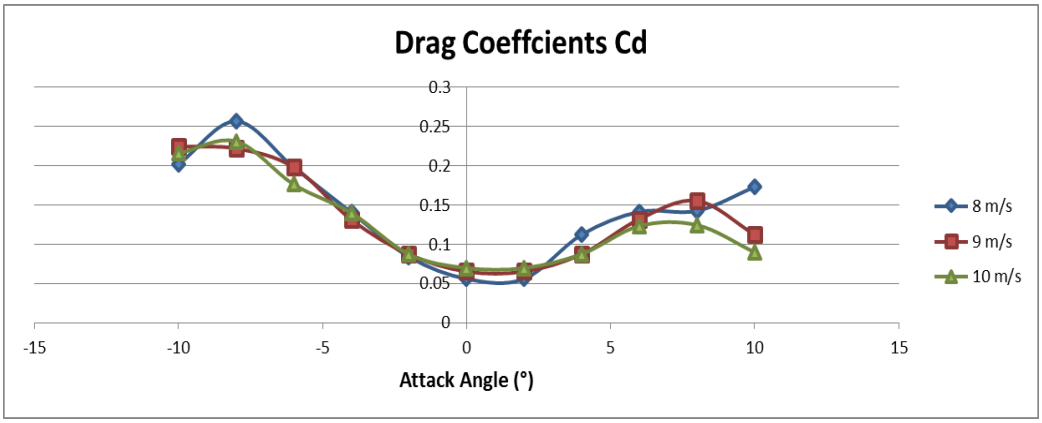

Figure 4.2.4 Drag coefficients obtained from the last three wind speed cases

Using the calculated static coefficients, the galloping theory established by Den Hartog in 1932 [2] which is the first stability criterion to estimate the possibility for a section model to encounter galloping for wind speeds exceeding critical values can be applied for each case. Since mechanical damping is usually positive for real structures, it means that the aerodynamic damping must be negative, in order to achieve amplification of the structural vibrations and for the appearance of galloping. The Den Hartog galloping instability formula [2] below was applied and results are shown in Figure 4.2.5.

$$\left(\frac{dC_L}{d\alpha} + C_D\right)_\alpha < 0 \tag{4.3}$$

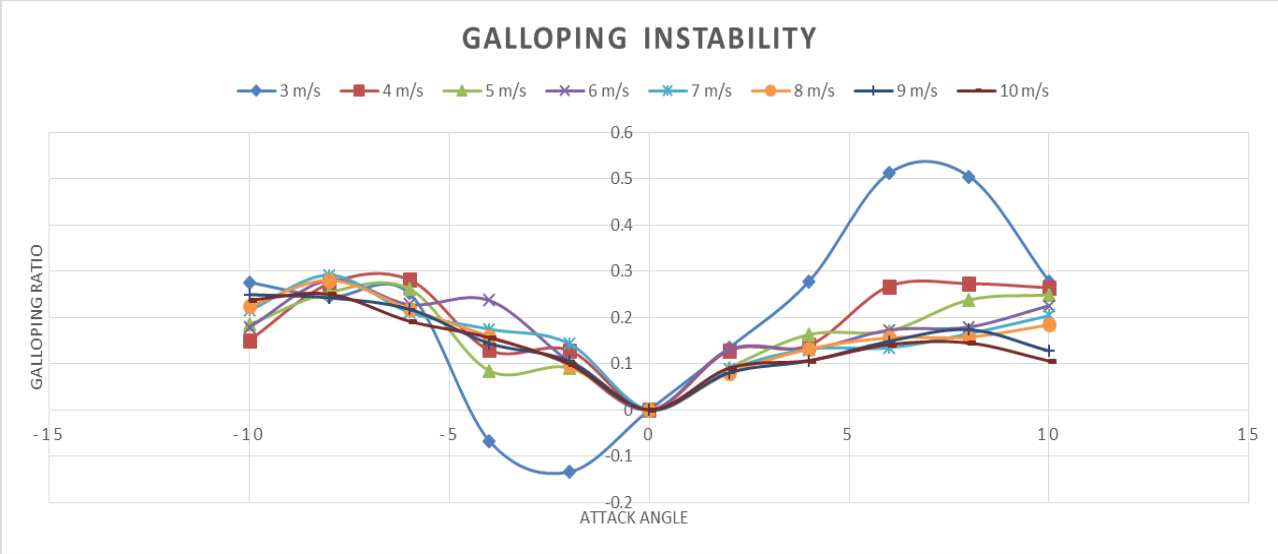

Figure 4.2.5 Galloping ratio for each attack angle under different wind speed

Through the results, obviously the Megane Bridge deck model presented a good stability against galloping for all the tests scenarios, except for the two negative values that were found at attack angles of -2 ° and -4 °. However, the negative values appear only for the wind speed of 3 m/s, which is the beginning value for the tests and the galloping aerodynamic instability, is unlikely to occur under such small wind speed scenario. Again this reveals the fact that some inaccurate data were collected for the 3 m/s wind speed.

4.3 Spring system results

4.3.1 Time displacement histories

The displacements of the bridge model during the dynamic tests were detected by the two laser sensors located at the two sides of the model, the leeward and windward edges, at a distance of 57.5 cm. These displacements were transmitted through the data acquisition system and were recorded into the txt files through the Labview program. Subsequently the data obtained from each wind speed case investigated were modified to reveal the vibration of the

bridge. For the vertical mode, the mean deflection at any instance was calculated by averaging the two displacement data measured at the two ends as follows:

$$C(t) = \frac{dA(t) + dB(t)}{2} \tag{4.4}$$

where C(t) is the vertical movement at the center of the bridge, $dA(t)$ and $dB(t)$ are the displacement at the two ends for each instance in time. For the torsional mode, since the amplitude of the torsional angle is relatively small it means that the algebraic processing of the vibration data can be written as:

$$\alpha(t) = \frac{dA(t) - dB(t)}{D} \tag{4.5}$$

where, D is the distance between the two measurement sensors which is 57.5 cm (Figure 4.3.1). The time displacement histories with respect to the vertical and torsional movement were plotted and compared with each other (Figure 4.3.2 to Figure 4.3.8).

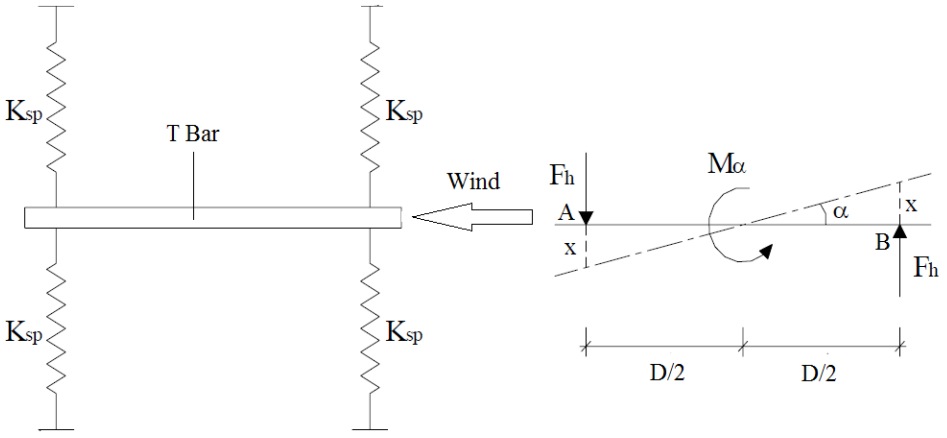

Figure 4.3.1 Sketch of the spring system [59]

In general wind induced vibrations of a structure should be symmetric with regard to a position of equilibrium, however the time displacement history at each wind speed case showed big differences with respect to the x axis, due to the wind attack angle and due to the

aerodynamic static force acting on the bridge section which tend to push the bridge and create an offset initial displacement. In order to have a correct comparison for all the time displacement histories, these were modified: the average value of deflection for a sample period was calculated by:

$$\bar{C} = \frac{1}{N}\sum_{t=1}^{N} C(t) \tag{4.6}$$

$$h(t) = C(t) - \bar{C} \tag{4.7}$$

where N is the number of samples, C(t) is the mean deflection value at each instance of time calculated above by Eq. 4.6. By subtracting the instantaneous mean deflections from the averaged value of deflection the fluctuating part of the net displacements are obtained and these were used for plotting. Figure 4.3.2 to Figure 4.3.8 show the vertical and torsional movement recorded for angles between -8 °to 4 °minimum and maximum wind speeds of 3 m/s and 13 m/s. The vertical and torsional induced vibrations recorded for wind speeds between 5 m/s and 12 m/s are shown in Appendix A. Also it should be mentioned that the case of 3 m/s performed for the dynamic spring test is absolutely different from the case of 3 m/s performed for the static case, therefore the inaccurate data discussed for the drag and lift static coefficients did not affect the vertical and torsional vibrations presented herewith.

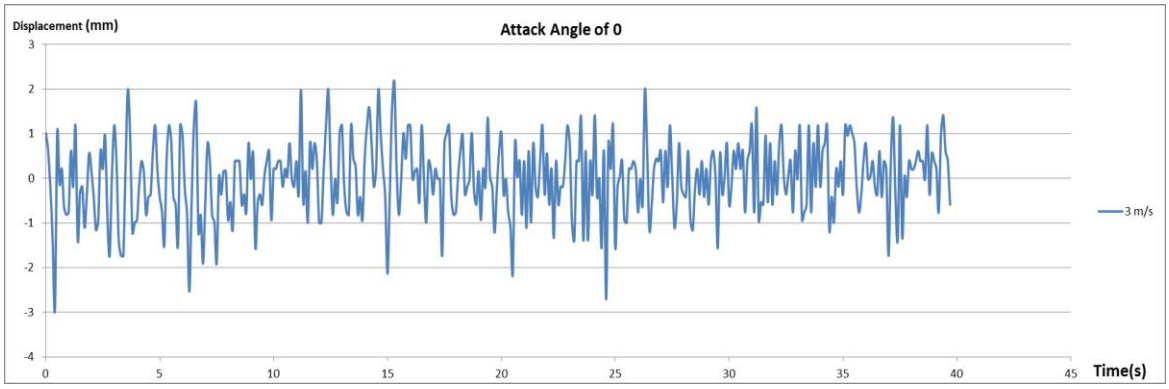

Figure 4.3.2 a) 3 m/s Vertical time displacement history at 0 °attack angle

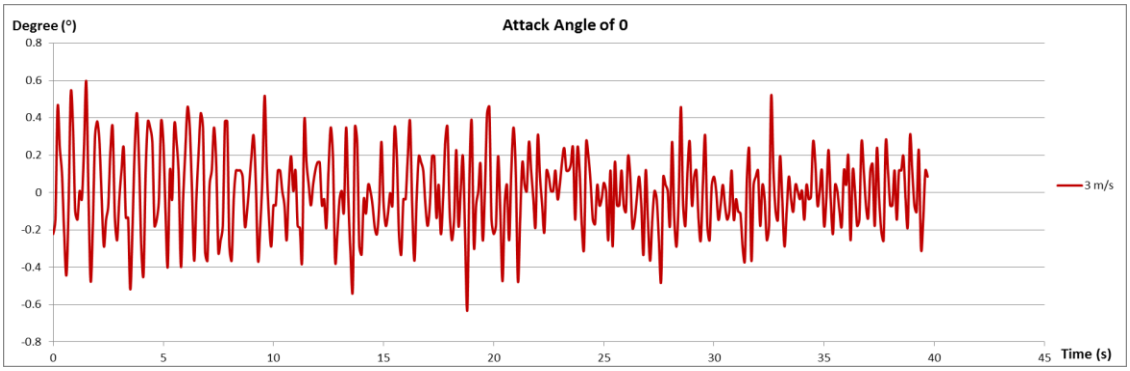

Figure 4.3.2 b) 3 m/s Torsional time displacement history at 0 ° attack angle

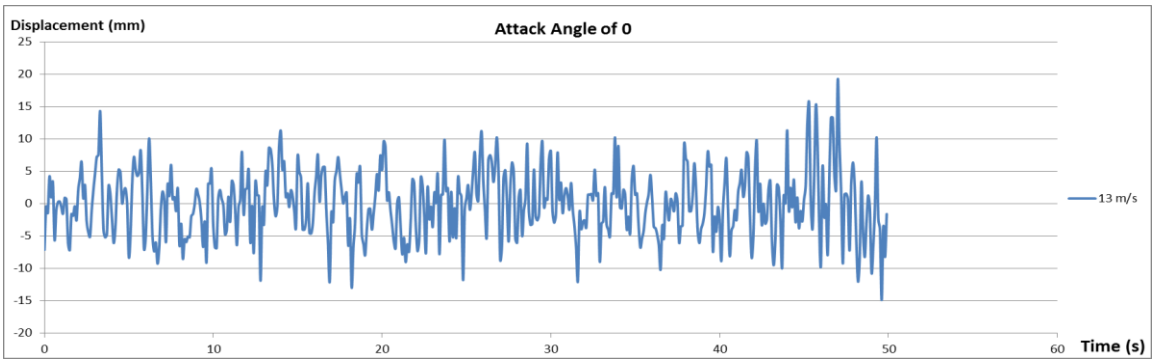

Figure 4.3.2 c) 13 m/s Vertical time displacement history at 0 ° attack angle

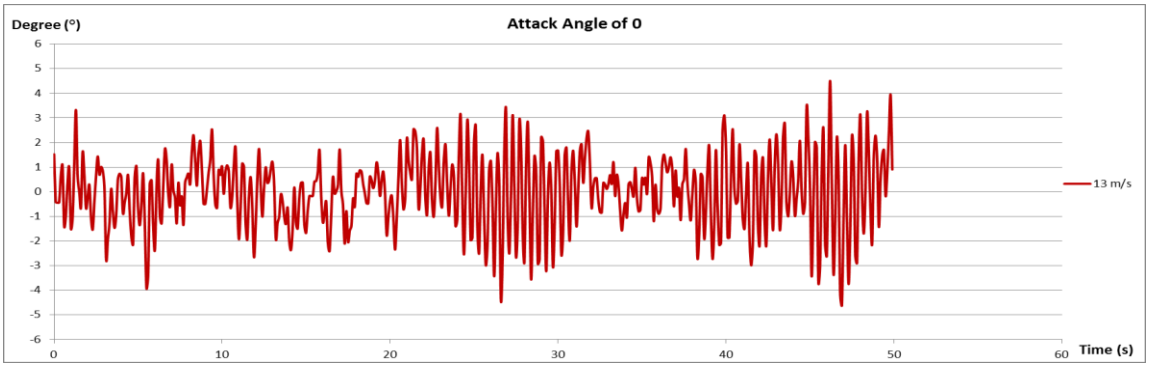

Figure 4.3.2 d) 13 m/s Torsional time displacement history at 0 ° attack angle

Figure 4.3.2 Time displacement histories for the vertical and torsional modes at 3 m/s and 13 m/s wind speed under 0 ° attack angle

The data sampling rate was 10 Hz and recording was performed for an interval of 60 sec for each wind speed case. For the responses measured for the minimum wind speed of 3 m/s, it is

obviously that despite some isolated spikes, both the vertical and torsional vibrations were relatively small having values within the range of -2 mm to 2 mm and -0.4 ° to 0.4 ° respectively (Figure 4.3.2 a) and b)). Along with the increasing wind speed the absolute vibration magnitudes grow as well reaching amplitudes of up to the average of 17.0 mm and 4.6 ° for the vertical and torsional vibrations recorded for the maximum wind speed of 13 m/s and for 0 ° angle of attack. Unlike the case of 3 m/s where the bridge section model underwent a harmonic motion, with relatively constant amplitude for either vertical or rotational motions, the responses observed at 13 m/s (Figures 4.3.2 c) and d)) were more irregular, containing more fluctuations in the vibration amplitude, especially for the torsional movement. The same evolution of the vibration pattern and the increasing of the amplitude were found for the other test cases for wind speeds between 5 m/s and 12 m/s for 0 ° attack angle. Because all these displacements are obtained experimentally, the time displacement history is not recorded as a perfect sinus or cosines functions and the magnitude of the vibration varies with time due to the changing aerodynamic damping. Therefore those vibration magnitudes were taken as an index for reflecting the effect of wind speed and attack angle on the overall vibration motion of the bridge model. For the minimum wind speed of 3 m/s, under attack angles of 2 ° and -2 ° (Figures 4.3.3 and Figures 4.3.4), the vibration displacements all began from a value of to 2 mm for the vertical and 0.4 ° for the torsional responses, which are actually the same with the responses presented for the case of 0 ° attack angle (Figures 3.4.2 a) and b)). When the test wind speed was up to 12 m/s and the attack angle is -2 °, the vertical displacement reached a maximum of 12.88 mm while only 10.88 mm for the case of 2 ° (Figures 4.3.3 c) and 4.3.4. c)). In contrast, the torsional vibration for the same wind speed but under the attack angle of 2 ° was larger than that for -2 ° which yielded values of 3.88 ° and 2.82 °, respectively (Figure 4.3.3 d) and 4.3.4 d)).

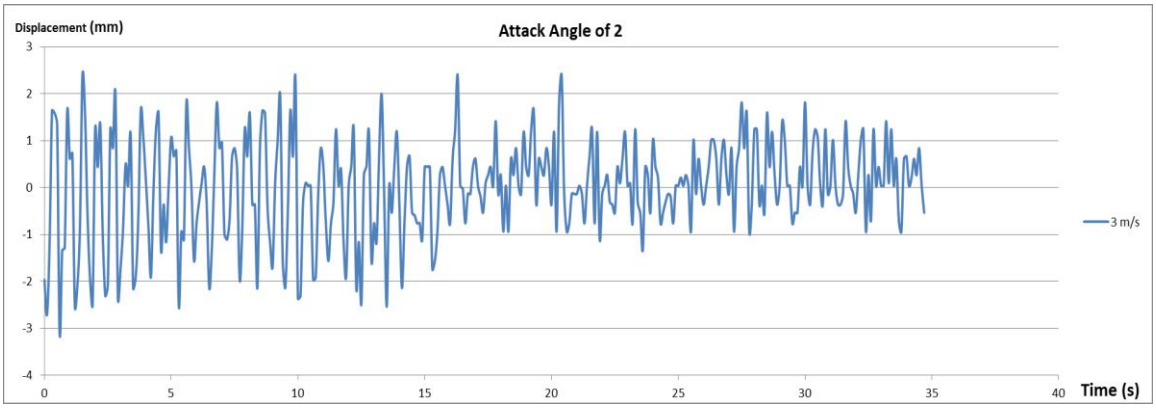

Figure 4.3.3 a) 3 m/s Vertical time displacement history at 2 °

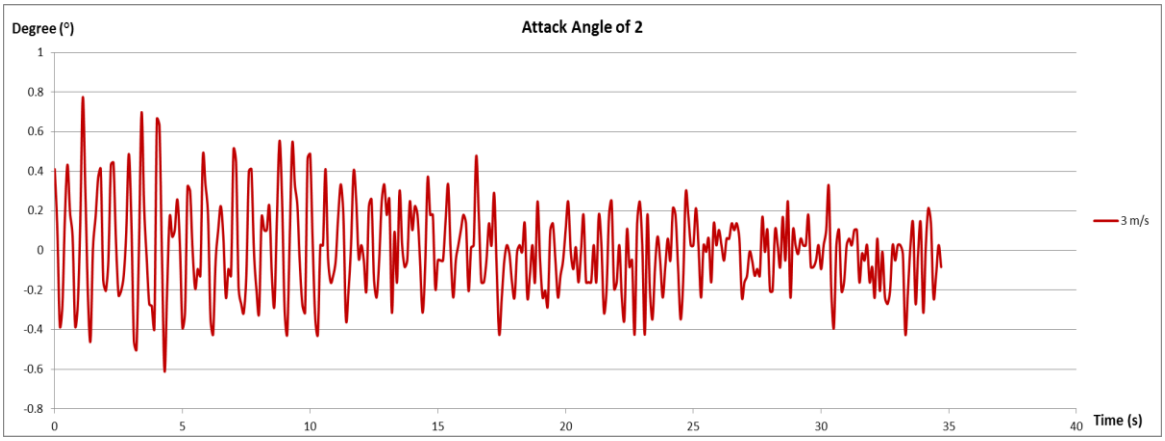

Figure 4.3.3 b) 3 m/s Torsional time displacement history at 2 °

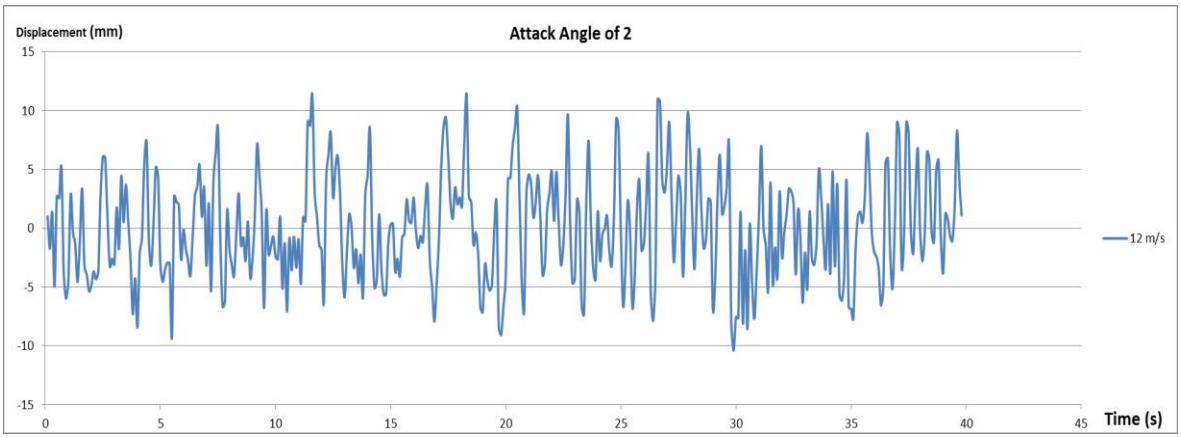

Figure 4.3.3 c) 12 m/s Vertical time displacement history at 2 °

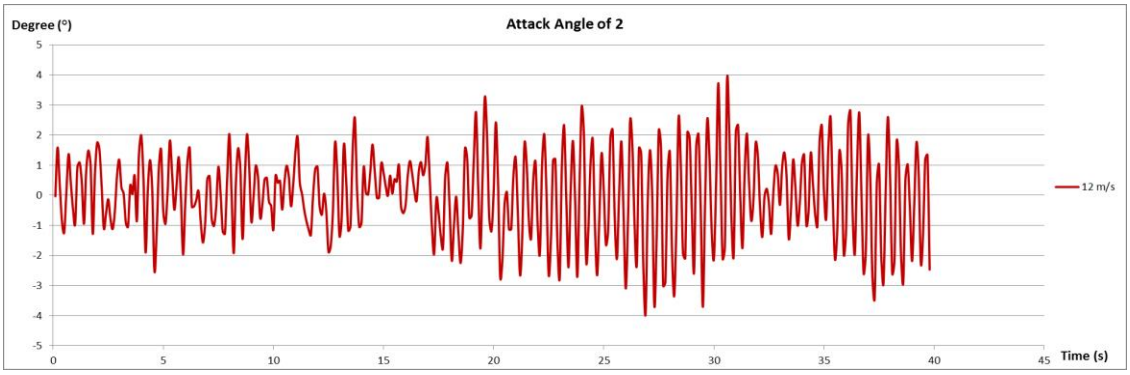

Figure 4.3.3 d) 12 m/s Torsional time displacement history at 2 °

Figure 4.3.3 Time displacement histories for the vertical and torsional modes at 3 m/s and 12 m/s wind speed under 2 °attack angle

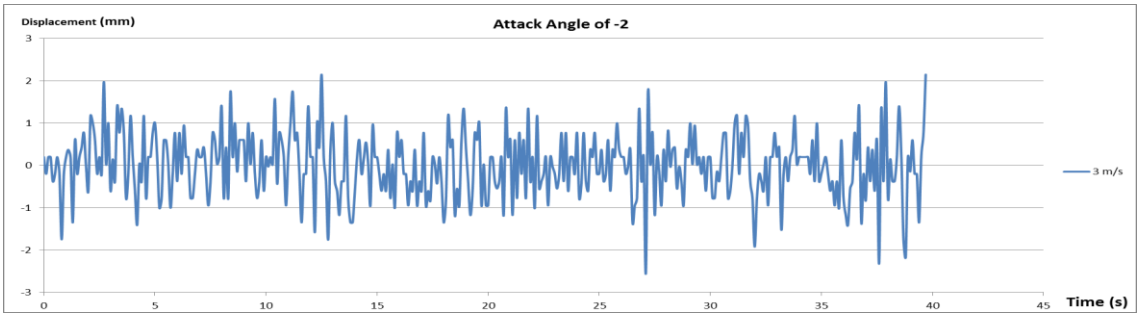

Figure 4.3.4 a) 3 m/s Vertical time displacement history at -2 °

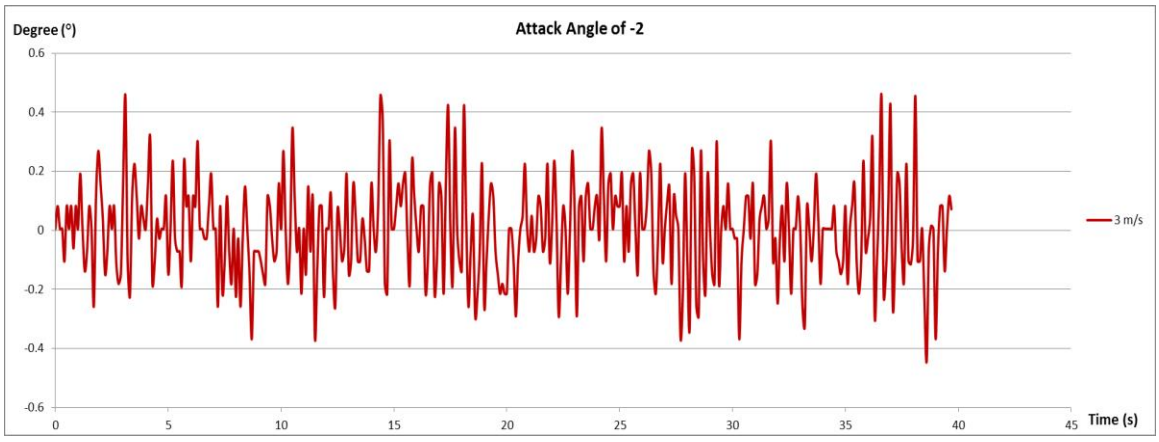

Figure 4.3.4 b) 3 m/s Torsional time displacement history at -2 °

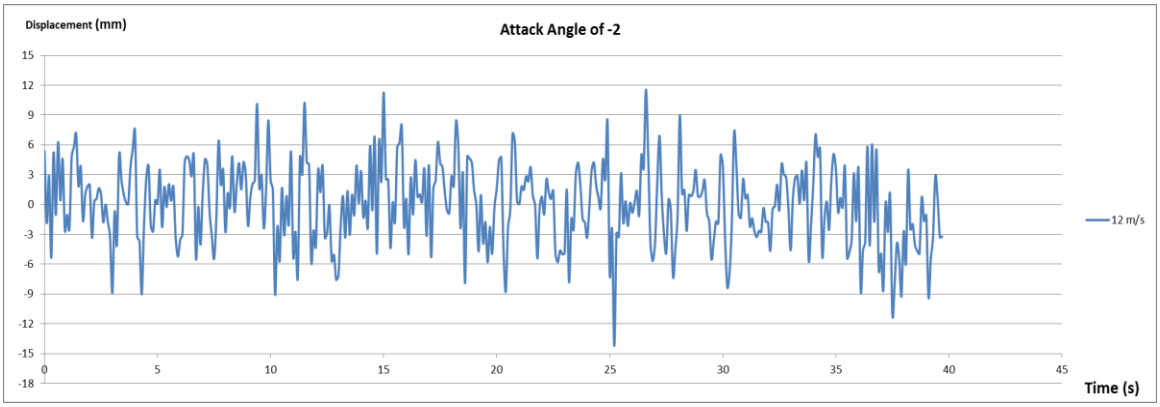

Figure 4.3.4 c) 12 m/s Vertical time displacement history at -2 °

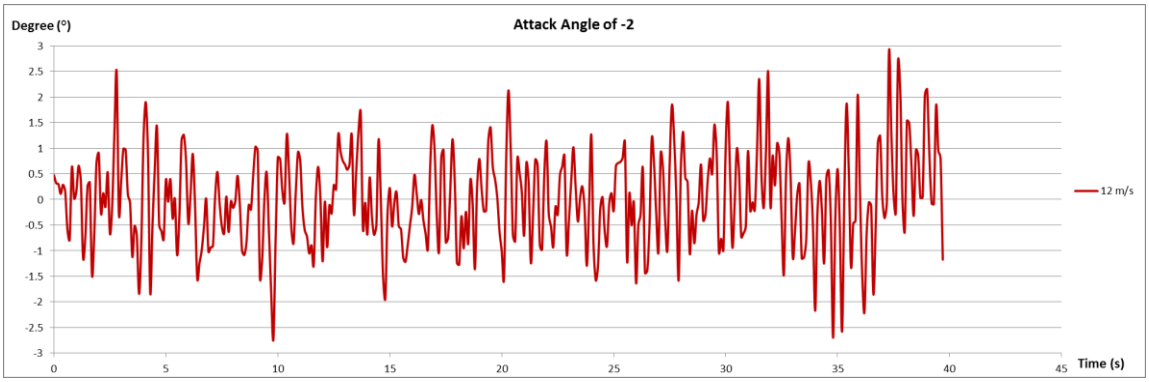

Figure 4.3.4 d) 12 m/s Torsional time displacement history at -2 °

Figure 4.3.4 Time displacement histories for the vertical and torsional modes at 3 m/s and 12 m/s wind speed under -2 °attack angle

Wind flow attack angle plays an important role in determining the bridge aerodynamic properties. The effect to the bridge model vibration amplitude is not only found at the maximum testing wind speed, but also can be spotted from the displacements at the minimum wind speed especially for higher attack angles. At 3 m/s, the averaged vertical displacement is 2.9 mm for 4 °, and 2.6 mm for - 4 ° (Figure 4.3.5 a) and Figure 4.3.6 a)), both of which are slightly larger than the response of the bridge model recorded under the attack angle of 2 ° and - 2 ° (Figure 4.3.3 a) and Figure 4.3.4 a)). The torsional displacement has also increased from 0.1 ° up to 0.55 °. The test performed for 4 ° was stopped at 10 m/s, due to the very large oscillation observed, which could have damaged the model or the suspension system, if the wind speed would have been further increased. The vertical oscillation magnitude at that time was already 9.328 mm which is close to the value of the vertical response of the bridge model performed at 12 m/s, under 2 ° and

-2 ° angle of attack (Figure 4.3.3 c) and Figure 4.3.4 c)). The case of -4 ° is similar except for the fact that the maximum testing speed was taken a step further to 11 m/s leading to a dramatic increase of the vertical displacement to 16 mm. From the Fast Fourier Transformation (FFT) analysis performed afterwards, the sudden increase of the vertical vibration amplitude could be explained as the result of the coupling between two vibration modes and also from the high magnitude of the testing wind speed it could conclude that the bridge deck model was approaching the critical flutter instability speed. On the other hand, unlike the vertical displacement, the torsional displacement was not very sensitive to the change of angle of attack. The magnitude the bridge deck model encountered for the torsional vibration was around 2 ° and 3 ° for the case of 4 ° and -4 ° attack angle respectively (Figure 4.3.5 d) and Figure 4.3.6 d)).

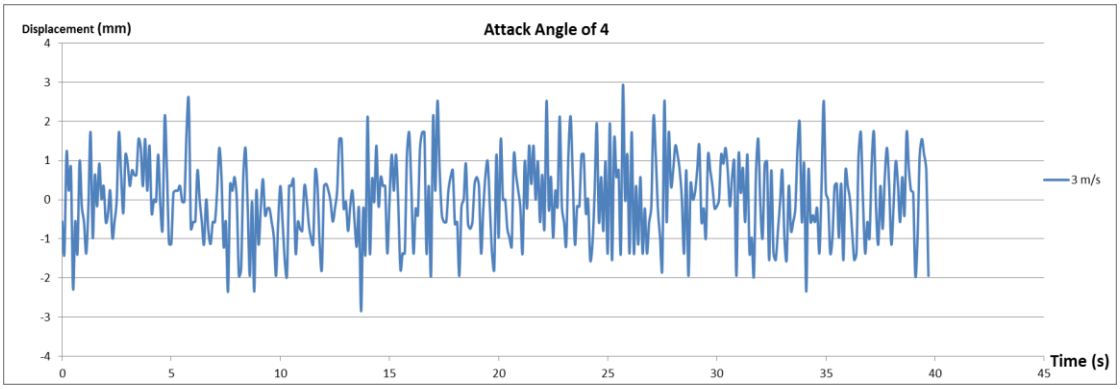

Figure 4.3.5 a) 3 m/s Vertical time displacement history at 4 °

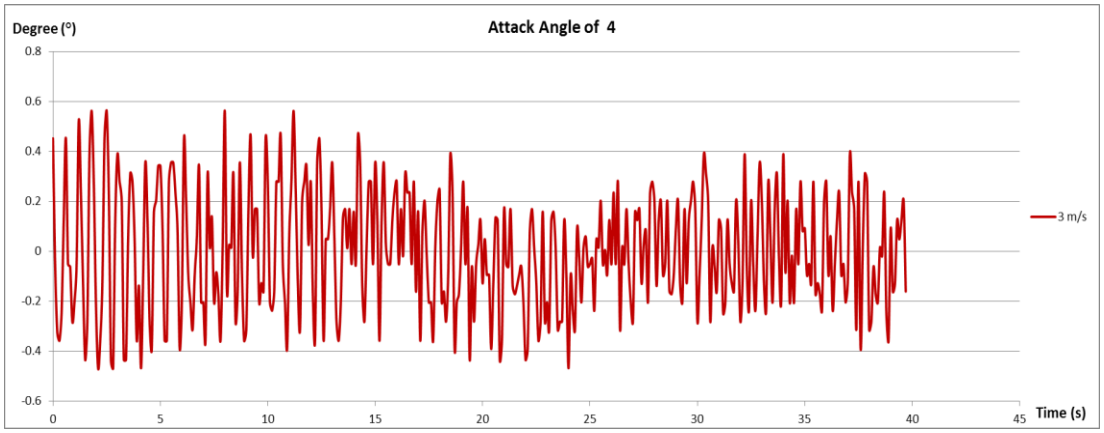

Figure 4.3.5 b) 3 m/s Torsional time displacement history at 4 °

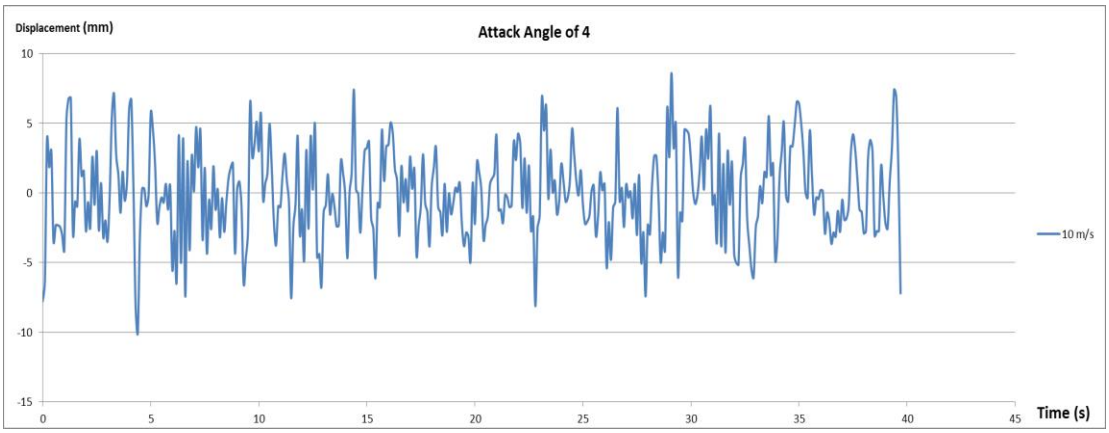

Figure 4.3.5 c) 10 m/s Vertical time displacement History at 4 °

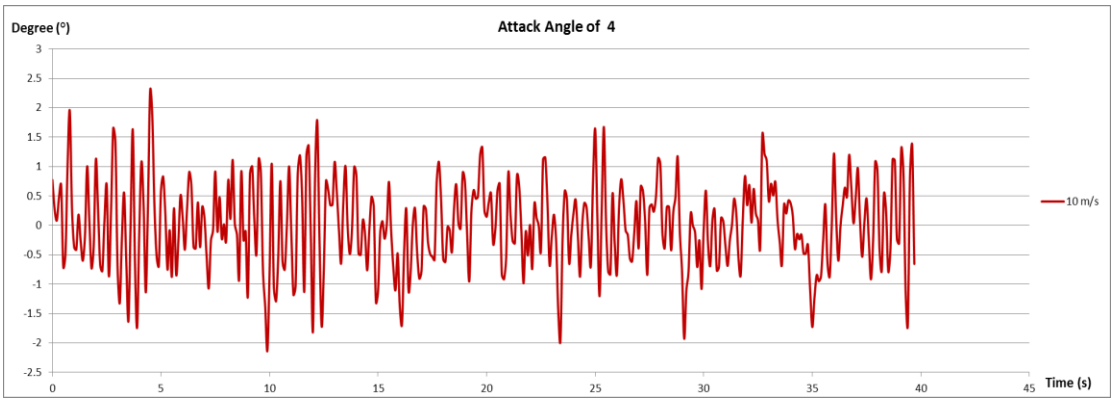

Figure 4.3.5 d) 10 m/s Torsional time displacement history at 4 °

Figure 4.3.5 Time displacement histories for the vertical and torsional modes at 3 m/s and 10 m/s wind speed under 4 ° attack angle

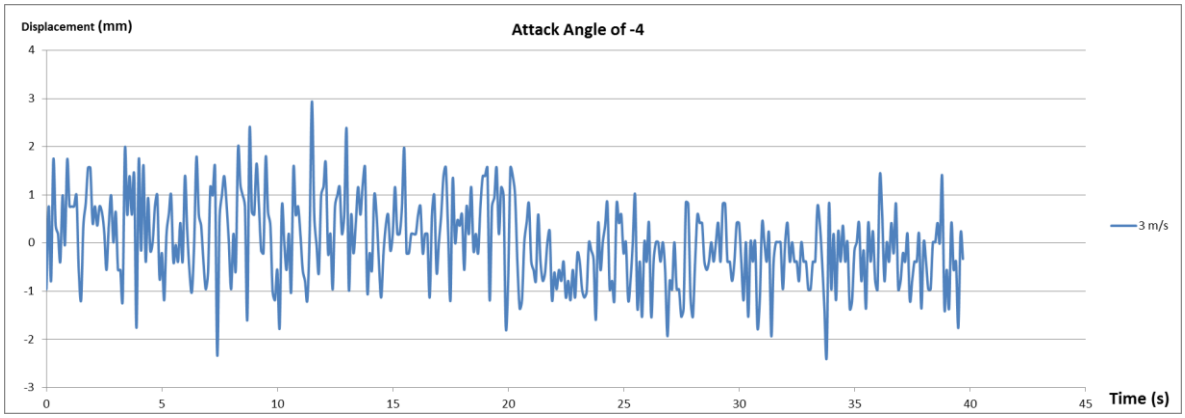

Figure 4.3.6 a) 3 m/s Vertical time displacement history at -4 °

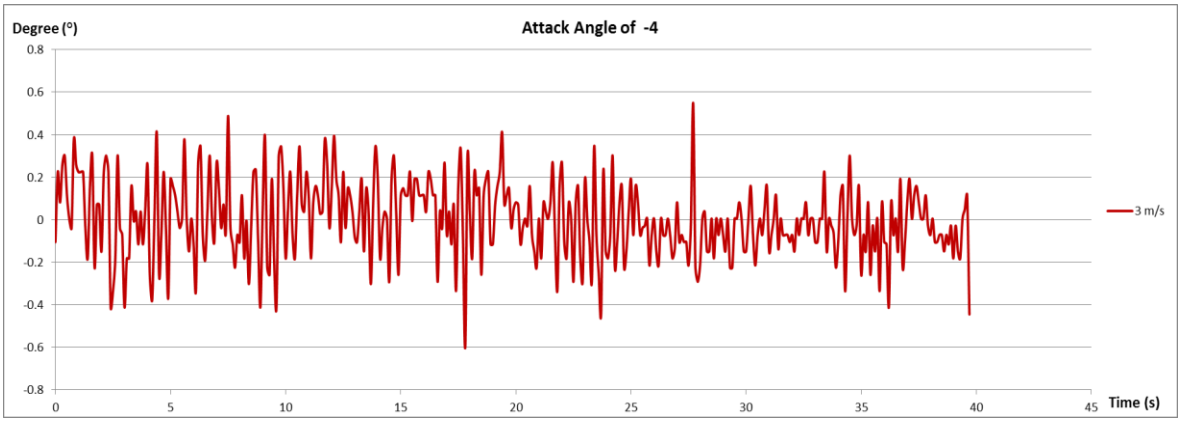

Figure 4.3.6 b) 3 m/s Torsional time displacement history at -4 °

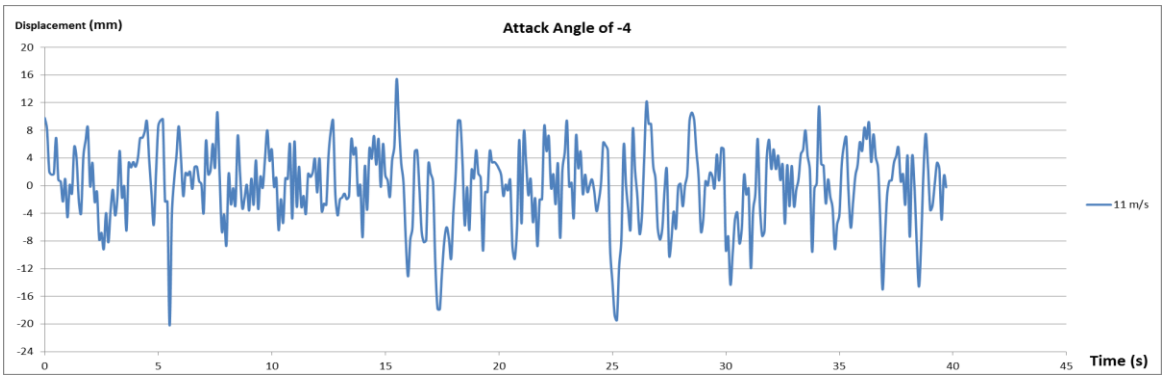

Figure 4.3.6 c) 11 m/s Vertical time displacement history at -4 °

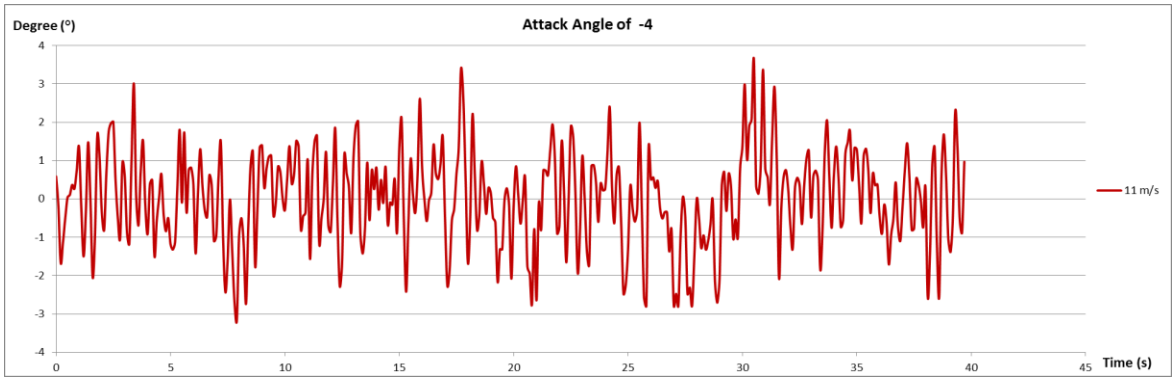

Figure 4.3.6 d) 11 m/s Torsional time displacement history at -4 °

Figure 4.3.6 Time displacement histories for the vertical and torsional modes at 3 m/s and 11 m/s wind speed under of -4 °attack angle

As mentioned in Chapter 3 the laser sensors were mounted on the wood plate with their reading heads towards the reflecting mirrors placed on the T bar which was held in place by the spring suspension system so that the distance between the fixed top point of the frame and the

moving bridge deck model can be recorded. However, at attack angles of 6° and 8°, due to the rotation of the wood plate plus the severe vibration of the bridge deck section model, the laser head position became too offset from the moving model and accidently the laser beam can miss the reflection mirrors, thus no displacement data would be recorded. As a result, the data collected under these two attack angles contained some amount of void data which was excluded from the analysis. Also, under large angles of attack the area of the bridge model exposed to the wind flow was greatly increased, which introduced a higher wind-force, acting on the bridge deck model itself, especially along the torsional direction (Figure 4.3.7 d) and Figure 4.3.8 d)). Consequently, the bridge deck model requires less wind speed to reach the same vibration magnitude as those registered for the cases performed under small angles of attack. The vertical vibrations indicated magnitudes of up to 17.764 mm and 10.669 mm for -6 ° and -8 ° angles of attack (Figure 4.3.7 c) and Figure 4.3.8 c)), while the torsional displacement became more regular and went up to 5 ° even 6 ° rotation, for the attack angles of -6 ° and -8 °, respectively (Figure 4.3.7 d) and Figure 4.3.8 d)).

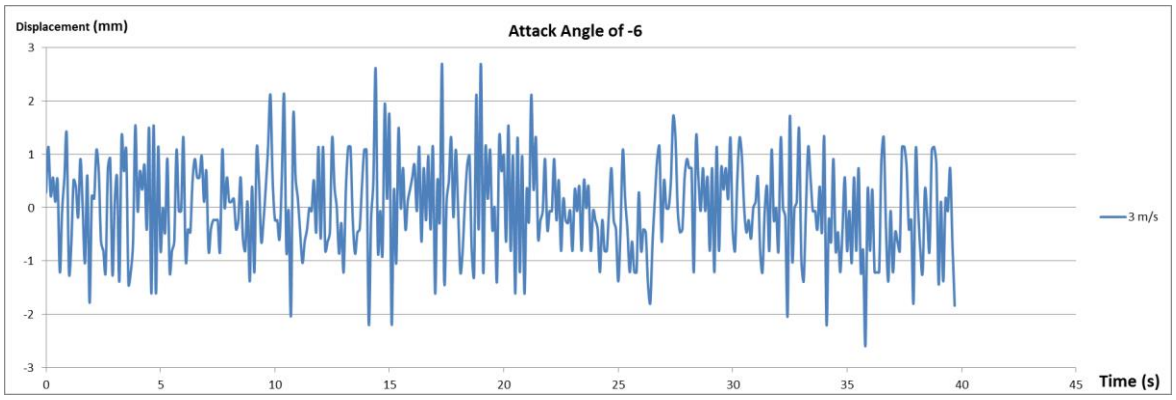

Figure 4.3.7 a) 3 m/s Vertical time displacement history at -6 °

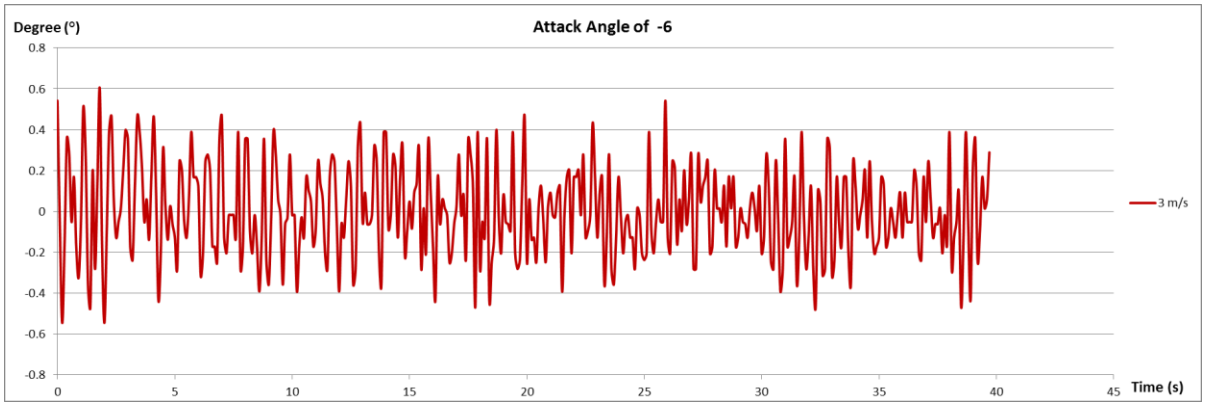

Figure 4.3.7 b) 3 m/s Torsional time displacement history at -6 °

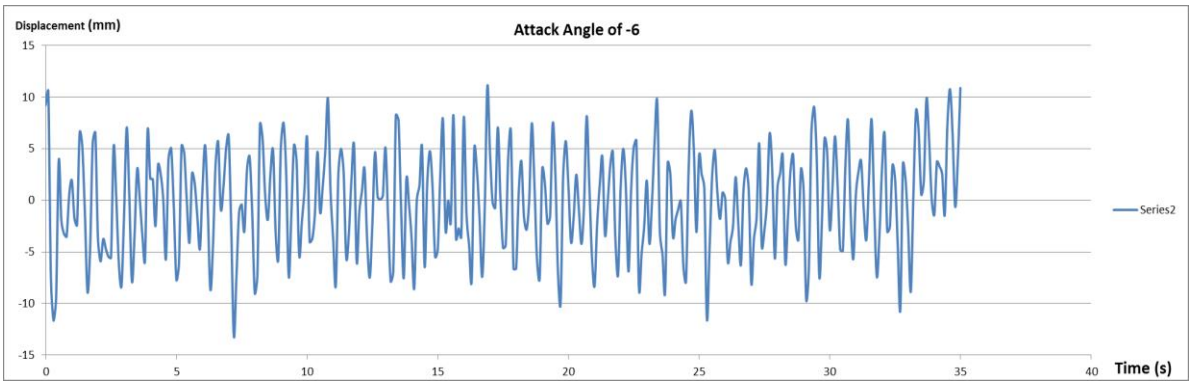

Figure 4.3.7 c) 9 m/s Torsional time displacement history at -6 °

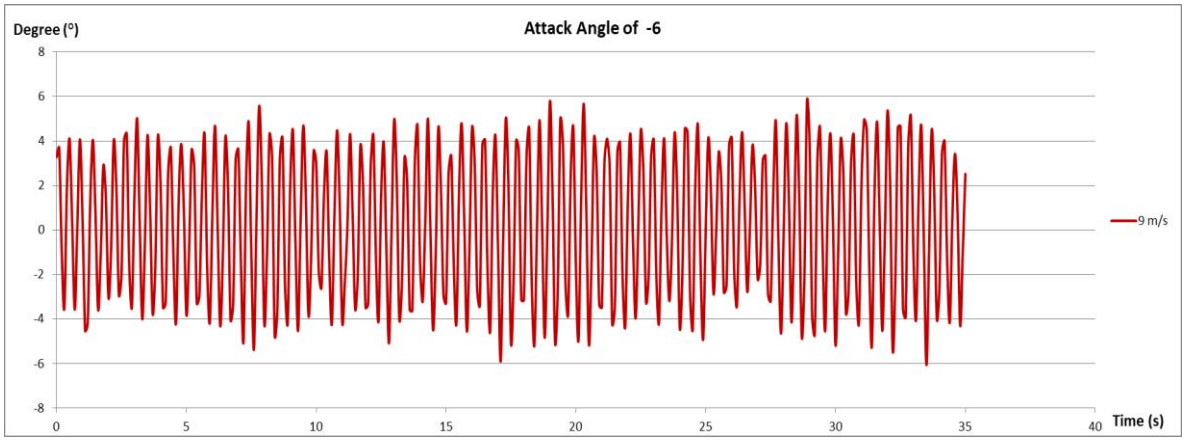

Figure 4.3.7 d) 9 m/s Torsional time displacement history at -6 °

Figure 4.3.7 Time displacement histories for the vertical and torsional modes at 3 m/s and 9 m/s wind speed under -6 °attack angle

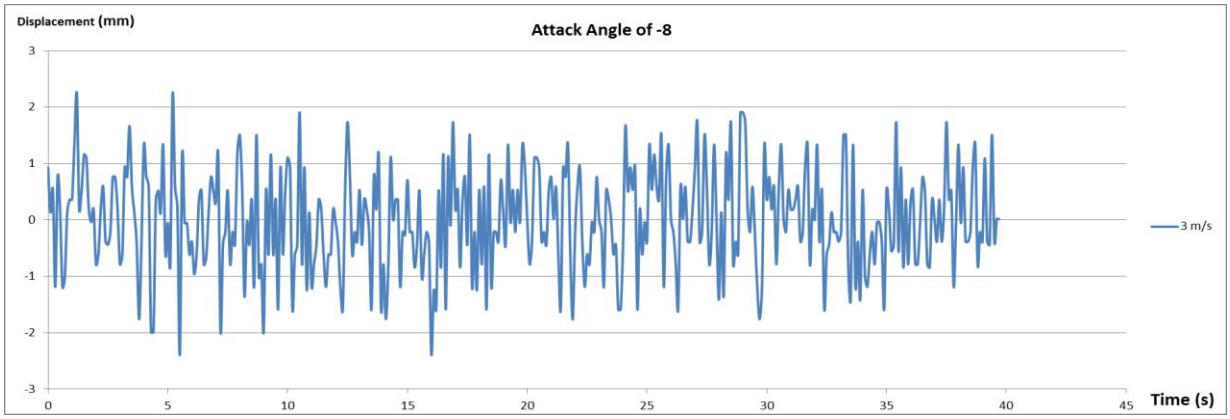

Figure 4.3.8 a) 3 m/s Vertical time displacement history at -8 °

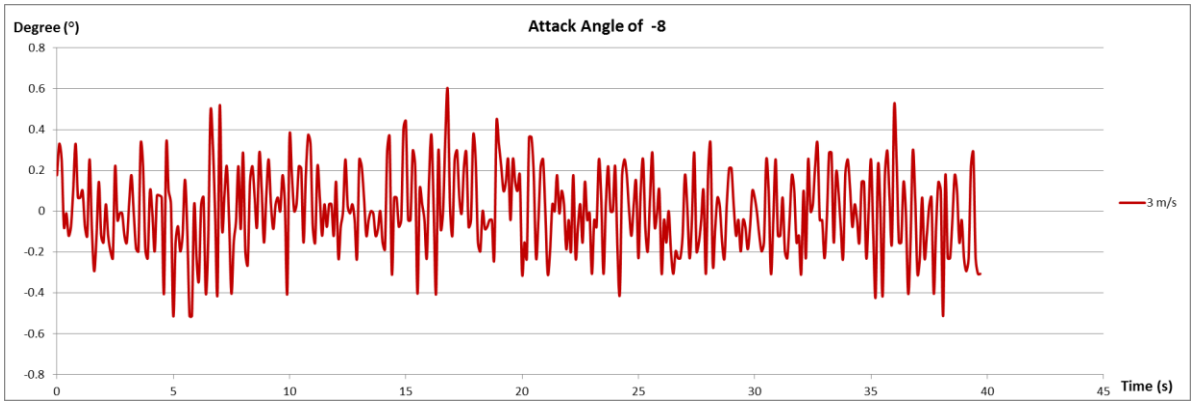

Figure 4.3.8 b) 3 m/s Torsional time displacement history at -8 °

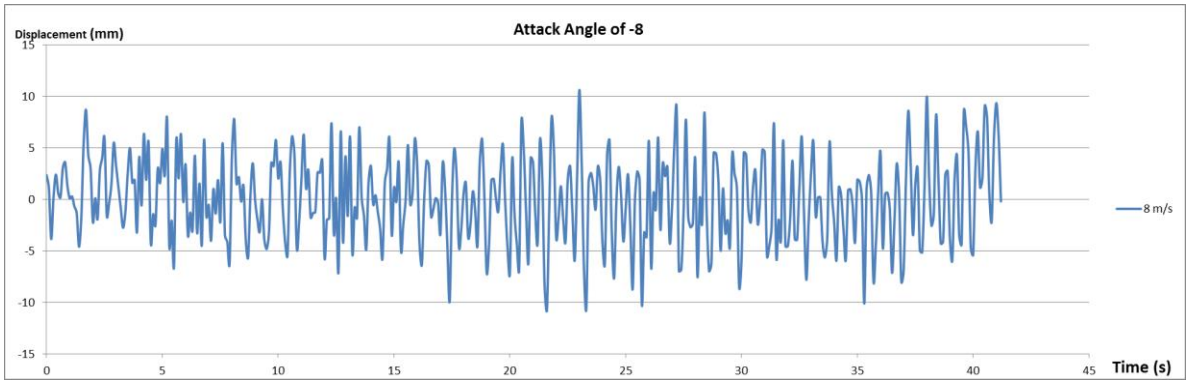

Figure 4.3.8 c) 8 m/s Vertical time displacement history at -8 °

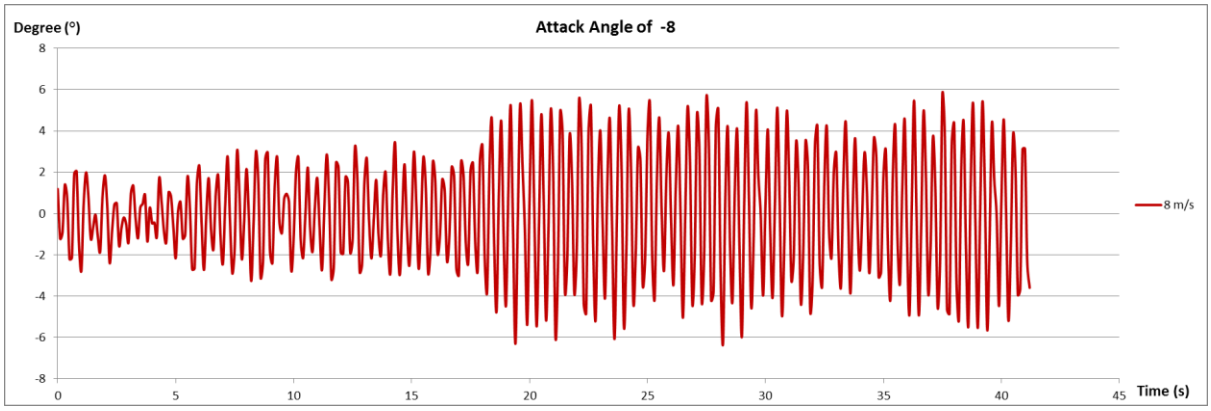

Figure 4.3.8 d) 8 m/s Torsional time displacement history at -8 °

Figure 4.3.8 Time displacement history for vertical and torsional modes at minimum and maximum wind speed under attack angle of -8 °

Table 4-1 Summary of the maximum test wind speed for each angle cases

Attack Angle	-8 °	-6 °	-4 °	-2 °	0 °	2 °	4 °	6 °	8 °
Maximum Test Wind Speed (m/s)	8	9	11	12	13	12	10	9	8

The moment coefficient could not be obtained during the static force tests, due to the instrumentation limitations, which means the critical flutter wind speed for the second test of the bridge deck model involving the spring system cannot be estimated beforehand, and can be determined only by running the experiments until the maximum possible wind speed allowed by the strong motion of the bridge deck model. Thus, in order to ensure that the bridge deck model would not be damaged during the test, the increasing wind speed was stopped once severe magnitudes of vibrations were observed. Therefore, the maximum test wind speeds for each attack angle case performed are different, and these are listed in Table 4-1 above.

The average values recorded for the vertical and torsional vibration amplitudes obtained from each wind speed test are plotted case by case in Figures 4.3.9 to 4.3.15 below to provide a better comparison and to show the variation of the bridge vibration with the increase of wind speed used on the experiments.

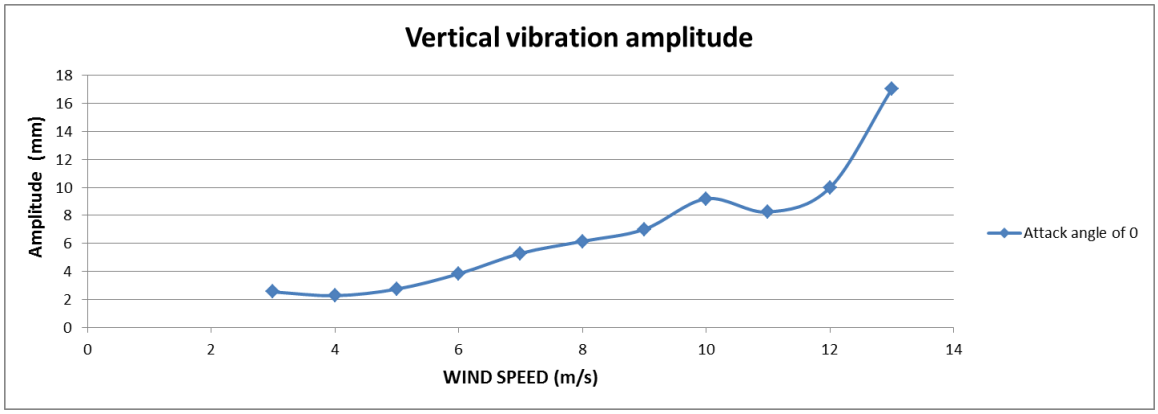

a) Vertical vibration amplitude

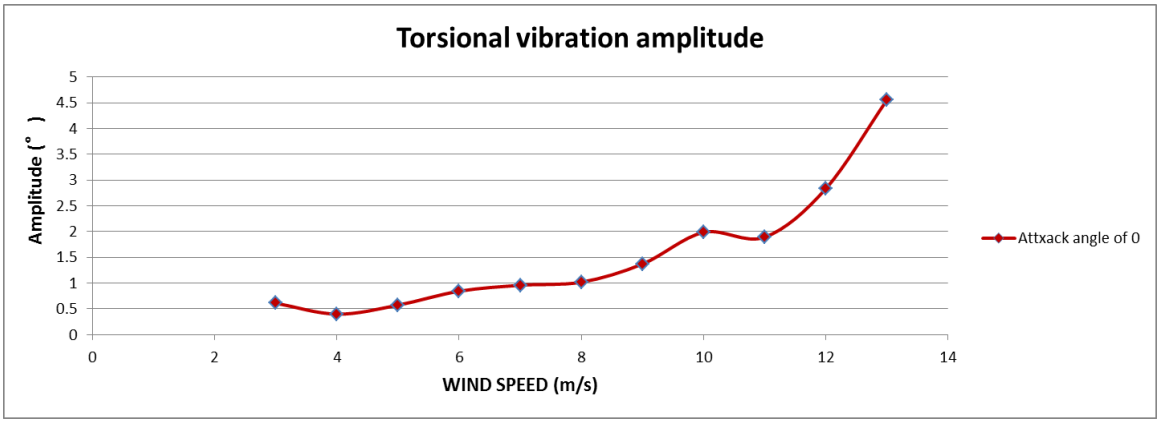

b) Torsional vibration amplitude

Figure 4.3.9 Vibration amplitude at attack angle of 0 °, a) Vertical, b) Torsional

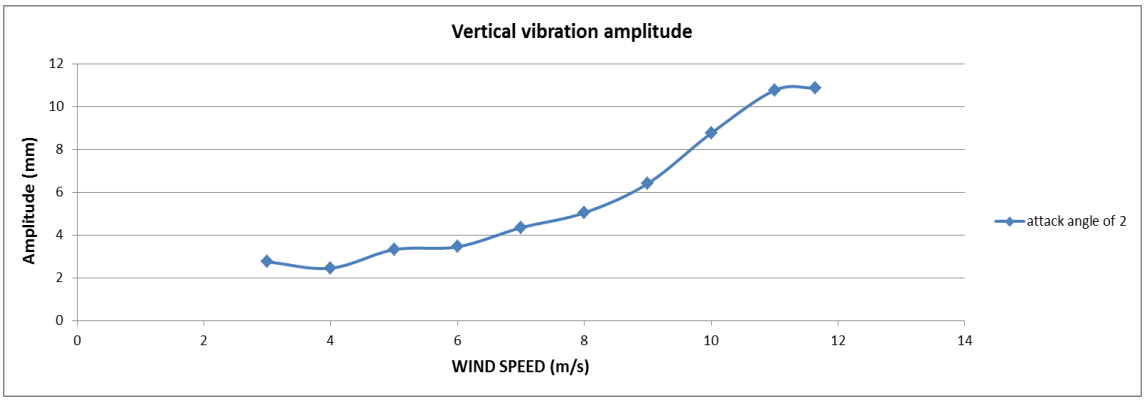

a) Vertical vibration amplitude

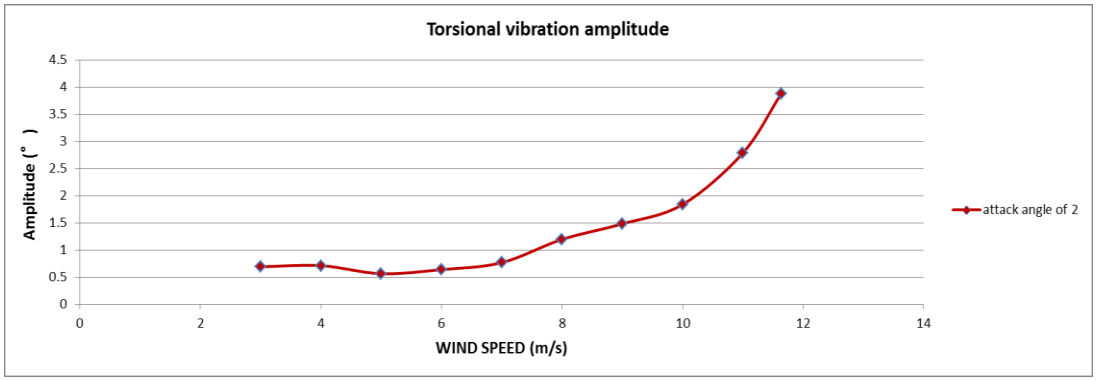

b) Torsional vibration amplitude

Figure 4.3.10 Vibration amplitude at attack angle of 2 °, a) Vertical, b) Torsional

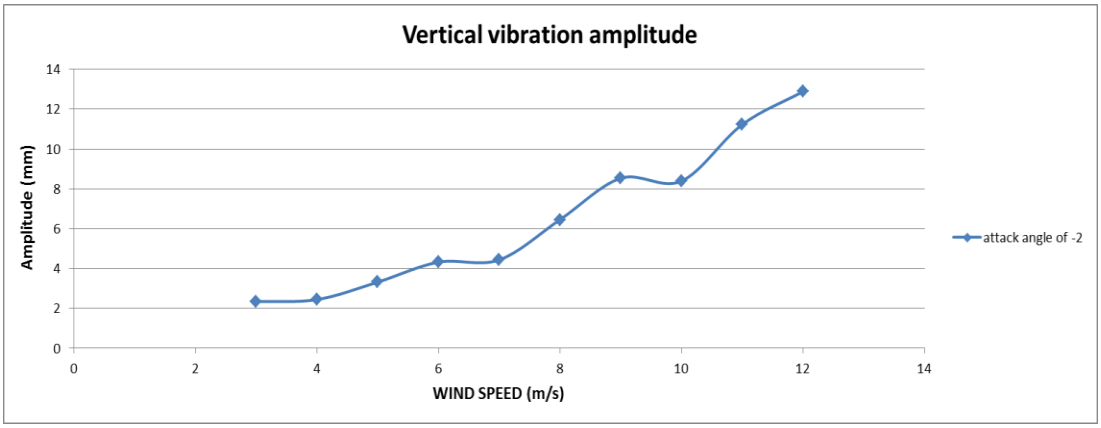

a) Vertical vibration amplitude

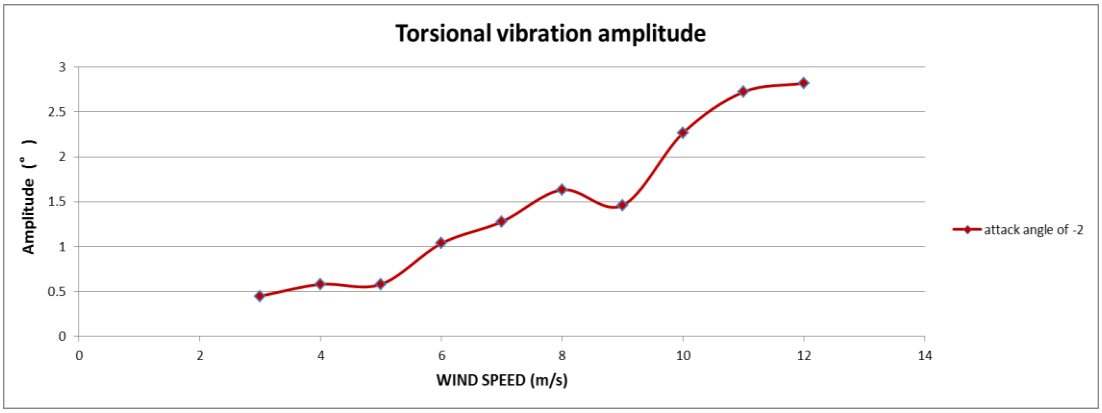

b) Torsional vibration amplitude

Figure 4.3.11 Vibration amplitude at attack angle of -2 °, a) Vertical, b) Torsional

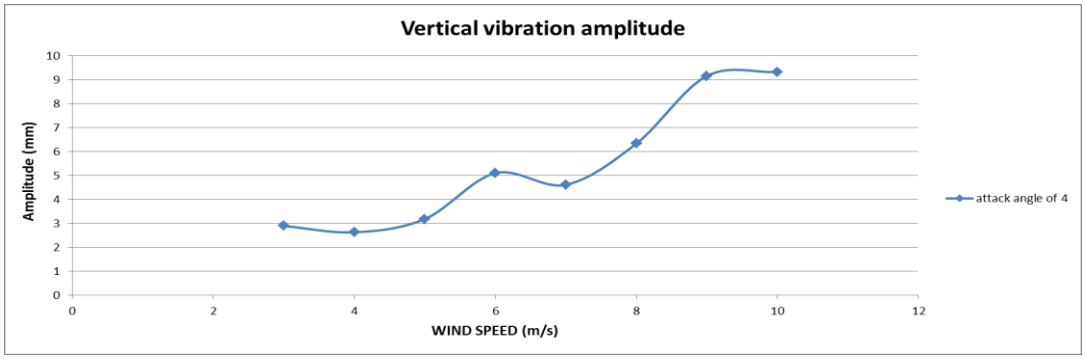

a) Vertical vibration amplitude

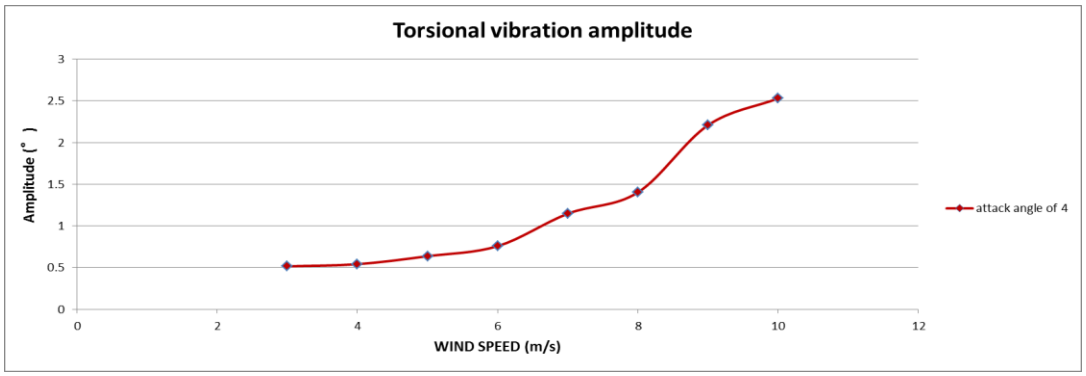

b) Torsional vibration amplitude

Figure 4.3.12 Vibration amplitude at attack angle of 4 °, a) Vertical, b) Torsional

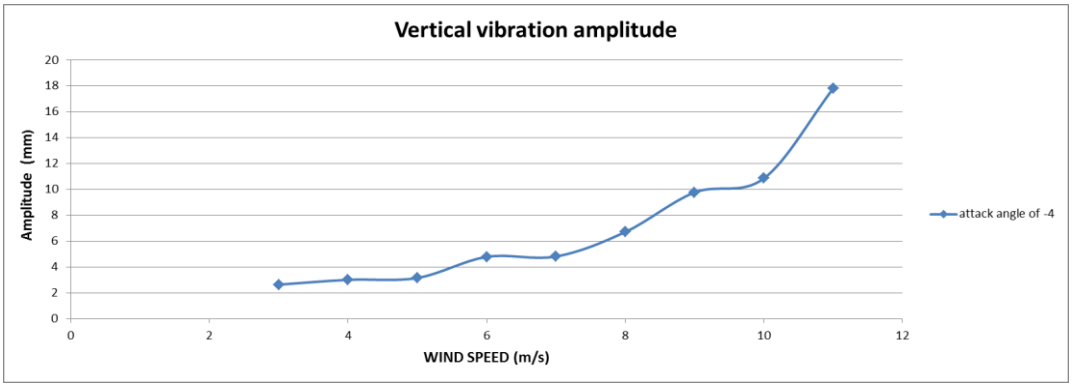

a) Vertical vibration amplitude

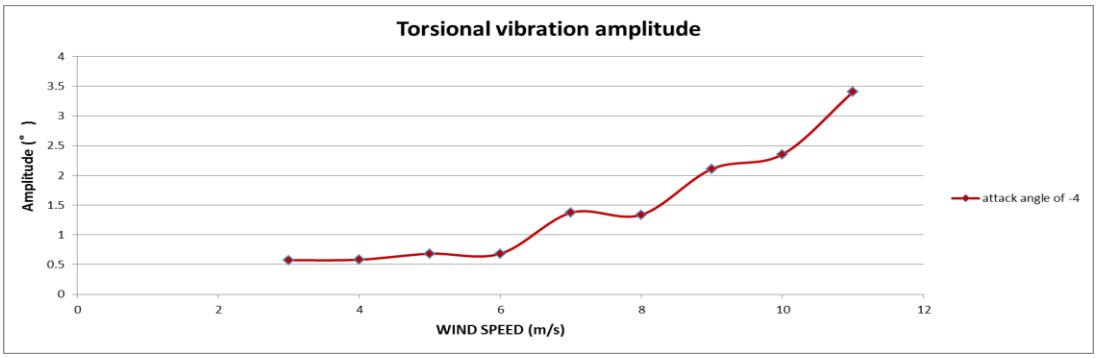

b) Torsional vibration amplitude

Figure 4.3.13 Vibration amplitude at attack angle of -4 °, a) Vertical, b) Torsional

It is interesting to notice that, the vertical vibration amplitude for attack angles 0°, 2° and 4°(Figure 4.3.9, Figure 4.3.10 and Figure 4.3.12) are showing a small decline at the beginning of the tests, where wind speeds are still very small, but the same decrease was not found for the negative attack angles of -2° and -4° (Figure 4.3.11 and Figure 4.3.13). According to the aerodynamic theory of bridge structures [2], VIV (vortex induced vibrations) will occur for the the bridge deck section models before the appearance of the flutter phenomenon. The vibration amplitudes will experience a gradual increase, untill the wind speed reaches the point where VIV occours. After that, the vibration amplitude will drop a certain amount based on the structural properties of the bridge deck section model, then will remain constant until larger wind speeds where the vibrations peak towards the onset of flutter. However, throughout the current experiment no obvious VIV phenomenon was observed and based on the variation of the vibration amplitude it is believed that the critical wind speed for VIV is smaller than 3 m/s. Due to the limitations of the wind tunnel fan whose lower wind speed is 3 m/s there is a need to perform tests in a different wind tunnel facility in order to confirm the appearance of VIV.

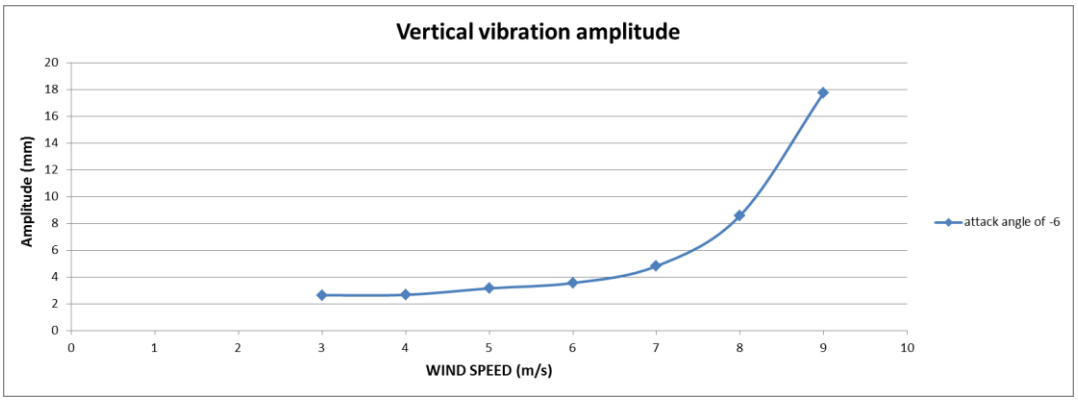

a) Vertical vibration amplitude

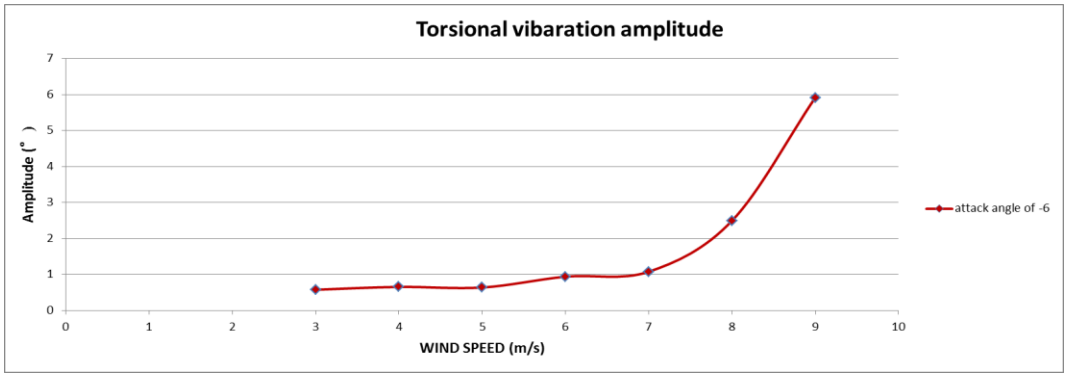

b) Torsional vibration amplitude

Figure 4.3.14 Vibration amplitude at attack angle of -6 °, a) Vertical, b) Torsional

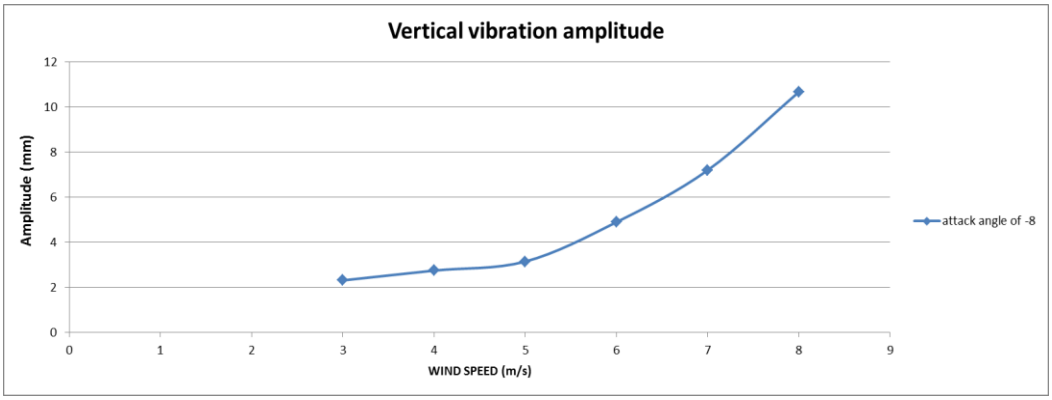

a) Vertical vibration amplitude

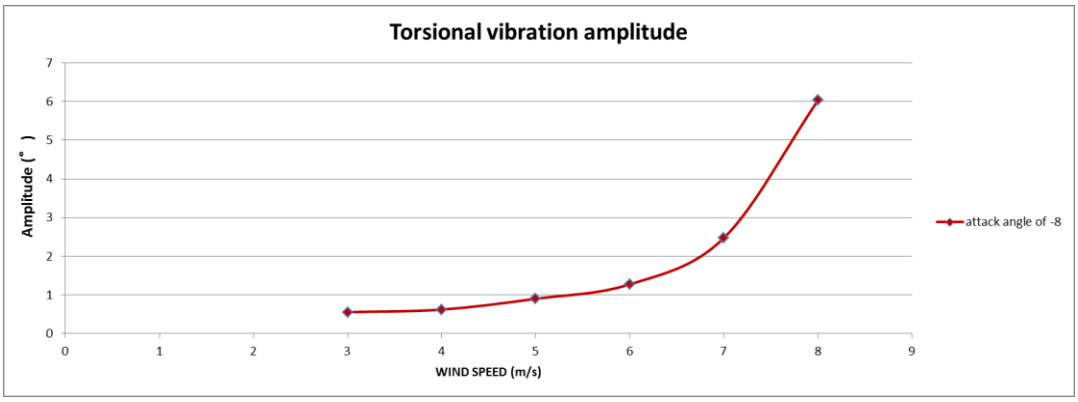

b) Torsional vibration amplitude

Figure 4.3.15 Vibration amplitude at attack angle of -8 °, a) Vertical, b) Torsional

The amplitudes for both vertical and torsional displacement for each test case are plotted together for comparison in Figure 4.3.16 and Figure 4.3.17 which demonstrate the infuence of the attack angle to the bridge vibration. The vertical amplitude curves for all angles of atack Figure 4.3.16 and Figure 4.3.17 experienced similar steady increase from 3 m/s to 7 m/s, after which showed differences with each other, especially fot the attack angle of $\alpha = -4^{\circ}$ where a sudden climb of vertical amplitudes from 10.8 mm up to 15.8 mm was recorded at wind speed of 11 m/s, which is evidence of flutter instability occurrence. Similar trends variation are spotted for the vertical vibrations of other two cases which are $\alpha = 0^{\circ}$ and $\alpha = -6^{\circ}$ yelding amplitudes of 17.03 mm and 12.31 mm at their maximum test wind speeds, respectively. It is interesting to notice that, the vibration amplitudes curves at negative attack angles are all slightly higher than those of the positive ones, indicating the bridge virbation is more likely to be affected for negative attack angles. Similar variation is reflected among the torsional vibrations under the attack angles from $\alpha = -4^{\circ}$ to $\alpha = 4^{\circ}$. The torsional amplitude curves for $\alpha = 0^{\circ}$ and 2° had similar evoluiton increasing gradualy in respect to the increasing wind speed. The suddent rise in vibration average amplitudes were noticed at test wind speed of 11 m/s for attack angles of $\alpha = 0^{\circ}$ and 2° repectively. For attack angles of $\alpha = -2°, -4°$ and $-4°$, no obviouse increase of the vibration amplitudes were observed for the high wind speed region, however the effects of the negative attack angles could be noticed. Comparing with the other attack angle cases, the section

model's torsional vibrations were more sensitive at higher attack agnles, such as $\alpha = -6^{\circ}$ and $\alpha = -8^{\circ}$. The vibration amplitude curves for these two cases separated from the other cases and rapidly spiked to a maximum value of 6° torsion at relative low wind speed of 9 m/s and 8 m/s. Overall, it could be concluded that, for the same amplitude of vibration, the instability of the bridge deck is achieved faster for large attack angles (Figure 4.3.16 and Figure 4.3.17).

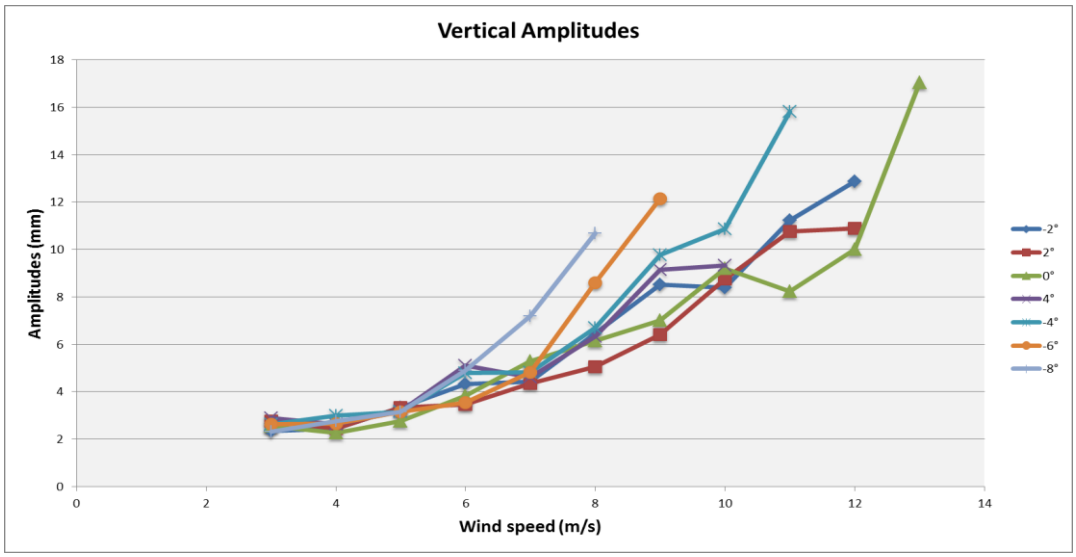

Figure 4.3.16 Vertical amplitudes variation for all wind test cases

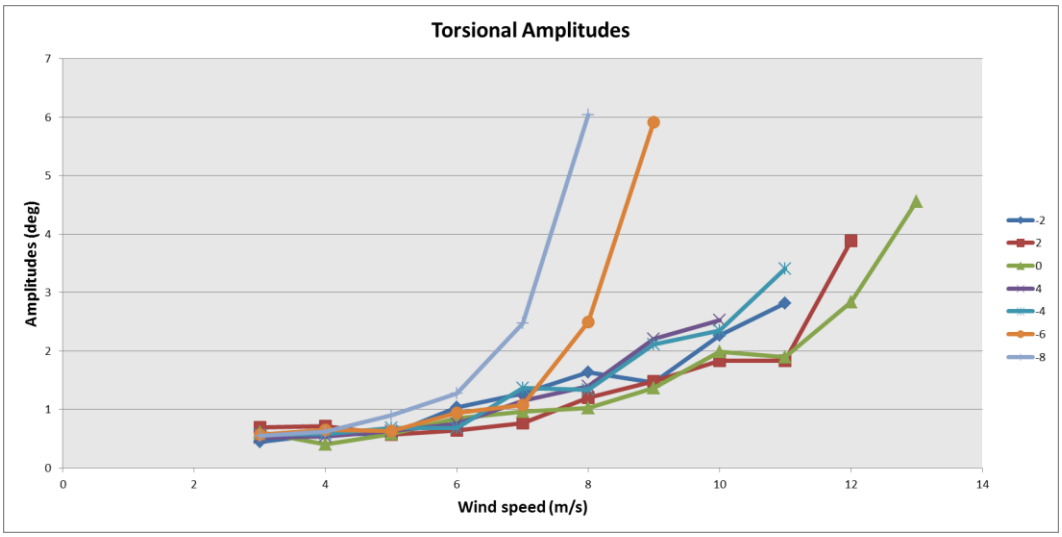

Figure 4.3.17 Torsional amplitudes variation for all wind test cases

4.3.2 Fast Fourier transform

A basic Matlab code was built for performing Fast Fourier Transform applied to the measured displacement time histories. The purpose of performing the Fast Fourier Transform analysis was to covert the data measured in the time domain into the frequency domain. By doing this, the variation of the bridge deck model vibration frequency under each test cases can be revealed. However, the collected data contain high level of noise which will alter the accuracy of the FFT analysis. Figure 4.3.18 shows the FFT of unfiltered vertical displacement data which was recorded at the minimum and maximum wind speeds, under the attack angle of 0°, respectively. It is obvious that besides the predominant vertical vibration frequency, which is 2.261Hz at the maximum wind speed, three additional spikes also appear in the same FFT figure. According to the free-vibration test, the bridge deck natural frequency was 1.667 Hz for the vertical vibration mode. Clearly, the spikes generated at less than 1.5 Hz do not represent the natural frequency of the bridge deck model and should be removed from the FFT results, not only for a better estimation on bridge vibration frequency, but also for the data preparation for extracting the flutter derivatives. Therefore a low-pass filter, which can eliminate the noise from the measured time displacement histories, was applied to both vertical and torsional displacement time histories before performing the FFT and a specific cut-off frequency was

selected according to the particular situation of each case as it will be explained in detail in the next chapter.

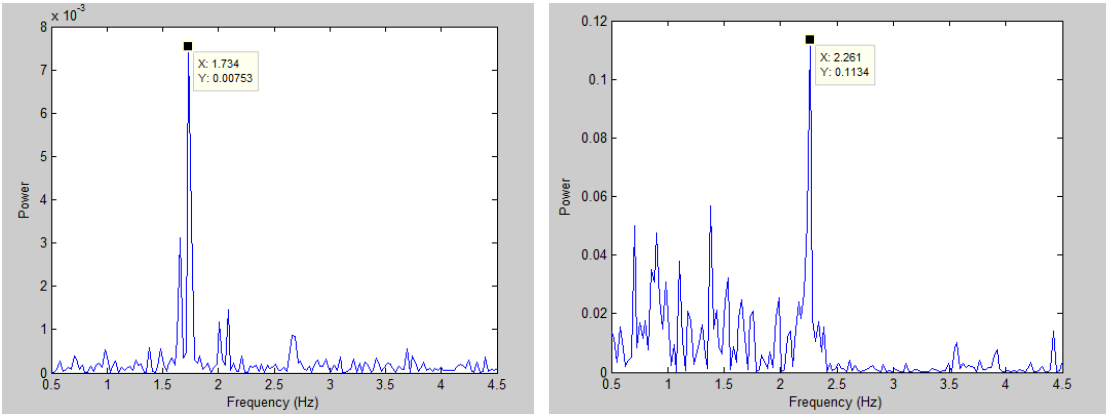

Figure 4.3.18 FFT before applying the low-pass filter

The results of FFT applied to the measure data for all attack angles for the minimum and maximum wind speeds of 3 m/s and 13 m/s, are presented in Figure 4.3.19 (a) to Figure 4.3.25(a). For all wind speeds cases, it is clear that the predominant vertical motion frequency at the wind speed of 3 m/s is located around 1.7 Hz followed by a steady increase along the wind speed ends at various frequencies from 1.844 Hz to 2.27 Hz, depending on the attack angle (Figure 4.3.19 (b) to Figure 4.3.25 (b)). On the other hand, predominant torsional frequency for each attack angle case underwent an opposite trend, starting at around 2.7 Hz and ending at a close or even equal value with the vertical ones especially for $\alpha = 0^{\circ}$ at the maximum wind speed (Figure 4.3.19 a)). From the vibration FFT results obtained under attack angle of 0°, the several additional frequency spikes besides the dominant ones were noticed and these are considered as the indication of the second-order of the vibration of the model, or might indicate the vibration frequencies of other elements, than the bridge model itself, such as steel frames, or other equipment, which however cannot be confirmed. However, the magnitudes of all these additional spikes are quite small and less than half of the predominant ones. Therefore, these frequency values are not taken into account for the bridge section frequency analysis. The predominant vibration frequencies for both vertical and torsional vibrations are collected and plotted in Figure 4.3.19 (b). As mentioned above, vertical and torsional frequencies start at 1.734 Hz and 2.67 Hz, respectively and these two modes get closer to each other along as the wind speed increase. The vertical frequency increases with aerodynamic damping, while the torsional decreases due to the increasing aerodynamic damping. For the case of $\alpha = 0^{\circ}$, at wind speed of 12 m/s, two

frequencies match each other and this point is considered as the appearance of coupled flutter (Figure 4.3.19 (b).). Due to the resonance between the two vibration modes, the amplitudes of the bridge model self-excited oscillation grow rapidly, and these can also be observed from Figure 4.3.16 and Figure 4.3.17.

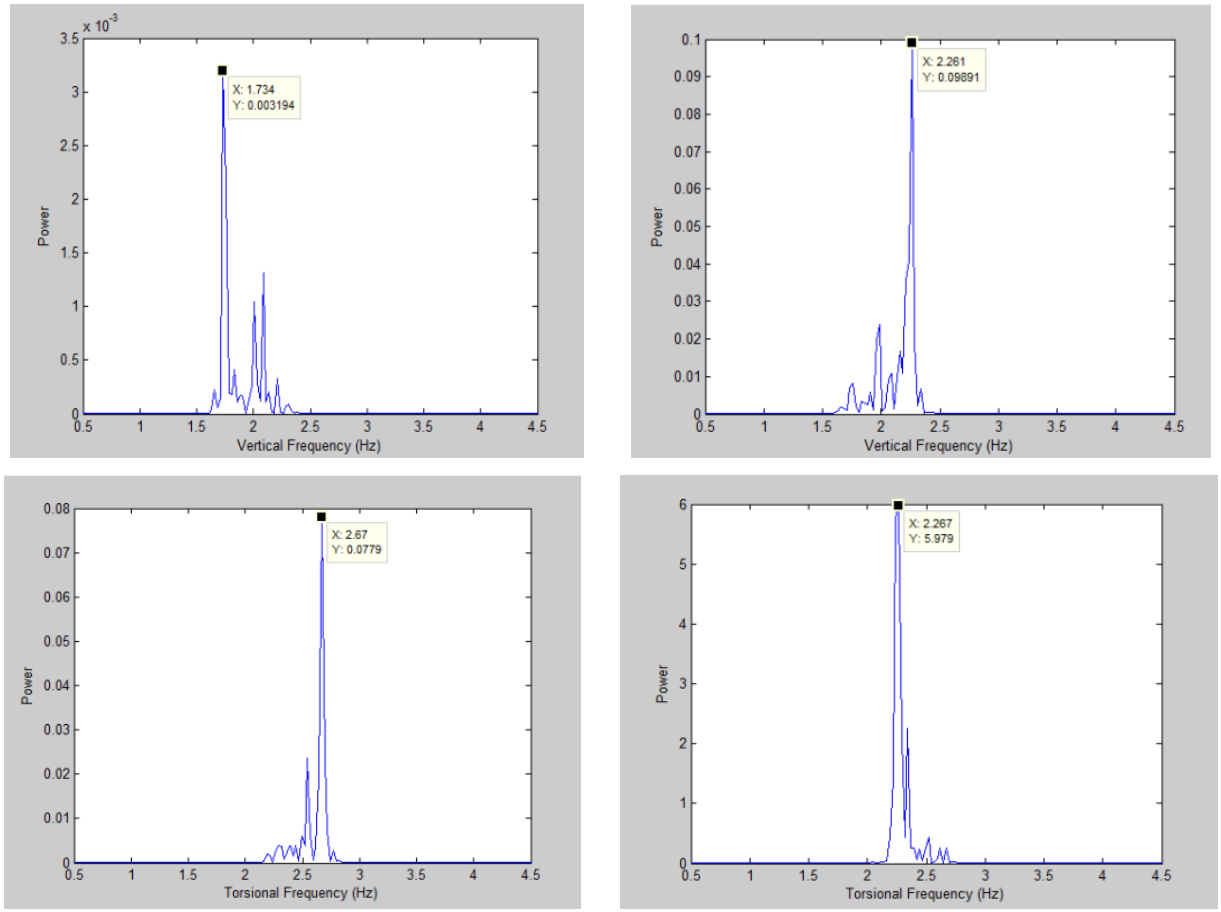

Figure 4.3.19 a) FFT of the bridge vibration under wind speed of 3 m/s and 13 m/s for attack angle of 0°

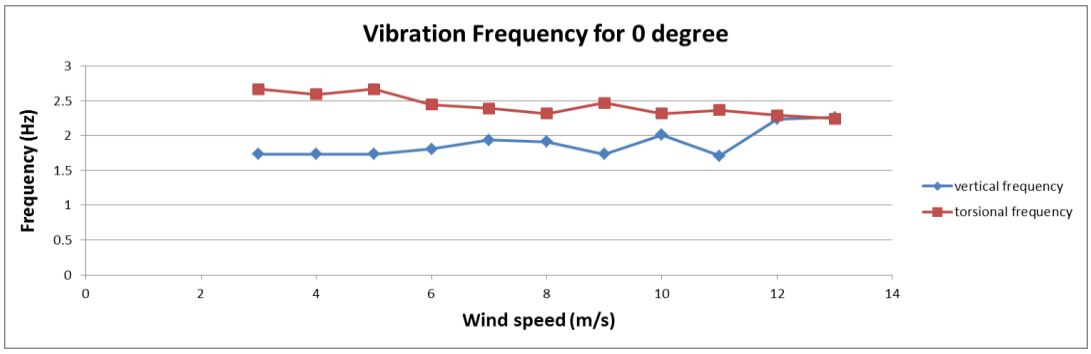

Figure 4.3.19 b) Frequency variation for vertical and torsional vibration modes for attack angle of 0°

Similar variation is found for the case of attack angle $\alpha = 2^{\circ}$, the minimum vertical vibration frequency and maximum torsional frequency are 1.738 Hz and 2.698 Hz for the wind speed of 3 m/s (Figure 4.3.20 (a)). Several additional spikes are also identified and due to their small magnitudes and distance from the predominant frequencies the additional frequency spikes are not considered in the frequency variation analysis of the bridge deck section model under this attack angle scenario. Figure 4.3.2(b) shows clearly that the resonance frequency is close to 2.34 Hz which occurs at the wind speed of 11 m/s. The critical flutter wind speed for $\alpha = 2^{\circ}$ is 11 m/s which is smaller than the case of attack angle 0°, reflecting that the aerodynamic stability for flutter of the bridge deck model is decreasing with the increase of the wind attack angle. Also regardless of the measured frequencies, for the attack angle of $\alpha = 2°$, the increment of torsional vibration amplitudes after the occurrence of the coupled flutter, at 11 m/s, is larger than those of the vertical vibration amplitudes (Figure 4.3.16 and Figure 4.3.17), which is not quite the same pattern under the attack angle of $\alpha = 0^{\circ}$.

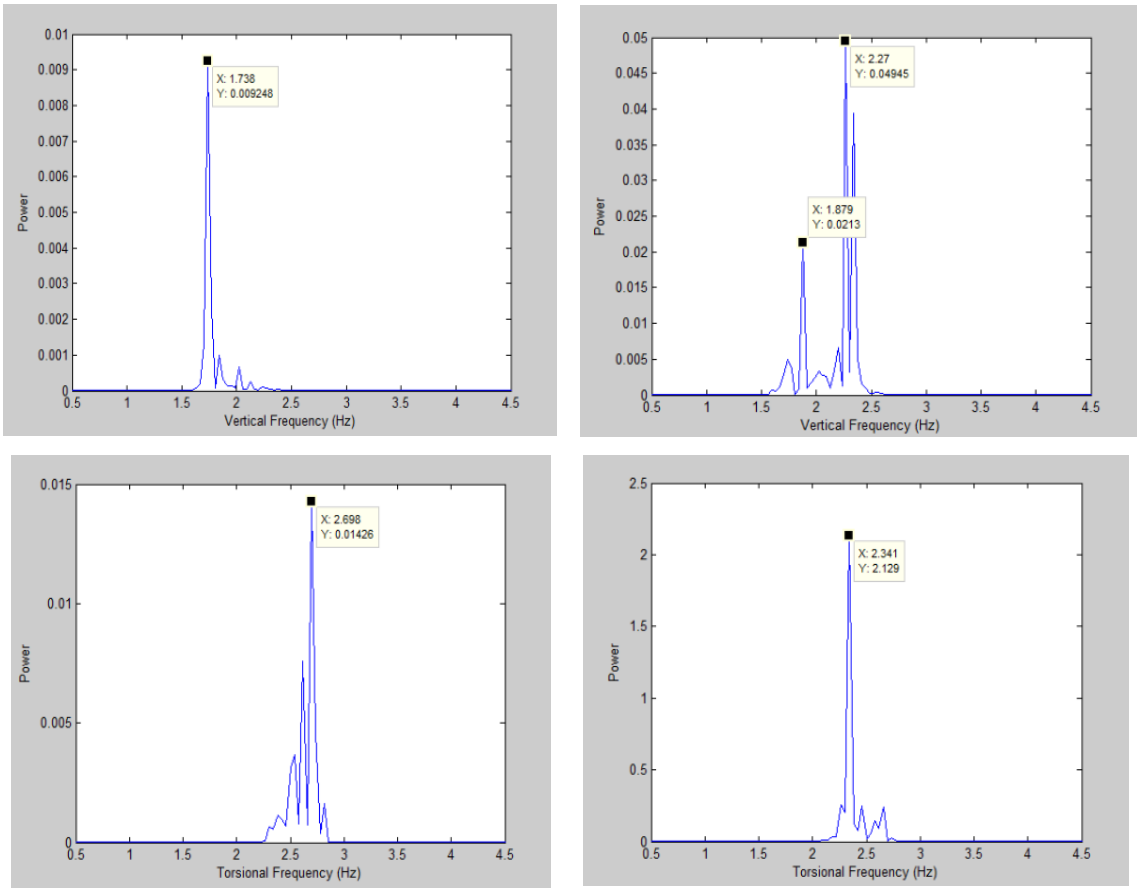

Figure 4.3.20 a) FFT of the bridge vibration under wind speed of 3 m/s and 12 m/s for attack angle of 2 °

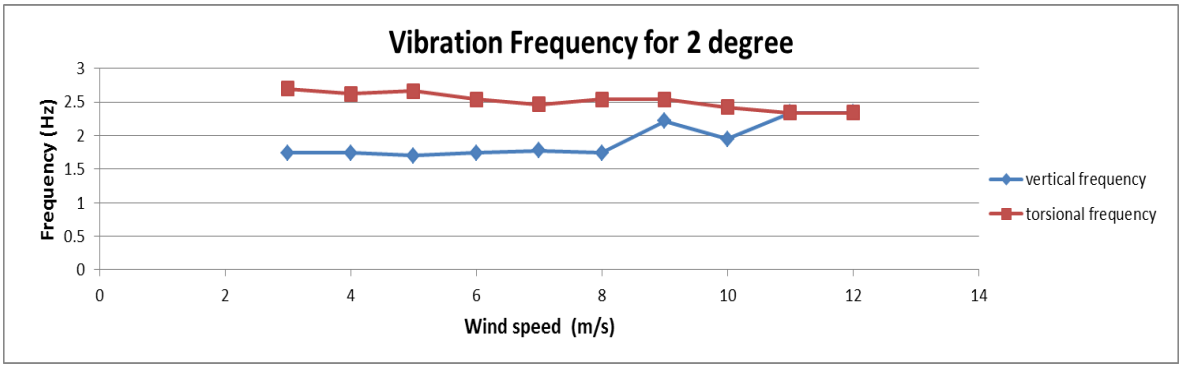

Figure 4.3.20 b) Frequency variation for vertical and torsional vibration modes for attack angle of 2 °

The frequency pattern for the case of $\alpha = -2^{\circ}$ seems to be more complicated in the sense that not only this has relatively more frequency spikes, than the other attack angle cases for the vertical vibration, but also these spikes of similar magnitudes are identified, very close to each

other. For the vertical vibration at 3 m/s, the first and second dominant frequencies are 1.702 Hz and 1.773 Hz and these are considered to be the first vibration mode of the bridge deck section model. However, the existence of the other spikes at 1.9 Hz and even beyond 2 Hz can't be neglected. The causes of these spikes were partly from the motions of the experimental instruments, like the vibration of the steel frames. Another cause might be the wooden plates which may also introduce extra frequencies to the bridge spring supporting system. A study of the frequency of the bridge in vibration higher modes would further clarify the presence of these peaks. As a consequence, the determination of the predominant frequency for the vertical motion becomes more complex for higher angles of attack, and for the purpose of the analysis the average of the spikes located near the natural frequency is treated as the predominant one. Based on this assumption, from the tendencies of the two vibration modes it can be concluded that the coupling between the vibration modes determined for the other attack angles by the slight drop of the torsional frequency and the increase of the predominant vertical frequency, here ($\alpha = -2^{\circ}$) could not be noticed, as no large difference between the vertical and torsional frequencies reported for minimum and maximum wind speeds was observed (Figure 4.3.21(b)). Consequently, the oscillation amplitudes of the bridge deck section model grows steadily with the increasing wind speed (Figure 4.3.16 and Figure 4.3.17), however the appearance of critical flutter instability didn't occur until at the wind speed of 12 m/s.

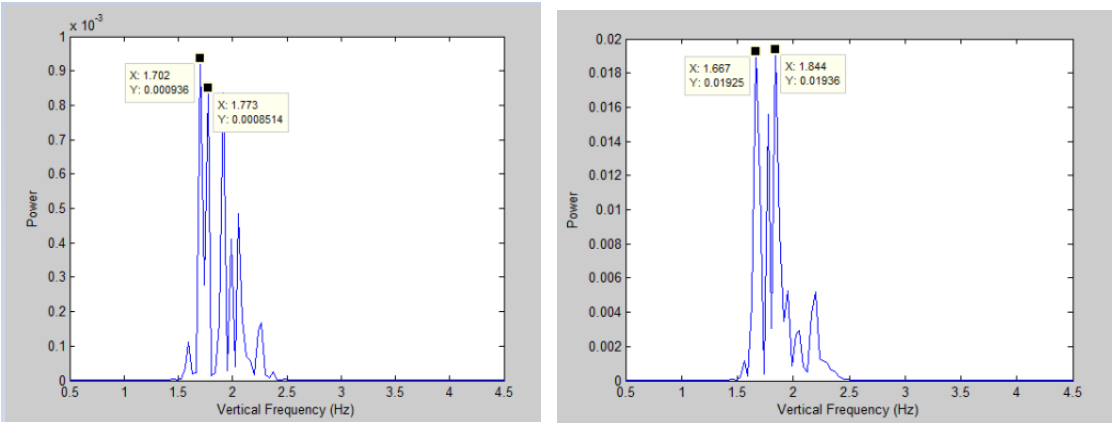

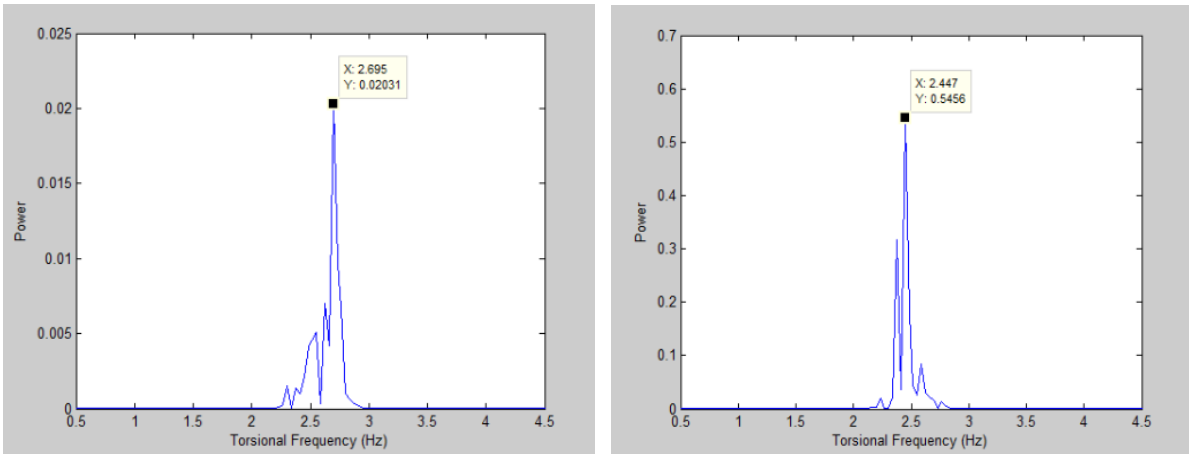

Figure 4.3.21 a) FFT of the bridge vibration under wind speed of 3 m/s and 12 m/s for attack angle of -2 °

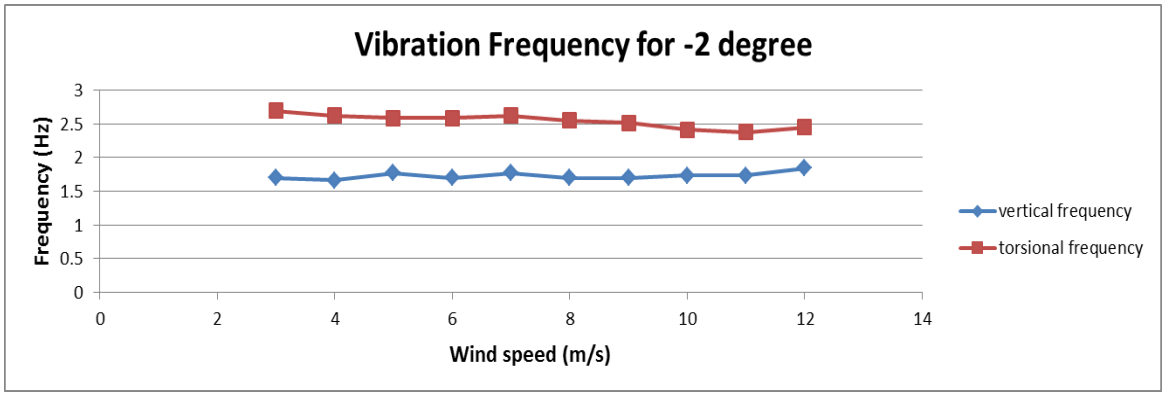

Figure 4.3.21 b) Frequency variation for vertical and torsional vibration modes for attack angle of -2 °

Figure 4.3.22 and Figure 4.3.23 present the frequency variation of the bridge deck section model, under the attack angles of $\alpha = 4^{\circ}$ and $\alpha = -4^{\circ}$, respectively. Once again, for $\alpha = 4^{\circ}$ the predominant frequency was taken from the average values of the additional spikes encountered very close to the natural frequency of the bridge deck section model. The spike at 1.894 Hz was excluded from the calculation of the vertical frequency. Similar with the case of $\alpha = -2^{\circ}$, the meeting point of vertical and torsional frequency is expected to be located between 1.86 Hz and 2.392 Hz (Fig. 4.3.22(a)). The experiment stopped at the test wind speed of 10 m/s due to the observation of large oscillation of the bridge deck model however, the critical flutter wind speed is apparently beyond the 10 m/s, which can be seen from Figure 4.3.22(b). For the test of $\alpha =$

-4°, less extra spikes were observed from the FFT results and the maximum test speed was 11 m/s (Fig. 4.3.23 (a)). The variation of the frequency is similar with that of $\alpha = 4^{\circ}$ and the critical flutter instability also didn't occur. Despite of that, the effect of attack angle on the increasing amplitude of vibration is still confirmed from Figures 4.3.16 and 4.3.17. For the same values of the testing wind speed, especially if these are above 8 m/s, the bridge deck model is more likely to exhibit an oscillation with larger amplitudes under bigger angle of attack. In addition, even for the same magnitude of the testing wind speed, there are slight differences between the responses recorded for positive and negative attack angles.

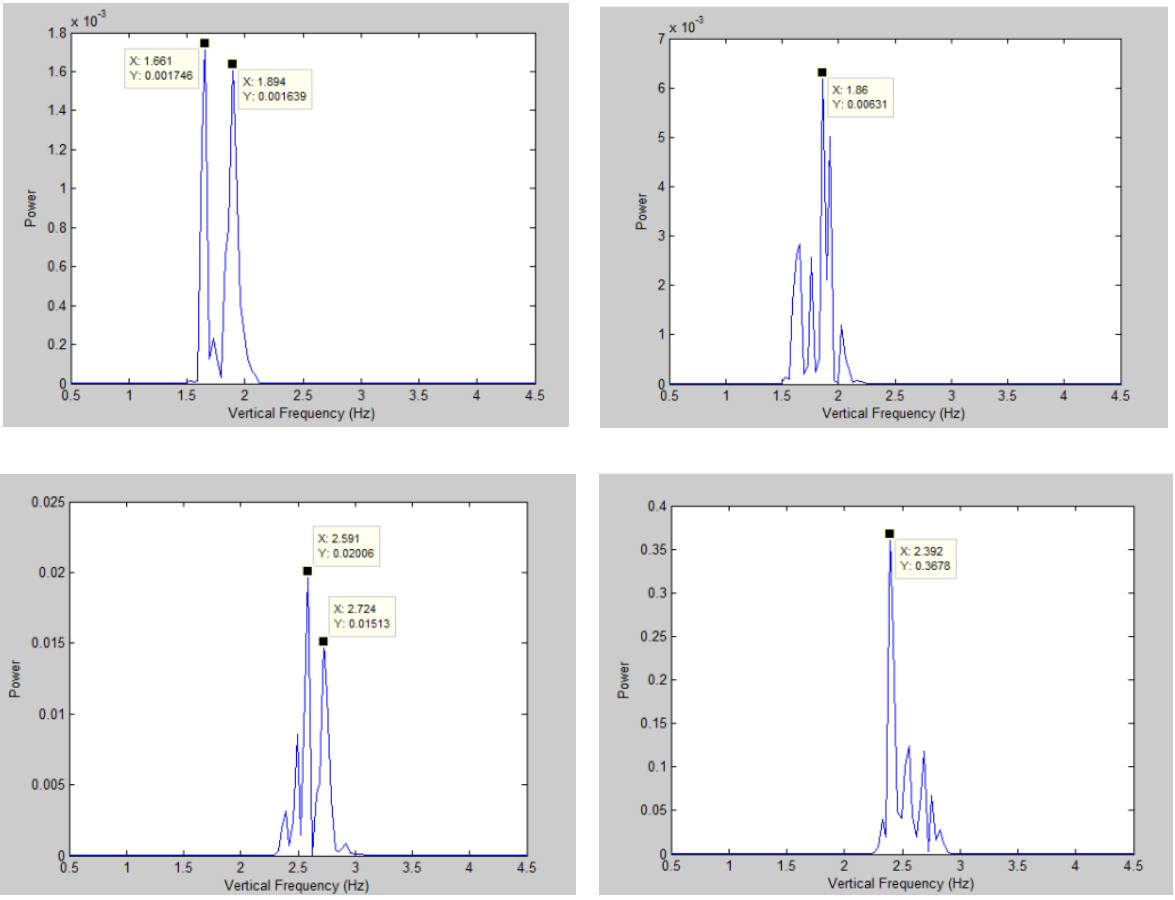

Figure 4.3.22 a) FFT of the bridge vibration under wind speed of 3 m/s and 10 m/s for attack angle of 4 °

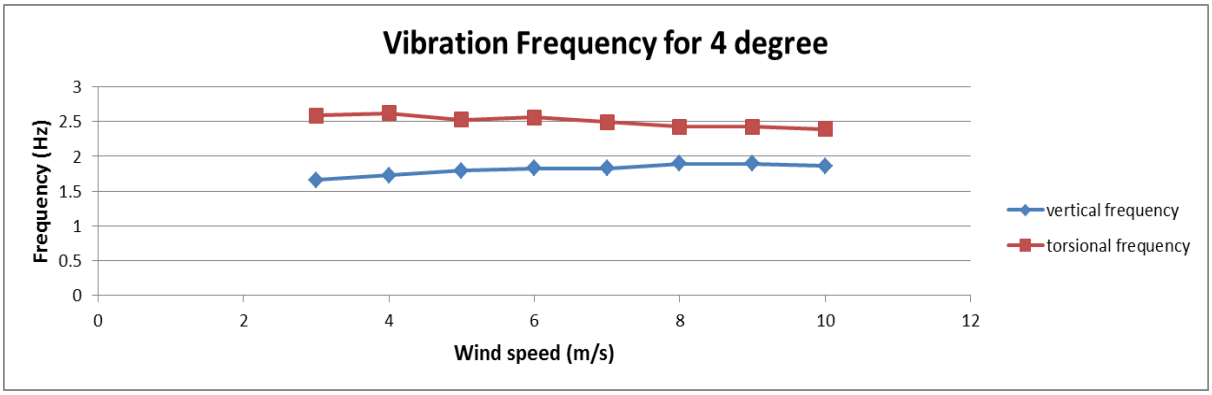

Figure 4.3.22 b) Frequency variation for vertical and torsional vibrationmodes for attack angle of 4 °

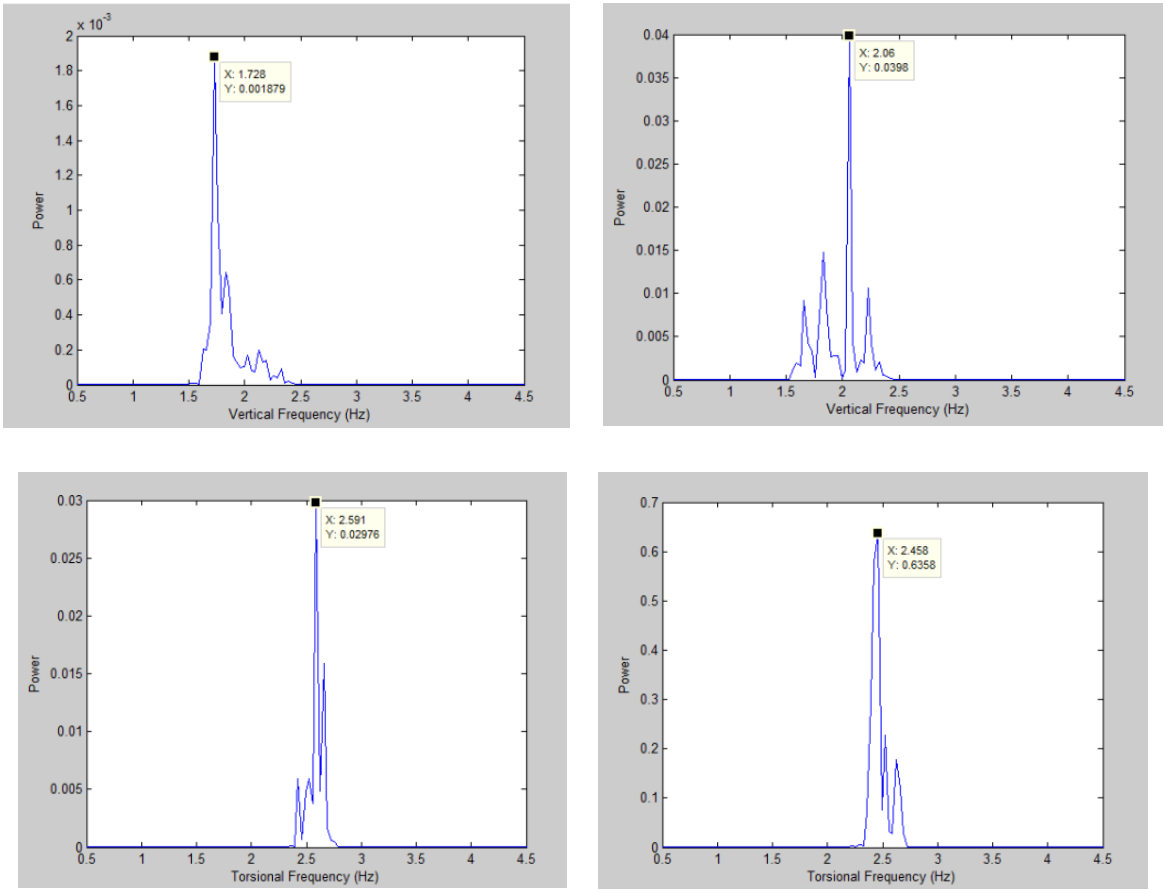

Figure 4.3.23 a) FFT of the bridge vibration under wind speed of 3 m/s and 11 m/s for attack angle of -4 °

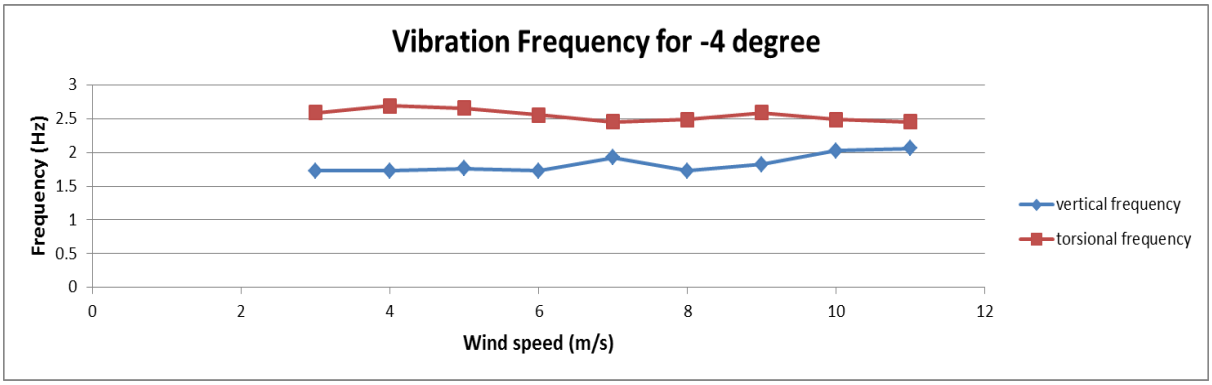

Figure 4.3.23 b) Frequency variation for vertical and torsional vibration modes for attack angle of -4 °

For the attack angle of $\alpha = 6^{\circ}$ and $\alpha = 8^{\circ}$, because of the inclination of the suspension system, the measured displacements by the measurement sensors were out of the reading limits of the sensor, due to the inaccurate installation of the reflection of the mirror pad. The bridge deck model vibration frequency was only analysed for $\alpha = -6^{\circ}$ and $\alpha = -8^{\circ}$(Figure 4.3.24 and Figure 4.3.25). The torsional frequency started at 2.771 Hz for $\alpha = -6^{\circ}$ and kept dropping until 2.343 Hz, while two very different vertical frequencies of 1.784 HZ and 2.236 Hz were found from FFT result at 3 m/s (Fig. 4.3.24 (a)). Based on the measured natural frequency of the bridge deck section model itself 1.667 Hz the closer frequency of 1.784 Hz was selected for further analysis. The frequencies of the two vibration modes met each other at 2.34 Hz, at the wind speed of 9 m/s and thus the appearance of critical flutter is confirmed (Fig. 4.3.24. (b)). It must be pointed out that, under the attack angle of -8° the two vibration modes met at 8 m/s wind speed as it can be noticed in Figure 4.3.25 (b), but the actual critical flutter instability should occur beyond this value. After the experiment, one end of the bridge spring system was found damaged for that wind speed and lost the ability to fasten appropriately the model along the torsional direction which led to the sudden upward movement of vertical frequency. The experiments were stopped due to this damage.

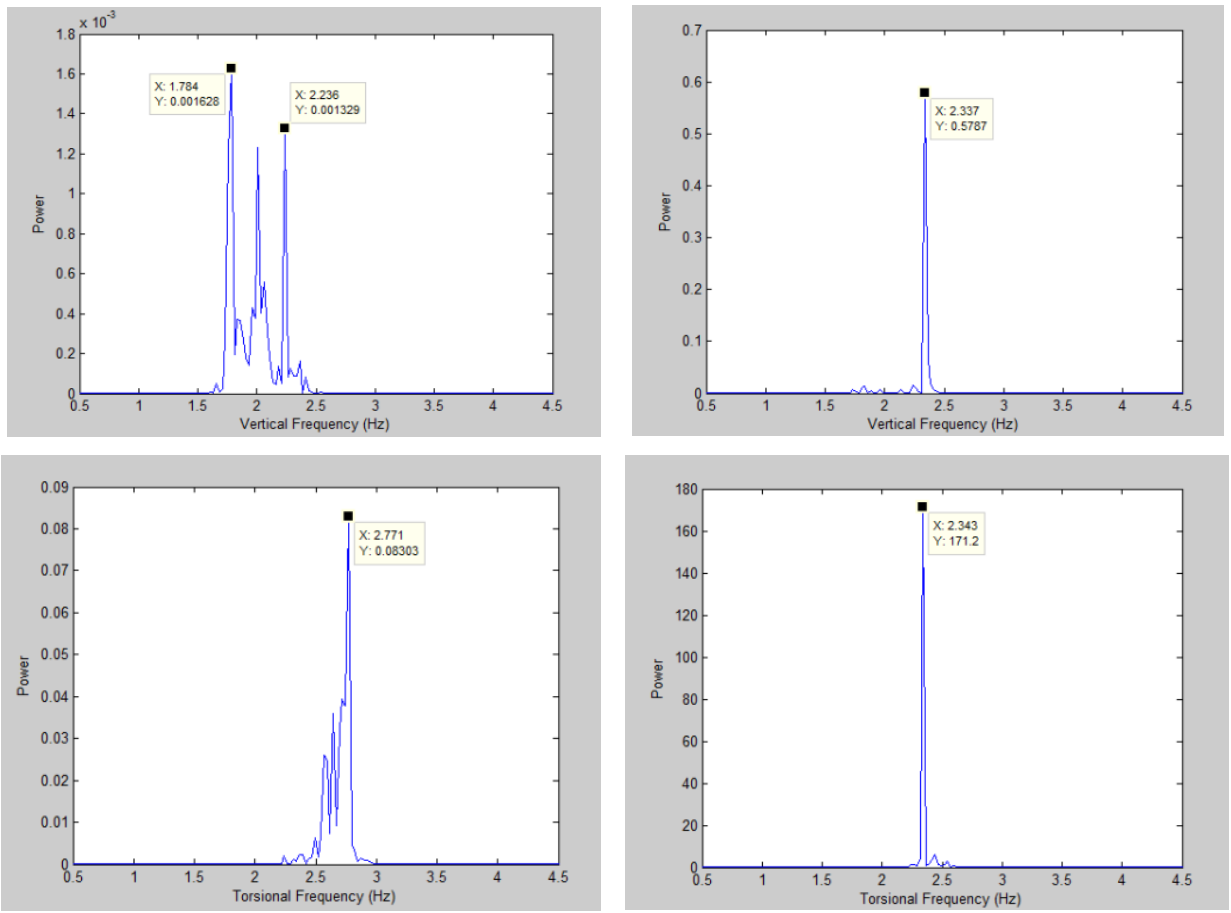

Figure 4.3.24 a) FFT of the bridge vibration under wind speed of 3 m/s and 9 m/s for attack angle of -6 °

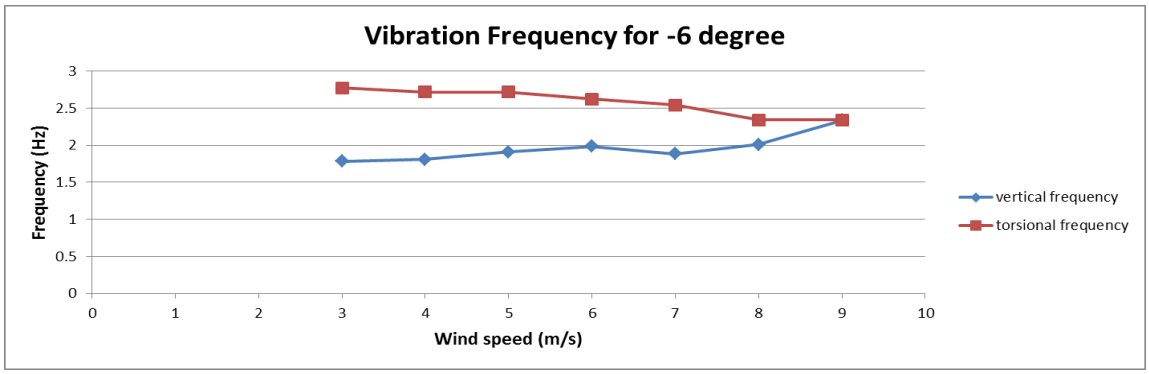

Figure 4.3.24 b) Frequency variation for vertical and torsional vibration modes for attack angle of -6 °

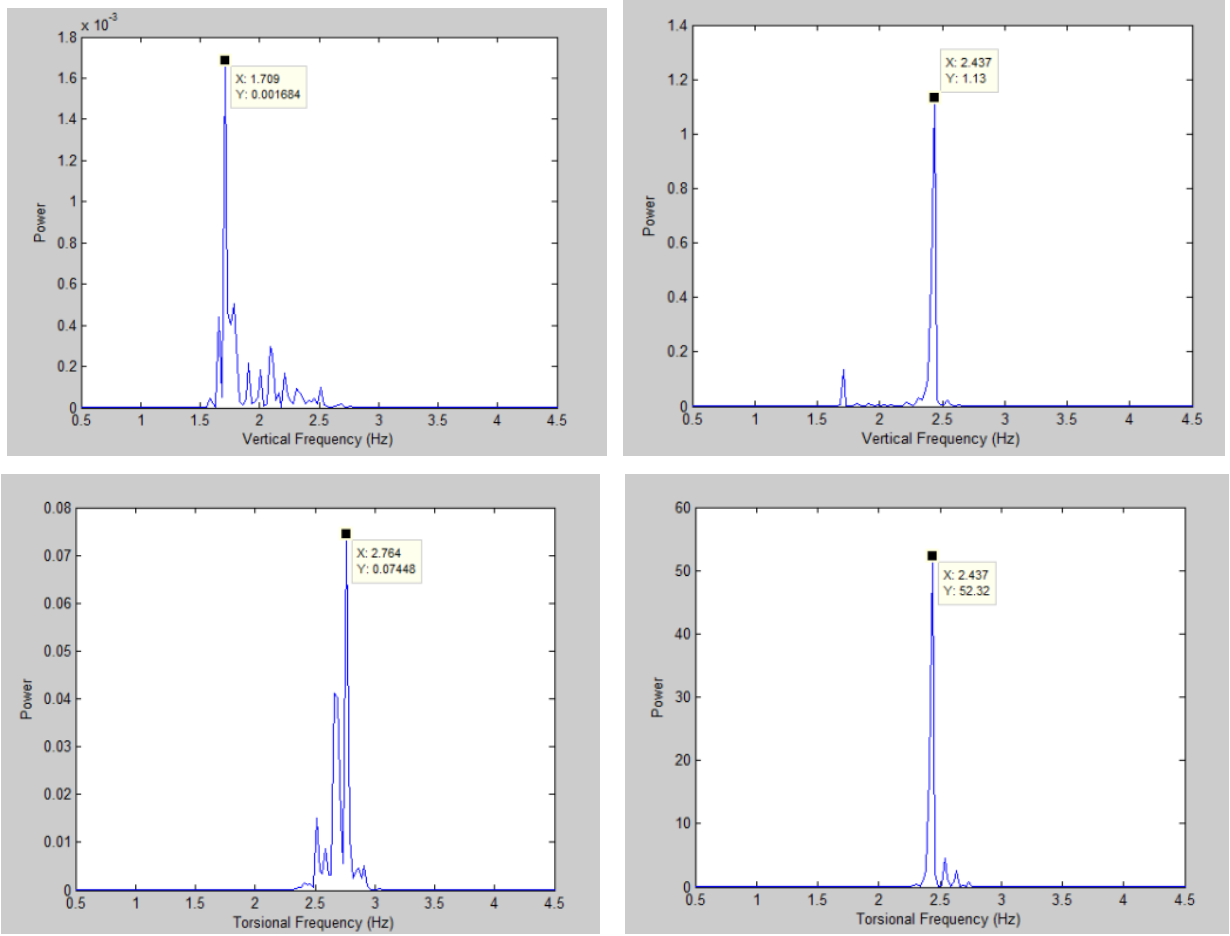

Figure 4.3.25 a) FFT of the bridge vibration under wind speed of 3 m/s and 8 m/s for attack angle of -8 °

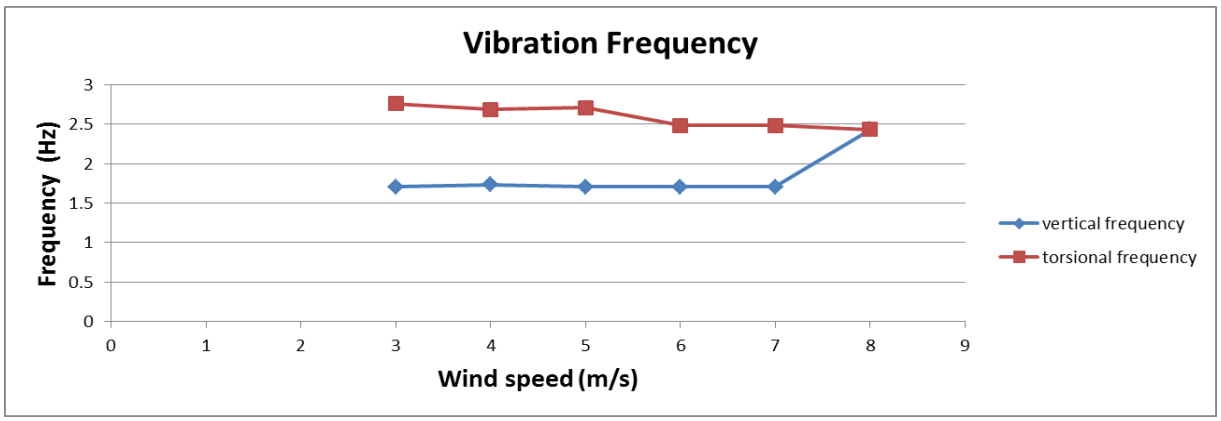

Figure 4.3.25 b) Frequency variation for vertical and torsional vibration modes for attack angle of -8 °

Overall the wind attack angle didn't show much impact on the bridge deck model vibration for the low wind speeds. Among all cases investigated, the vibration frequencies for both modes were close to the bridge natural vibration frequencies for the 3 m/s wind speed. Due to the aerodynamic force which causing increasement in aerodynamic stiffness but also a decrease in the aerodynamic damping, the predominant fequencies for the vertical and torsional vibration modes approaching each other were expected to meet around 2.3 Hz, as it was noticed for the case of $\alpha = 0^{\circ}$. The meeting point however shifted to the smaller wind speed values for the other angles of attack, which means that flutter instability can be encountered earlier, if the attack angles changes.

Chapter 5 CFD Computational details and Results

5.1 Computational details

5.1.1 Numerical algorithms

The complex geometry of the Megane multi-box deck section complicates the wind-structure interaction phenomena therefore detailed investigations were performed employing three-dimensional CFD simulations, through the use of Fluent-Ansys commercial software. Two turbulent models, RANS and LES, were initially considered and the most accurate one was retained for further simulations. For both cases the incoming flow conditions were employed as per the smooth flow condition with wind speed constant throughout the incoming wind plane. A logarithmic law or the power law wind speed variation, for simulating the atmospheric boundary layer above the ground level, is not usually employed for the long span bridge decks, due to the high altitude at which these are expected to be installed. A brief description for RANS and LES is provided as follow:

1) RANS (Reynolds Average Navier-Stokes: RANS) first proposed by Osborne Reynolds in 1895 [40] is based on time-averaged Navier-Stokes equations for fluid flow. The basic concept behind this method is the composition of the instantaneous turbulent flow quantity into its time-average quantity and an extra fluctuating component. This calculates directly the average large-scale flow only and the effect brought by the flow turbulence to the average wind speed flow is reflected into the fluctuation part also known as the Reynolds stress. Therefore the required computational costs are greatly reduced. For an incompressible Newtonian fluid, the Navier-Stokes equations can be written as[41]:

$$\frac{\partial U_i}{\partial t} + U_j \frac{\partial U_i}{\partial x_j} = -\frac{1}{\rho}\frac{\partial}{\partial x_i}[\overline{p}\delta_{ij} + \mu(\frac{\partial U_i}{\partial x_j} + \frac{\partial U_j}{\partial x_i}) - \rho u_i u_j] \quad (5.1)$$

Where U_i and u_i are the mean and fluctuating velocities in the x_i -direction, respectively, P is the mean pressure. The appearance of the Reynolds stresses term $(-\rho u_i u_j)$ at right hand side of the equation requires an extra modeling assumption to close the RANS equation. Two main approaches are generally used in conjunction with RANS algorithms: the Reynolds stress model and the eddy viscosity model [41]. The Reynolds stress model (RSM) is based on satisfying the Reynolds stress equation, with $u_i' \; and \; u_j'$

as dependent variables in the partial differential equations to be solved. However, introducing the transport equations for the Reynolds stresses in all the domain nodes, leads to high computational costs. For limited domain sizes and for structures of standard geometry, this method can provide an accurate estimation of the Reynolds stress variation with space and time, and wind flow patterns around the investigated structures can be captured. This model is based on the idea of the molecular viscosity and it was proposed by Boussinesq [41]. The Reynolds stress tensor is expressed as [41]:

$$-u_i u_j = v_T S_{ij} - \frac{2}{3} k \delta_{ij} \tag{5.2}$$

Here $k = \frac{1}{2}\overline{u_i' u_j'}$ is the turbulent kinetic energy and v_T is the viscosity coefficient and $S_{ij} = \frac{1}{2}\left(\frac{\partial U_i}{\partial x_j} + \frac{\partial U_j}{\partial x_i}\right)$ is the strain-rate tesnor. This is the first proposed eddy viscosity model, which assumes that the relationship between the average speed of the Reynolds stress and the strain rate is linear. Once the average speed strain rate is determined, the six Reynolds stresses need only one viscosity coefficient to be fully identified. Also the viscosity is isotropic, which means that this can be modelled through additional turbulence variables, such as the turbulent kinetic energy k and dissipation rate ε. Depending on the turbulent variable introduced into the equation, eddy viscosity models can be expressed differently [41]. $k - \varepsilon$ and $k - \omega$ are the most commonly used models. RANS can get the results which meet the engineering requirements with less demanding computational costs. Thus the reasonable Reynolds stresses model can make the solving process easier, but the disadvantages are, different turbulence type needs different Reynolds stresses models even for the same type of problem and the boundary conditions corresponding to different constant need to be modified for the model. Besides, for the cases of unsteady flow, large separated flow, inverse pressure gradient numerical simulation and some other issues, due to the turbulence model restriction it is difficult to always get satisfactory calculation results. Also it depends heavily on the shape of the flow field and boundary conditions thus the calculation assumptions are largely dependent on the experience.

2) The Large Eddy Simulation (LES) algorithm considers that the turbulent flow is composed of many eddies of different sizes, however only the large-scale eddies would

have significant influence on the mean flow, which is fundamentally different from the RANS approach. Thus the LES decomposes the turbulent flow into large-scale and small-scale flow formations by applying a filter at the sub-gird scale model [38]. Only the large scale turbulent flow is retained around the structure and is solved by directly numerical simulations. The Navier-Stokes equations are averaged in the domain delimited by the filter, to remove the small-scale eddies. The filtering process in the LES is most commonly achieved through the Deardorff cassette (BOX) filtering functions, the Fourier filtering functions or the truncated Gaussian (Gauss) filter function. After each of the parts of the N-S equations gets filtered the governing equations can be expressed as follow [38].

$$\frac{\partial \rho \overline{u_i}}{\partial x_i} = 0, \frac{\partial}{\partial t}(\rho \overline{u_i}) + \frac{\partial}{\partial x_j}\left(\rho \overline{u_i}\,\overline{u_j}\right) = \frac{\partial}{\partial x_j}\left(\mu \frac{\partial \overline{u_i}}{\partial x_j}\right) - \frac{\partial \bar{p}}{\partial x_i} - \frac{\partial \tau_{ij}}{\partial x_j} \tag{5.3}$$

Where $\overline{u_j}$ and p are filtered mean velocity and filtered pressure, respectively. τ_{ij} is the subgrid-scale stress resulting from the filtering operation indicating the impact of small eddies to the large eddies. τ_{ij} is unknown and is modeled as:

$$\tau_{ij} = -2\mu_t \overline{S_{ij}} + \frac{1}{3}\tau_{kk}\delta_{ij},\ \overline{S_{ij}} = \frac{1}{2}\left(\frac{\partial \overline{u_i}}{\partial x_j} + \frac{\partial \overline{u_j}}{\partial x_i}\right) \tag{5.4}$$

where μ_t is the subgrid scale turbulent viscosity, and $\overline{S_{ij}}$ is the rate-of-strain tensor. Currently, the SGS (subgrid scale) models which have been adopted for LES simulation are the standard Smagorinsky model, dynamic eddy viscosity models, dynamic hybrid model and gradient model, etc. Among them, the Smagorinsky-Lilly model is the most widely used algorithm. It was proposed in 1963 by Smagorinsky [42] and he also defined the eddy viscosity coefficient as:

$$v_T = (C_S \Delta)^2 |\bar{S}| \tag{5.5}$$

where $|\bar{S}| = (2\overline{S_{ij}S_{ij}})^{1/2}$ is the rate-of-strain tensor, Δ is the filter scale and C_S is dimensional parameter called Smagorinsky coefficient. The advantage of LES is that this model is able to describe the small-scale turbulent flow and also the computational cost is much smaller than the direct numerical simulations (DNS). The boundary geometry and the flow category have less impact on the SGS stress model when compared to the Reynolds stress model and its application is more universal. Unavoidably, high-speed numerical processing capability is required for processing large amounts of data and

solving nonlinear partial differential equations. For the multi-deck bride deck simulation experiment, the Large Eddy Simulation (LES) with the Smagorinsky subgrid-scale model were employed for the CFD simulation. The three-dimensional incompressible Navier-Stokes equation and the equation of continuity in non-dimensional form were used, with Δ as the filter width given as the cubic-root of grid volume and the Smagorinsky constant, Cs = 0.12. The inviscid flux vector was determined by a standard upwind, flux-difference splitting through the low diffusion Roe approach. For estimation of the secondary diffusion terms and velocity derivatives, the least square cell based spatial discretization was employed and Third-Order MUSCL equation was considered for the flow density-based solver. The time step was chosen as Δ_t= 0.0003 s; pressures along the entire surface of the model were integrated, and lift and drag aerodynamic forces were determined.

5.1.2 Boundary conditions and mesh details

The geometric dimensions for the multi-box deck model set for the three-dimensional CFD simulations were 8.0 m width for the traffic decks, 5.0 m width for the railway decks, representing a model scaled 1:2 from the prototype, as represented in Figure 5.1.1. A transversal segment of the deck of 20.0 m was used for the tests, and between the split decks, connecting beams of 1.5 m width were assigned at 5.0 m intervals.

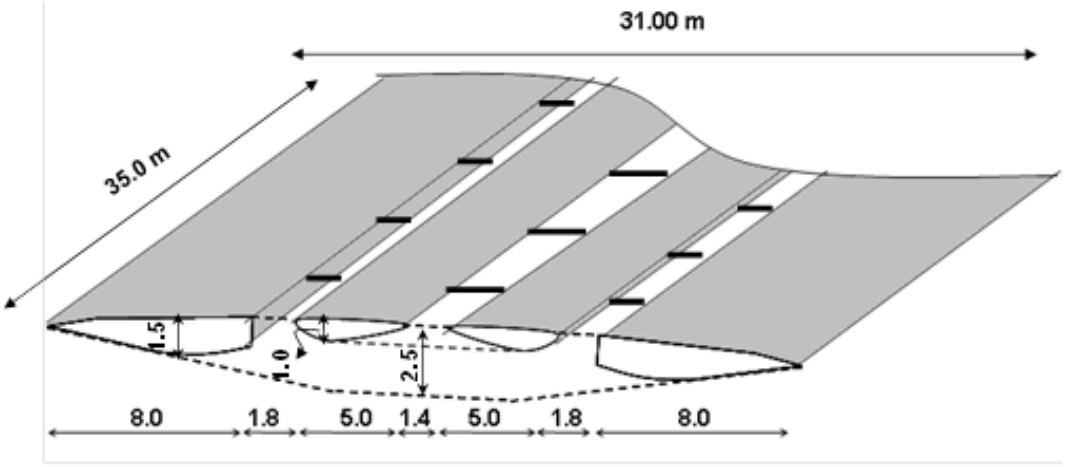

Figure 5.1.1 Geometry of the Bridge Deck model scaled 1:2

The computational domain had the major axis of 3D, the minor axes were L and 1.5 L, where D is the entire width of the deck and L is the total length of the deck segment, as

schematically represented in Fig. 5.1.1 After considering the set-up time, computational cost, as well as the numerical diffusion, structured tetrahedral mesh containing triangular faces was selected for the CFD simulation. A total number of 3.62 million cells were used for the entire domain, with 7.22 million triangular interior faces and 3.3 million faces along the domain's walls. Around the bridge model a very fine mesh was employed with a total of 1.3 million cells (Figure 5.1.2) and 1.5 million triangular faces only at the surface of the bridge deck model. Angles of attack of α = -4 °, -2 ° 0 °, 2 ° and 4 ° were achieved by changing the orientation of the deck model and re-meshing the domain, preserving as much as possible the mesh parameters expressed above. Varying the inclination of the incoming velocity vectors at the inlet plane was also attempted; however the simulations have failed repeatedly, therefore such vectorial method of varying the attack angle was not used in the current numerical study. The non-slip boundary conditions were specified on the surfaces of the deck, while for the in-flow the boundary condition was set to ux = V, uy = uz = 0, where V is the mean wind speed. The lateral walls of the simulation domain were considered as symmetric slip, penetration boundary conditions, so that the end effect was avoided and the wind flow would actually develop beyond the limits of the domain, however, without the data storage option.

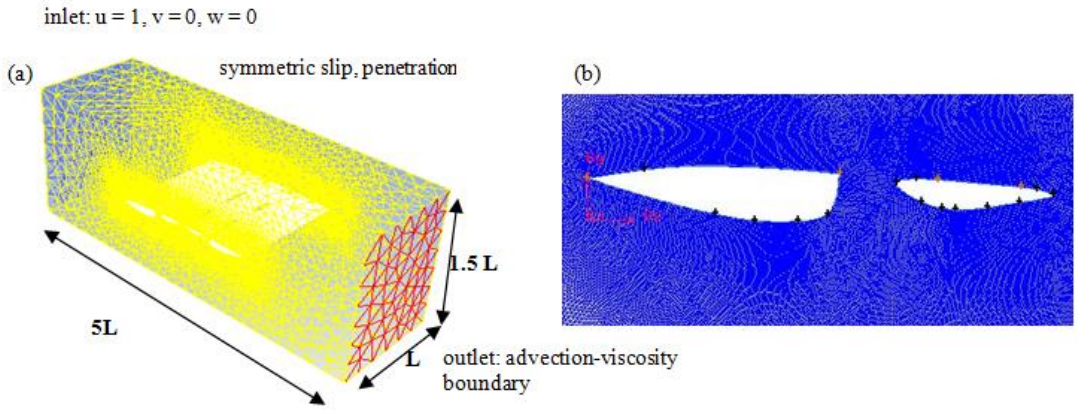

Figure 5.1.2 Mesh Detail for Simulation

Pressure was monitored along the surface of the entire deck segment, on several rings around the four individual decks and also on several lines around the connecting beams. Velocity profiles were established at the middle of each of the individual decks up to a height of 10 m and wind flow streamlines and vortices distribution were determined for the wind field domain, in the immediate vicinity of the deck.

5.2 LES model validation with experimental results

The turbulent flows formed around the deck segment have a direct effect on the drag and lift forces induced by the wind to the entire deck. Therefore an accurate estimation, especially when the CFD analytical simulations are employed is very important. Two flow models RANS and LES were used in the investigation for which the main concepts have been detailed in the section 5.1above. For a simulated wind speed of 50 m/s, at 0° attack angle, the RANS, which considers the Reynolds stresses when calculating the fluctuating wind speed component in the governing equations, showed more uniform eddy viscosity distribution around the individual decks indicating a consistent turbulent flow formation shedding downstream from the top surface of the last deck (Fig. 5.2.1 a)).

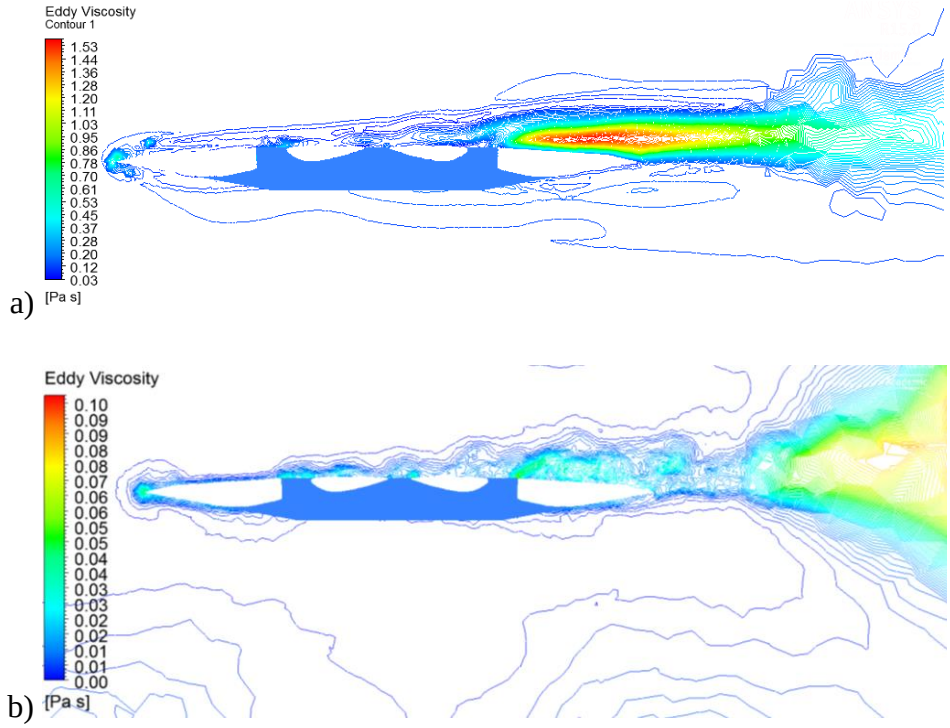

Figure 5.2.1 Eddy viscosity distribution around the Megane deck for 50 m/s for a) RANS, b) LES

The LES however, which filters out the smaller eddies and numerically solves the large scale eddies formed around the structure, provided more detailed information regarding the eddy

viscosity showing the development of the turbulent flow not only at the edge of the deck, but shortly downstream of each deck as well (Fig. 5.2.1 b)). This method was considered more appropriate for the current CFD simulation because the Megane section has multiple decks situated close to each other, hence the wake from the upstream decks will always influence the downstream decks. The differences between the results obtained from the two algorithms, the RANS and LES could be found from the instant pressure distribution around individual decks. As it can be noticed in Figure 5.2.2, the RANS method tended to underestimate the pressure for the decks A and D, which are the most exposed decks to wind flow variation, when comparing to the LES pressure results. After that, the CFD simulation results using LES were compared with the experimental results to validate the CFD simulation model for the Megane Bridge multi-deck.

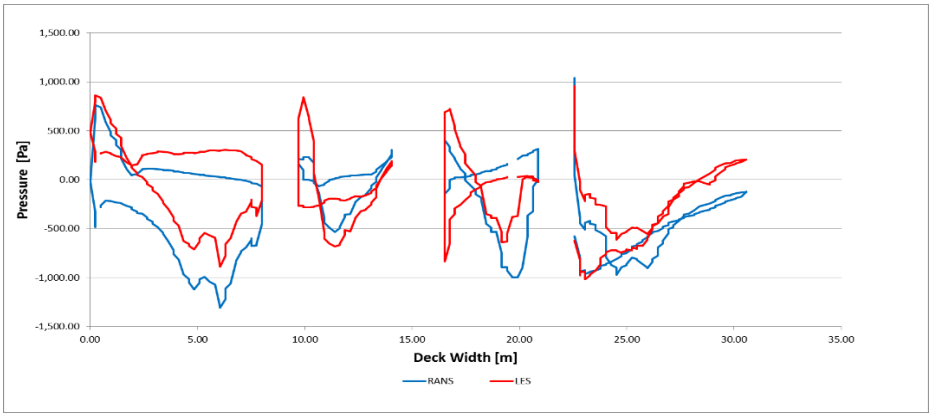

Figure 5.2.2 Instant pressure distribution around each deck with LES and RANS model

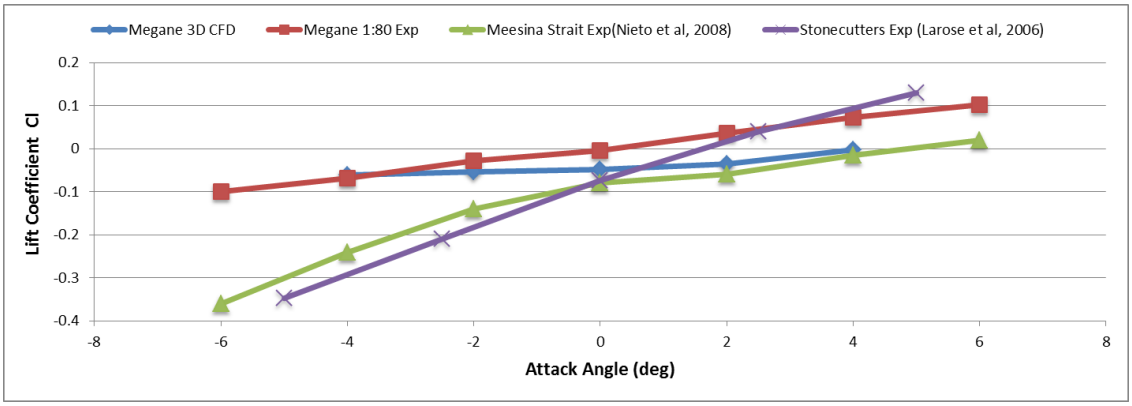

Figure 5.2.3 CFD lift coefficient vs. experiment lift coefficient

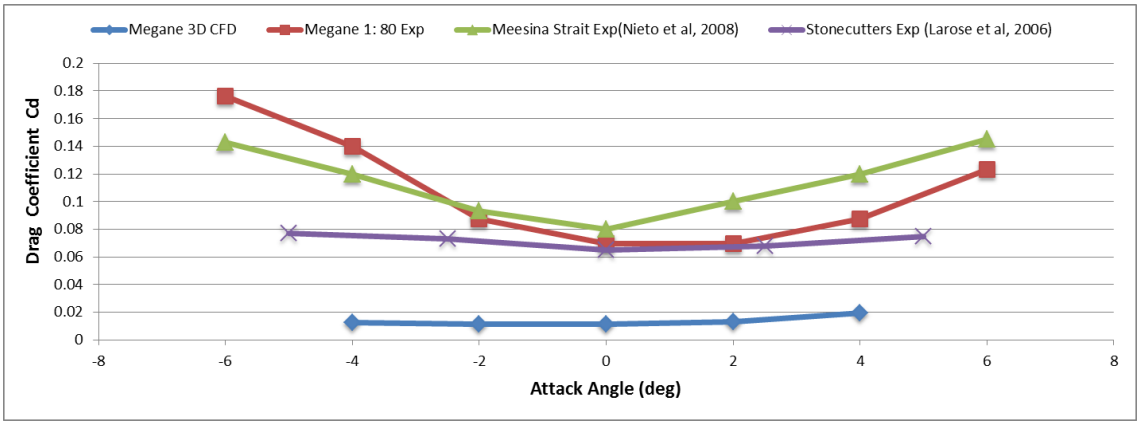

Figure 5.2.4 CFD drag coefficient vs. experiment drag coefficient

The lift coefficients measured in the wind tunnel experiment were in very good agreement with the results obtained from the CFD-LES simulation for the multiple-decks Megane Bridge deck section (Figure 5.2.3 and Figure 5.2.4). Also due to the similar geometry, comparison was made with the results reported for the Messina Bridge deck documented by Nieto et al, 2008 [43]. Similar trend and values were noticed for the experimentally obtained lift coefficients for the Messina bridge deck and the Megane Bridge deck section and also with the LES-CFD simulation results performed for the Megane Bridge deck. For the reference, the lift coefficients experimentally obtained by Larose et al, 2006[44] for the Stonecutters twin-box deck bridge is also represented in Figure 5.2.3 and Figure 5.2.4. The drag coefficients of the Megane Bridge deck, in particular the wind tunnel experiments, yielded slightly higher values than the LES-CFD simulations (Figure 5.2.4), which were considered to be the effect of the two rectangular foam endplates, which were attached to both sides of the model tested in the wind tunnel. The windward area of the end plate is relatively large when comparing to the area of the bridge model itself and as a result, extra drag force may be introduced to the model thus leading to a higher drag coefficients. However considering the overall good agreement between the aerodynamic coefficients measured in the wind tunnel and the coefficients obtained from the three-dimensional LES – CFD model of the Megane multiple-deck bridge section, it can be concluded that the LES algorithm can lead to accurate enough estimation of the wind flow effect on such complex geometry decks. Therefore, by the aid of the three-dimensional LES-CFD simulations, extraction of the flow turbulent characteristics, which cannot be directly noticed or measured in the wind tunnel experiments, will be presented hereafter.

5.3 Wind flow characteristics

As pointed out by other researchers (Larsen et al, 2008) [45] for a twin box deck section, at lower *Re* numbers, the decks are individually immersed in the wind flow, and each might encounter vortex shedding phenomena, while for higher *Re* the wind flow would change to a turbulent regime and shear layers will be generated instead engulfing the entire deck which behaves like a single bluff body; Larsen et al, 2008 [45] and Chen et al, 2013[46] pointed out that for $Re = 0.05$ to 1.8×10^4, the pressure fluctuation was much higher for the downstream deck for the twin deck configuration. Therefor the current CFD simulation focused on revealing the flow patterns around the multi-box Megane deck section, for angles of attack $\alpha = -4°, -2°, 0°, 2°, 4°$ at $Re = 9.3 \times 10^7$. In general, the wind flow had a complex behaviour, slipping through the gaps of the deck and shifting from the upper deck to the lower deck or the other way around, depending on the angle of attack. It was noticed that for positive angles of attack the first two decks, named as decks A and B, acted as a single bluff body from which shear layers were shed and re-attached onto the upper surface of the last two decks, C and D. The reattaching layers combined with those flows passing upwards through the middle gap, especially for $\alpha = 0°$ and 2° (Figure 5.3.1 (a)-(c)) and finally the combination shed from the downstream edge of the last deck D. Also the instantaneous vorticity isosurfaces, indicated by the color scale of the reduced velocity magnitude Ur, in Figure 5.3.1 (b), showed a deviation in the wind direction on the upper deck surface located at the middle of the Megane deck section forming a split-flow. It is worth mentioning that a similar split-flow pattern was identified by smoke visualization during the wind tunnel tests performed for a modified Messina bridge multi-box deck section by Belloli et al, 2013 [47]. The lower surfaces of deck A, B and C sustained most of the turbulent flow for attack angles $\alpha = 2°$ and 4°, (Figure 5.3.1 (a) and (b)) and a flow separation was indicated by the increased U_r values, on the first corner of the deck A. For the negative angles of attack, $\alpha = -2°$ and $-4°$ the wind flow transited upwards through the last two gaps, the intensity of the reduced wind speed increasing on the upper surface of deck C; also a separation bubble was noticed on the deck D, caused by the flow detachment at the windward edge of deck, followed by a periodic flow re-attachment at the middle of deck D (Figure 5.3.1 (c) and (d)). Intermittent shear layers detached from the corner of the deck B, however these did not re-attach on the decks C and D, instead they traveled upwards into the flow.

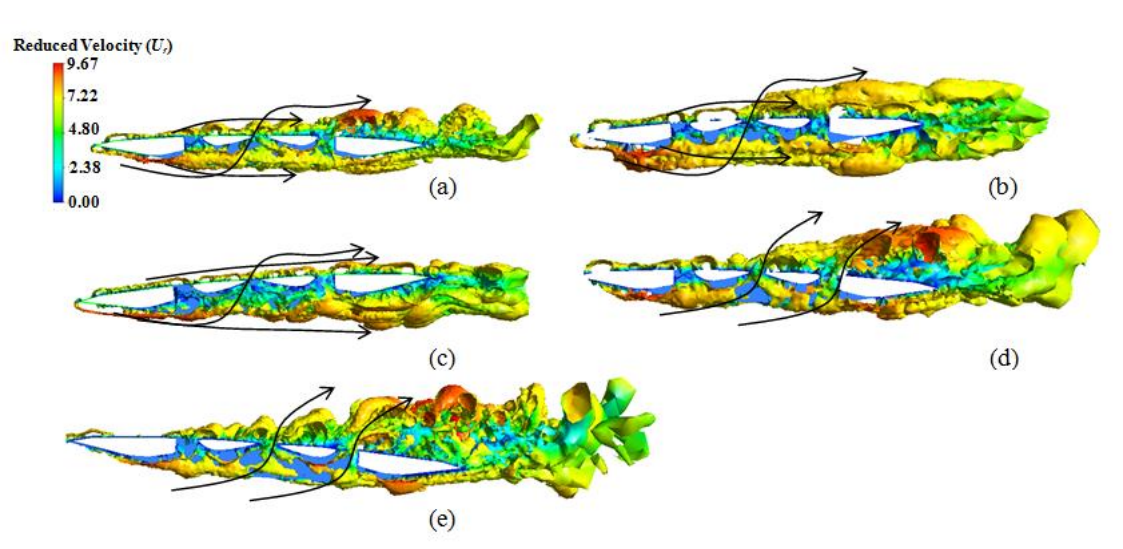

Figure 5.3.1 CFD simulation about the flow pattern around Megane Bridge deck for (a) α= 0 °, (b) α = 2 °, (c) α = 4 °, (d) α = -2 °, (e) α = -4 °

The three dimensional flow patterns presented in Figure5.3.2 (a) to (j) showed that, for the upper decks' surfaces, the main difference between the positive and negative angles of attack consisted of the presence of the wind flow formations along the edges (Figure 5.4 (a) and (e)) or almost enveloping the entire decks (Figure 5.3.2 (c)) for positive angles, while for negative angles of attack the flow on the last two decks became highly turbulent (Figure 5.3.2 (g) and (i)). Also for negative angles of attack, a sudden increase of the reduced wind speed was noticed on top of the deck D which indicates flow separation. The split-flow pattern was identified for $\alpha = -2°$ and $2°$ starting from the front edge of deck C (Figure 5.3.2 (c) and (g)). Again, similar split-flow pattern was identified by smoke visualization during the wind tunnel tests performed for a modified Messina bridge multi- deck section by Belloli et al, 2013[47]. If on the upper deck, the generation of the flow formations was controlled by the gaps position and dimensions, then on the lower deck, the position of the connecting beams significantly influenced the flow patterns. For all analyzed cases, the wind flow generated on both sides of the connecting beams formed a longitudinal vortex trail towards the edge of the deck D, which was further shed upwards into the flow (Figure 5.3.2 (b), (d), (f), (h) and (j)). For negative angles of attack, those vortex trails combined with the flow incoming from the main body of the upper deck D created turbulence for the downstream flow.

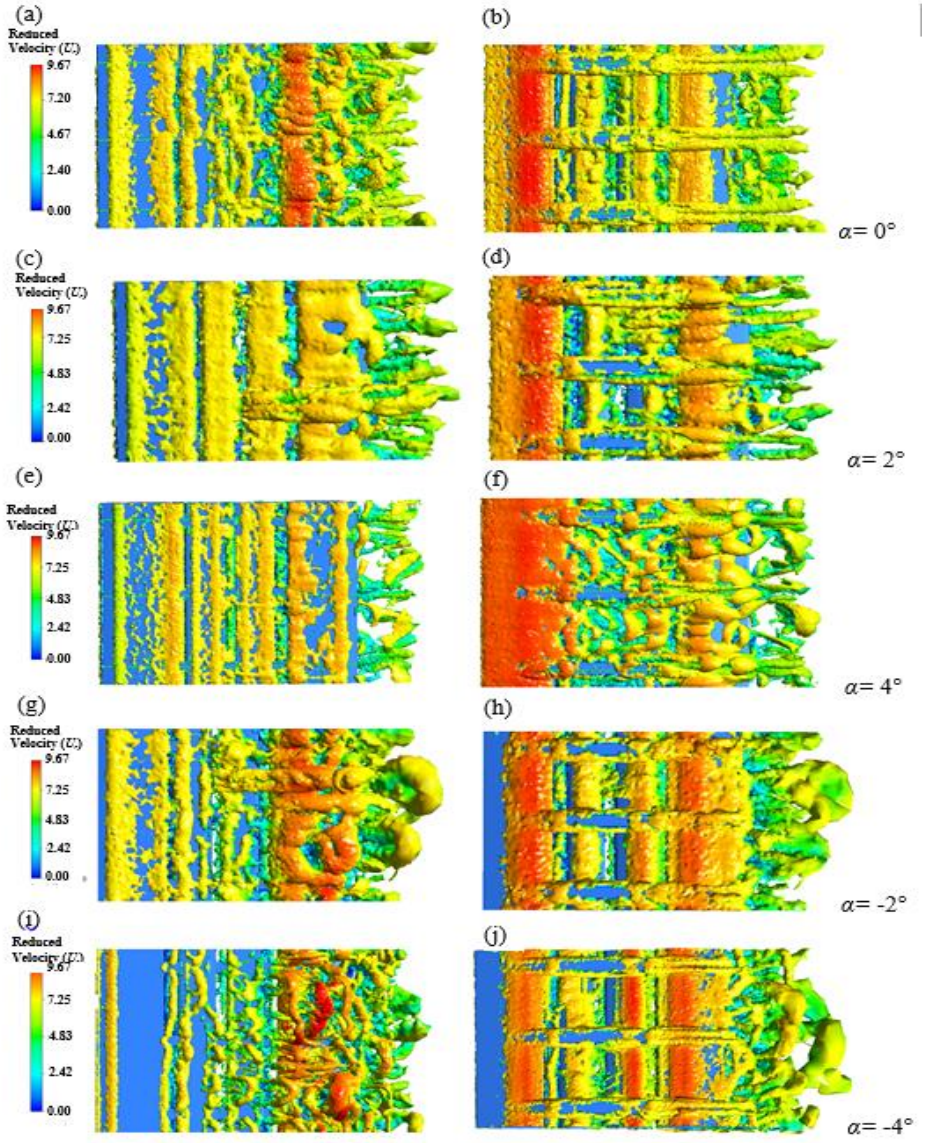

Figure 5.3.2 Three-dimensional flow patterns around the Megane Bridge deck for a) 0° front, (b) 0° back, (c) 2° front, (d) 2° back, (e) 4° front, (f) 4° back, (g) -2° front, (h) -2° back, (i) -4° front, (j) -4° back

5.4 Pressure distribution for the three-dimensional model

The wind-induced pressure and the effect of the connecting beams on the flow patterns, was more comprehensible through the investigation of the three-dimensional model. Figure 5.4.1 (a) – (j) represent the wind-induced pressure on the surface of the Megane Bridge deck segment. at an angle of attack $\alpha = 0°$ showed, a positive pressure on the upwind edge of deck A, of up to 1.5 × 103 Pa which gradually decreased along the upper surface of decks A, B and C (Figure 5.4.1(a)). Also, a strong negative pressure up to -1.2×10^3 Pa, was noticed on the upper surface of deck D, near the upwind edge. This negative pressure indicates the detachment of the wind flow, corresponding to the increased wind speed region showed in Figure 5.3.1 (a). Pressure variation was more stable on the lower surface of the deck, a slight suction being indicated along the traffic deck D of up to -4.5×10^2 Pa, on the same upper surface region, as it can be noticed in Figure 5.4.1 (b). The changing of the attack angle has influence to the wind-induced pressure on the upper surface of the deck for $\alpha = 2°$ (Figure 5.4.1 (c)) showing much smaller negative values, of up to -8.5×10^2 Pa, for the traffic deck D and on the lower surface of deck A (Figure 5.4.1 (c) and (d)). For $\alpha = 4°$ (Figure 5.4.1 (e)), the downward inclination of the deck caused the incoming flow to hit the upwind edge of deck A, where a high pressure of 1.0×10^3 Pa is shown. The longitudinal vortex formations present on the upper surface on each of the decks A, B and C, described in Figure 5.3.2 (e), induced a suction on the entire upper surface of these decks, especially on the edge of the traffic deck D, where the flow detachment determined negative pressures of up to -1.0×10^3 Pa. Also, the flow detachment signaled by the high wind speed on the lower surface of deck A in Figure 5.3.2 (f), was reconfirmed by the suction of -1.2×10^3 Pa distributed almost uniformly along the lower deck A, as it can be noticed in Figure 5.4.1 (f). Because of the sharp geometry of the corner, the pressure induced by the impinging incoming flow was lower than the previous cases, registering values of 0.7×10^3 Pa, for $\alpha = -2°$ (Figure 5.4.1 (g)). However the increased wind speed on the deck D which was shown in Figure 5.3.2(g), has determined a flow re-attachment in the gap region, which would induce very high pressures of up to 1.0×10^3 Pa, on the inner wall of the gap preceding the deck D (Figure 5.4.1 (g) and (h)). A negative pressure is noticed along the upper surface of the deck D, of up to -1.5×10^3 Pa, which is determined by the increased wind speed represented in Figure 5.4 (g). There is no effect of the split-flow localized behaviour signaled above, which means that the vortex formation detaches from the deck B and sheds upstream into the stream, without re-attaching on the upper

surface of decks C and D, as it can be seen clearly in Figure 5.3.1 (d). In spite of the negative angle of attack, even on the lower deck, there is no strong positive pressure on the incoming corner of deck A (Figure 5.4.1 (h)). A strong suction can be noticed however from the middle region of the lower surface of the deck A which can be associated with the high wind speed noticed in the same region in Figure 5.3.2 (h). Figure 5.4.1 (i) and (j) show a distinct pressure distribution for α = -4 ° when compared with the other angles of attack. For the upper surface of the deck, especially for the traffic deck A, suctions of up to -1.5×10^3 Pa towards the edge were registered, corresponding to a longitudinal vortex formation which detached from the surface in this region and shed upwards into the flow as per the description of the flow pattern presented in Figure 5.3.2 (i), the rest of the decks B, C and D, recording average positive pressures along their upper surface, in spite of the turbulent flow incoming from the lower deck and passing through the gaps. Along the lower A and especially B decks negative pressures of up to -1.5×10^3 Pa were induced, while high positive pressures of up to 1.0×10^3 Pa were recorded only along the downwind edge of the deck D, caused by the trail of turbulent formations visualized in Figure 5.3.2 (h) .

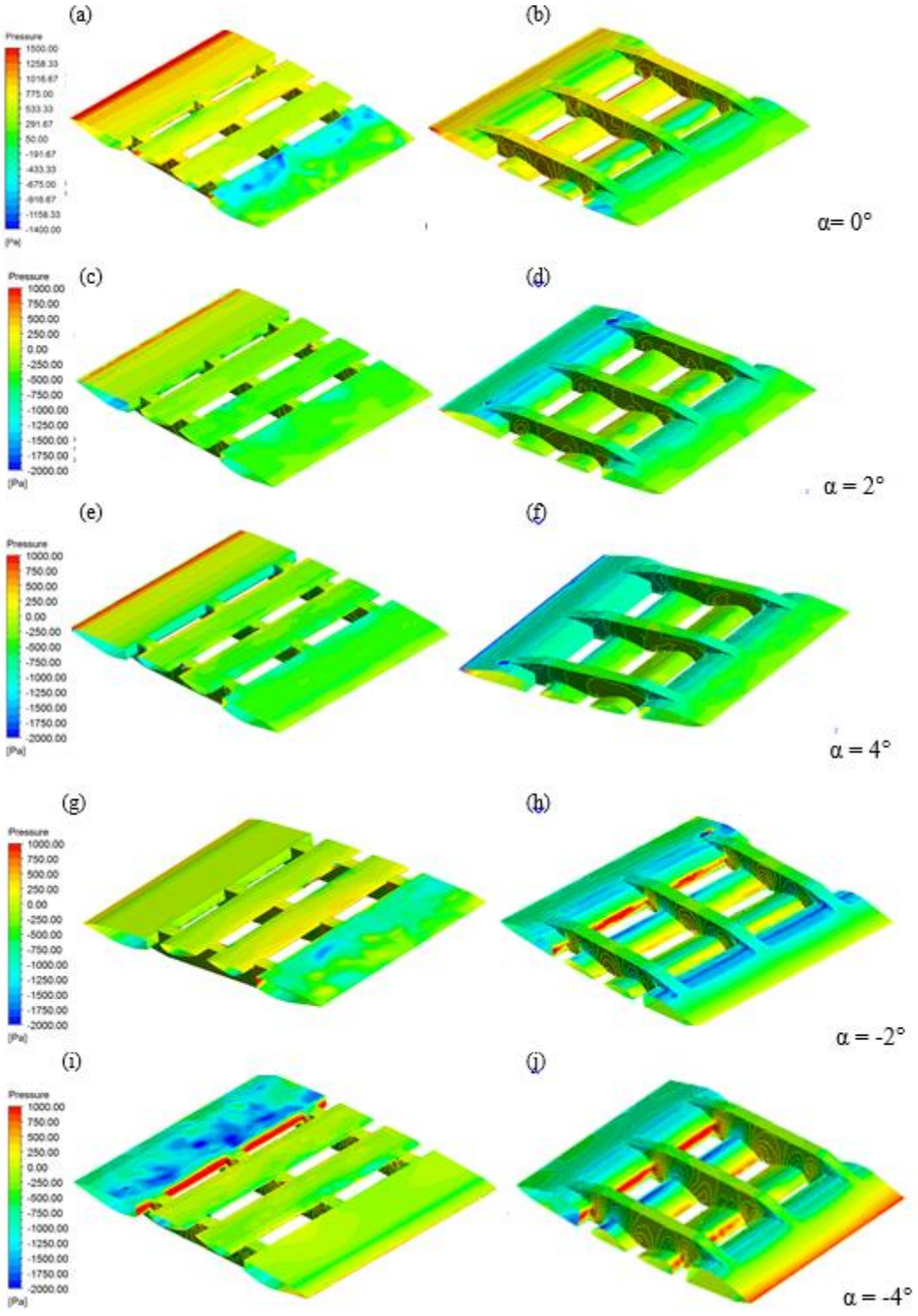

Figure 5.4.1 Three-dimensional stress distributions for Megane Bridge Deck for a) 0° front, (b) 0° back, (c) 2° front, (d) 2° back, (e) 4° front, (f) 4° back, (g) -2° front, (h) -2° back, (i) -4° front, (j) -4° back

In order to determine the turbulent flows and vortices formations around the multi-box Megane bridge deck surface, especially at the locations where the pressure registered strong positive and negative peaks among all flow cases the pressure contours for the flow field around the deck section were represented in Figure 5.4.2 (a) – (e), for angles of attack, $\alpha = 0°$, 2°, 4°, -2 ° and -4 °. The pressure contours were consistent with the pressure distribution represented in Figure 5.4.1 and with the flow patterns described in Figure 5.3.2 above. For $\alpha = 0°$, when the first traffic decks A and the railway decks B and C, formed a bluff body, and continuous shear layers were shed towards the deck D, the presence of a separation bubble with negative pressure was noticed at the upwind edge of deck D (Figure 5.4.2 (a)). For $\alpha = 2°$ and 4°, no major variations were noticed in the pressure field around the Megane deck section, except for the suction bubble created on the lower deck at the corner of the first deck A (Figure 5.4.2 (b) and (c)), which confirms the negative pressure peaks in Figure 5.4.1 (d) and Figure 5.4.1 (f). Also, for positive angles of attack, suction was registered underneath the decks A and D. For the negative angles of attack, $\alpha = -2°$ and -4 °, clear vortices of negative pressure were noticed travelling along the traffic deck D, detaching around its middle region and shedding upwards into the flow (Figure 5.4.2 (d) and (e)). These are consistent with the flow patterns description in Figure 5.3.1, where longitudinal turbulent formations were reported, which now can be confirmed to be the high speed vortices shedding.

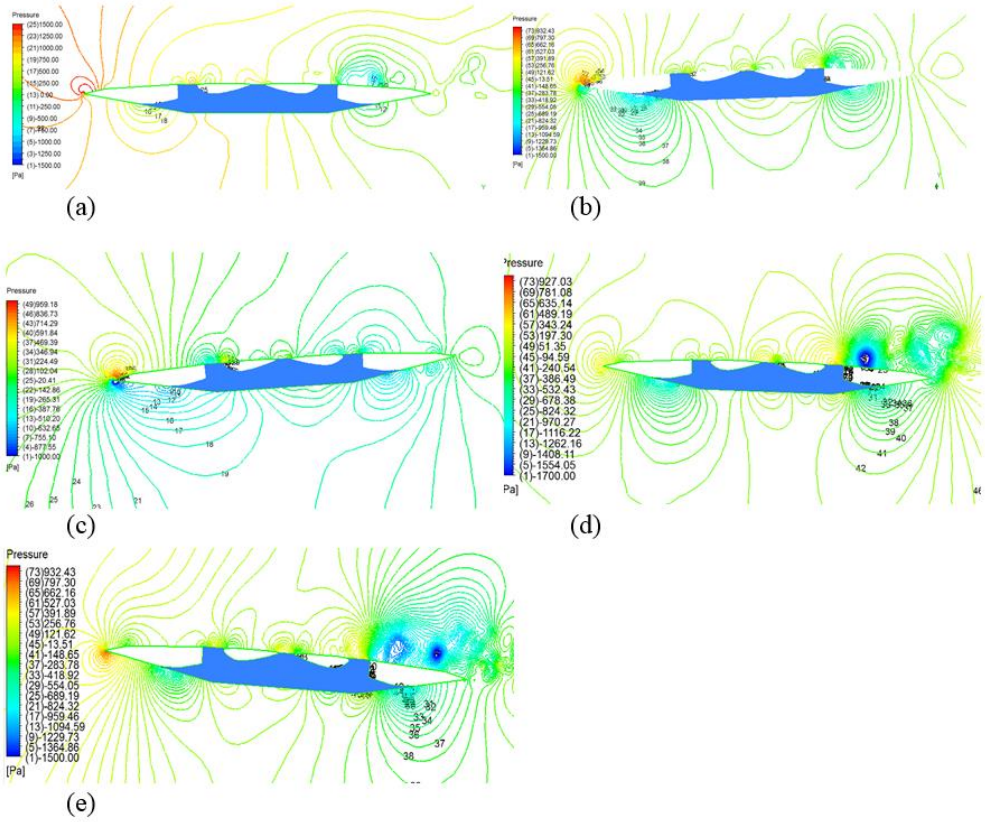

Figure 5.4.2 Pressure contours for the flow field around the Megane deck section, (a) α= 0 °, (b) α = 2 °, (c) α = 4 °, (d) α = -2 °, (e) α = -4 °

5.5 Aerodynamic force coefficients for the individual decks

The pressure contours and velocities obtained for the multi-box deck section of the Megane Bridge indicated that traffic and railway decks A, D, B and D, and the three connecting beams registered different values, some of them being totally in suction while some of them registered high positive and negative pressure peaks, due to the effect of the gaps as well as the angles of attack. Despite the aerodynamic force coefficients for the entire bridge deck which were presented above (Figure 5.2.3 and Figure 5.2.4), still there is a need to further investigate the force coefficients with respect to the individual deck, especially for the last Deck D, which was shown to be greatly affected by vortex shedding. Therefore the mean aerodynamic drag, and lift coefficients for each of the traffic and railway decks A, D, B and C, for the three connecting

beams and for the entire Megane Bridge deck section are presented in Figure 5.5.1 and Figure 5.5.2 below. The coefficients were normalized with the widths of each deck segment as presented in this section (namely 8.0 m for traffic decks A and D, 5.0 m for railway decks B and C and 2.5 m for beams) and with the entire deck width B, for the Megane Bridge deck. The two middle railway decks, B and C have encountered very similar distribution, with the drag coefficient C_D increasing slightly for $\alpha = 4°$, and lift coefficient increasing up to $C_L = 0.1$ for the negative angles of attack $\alpha = -2°$ and $-4°$ and decreasing up to $C_L = -0.14$ for positive angles, $\alpha = 2°$ and $4°$ (interrupted lines in Figure 5.5.1 and Figure 5.5.2). The traffic decks A and B had almost opposite distribution of the drag and lift coefficients, with a particularly high drag of up to $C_D = 0.16$ for the last deck segment D at positive angles of attack (full lines in Figure 5.5.1). The negative drag force experienced at $\alpha = -2°$, $-4°$ and $0°$, especially for deck A, might be caused by the flow re-attachment inside the gap region between the decks A and B, as it can be noticed in Figure 5.4.1 (g), (h), (i), and (j) as a high pressure acting on the inside wall of the gap preceding the deck A shows. Also the lift coefficient for the deck D had a broader variation when compared with the other three decks, from $C_L = -0.16$ for $\alpha = -4°$, to $C_L = 0.24$ for $\alpha = 4°$ (full lines in Figure 5.5.2 (b)). This is explained by the strong wind-induced suction distributed underneath the deck D, near the up-wind edge, as described in Figure 5.4.1 (h), phenomena which is not so obvious for other angles of attack. It is interesting to note that the overall drag and lift coefficients for the entire Megane deck sections, as well as for the connecting beams, maintained very low values of $C_D = 0.01$ to 0.02 and $C_L = -0.06$ to -0.002, in spite of the high variation recorded for some of the individual decks.

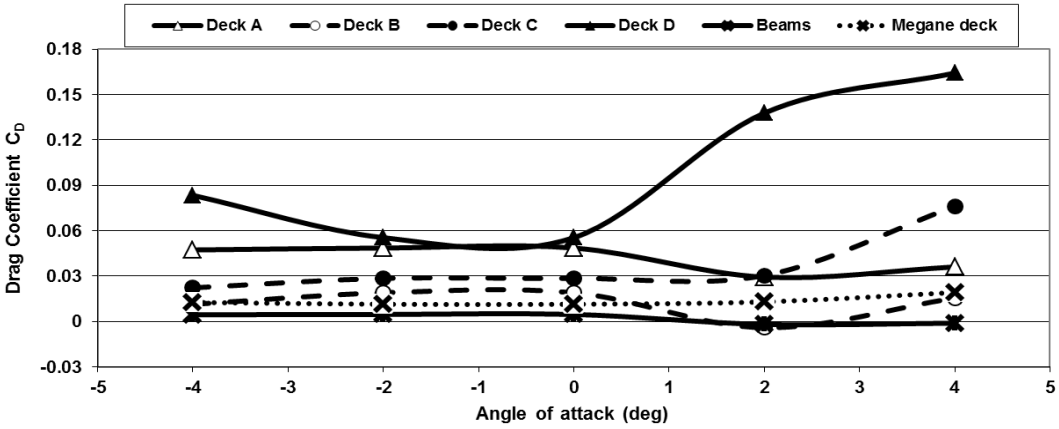

Figure 5.5.1 Drag coefficient for individual decks of the Megane Bridge

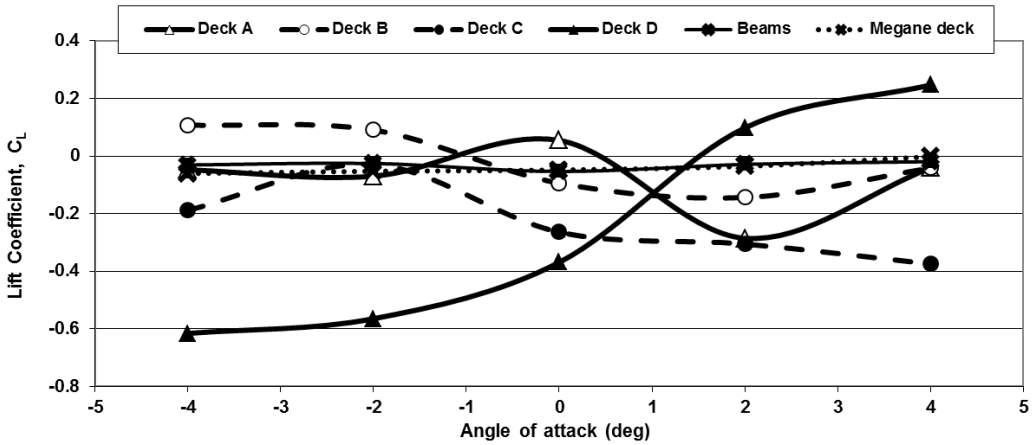

Figure 5.5.2 Lift coefficients for individual decks of the Megane Bridge

Chapter 6 Flutter Derivatives Extraction

6.1 Flutter derivatives

During the designing stage of a bridge, the aerodynamic stability verification of the flutter of the bridge deck is the most critical issue which needs to be considered. As explained in Chapter 2, various experimental an theoretical formulations have been employed for trying to determine the linear expressions for the aerodynamic drag, lift and moment forces. However, comparing to these earlier methods, which contain complex parameters, the linearized forms proposed by Scanalan and Simiu, 1996 [2] are widely accepted by wind engineers worldwide and has become the standard expressions for aerodynamic flutter forces per unit deck:

$$L_{ae} = \frac{1}{2}\rho U^2 B(KH_1^*\frac{\dot{h}}{U} + KH_2^*\frac{B\dot{\alpha}}{U} + K^2H_3^*\alpha + K^2H_4^*\frac{h}{B}) \tag{6.1}$$

$$M_{ae} = \frac{1}{2}\rho U^2 B^2(KA_1^*\frac{\dot{h}}{U} + KA_2^*\frac{B\dot{\alpha}}{U} + K^2A_3^*\alpha + K^2A_4^*\frac{h}{B}) \tag{6.2}$$

where the B is the deck width, ρ is the air density, U is the wind velocity and the coefficients H_i^* and A_i^* (i=1,2,3,4) are known as the Scanlan flutter derivatives. These terms are non-dimensional functions of reduced frequency K which are defined as:

$$K = \omega B/U \tag{6.3}$$

The adoption of flutter derivatives ensures the quantification of dynamic instability for bridge decks and also provides the unique formulations for aerodynamic forces regardless of the bridge deck section. The flutter derivatives can be interpreted as the relative changes of the system damping and stiffness with regards to the variation of the wind speed and, unlike the static aerodynamic coefficients, which can be obtained under static conditions, the flutter derivatives can be measured only if the body is in an oscillatory state [2]. However, the identification of flutter derivatives is quite complicated and Scanlan and Tomoko (1971) [16] introduced the methodology of extracting the flutter derivatives based on the exponentially decaying signals of the structural response of the bridge model. They used one-degree-freedom heaving and pitching elastic systems to obtain the “direct” flutter derivatives through wind tunnel testing. With these results, they conducted two-degree-freedom analysis with nearly coupled

frequencies, to extract the rest of the flutter derivatives. The natural frequencies and damping coefficients obtained for the wind-off test condition are required for using this approach. However, due to the complexity of the procedure the efficiency and the reliability of this flutter identification method is still debated, as already remarked by Sarkar (1994) [49].

6.2 Extraction of the flutter derivatives

Considering the 2-DOF bridge model subjected to aerodynamic forces, the equations of motion along the vertical and rotational directions can be expressed as [2]:

$$m_h\left(\ddot{h} + 2\zeta_h\omega_h\dot{h} + \omega_h^2 h\right) = L_h \tag{6.4}$$

$$I_\alpha(\ddot{\alpha} + 2\zeta_\alpha\omega_\alpha\dot{\alpha} + \omega_\alpha^2\alpha) = M_\alpha \tag{6.5}$$

where L_h and M_α are the aerodynamic force and moment working on the bridge deck. The equation can be rewritten into the matrix form, and as a result the normalized aeroelastic equation of motion of the bridge model can be obtained [5]:

$$\underline{I}\,\underline{\ddot{y}} + \underline{M^{-1}}\,\underline{C\dot{y}} + \underline{M^{-1}}\,\underline{Ky} = \underline{M^{-1}}\underline{F_{ae}} \tag{6.7}$$

Where I is the identity matrix, $\underline{I} = \begin{bmatrix}1 & 0\\ 0 & 1\end{bmatrix}$, $\underline{y} = \{h \quad \alpha\}^T$ represents the displacement along the vertical and rotational directions

$$\underline{M} = \begin{bmatrix}m_h & 0\\ 0 & I_\alpha\end{bmatrix} \qquad \underline{M}^{-1}\underline{C} = \begin{bmatrix}-2\zeta_h\omega_h & 0\\ 0 & -2\zeta_\alpha\omega_\alpha\end{bmatrix} \qquad \underline{M}^{-1}\underline{K} = \begin{bmatrix}-{\omega_h}^2 & 0\\ 0 & -{\omega_\alpha}^2\end{bmatrix} \tag{6.8}$$

For a 2-DOF system only lift and moment forces are considered, so these aerodynamic forces can be written as [5]

$$\underline{F_{ae}} = \begin{Bmatrix}L_h\\ M_\alpha\end{Bmatrix} = \begin{bmatrix}0.5\rho U^2 B & 0\\ 0 & 0.5\rho U^2 B^2\end{bmatrix}\begin{bmatrix}KH_1^*/U & KH_2^*B/U & K^2H_3^* & K^2H_4^*/B\\ KA_1^*/U & KA_2^*B/U & K^2A_3^* & K^2A_4^*/B\end{bmatrix}\{\dot{h}\ \ \dot{\alpha}\ \ h\ \ \alpha\}^T \tag{6.9}$$

Then moving the right hand side term to the left hand side of the equation 6.7, a modified free-vibration equations of motion is obtained:

$$\underline{\ddot{y}} + \underline{C^{eff}}\,\underline{\dot{y}} + \underline{K^{eff}}\,\underline{y} = 0 \tag{6.10}$$

where C^{eff} and K^{eff} are the system aeroelastically effective damping and stiffness matrices, respectively. Under zero wind speed condition, the effective damping and the stiffness are equal to the system mechanical damping and stiffness, respectively. For wind on conditions, the system damping can be separated into two parts, one is the system mechanical damping and the other one is the damping introduced by the aerodynamic forces, which is expressed in the form of flutter derivatives [50].

$$\underline{C^{eff}} = \begin{bmatrix} C_{11}^{mech} - \frac{\rho B^2 \omega_h}{2m} H_1^* & C_{12}^{mech} - \frac{\rho B^3 \omega_\alpha}{2m} H_2^* \\ C_{21}^{mech} - \frac{\rho B^3 \omega_h}{2I} A_1^* & C_{22}^{mech} - \frac{\rho B^4 \omega_\alpha}{2I} A_2^* \end{bmatrix},$$

$$\underline{K^{eff}} = \begin{bmatrix} K_{11}^{mech} - \frac{\rho B^2 {\omega_h}^2}{2m} H_4^* & K_{12}^{mech} - \frac{\rho B^3 {\omega_\alpha}^2}{2m} H_3^* \\ K_{21}^{mech} - \frac{\rho B^3 {\omega_h}^2}{2I} A_4^* & K_{22}^{mech} - \frac{\rho B^4 {\omega_\alpha}^2}{2I} A_3^* \end{bmatrix}, \tag{6.11}$$

All these parameters of the model can be determined through the free vibration tests. Two column vectors are created for reconstructing the C^{eff} and K^{eff}.

$$X = [h\,, \alpha\,, \dot{h}\,, \dot{\alpha}]^T$$

$$\dot{X} = [\dot{h}\,, \dot{\alpha}\,, \ddot{h}\,, \ddot{\alpha}]^T \tag{6.12}$$

A discrete time state space representation of a two-degree-of freedom free vibrating system is given as [5]:

$$X = A\dot{X}$$

$$A = \begin{bmatrix} 0 & I \\ -K^{eff} & -C^{eff} \end{bmatrix} \tag{6.13}$$

The matrix A has the dimension of $2m \times 2m$, where m is the number of degrees of freedom. By reconstructing the C^{eff} and K^{eff} matrices based on the results obtained from each

wind speed testing case, the flutter derivatives can be calculated from the difference between these parameters at the tested wind speed, to those obtained in the wind-off condition:

$$H_1^*(K) = -\frac{2m}{\rho B^2 \omega_h}\left(C_{11}^{eff} - C_{11}^{mech}\right)$$

$$H_2^*(K) = -\frac{2m}{\rho B^3 \omega_\alpha}\left(C_{12}^{eff} - C_{12}^{mech}\right)$$

$$H_3^*(K) = -\frac{2m}{\rho B^3 \omega_\alpha^2}\left(K_{12}^{eff} - K_{12}^{mech}\right)$$

$$H_4^*(K) = -\frac{2m}{\rho B^2 \omega_h^2}\left(K_{11}^{eff} - K_{11}^{mech}\right)$$

$$A_1^*(K) = -\frac{2I}{\rho B^3 \omega_h}\left(C_{21}^{eff} - C_{21}^{mech}\right)$$

$$A_2^*(K) = -\frac{2I}{\rho B^4 \omega_\alpha}\left(C_{22}^{eff} - C_{22}^{mech}\right)$$

$$A_3^*(K) = -\frac{2I}{\rho B^4 \omega_\alpha^2}\left(K_{22}^{eff} - K_{22}^{mech}\right)$$

$$A_4^*(K) = -\frac{2I}{\rho B^3 \omega_h^2}\left(K_{21}^{eff} - K_{21}^{mech}\right) \tag{6.14}$$

where $K = B\omega/U$ in the non-dimensional reduced frequency; U is the mean flow speed, ω_α and ω_h is the circular frequency of the oscillation with respect to the vertical motion and the torsional motion, m and I are the mass and mass moment of inertia of the model, per unit length. It is obvious that the flutter derivatives can be easily extracted once the system stiffness and the damping matrices are determined for both wind-off and wind-on experimental cases. In general, the unknown parameters of a system can be identified by applying various system identification methods, according to its output which is obtained through experimental means. However, due to a) a large size of the structure, as well as the complexity of creating an accurate mathematical model, b) limitations of the measured output data, which may contain high level of noise, especially when wind or earthquake forces are involved 3) for a damaged system the

behaviour of the structure may become highly nonlinear [51], not all the system identification methods are applicable to many structural dynamics problem.

Various time-domain approaches have been developed for identifying both direct and cross-flutter derivatives, from coupled free vibration time displacement history data, such as ITD (Ibrahim Time Domain), MITD (Modified Ibrahim Time Domain), ULS (Unifying Least Squares) and WELS (Weighting ensemble least-square method). However, regardless of the method applied, they all require the operation with complex numbers and the involvement of many initial assumptions which becomes relatively important for the success of the extraction method. Sarkar and Chowdhury, 2003 [5] proposed a system identification method entitled the Iterative Least Squares (ILS) which can extract 18 flutter derivatives from a 3-DOF structural system under oscillatory motion induced by wind. This approach has the following advantages: (1) one computer program is capable of extracting flutter derivatives for different DOF cases; (2) system stiffness and damping matrix can be obtained directly by using the free-vibration displacement time histories, instead of the calculation of the eigenvalue and eigenvectors. (3) the accuracy of the identification method has been validated numerically and experimentally [5] .

6.3 Iterative least squares method

The displacement time history plotted through the output data needs to be modified before applying any system identification method. According to the description of the ILS method, the first step is the elimination of the noise interferences from the obtained data, to generate modified time displacement histories, which could be used in ILS method. A low-pass digital 'Butterworth' filter was applied for this purpose. In order to determine the cut-off frequencies for the Butterworth filter, Fast Fourier transform was performed for the noise data, to reveal the possible predominant frequencies for each wind speed case as well as for the wind-off case; from this analysis the upper and lower values for the cut-off frequency were selected. For torsional motion, due to the property of the coupled flutter, the upper bound for cut-off frequencies is slightly higher than the natural frequency, at minimum wind speed of 3 m/s and the lower bound is slightly lower than the minimum natural frequency at maximum wind speed of 13 m/s. On the contrary, for the vertical motion the principle for choosing the cut-off

frequency was the reversed situation of the above. Specific values for each attack angle cases are presented in the Table 6-1.

Table 6-1 Cut-off frequency for each wind speed cases

Cut-off Frequency	Attack Angle ( )													
	0		-2		2		-4		4		-6		-8	
Lower bound (Hz)	1.7	2.1	1.6	2.2	1.7	2.2	1.6	2.2	1.6	2.3	1.7	2.3	1.6	2.4
Upper bounder (Hz)	2.3	2.7	2.3	2.8	2.3	2.8	2.3	2.7	2	2.8	2.4	2.8	2.5	2.8

It was found that the low-pass filter can effectively remove the noisy high frequencies and spurious modes from the response. However, some changes in the amplitude of the frequency response may be induced (Figure 6.3.1). The magnitude of the vertical frequency at the maximum wind speed of 13 m/s decreased from 0.12 to 0.1, this small discrepancy is within the tolerance and accurate identification of our system parameters which may be slightly affected. Once the filtered time displacement histories were obtained, the Matlab finite difference formulation was applied to generate velocity and acceleration time histories. After that, the "windowing" operation was used to minimize the filter and finite difference effect to the data by taking only the middle part of the three time histories for the construction of matrix A.

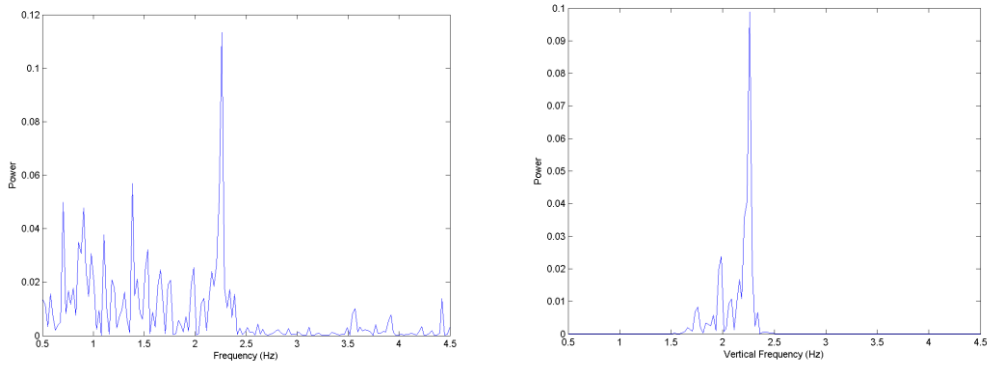

Figure 6.3.1 FFT before and after applying "Butterworth" filter

A Matlab code was developed for the algorithm for the ILS approach (Figure 6.3.2) as presented in the report of Sarkar and Chowdhury, 2003 [5]

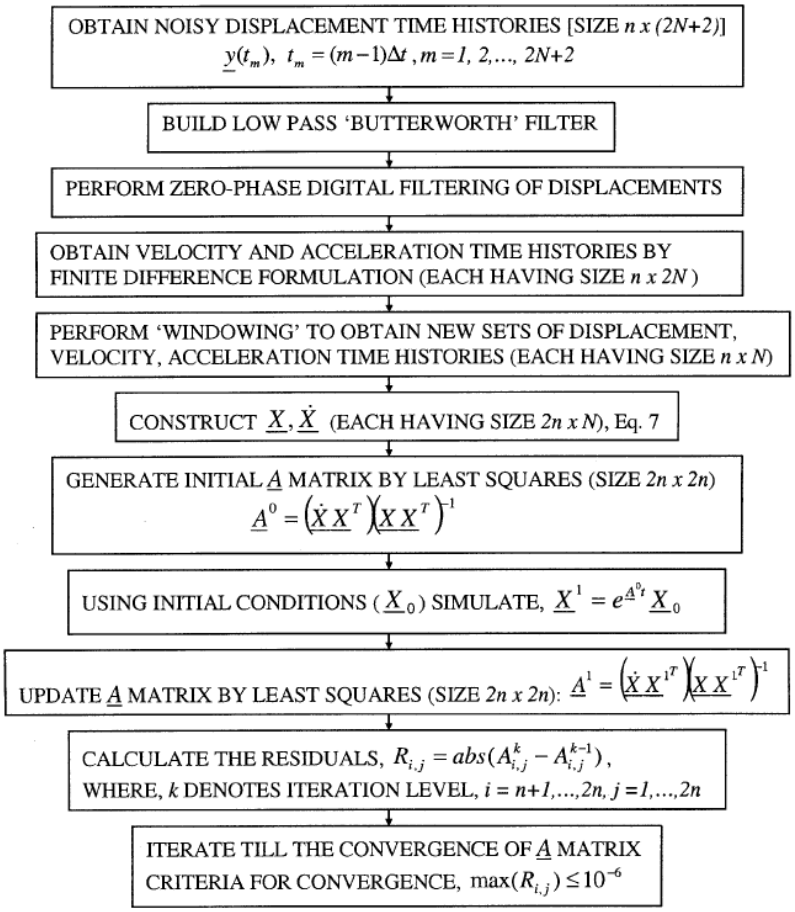

Figure 6.3.2 Algorithm for ILS used of the Matlab code

After obtaining the system stiffness and the damping for the attack angle of $0°$ from minimum wind speed to the maximum wind speed, the flutter derivatives were calculated based on equations (6.14).

6.4 Comparison of the Flutter Derivatives

6.4.1 Comparison of the Theodorsen thin plate with Megane Bridge deck section

As an alternative to using the complicated system ILS identification method, an approximate prediction of the flutter derivatives can be made, according to Theodorsen thin plate theory [2]. Theodorsen first presented the theoretical formulation for modelling the flutter forces acting on a two-dimensional airfoil (wing) section, in the incompressible potential flow [11].

Thus, the theoretical expression for flutter derivatives expressed in terms of the Theodorsen function can be extracted by matching the aerodynamic force terms in Theodorsen expressions, with those from Scanlan formulas. The flutter derivatives expressions obtained by this direct comparison are as follow:

$$KH_1^* = -2\pi F \qquad KH_2^* = -\frac{\pi}{2}\left(1 + F + \frac{4G}{K}\right)$$

$$K^2H_3^* = -\pi\left(2F - \frac{GK}{2}\right) \qquad K^2H_4^* = \frac{\pi}{2}(1 + \frac{4G}{K})$$

$$KA_1^* = \frac{\pi F}{2} \qquad KA_2^* = -\frac{\pi}{2}\left(\frac{1}{4} - \frac{G}{K} + \frac{F}{4}\right)$$

$$K^2A_3^* = \frac{\pi}{2}\left(\frac{K^2}{32} + F - \frac{GK}{4}\right) \qquad K^2A_4^* = -\frac{\pi}{2}(KG) \tag{6.15}$$

where F(K) and G(K) are the real and the imaginary parts of the Theodorsen functions C(K), respectively. The comparisons between the theoretical and the experimental values have been made before by Scanlan [2]. The results revealed a good agreement for an airfoil or a streamlined cross section. However, when it comes to bluff bodies like bridge deck sections, the expressions did not present very accurate results, but still could give a prediction for some of the flutter derivatives. For the Megane Bridge deck section investigated in the current research, the same comparison has been made to find out both similarities and discrepancies of the multi-deck section, to thin plate or streamlined section, from the aerodynamic point of view; the approximate formulations of F (K) and G (K) were adopted in this study which were presented by Fung [14].

$$C(K) = F(K) + iG(K)$$

$$F(K) = 1 - \frac{0.165}{1 + \left(\frac{0.0455}{K}\right)^2} - \frac{0.335}{1 + (\frac{0.3}{K})^2}$$

$$G(K) = -\frac{\frac{0.165 \times 0.0455}{K}}{1 + \left(\frac{0.0445}{K}\right)^2} - \frac{\frac{0.335 \times 0.3}{K}}{1 + (\frac{0.3}{K})^2}$$

(6.16)

where $K = B \cdot \omega / U$ is the reduced frequency, B is the width of the thin plate, ω is the natural frequency of the motion.

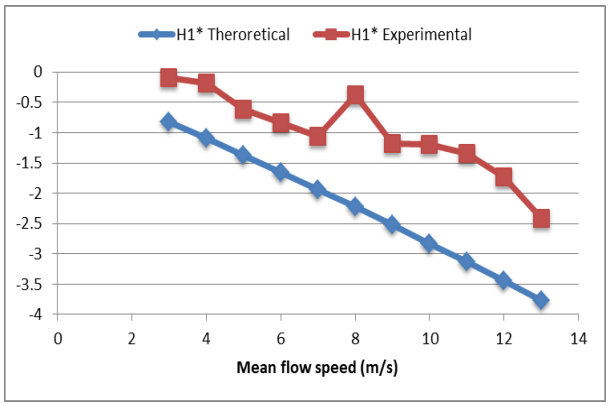

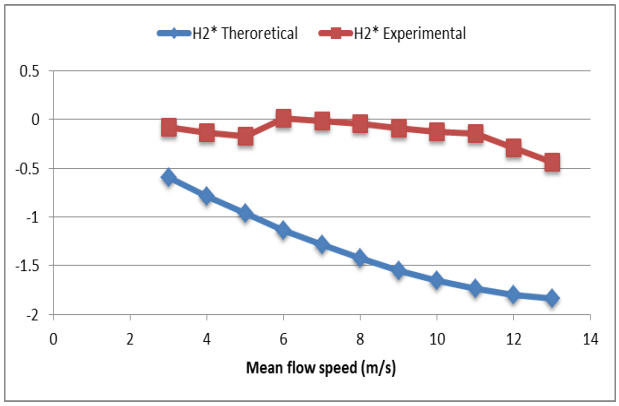

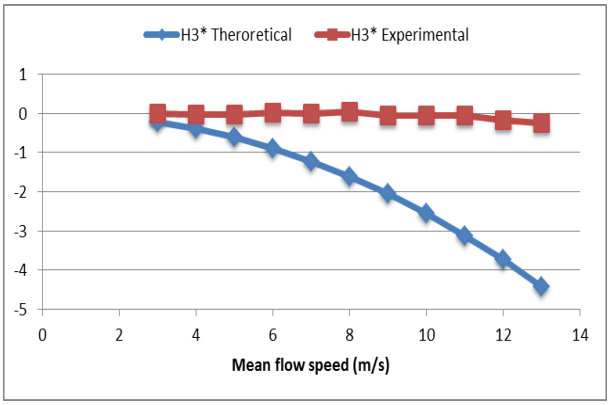

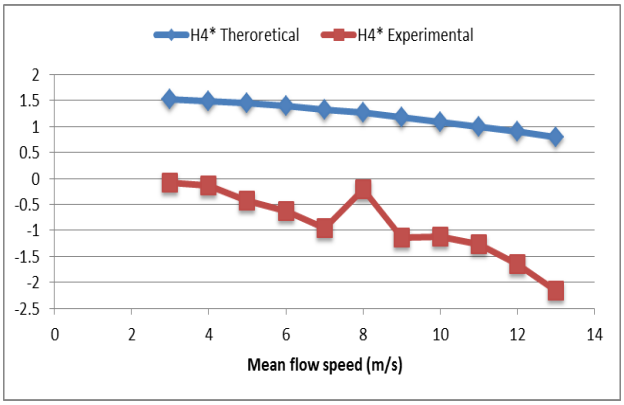

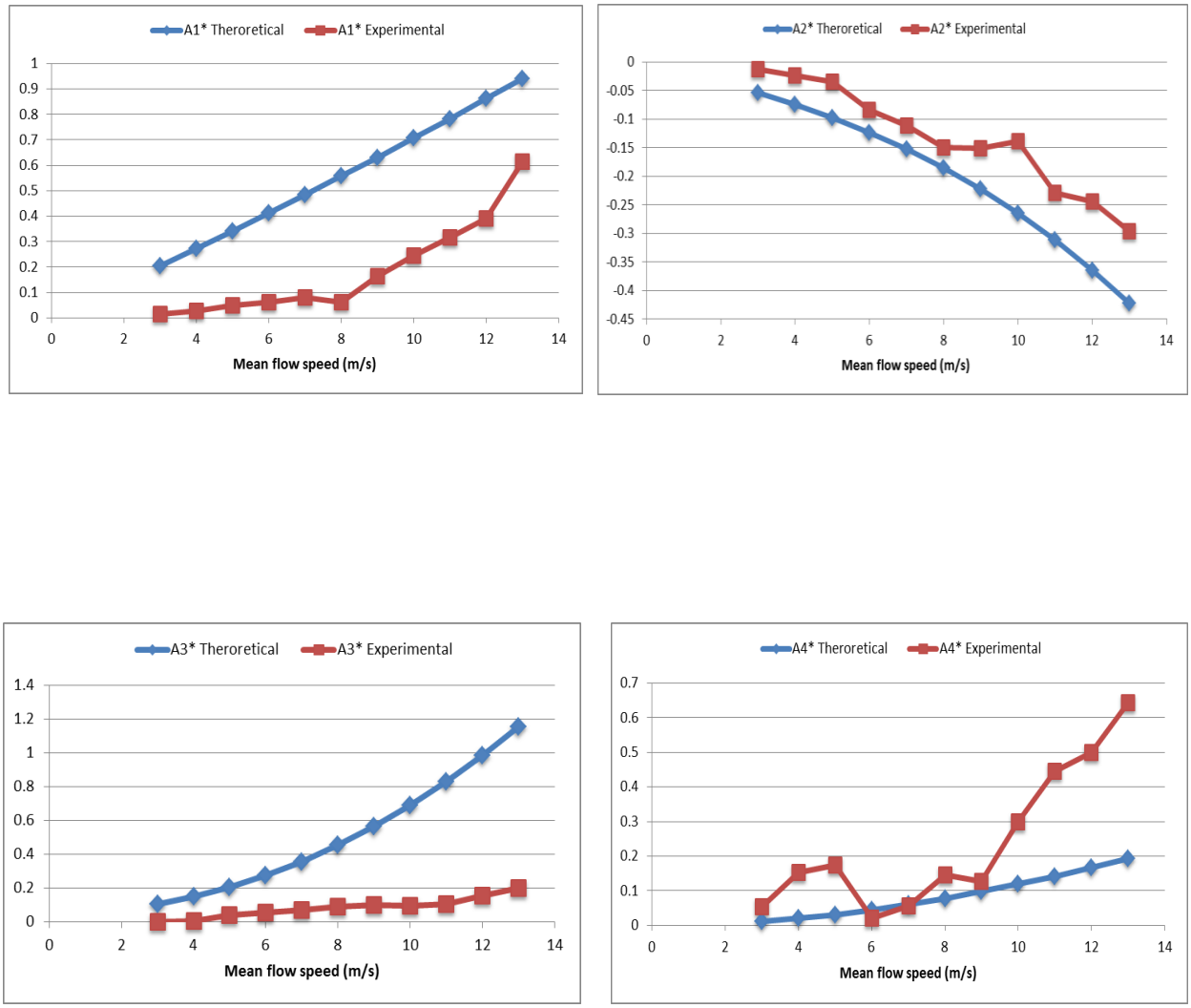

Figure 6.4.1 The experimentally extracted flutter derivatives vs. the theoretical thin plate results

As it can be seen from the Figure 6.4.1 almost all the flutter derivatives extracted from the ILS method applied to the experimental results obtained for the Megane Bridge deck for $\alpha = 0^{\circ}$, present similar trends with the Theodorsen's theoretical results obtained for the thin plate section, except for the flutter derivative A4*. Besides A2* and A4*, the magnitudes of the rest of the flutter derivatives based on the Theodorsen's theoretical functions are all higher than those obtained from the experiments, especially for the high wind speed range. One thing needs to be mentioned is that generally speaking the flutter derivatives should be close to 0 at the low wind speeds. However, for the case of H4* the theoretical value started from 1.5, decreasing along with the wind speed and was considered as the proof that the Theodorsen theory is not applicable in identifying flutter derivative of H4* for a multi-deck bridge section. Despite these discrepancies, the potential similarity in aerodynamic properties between the Megane deck and a

streamlined section has been confirmed, by the general trends of the theoretical and experimental flutter derivatives which are in agreement.

6.4.2 Comparison of the Megane Bridge Section with Other Deck Sections

In order to evaluate the aerodynamic properties of the Megane Bridge deck section, it is also necessary to compare the identified eight flutter derivatives with the results reported for other bridge decks of similar configuration. . Only six flutter derivatives are considered for the comparison, due to the discrepancies between the experimental and the theoretical results. In addition, according to the original work of Scanlan and Tomoko, 1971 [16] it is confirmed that that the errors that occur for the flutter derivatives of H_4^* and A_4^* do not affect significantly the overall flutter behaviour of the bridge ; moreover, most of the engineering reports contain only the first six flutter derivatives. For the purpose of comparison, a modification has been made for the ILS identified results by changing the x axis, which relates to the wind tunnel wind speed to the reduced wind speed. Reduced wind speed is the tool to normalize the flutter derivatives extracted from different wind tunnel tests, for various types of bridge decks and it can be expressed as [16]:

$$U_{red} = U/(B \cdot f) \tag{6.17}$$

where U is the mean wind speed, B is the width of the bridge deck and f is the vibration frequency of the system. Flutter derivatives of Höga Kusten Bridge single box deck (XU [52]), Stonecutters Bridge, twin-box deck (Larose, et al [24]) as well as the Strait of Messina Bridge, multi-box deck (XU [52]), are collected and the results are presented below.

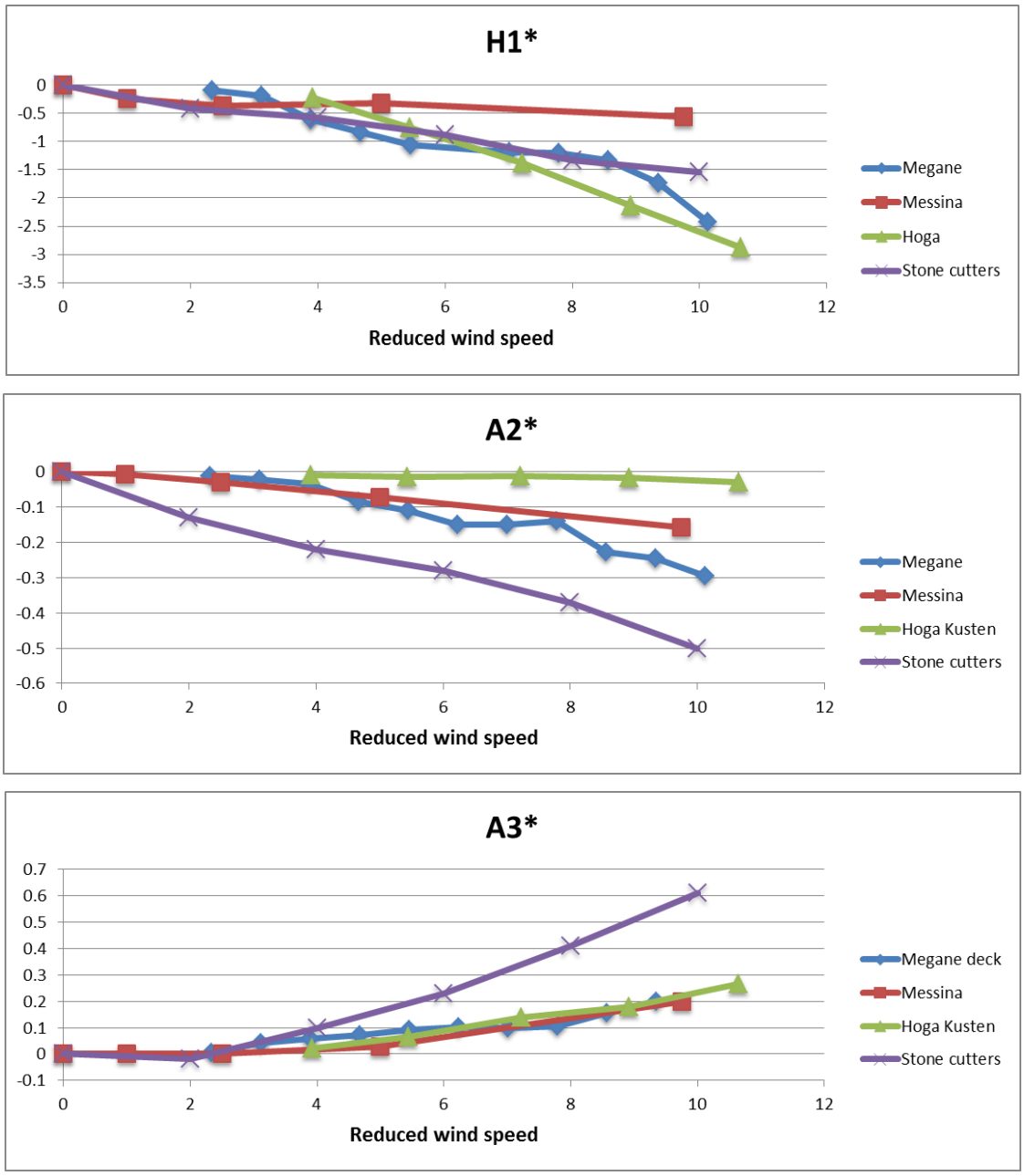

Figure 6.4.2 Direct flutter derivatives comparison between four bridge decks

The calculated minimum and maximum reduced wind speed for the Megane Bridge aerodynamic testing were Ur = 2.3 and 10.2 respectively. Since the magnitudes of the flutter derivatives below can't be determined in this study, the comparison was made only within this wind speed range.

H_1^* is one of the three direct flutter derivative terms which relates to the aerodynamic damping in the vertical mode and generally for most of the deck sections types, the H_1^* values are negative, which indicates a positive aerodynamic damping. The negative values are also observed for the Megane Bridge deck section starting from -0.088 and up to -2.42 (Fig. 6.4.2), which is close to with those of the Stonecutters Bridge. The A_2^* flutter derivative signifies the dimensionless aerodynamic damping term in torsion and the negative values of A_2^* imply positive aerodynamic damping acting for the torsional vibration. From the comparison results of A_2^* presented in Figure 6.4.2, it is found that for the wind attack angle of 0°, the aerodynamic behaviour with respect to the torsional motion for the Megane and Messina Strait Bridge decks, are quite similar. Unlike the flutter derivative H_1^*, the curve of A_2^* matches well with the one of the Messina Strait Bridge even in the high wind speed range. The last direct flutter derivative A_3^* signifies the dimensionless aerodynamic stiffness term, which relates to the decrease of the effective stiffness in motion. The comparison results are demonstrated in the Figure 6.4.2 and once again the plotted A_3^* of the Megane Bridge having a maximum value around 0.2, coincides with the other two bridge types which are the Messina Strain Bridge and the Hoga Kusten Bridge.

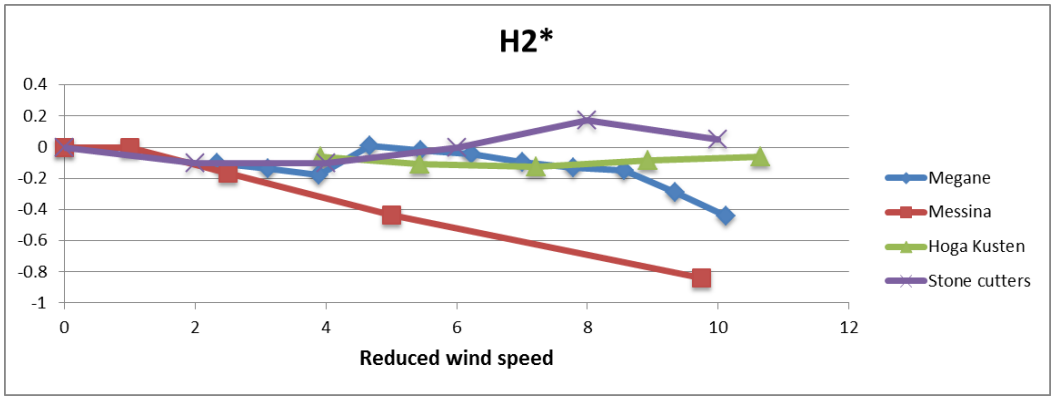

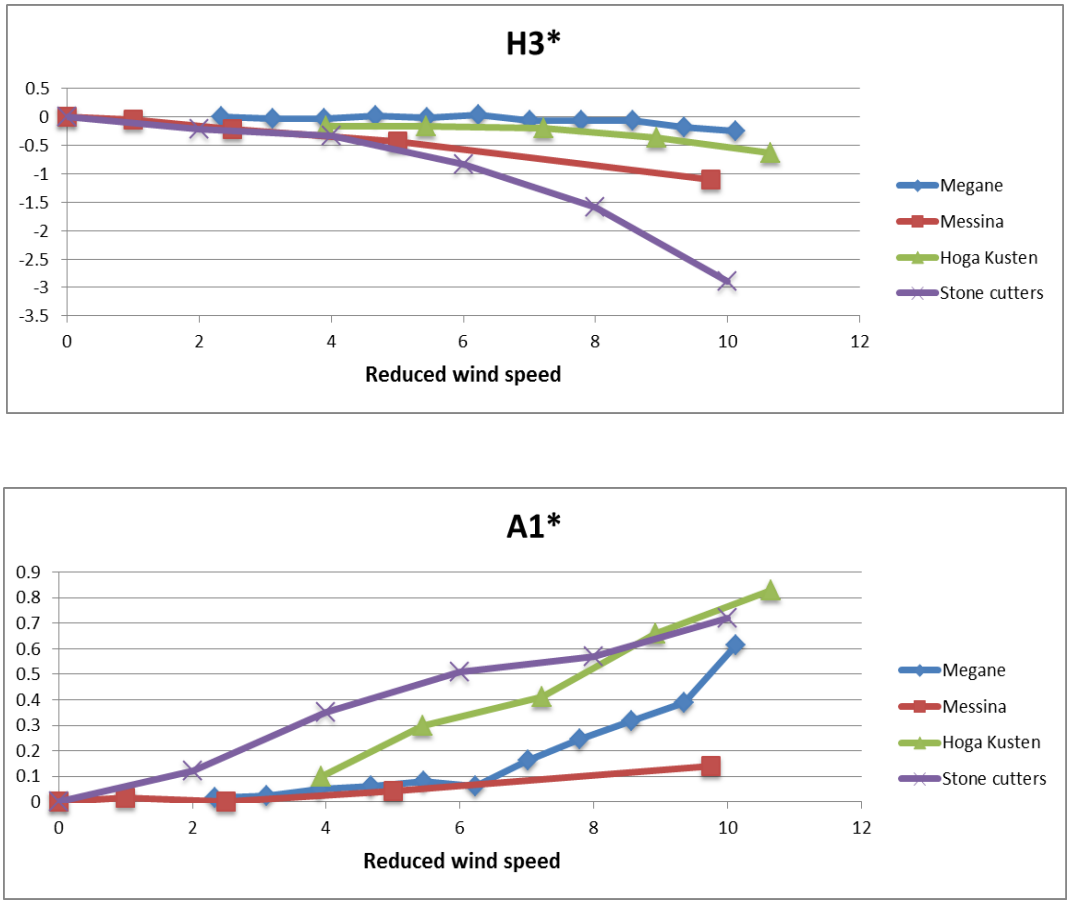

Figure 6.4.3 Cross flutter derivatives comparison between four bridge decks

As mentioned earlier, direct flutter derivatives can be obtained through the 1-DOF vibration however, the identification of the cross-flutter terms requires coupled motion vibration. Therefore, the obtained values through system identification displayed more discrepancies with the Messina Strain Bridge. The comparison of the dimensionless H_2^* related to the torsional damping in the coupled motion is shown in Figure 6.4.3. The trend starts from -0.01 and moves closely to the values reported for Messina Strait Bridge deck, then it deviates towards the curve reported for the Hoga Kusten Bridge deck, with the increasing wind speed; finally this ends at values between the Stonecutters and the Messina Bridge decks. It is interesting to notice that, the other dimensionless cross-flutter derivative term H_3^*, corresponding to the lift force contribution from the torsional displacement presents the smallest values among other three bridge deck types for the entire wind speeds range investigated. The trend of H_3^* follows none of the results reported for the Messina Strait deck, nor those of the Stonecutters Bridge deck, which may be

because of the error introduced from the procedure of system identification, as well as the experimental data. The comparison of the third dimensionless cross-flutter derivative A_1^* is shown in Figure 6.4.3. The curve of Megane Bridge deck locates between Stonecutters and Messina Bridge decks, with the values of 0.0158 at minimum reduced speed of 2.34 and 0.6132 at the maximum reduced wind speed of 10.12. The best consistency between the two multi-box decks of Megane and Messina is spotted from reduced wind speeds of 2.3 to 5.5, followed by a sudden increase approaching to the Stonecutters bridge twin-deck, for reduced wind speeds of 6.23. Overall, except for the H_3^*, the values of the flutter derivatives are located between the Messina Strait Bridge and the Stonecutters Bridge decks indicating a promising aerodynamic property for this new generation multi-box type of bridge decks.

6.5 Critical flutter velocity model and prototype prediction

A bridge deck starts vibrating due to the external wind load but the motion will be damped with time, especially for low wind speed region. With increasing wind speeds, the input energy from the wind flow gradually becomes larger than the energy lost through the bridge system mechanical damping. The point where the effective damping, represented by the difference between the mechanical and aerodynamic damping, equals to zero the oscillating motion starts diverging and this phenomenon is called the critical flutter condition while the wind speed where this occurs is called the critical flutter velocity [16]. Serberg [53] introduced a simplified empirical expression for estimating the critical flutter velocity. However, this equation is based on the thin plate theory and is not applicable to the bridge deck sections; therefore it cannot be used for the Megane Bridge deck section currently investigated. An alternative way of estimating the critical flutter velocity is to take the lowest velocity where the coupled flutter occurs in experiments [7]. Based on the FFT results presented in Chapter 4, the vertical frequency coupled with the torsional frequency at 2.26 Hz for the wind speed of 13 m/s for the case of 0° attack angle. Thus, the critical coupled flutter wind speed can be calculated based on the reduced wind speed similarity mentioned by Scanlan [2]:

$$\left(\frac{U_{cr}}{Bf}\right)_m = \left(\frac{U_{cr}}{Bf}\right)_p \tag{6.18}$$

The most important aerodynamic characteristic is the flutter instability, which can be characterized by simply stipulating the aspect of critical flutter speed which must be respected in the bridge design process. However, since the frequency of the prototype has not been finalized yet, a series of predictions for the critical flutter velocity has been considered with respect to frequencies from 0.1 Hz to 0.5 Hz (Table 6-2). The Megane Bridge deck with no further modification, such as a stabilizer, wind shields, or slots can sustain a critical wind speed of 62.8 m/s (Table 6-2) which is slightly higher than the design wind speed reported for the Messina Bridge deck (60 m/s) [54]. However, when the vertical frequency reaches 0.2 Hz, the critical flutter wind speed is about 125 m/s which is much larger than the Great Belt flutter wind speed, which is 74 m/s [55]. Thus the potential advantage of using the new multi-deck configuration has been confirmed, by showing that the flutter aerodynamic instability of such decks will be encountered however this will occur for wind speeds much higher than the standard bridge girder decks.

Table 6-2 Prediction of the critical flutter velocity

Model Width	Prototype Width	Vertical Frequency (Hz)	0.1	0.2	0.3	0.4	0.5
0.775 m	62 m	Critical Wind speed (m/s)	62.8	125.6	188.4	251.2	314.0

Chapter 7 Conclusion and recommendations

7.1 Conclusions

The rapid growth of the tendency to build suspension bridges with very long spans much higher than the maximum length currently used of 2,000 m (Akashi Bridge), caused the evolution of geometric shapes of the bridge decks, in order to fulfill the requirements of aerodynamic stability. Numerous studies have been conducted to analyze the aerodynamic behaviour of the twin-deck and the three-deck configurations, and these indicated a better aerodynamic performance than the traditional bridge girder decks. The latest development was recorded with the success of the three-deck Messina Bridge and this pointed toward proposing a new bridge multi-deck consisting of four separated decks for the Megane Bridge. Experimental and numerical studies were carried out for determining the aerodynamic properties of the Megane Bridge deck and these are summarised in the current paper.

Both static and free vibration wind tunnel testing were conducted in the Carleton closed-circuit ABL wind tunnel facility. Since the wind tunnel was not designed for bridge testing, various modifications were performed before carrying out the tests. Despite of the adaptations, a number of issues associated with the limitations of the facility testing conditions, such as the minimum test wind speed, the support of the model outside the wind tunnel, the orientation of the laser sensors, were noticed during the experiment set-up and during the operations. Several assumptions or elimination of data have been made for overcoming the issues and the factors which might have affected the testing results were individually explained when the experimental setup was introduced in Chapter 3.

The static tests results demonstrated that a variation of the static aerodynamic force coefficients occur due to the angles of attack and wind speeds. It is clear that both drag and lift coefficients show Reynolds number dependency for the low test wind speed range. However, with the increasing wind speed the static drag and lift force coefficients are no longer influenced by the Reynolds number and yielded relatively small values. Galloping possibility check for each wind speed case indicated that the Megane Bridge deck model is safe for galloping instability,

despite some negative values of the Den Hartog criterion found for wind speeds of 3 m/s, which is considered to be caused by the errors induced through the limitations of the data acquisition system. The effects brought by the change of the wind angle of attack on the bridge vertical and torsional responses have been confirmed from the results of the static and dynamic testing. In order to achieve the same vibration magnitude, the wind speed the bridge deck required under larger attack angles is much lower than those under smaller attack angles. On the other hand, for the same magnitude of the attack angle, the bridge deck model under negative attack angle senarios is more vulnerable and more likely to experience larger vibrations. This is also proven through the FFT analysis performed for the vertical and torsional displacement time histories. Instead of the pure torsional flutter, which was the case of the Tacoma Narrow Bridge collapse, the Megane Bridge deck section model like other streamlined sections exhibit the coupled-mode flutter. The predominant vertical frequency increases with the aerodynamic stiffness, while the torsional frequency decreases due to the increasing of the aerodynamic damping for all wind speed and attack angles cases investigated. Except for the case of $\alpha = -2^{\circ}$, the frequency pattern seems more complicated and the predominant vertical frequency showed no significant difference between the maximum wind speed and the lowest wind speed. The coupling between the two vibration modes is mostly caused by the drop of the torsional frequency only, while the vertical frequency maintains a stable trend. Due to the geometric characteristics of the model and also due to the testing facility, the maximum test wind speed varied from case to case which introduced some differences in estimating the wind speed required for the coupled-flutter occurrence.

The three-dimensional LES-CFD numerical analysis was verified by comparing the averaged static coefficients results with those obtained from the static tests for the Megane Bridge deck. The lift coefficients showed good agreement between the CFD simulations and the experimental ones, which indicated the use of appropriate modelling assumptions in CFD. However, the aerodynamic drag coefficients determined through the wind tunnel experiment for the Megane deck, were higher than those obtained from the CFD simulations, which was considered as the contribution of the drag forces introduced by the size of the two foam endplates installed at the extremities of the tested deck model. The averaged aerodynamic coefficients for the Megane multi-box deck section obtained from the numerical calculations and experimental

data manifested similar evolutions, when compared with the results from the experiments performed for the Messina Bridge three-decks section [Nieto et al, 2008] and the Stonecutters Bridge twind-deck section [Larose et al, 2006]. On the other hand, the model used for Messina Bridge had windshields and stabilizers installed, while the Megane deck model did not have any windshields or extended stabilizers to mitigate the aerodynamic instabilities.

From the flow pattern simulation through the LES model, the traffic and railway individual decks, behave differently under the effect of wind flow, thus the aerodynamic forces coefficients registered variations from one deck to another, the most affected being the last traffic deck D. However, the static aerodynamic forces measured in the wind tunnel experiment, for the entire model, cannot capture such variations for the Megane Bridge individual decks. This might become of great concern especially when considering the fact that the vortex shedding and turbulent flow formations are dominant only for one of the decks, usually the last deck in the arrangement (traffic deck D here). Indeed the three-dimensional LES-CFD investigations provided detailed information regarding the pressure and vorticity contours and offered a visual confirmation of the flow characteristics in the vicinity of the deck. For most of the Re numbers and angles of attack analyzed in the current study, the traffic deck D has shown a predisposition of generating longitudinal vortices and turbulent flow formations on both the upper and lower surfaces of the deck, more significant for negative angles of attack, because of the flow coming upwards through the last gap between the decks C and D. A localized split-flow phenomenon occurred for $\alpha = 2°$ and $-2°$ when a longitudinal turbulent flow shedding from deck C towards deck D was noticed, only on one side of the Megane deck.

In general, the prediction of the aerodynamic stability of the bridge deck is based on the estimation of the flutter derivatives. Eight flutter derivatives were identified from the free vibration time displacement histories of a two-degree of freedom system under zero degree angle of attack. The ILS identification method for flutter derivatives was selected among various methods due to the convenience in identifying system parameters without dealing with complex numbers and because of fewer requirements for data processing and filtering. The comparison between the Megane deck section and the thin plate confirms that the aerodynamic behaviour of the Megane section is similar to the streamlined sections, despite the discrepancy regarding the maximum and minimum values. Flutter derivatives reported for the Messina, Stonecutters and

Hoga Kusten Bridge decks were adopted as reference values and were compared together with those obtained for the Megane deck section model. As expected, the direct-flutter terms showed close resemblances with the values of the Messina Bridge, except for the H_1^* flutter derivative which deviated from the Messina Bridge deck but more close to the Stonecutters bridge deck. On the other hand, for the cross-flutter derivatives, more discrepancies with the referenced values were observed, which indicates the unique aerodynamic properties of the Megane multi-deck section.

From the results of the data analysis, it is believed that the extracted flutter derivatives can be used for the prediction of the aerodynamic stability of the Megane Bridge deck and it is proven the possibility of measuring and extracting the flutter derivatives for multi-deck sections. However, the accurate identification of the system parameters using noise-contained data is challenging. The unavoidable presence of errors during the measurements, due to the experiment condition affected the results of flutter derivatives extracted based on the ILS method. Besides, a series of critical flutter wind speeds have been predicted for different natural frequencies of the Megane Bridge deck prototype and promising results demonstrated the good applicability of this new deck configuration for better aerodynamic stability of long span bridges.

7.2 Recommendations and Future work

For future studies that might be conducted with regards to the topic of experimental tests, it is recommended that:

- For the static tests, the data acquisition system plays a very important role in the experiments. More accurate data acquisition needs to be employed for future investigations of the Megane deck section model with wind shield and stabilizers installed.
- The spring suspending system requires modifications due to the total stiffness of the spring which is slightly higher than required, restricting the flexibility of the vibration response of the bridge deck section model. As mentioned above, the wind tunnel facility at Carleton University is not designed for the bridge deck experiments like this and for the purpose of testing the Megane model the Plexiglas window was replaced by wooden

plates. However, the wind flow condition can be affected by the hole on the wooden plate, allowing the steel bar reaching out of the test section to move and to affect the data measurements.

- Since during the test, the initial conditions for each testing case were manually applied, the parametric estimation, especially of the mechanical damping, through the system identification method may affected by this issue. Therefore, an improved release system which can allow the same amount of vertical displacement for all the experiments should be employed for this purpose.

Future investigations need to be conducted to enhance the understanding regarding to the aerodynamics behaviour of the Megane Bridge deck section model:

- Since the natural wind flow is mostly turbulent, the analysis for the effects of turbulence to the bridge response is necessary.
- The function of the stabilizers and wind shields which are commonly installed on the bridge, to increase the aerodynamic stability needs to be studied.
- Systematic investigation of errors related to the extraction of the flutter derivatives and comparison between different system identification could be conducted.

References

[1] Norbert J. Delatte, *Beyond Failure: Forensic Case Studies for Civil Engineers.* ASCE Press, 2009

[2] E. Simiu, R.H. Scanlan, *Wind Effects on Structures: fundamentals and applications to design, 3rd Edition*. John Wiley & Sons, Inc. Canada, 1996.

[3] Y.J. Ge, H.F. Xiang, 2009, "Aerodynamic Challenges of Major Chinese Bridges." IABSE Symposium Report, IABSE Workshop, Shanghai 2009, pp. 142-164(23).

[4] G.L. Larose[a], A. Damsgaard[a], G. Diana[b] and M. Falco[b], "Wind tunnel investigations of the tower for the Stretto di Messina Bridge," Journal of Wind Engineering and Industrial Aerodynamics 48 (1993) 379-393

[5] Arindam Gan Chowdhury, Partha P. Sarkar. "A new technique for identification of eighteen flutter derivatives using a three-degree-of-freedom section model," Engineering Structures Volume 2, December 2003, Issue 14, Pages 1763–1772.

[6] R. Wille, "Kármán Vortex Streets," Advances in Applied Mechanics Volume 6, 1960, Pages 273–287.

[7] Emil Simiu and Toshio Miyata. 2006. *Design of Buildings and Bridges for Wind: A Practical Guide for ASCE-7 Standard Users and Designers of Special Structures*. New York: John Wiley & Sons Inc, 2006.

[8] Blevins R. D, *Flow Induced Vibrations*. Van Nostrand Reinhold Co, 1990.

[9] W.F , Lian Duan, *Bridge Engineering Handbook.* CRC Press; 1 edition, 1990.

[10] A.L.Braun, A.M. Awruch, "Numerical Simulation of the Wind Action on a Long-Span Bridge Deck," J. of the Braz. Soc. of Mech. Sci. & Eng. October- December 2003, Vol. XXV.

[11] T. Theodorsen, "General theory of aerodynamic instability and the mechanism of flutter," National Advisory Committee for Aeronautics (NACA), Washington, D. C., 1934, Technical Report No. 496, pp. 413-433, 1935.

[12] Larsen, A., October 1993, "Aerodynamic aspects of the final design of the 1624m suspension bridge across the Great Belt," Wind Engineering and Industrial Aerodynamics, Vol. 48, Issue 2-3, pp. 261-285, 1993.

[13] J. A. Jurado, S. Hernandez, F. Nieto, A. Mosquera, *Bridge Aeroelasticity: Sensitivity Analysis and Optimum Design.* WIT Press / Computational Mechanics, 2011.

[14] Yuan-Cheng Fung, *An Introduction to the Theory of Aeroelasticity*. John Wiley & Sons, 1955 edition.

[15] Bleich F., "Dynamic Instability of Truss-Stiffened Suspension Bridges Under Wind Action," Proceedings ASCE, Vol 75, No 8. 1948.

[16] R.H. Scanlan, J.J. Tomoko, "Airfoil and bridge deck flutter derivatives," Journal of the Engineering Mechanics, ASCE 97 (1971) 1717-1737.

[17] Sarkar, P. P, "New identification methods applied to the response of flexible bridges to wind," PhD thesis, The John Hopkins University, Baltimore, Md. 1992.

[18] Jain, A., Jones, N. P., and Scanlan, R. H. ''Coupled flutter and buffeting analysis of long-span bridges,'' J. Structure Engineering, ASCE, 122(7), 716–725, 1996.

[19] Scanlan, R. H., and Gade, R. H, "Motion of suspended bridge spans under gusty wind," Journal of Structure Division, ASCE, 103(ST9), 1867-1883, 1977.

[20] J. E. Cermak , Nicholas Isyumov, *Wind Tunnel Studies of Buildings and Structures (Asce Manual and Reports on Engineering Practice).* American Society of Civil Engineers, 1998.

[21] Hiroshi Sato[a,*], Nobuyuki Hirahara[a], Koichiro Fumoto[a], Shigeru Hirano[b], Shigeki Kusuhara[b], "Full aeroelastic model test of a super long-span bridge with slotted box girder," Journal of Wind Engineering and Industrial Aerodynamics 90 (2002) 2023–2032.

[22] Günter Schewe[a], Allan Larsen[b], "Reynolds number effects in the flow around a bluff bridge deck cross section," Journal of Wind Engineering and Industrial Aerodynamics Volumes 74–76, 1 April 1998, Pages 829–838.

[23] K Matsuda[a], K.R Cooper[b], H Tanaka[c], M Tokushige[a], T Iwasaki[a], "An investigation of Reynolds number effects on the steady and unsteady aerodynamic forces on a 1: 10 scale bridge deck section model," Journal of Wind Engineering and Industrial Aerodynamics Volume 89, Issues 7–8, June 2001, Pages 619–632.

[24] G.L. Larose[a,*], A. D'Auteuil[b], "On the Reynolds number sensitivity of the aerodynamics of bluff bodies with sharp edges," Journal of Wind Engineering and Industrial Aerodynamics 94 (2006) 365–376.

[25] Yuh-Yi Lin*, Chii-Ming Cheng, Jong-Cheng Wu, Tsang-Lien Lan and Kuo-Ting Wu, "Effects of Deck Shape and Oncoming Turbulence on Bridge Aerodynamics," Tamkang Journal of Science and Engineering, Vol. 8, No 1, pp. 4356 (2005).

[26] Y.J. Ge, H.F. Xiang, "Recent development of bridge aerodynamics in China," Journal of Wind Engineering and Industrial Aerodynamics Volume 96, Issues 6–7, June–July 2008, Pages 736–768.

[27] Guy L. Larose, Flora M. Livesey, "Performance of streamlined bridge decks in relation to the aerodynamics of a flat plate," Journal of Wind Engineering and Industrial Aerodynamic, Volumes 69–71, July–October 1997, Pages 851–860.

[28] K.C.S. Kwok, X.R. Qin, C.H. Fok, P.A. Hitchcock, "Wind-induced pressures around a sectional twin-deck bridge model: Effects of gap-width on the aerodynamic forces and vortex shedding mechanisms," Journal of Wind Engineering and Industrial Aerodynamics Volume 110, November 2012, Pages 50–61.

[29] M. Matsumoto, K. Mizuno, K. Okubo, Y. Ito, H. Matsumiya. "Flutter instability and recent development in stabilization of structures," Journal of Wind Engineering and Industrial Aerodynamics, 95(2007)888-907.

[30] Robby Permata, Kazuhide Yonamine Hiroshi Hattori, Hiromichi Shirato, "Use of Double Slot as Countermeasure Against Coupled Flutter Instability of Bridge Deck," Kyoto University, Port and airport research institute, J-STAGE 20130326.

[31] G. Diana[a], M. Falco[a], S. Bruni[a], A. Cigada*['a], G.L. Larose[b], A. Damsgaard[b], A. Collina[a], "Comparisons between wind tunnel tests on a full aeroelastic model of the proposed bridge over Stretto di Messina and numerical results," Journal of Wind Engineering and Industrial Aerodynamics 54/55 (1995) 101-113.

[32] G. Diana, F. Resta, A. Zasso, M. Belloli, D. Rocchi, "Forced motion and free motion aeroelastic tests on a new concept dynamometric section model of the Messina suspension bridge," Journal of Wind Engineering and Industrial Aerodynamics, Volume 92, Issue 6, May 2004, Pages 441–462.

[33] John D. Anderson Jr., *Computational Fluid Dynamics The basics with application*. McGraw-Hill Science/Engineering/Math; 1 edition, 1995. .

[34] Wilcox, D.C., *Turbulence modeling for CFD.* D C W Industries; 2nd edition (July 1998).

[35] Shuji Shirai*, Toshio Ueda, "Aerodynamic simulation by CFD on flat box girder of super-long-span suspension bridge," Journal of Wind Engineering and Industrial Aerodynamics 91 (2003) 279–290.

[36] F.Brusiani[a], S.deMiranda[b], L.Patruno[b,*] F.Ubertini[b], P.Vaona[b], "On the evaluation of bridge deck flutter derivatives using RANS turbulence models," J. Wind Eng. Ind. Aerodynamic 119(2013)39–47.

[37] Shigeru Watanabe[a,*], Koichiro Fumoto[b], "Aerodynamic study of slotted box girder using computational fluid dynamics," Journal of Wind Engineering and Industrial Aerodynamics 96 (2008) 1885–1894.

[38] M.W. Sarwar[a,*], T. Ishihara[a], K. Shimada[b], Y. Yamasaki[c], T. Ikeda[d], "Prediction of aerodynamic characteristics of a box girder bridge section using the LES turbulence model," Journal of Wind Engineering and Industrial Aerodynamics 96 (2008) 1895–1911.

[39] Sean McTavish. "Identification of wind tunnel testing practices and investigation of the performance benefits of closely-spaced lateral wind farm configurations." 2013,pp.91..https://curve.carleton.ca/system/files/theses/30274.pdf

[40] Reynolds, Osborne, "On the Dynamical Theory of Incompressible Viscous Fluids and the Determination of the Criterion," Philosophical Transactions of the Royal Society of London. A, v. 186, pp. 123-164, 1985

[41] Bengt Andersson, Ronnie Andersson, Love Håkansson, Mikael Mortensen, Rahman Sudiyo, Berend van Wachem, *Computational Fluid Dynamics for Engineers.* Cambridge University Press, 2011.

[42] Smagorinsky, Joseph. "General Circulation Experiments with the Primitive Equations," Monthly Weather Review 91 (3): 99–164, March 1963.

[43] Félix Nieto, Alberto Zasso, Daniele Rocchi and Santiago Hernández, "CFD verification of aerodynamic devices performance for the Messina Strait Bridge," BBAA VI International Colloquium on: Bluff Bodies Aerodynamics and Applications Milano, Italy, July, 20-24 2008.

[44] G.L Larose, M.G. Savage and A. Lafreniere, "Sectional Model Experiments for Verification of the Aerodynamic Properties at High Reynolds Number of the Stonecutters Bridge, Hong Kong," LTR-AL-2006-0013, 2006.

[45] Allan Larsen, Mike Savage, Andréane Lafrenière, Michael C.H. Hui, Søren V. Larsen, "Investigation of vortex response of a twin box bridge section at high and low Reynolds numbers," Original Research Article Journal of Wind Engineering and Industrial Aerodynamics, Volume 96, Issues 6–7, June–July 2008, Pages 934-944.

[46] Wen-Li Chen[a,b,c], Hui Li[a,b,]n, Hui Hu[c], "An experimental study on the unsteady vortices and turbulent flow structures around twin-box-girder bridge deck models with different gap ratios," Journal of Wind Engineering and Industrial Aerodynamics, 132 (2014) 27–36.

[47] Belloli, M., Fossati, F., Giappino, S. and Muggiasca, S., "Vortex induced vibrations of a bridge deck: dynamic response and surface pressure distribution." In the Proceedings of the ACWE 2013 Conference, Seattle, USA, 2013.

[48] Gil H.B, "Bridges in Korea Long Span Bridges," In the proceedings seminar at the Norwegian Public Roads Administration, 2012.

[49] Sarkar, P. P., Jones, N. P., and Scanlan, R. H., "Identification of aeroelastic parameters of flexible bridges," J. Eng. Mech., 1718–1742, 1994.

[50] Leonardo Gunawan, Hadyan Hafizh, Hari Muhammad, "Measurements of Flutter Derivatives of a Bridge Deck Sectional Model," Journal of KONES Powertrain and Transport, Vol. 20, No. 4, 2013. p. 107-116, 2003

[51] H. Imai, C.-B. Yun, O. Maruyama, M. Shinozuka, "Fundamentals of system identification in structural dynamics" Probabilistic Engineering Mechanics Volume 4, Issue 4, Pages 162–173, December 1989.

[52] Xu XU., "Parametric studies on relationships between flutter derivatives of slender bridge," Appl. Math. Mech. -Engl. Ed. 30(2), 237–245 (2009) DOI: 10.1007/s10483-009-0211-2, 2009.

[53] Selberg A., "Oscillation and aerodynamic stability of suspension bridge," ACTA Polytech. Scand., Ci 13, 1961.

[54] Fabio Brancaleonia, Giorgio Diana, "The aerodynamic design of the Messina Straits Bridge," Journal of Wind Engineering and Industrial Aerodynamics 48 (1993) 395 409, 1993.

[55] Hao Zhana,Tao Fangb, "Flutter stability studies of Great Belt East Bridge and Tacoma Narrows Bridge by CFD numerical simulation," The Seventh International Colloquium on Bluff Body Aerodynamics and Applications (BBAA7) Shanghai, China, 2012.

[56] G. Diana, D. Rocchi*, T. Argentini, S. Muggiasca, “Aerodynamic instability of a bridge deck section model: Linear and nonlinear approach to force modeling,” Journal of Wind Engineering and Industrial Aerodynamics, 98 (2010) 363–374.
[57] J.B. Frandsen*, “Numerical bridge deck studies using finite elements. Part I: flutter,” Journal of Fluids and Structures 19 (2004) 171–191
[58] M. Matsumoto et al., "Study on aerodynamic behaviour of long-span bridge and its stabilization,” Technical Report BWKU Y96640, Department of Global Environment Engineering Kyoto University, Japan, 1997.
[59] Master_Thesis_Avasar,http://www.tuhh.de/sdb/Diplomarbeiten/Diplomarbeiten/Master_Thesis_Avasar.pdf.

Appendix A

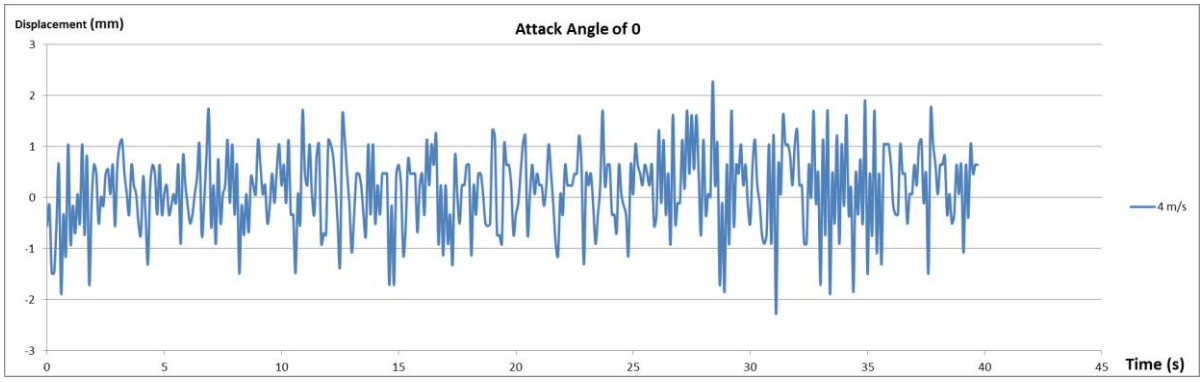
Displacement (mm)
Attack Angle of 0
3
2
1
0
-1
-2
-3
0
5
10
15
20
25
30
35
40
45
Time (s)
4 m/s

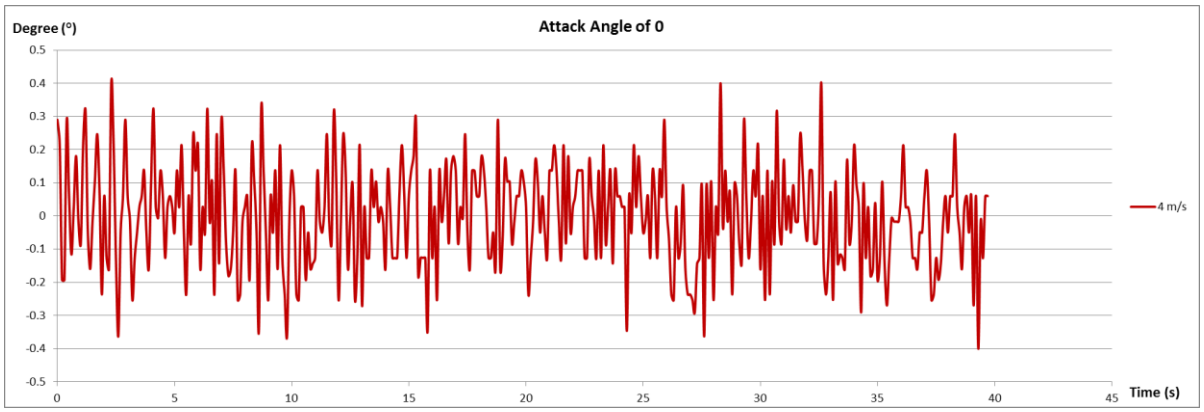
Degree (°)
Attack Angle of 0
0.5
0.4
0.3
0.2
0.1
0
-0.1
-0.2
-0.3
-0.4
-0.5
0
5
10
15
20
25
30
35
40
45
Time (s)
4 m/s

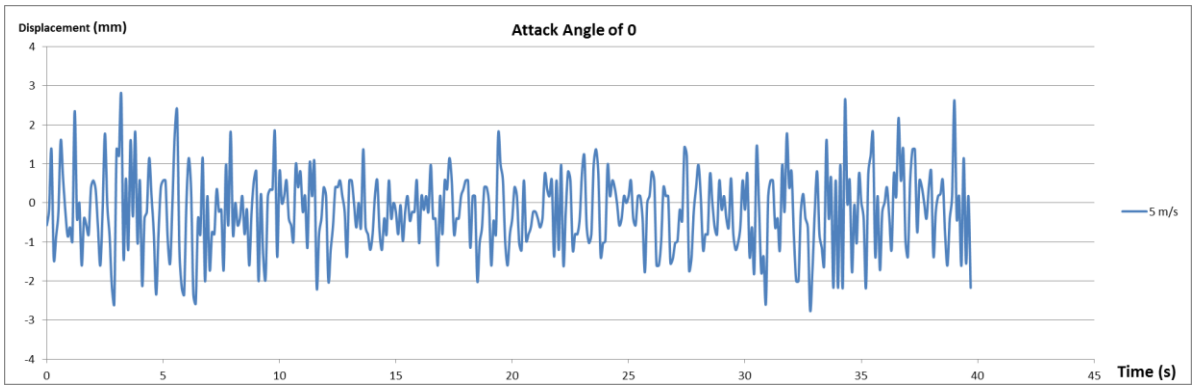
Displacement (mm)
Attack Angle of 0
4
3
2
1
0
-1
-2
-3
-4
0
5
10
15
20
25
30
35
40
45
Time (s)
5 m/s

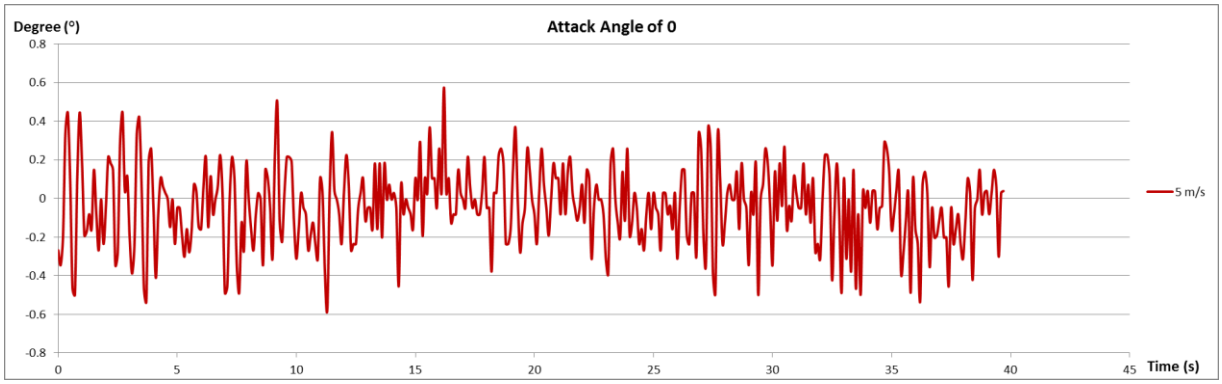
Degree (°)
Attack Angle of 0
0.8
0.6
0.4
0.2
0
-0.2
-0.4
-0.6
-0.8
0
5
10
15
20
25
30
35
40
45
Time (s)
5 m/s

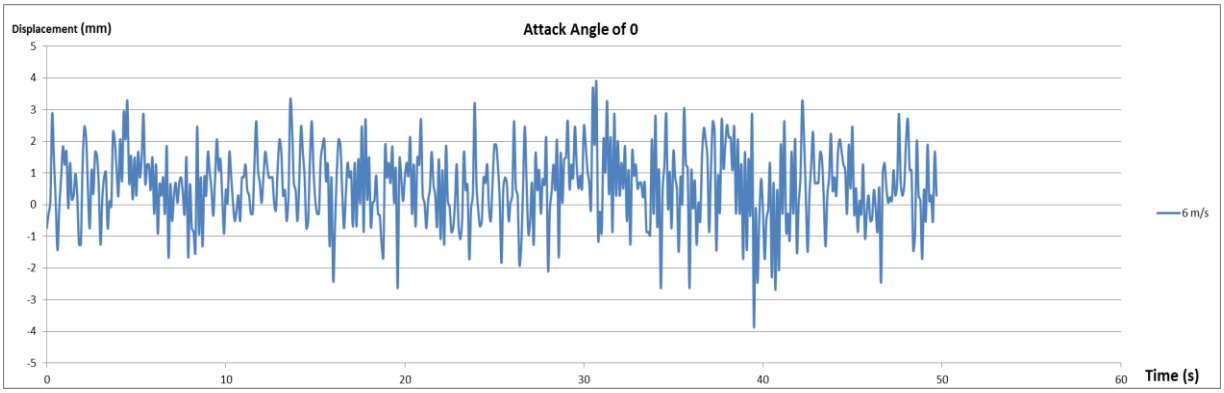
Displacement (mm)
Attack Angle of 0
5
4
3
2
1
0
-1
-2
-3
-4
-5
0
10
20
30
40
50
60
Time (s)
6 m/s

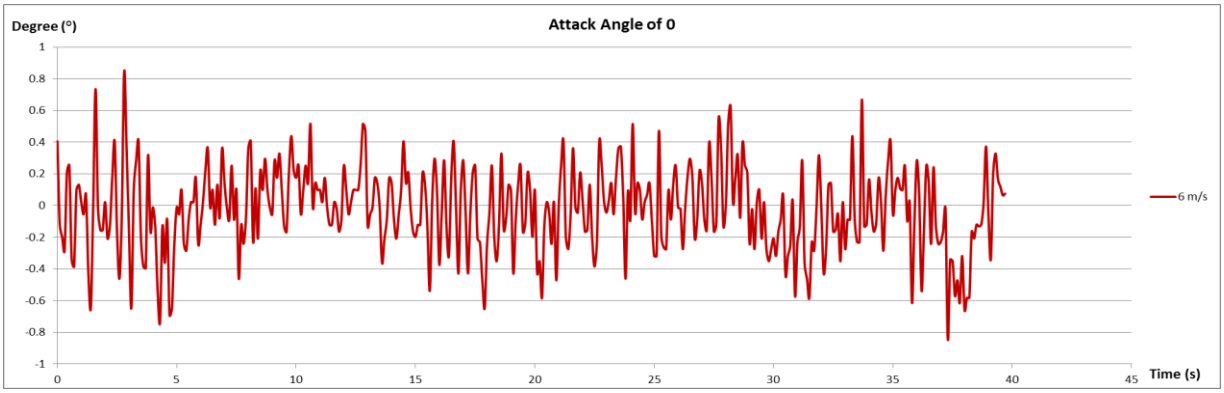
Degree (°)
Attack Angle of 0
1
0.8
0.6
0.4
0.2
0
-0.2
-0.4
-0.6
-0.8
-1
0
5
10
15
20
25
30
35
40
45
Time (s)
6 m/s

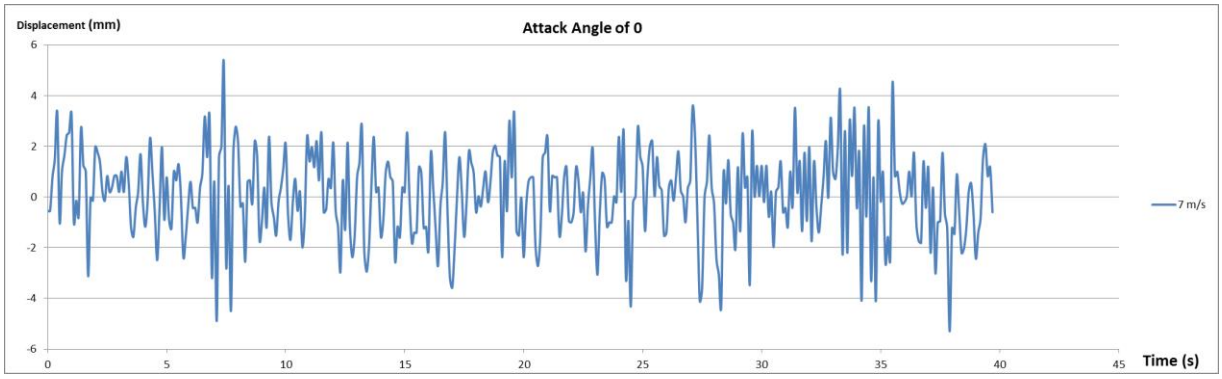
Displacement (mm)
Attack Angle of 0
6
4
2
0
-2
-4
-6
0
5
10
15
20
25
30
35
40
45
Time (s)
7 m/s

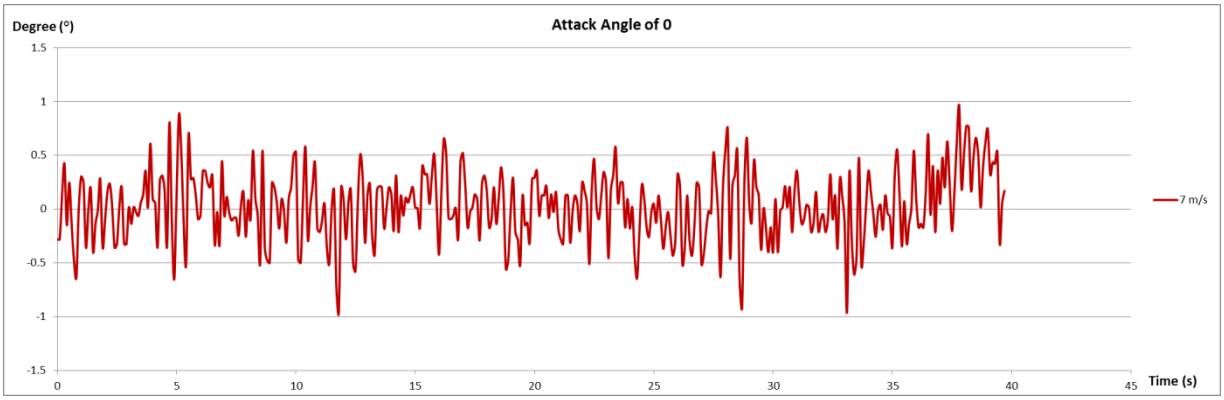
Degree (°)
Attack Angle of 0
1.5
1
0.5
0
-0.5
-1
-1.5
0
5
10
15
20
25
30
35
40
45
Time (s)
7 m/s

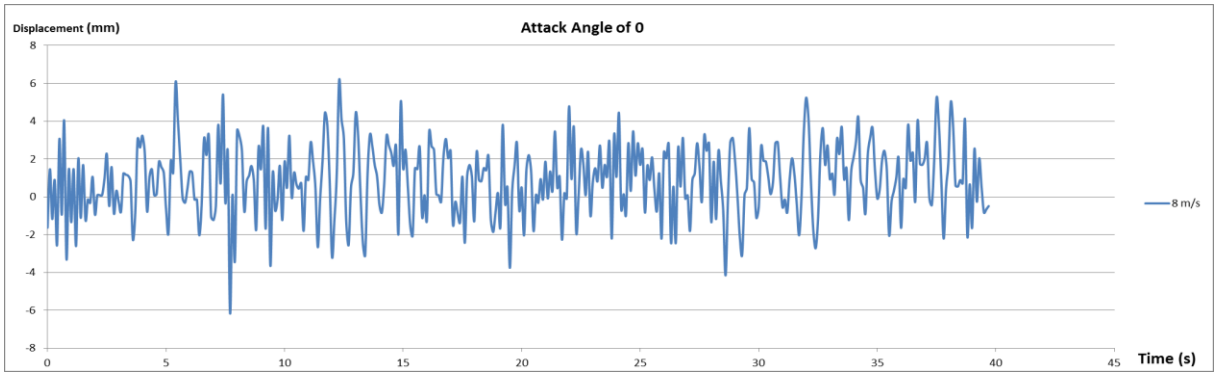
Displacement (mm)
Attack Angle of 0
8
6
4
2
0
-2
-4
-6
-8
0
5
10
15
20
25
30
35
40
45
Time (s)
8 m/s

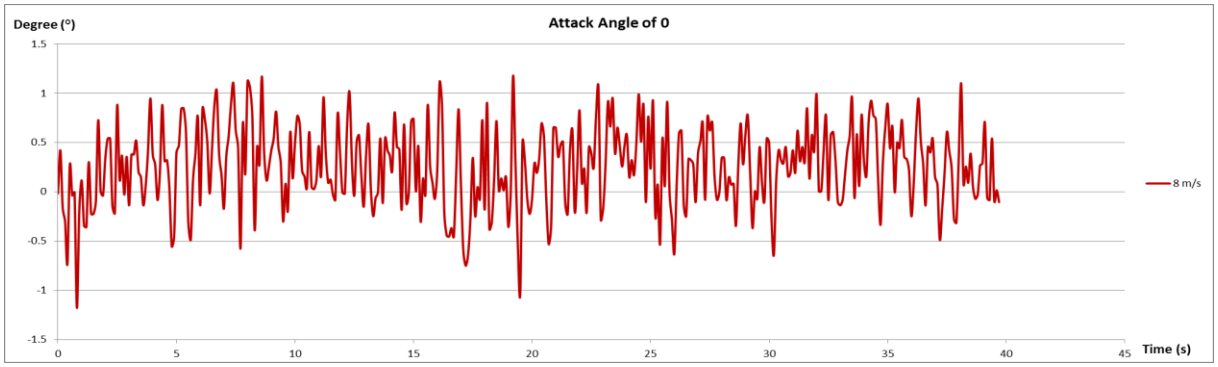
Degree (°)
Attack Angle of 0
1.5
1
0.5
0
-0.5
-1
-1.5
0
5
10
15
20
25
30
35
40
45
Time (s)
8 m/s

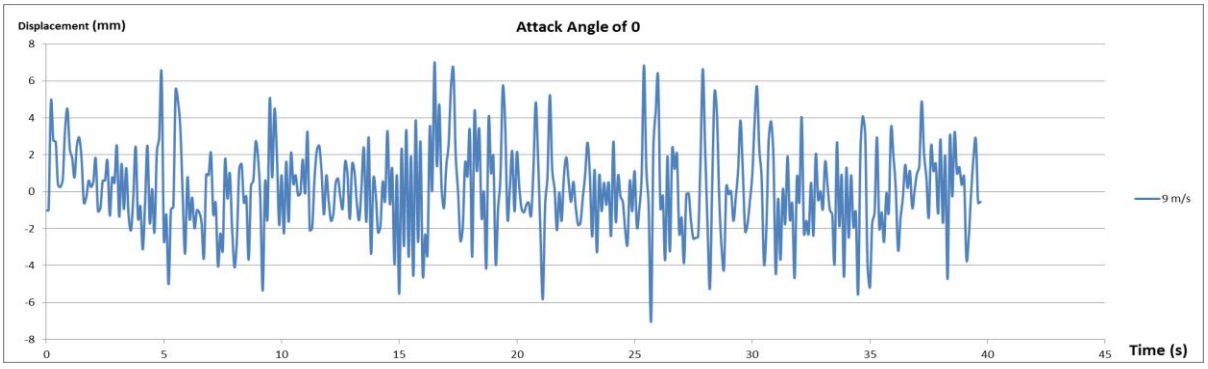
Displacement (mm)
Attack Angle of 0
8
6
4
2
0
-2
-4
-6
-8
0
5
10
15
20
25
30
35
40
45
Time (s)
9 m/s

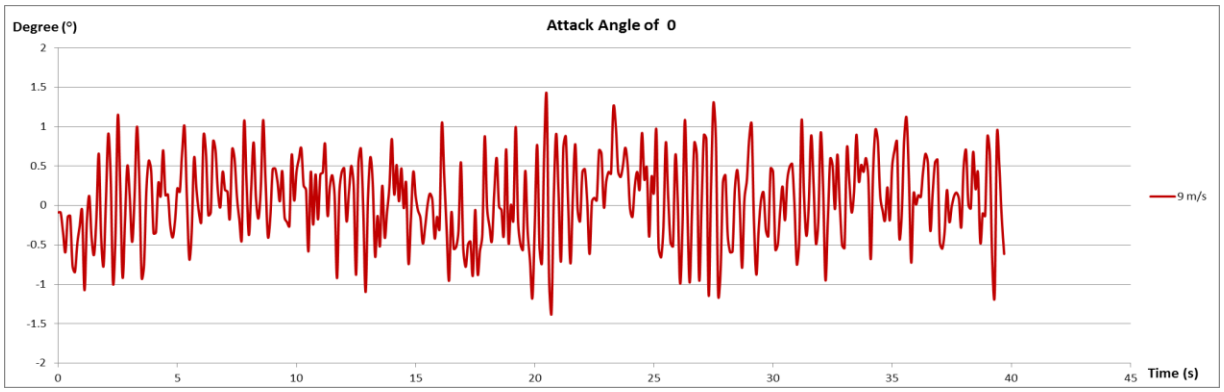
Degree (°)
Attack Angle of 0
2
1.5
1
0.5
0
-0.5
-1
-1.5
-2
0
5
10
15
20
25
30
35
40
45
Time (s)
9 m/s

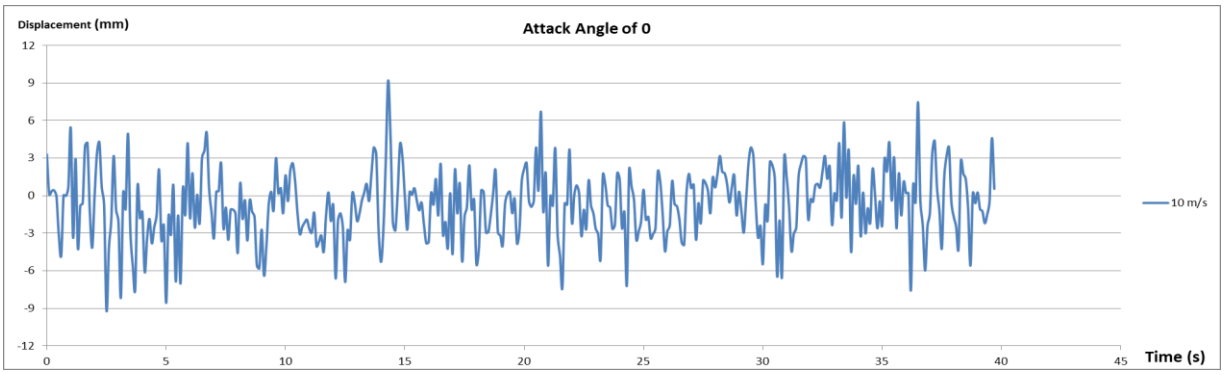
Displacement (mm)
Attack Angle of 0
12
9
6
3
0
-3
-6
-9
-12
0
5
10
15
20
25
30
35
40
45
Time (s)
10 m/s

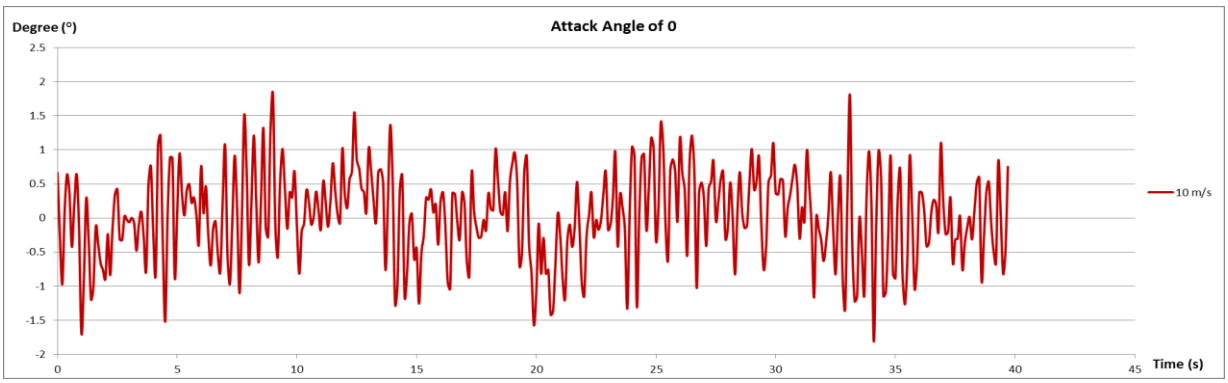
Degree (°)
Attack Angle of 0
2.5
2
1.5
1
0.5
0
-0.5
-1
-1.5
-2
0
5
10
15
20
25
30
35
40
45
Time (s)
10 m/s

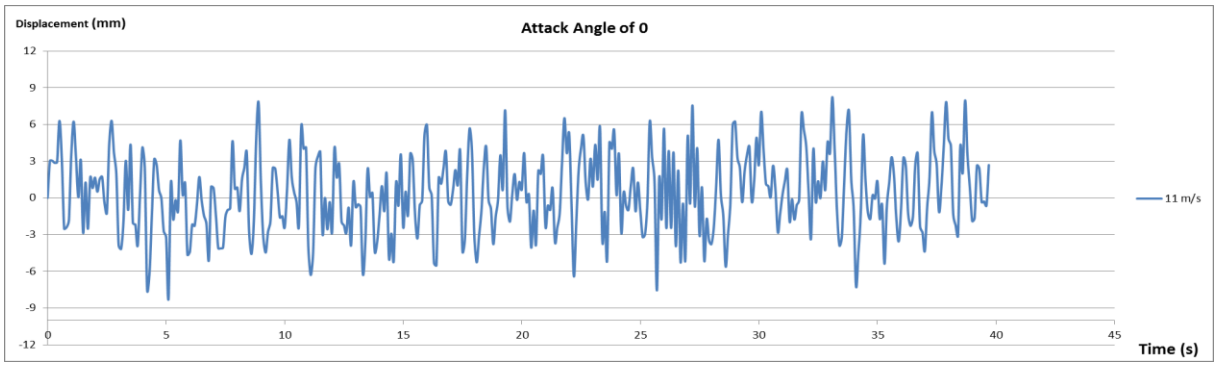
Displacement (mm)
Attack Angle of 0
12
9
6
3
0
-3
-6
-9
-12
0
5
10
15
20
25
30
35
40
45
Time (s)
11 m/s

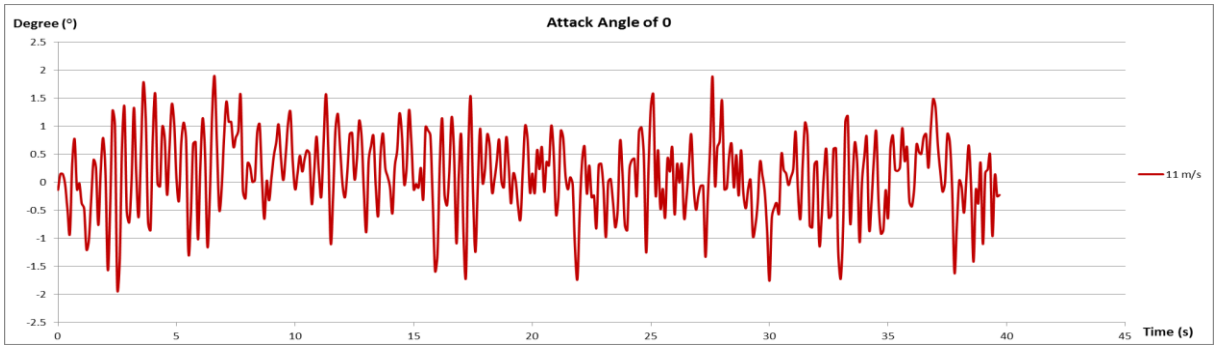

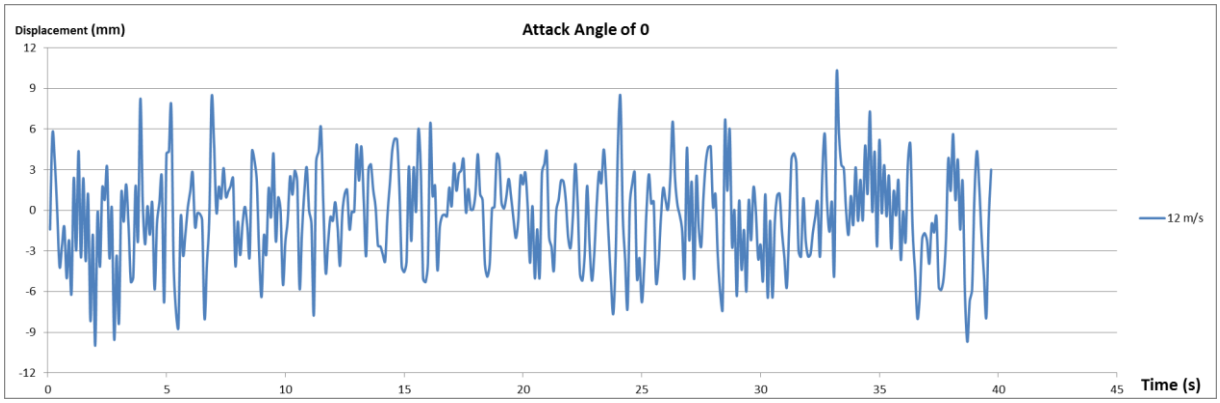

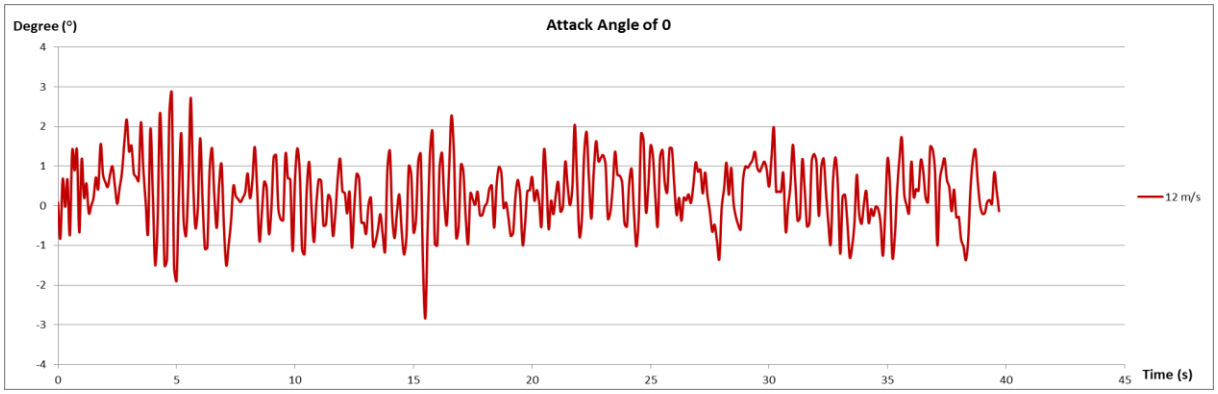

Time displacement histories for the vertical and torsional modes from 4 m/s and 12 m/s wind speed under 0 ° attack angle

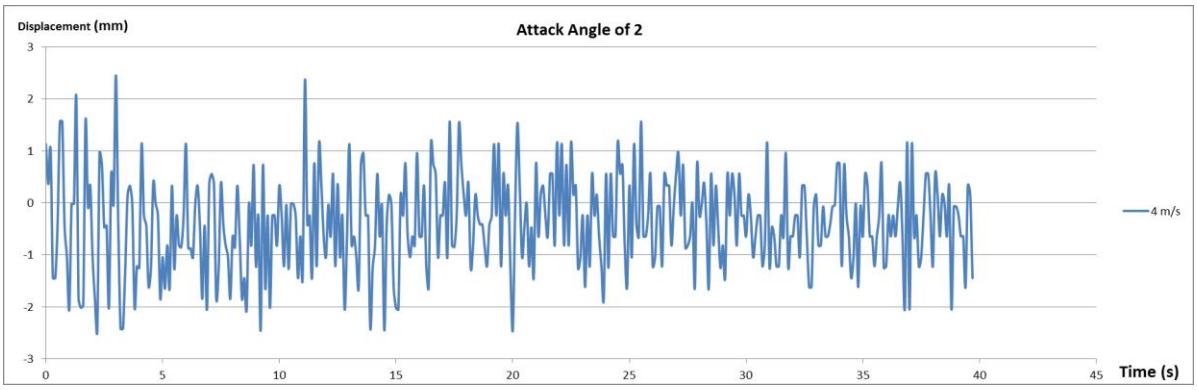
Displacement (mm)
Attack Angle of 2
3
2
1
0
-1
-2
-3
0
5
10
15
20
25
30
35
40
45
Time (s)
4 m/s

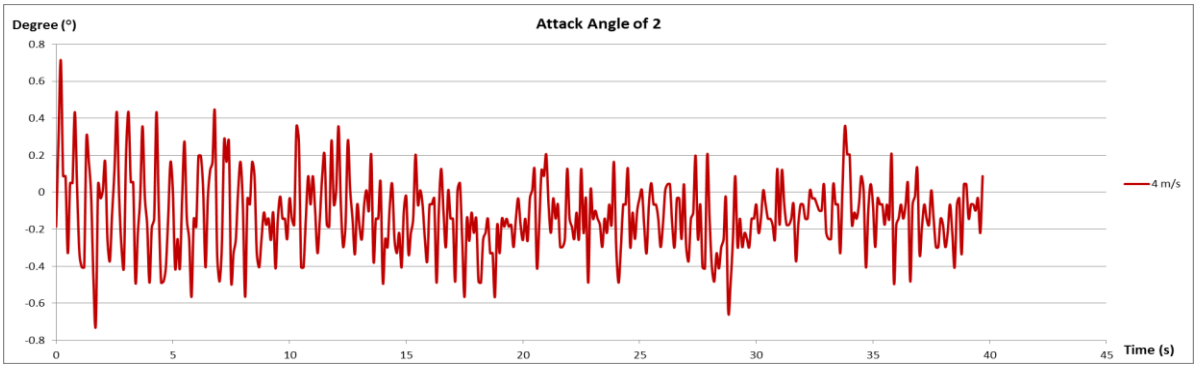
Degree (°)
Attack Angle of 2
0.8
0.6
0.4
0.2
0
-0.2
-0.4
-0.6
-0.8
0
5
10
15
20
25
30
35
40
45
Time (s)
4 m/s

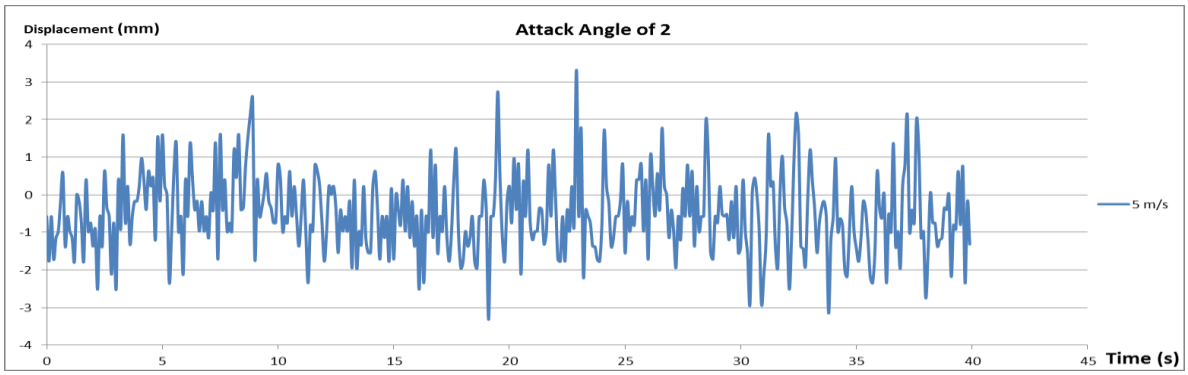
Displacement (mm)
Attack Angle of 2
4
3
2
1
0
-1
-2
-3
-4
0
5
10
15
20
25
30
35
40
45
Time (s)
5 m/s

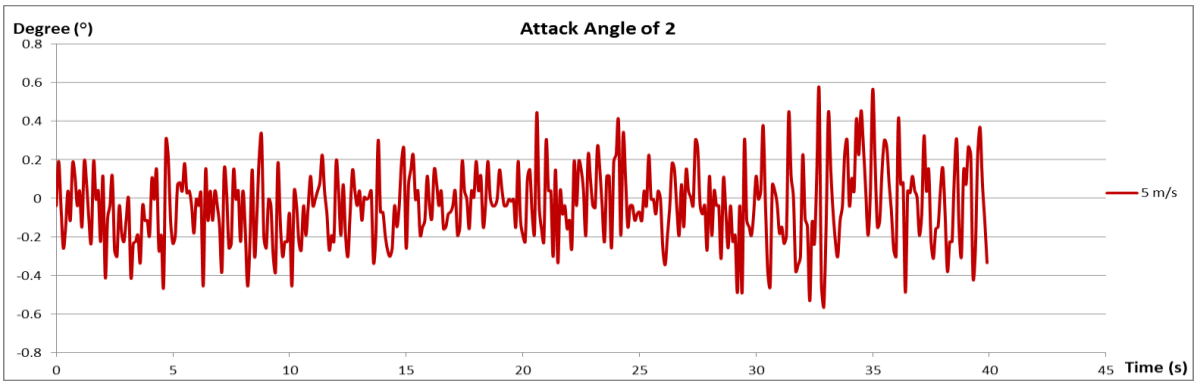
Degree (°)
Attack Angle of 2
0.8
0.6
0.4
0.2
0
-0.2
-0.4
-0.6
-0.8
0
5
10
15
20
25
30
35
40
45
Time (s)
5 m/s

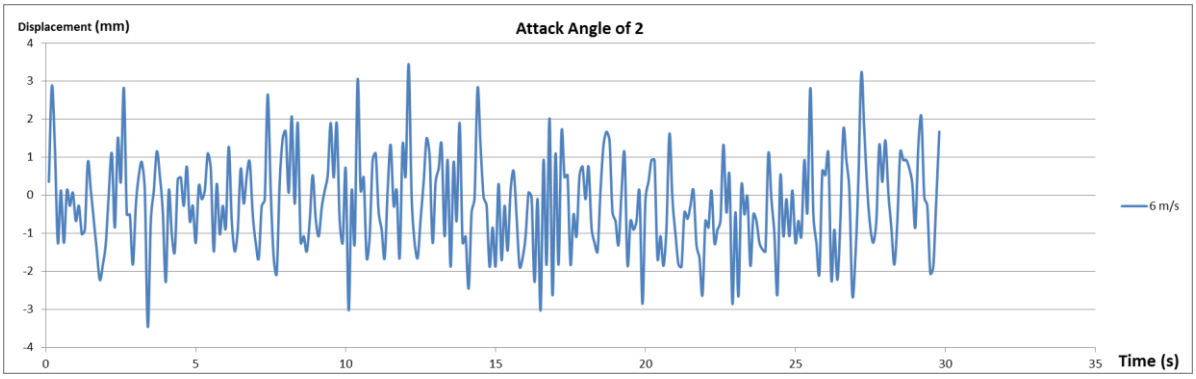
Displacement (mm)
Attack Angle of 2
4
3
2
1
0
-1
-2
-3
-4
0
5
10
15
20
25
30
35
Time (s)
6 m/s

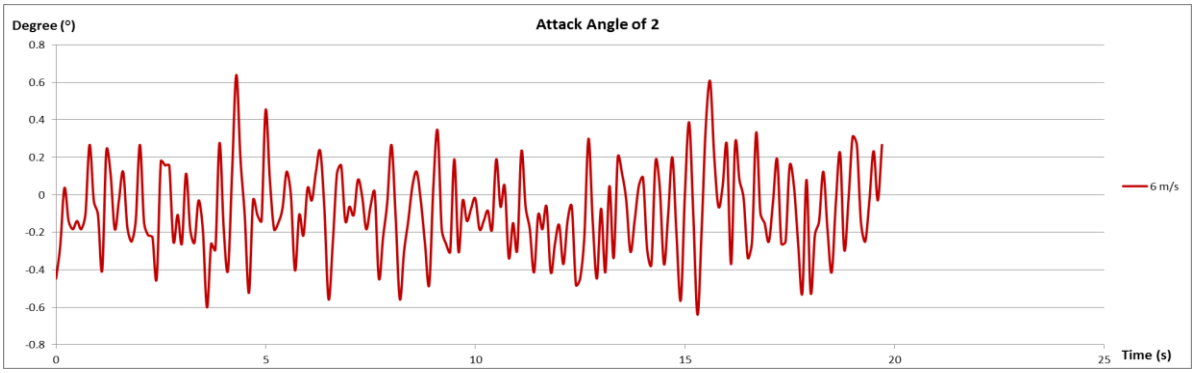
Degree (°)
Attack Angle of 2
0.8
0.6
0.4
0.2
0
-0.2
-0.4
-0.6
-0.8
0
5
10
15
20
25
Time (s)
6 m/s

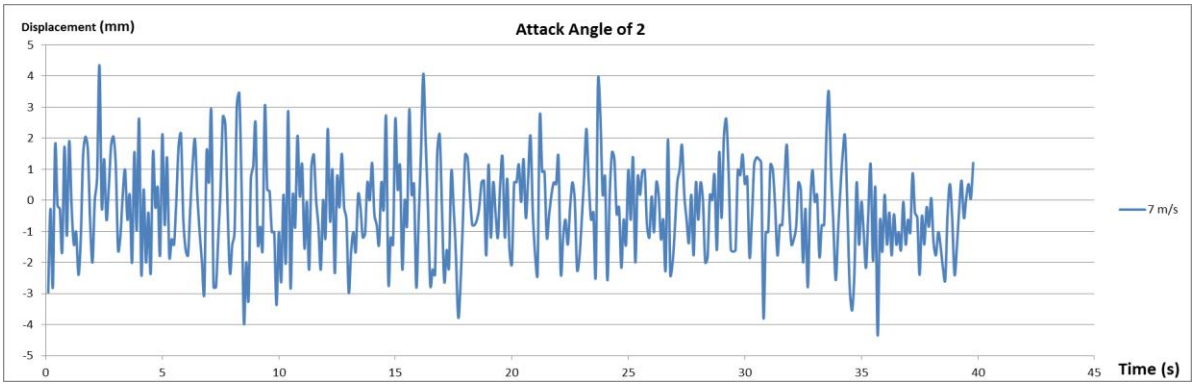
Displacement (mm)
Attack Angle of 2
5
4
3
2
1
0
-1
-2
-3
-4
-5
0
5
10
15
20
25
30
35
40
45
Time (s)
7 m/s

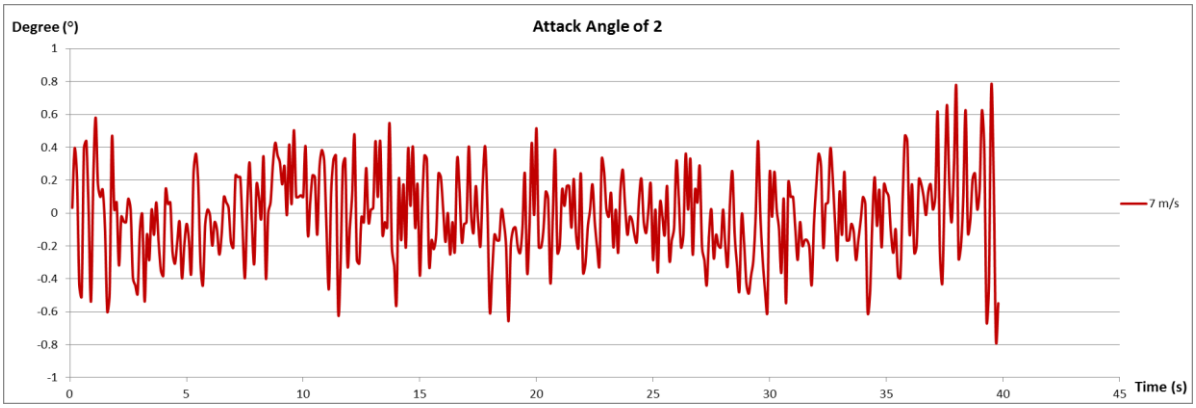
Degree (°)
Attack Angle of 2
1
0.8
0.6
0.4
0.2
0
-0.2
-0.4
-0.6
-0.8
-1
0
5
10
15
20
25
30
35
40
45
Time (s)
7 m/s

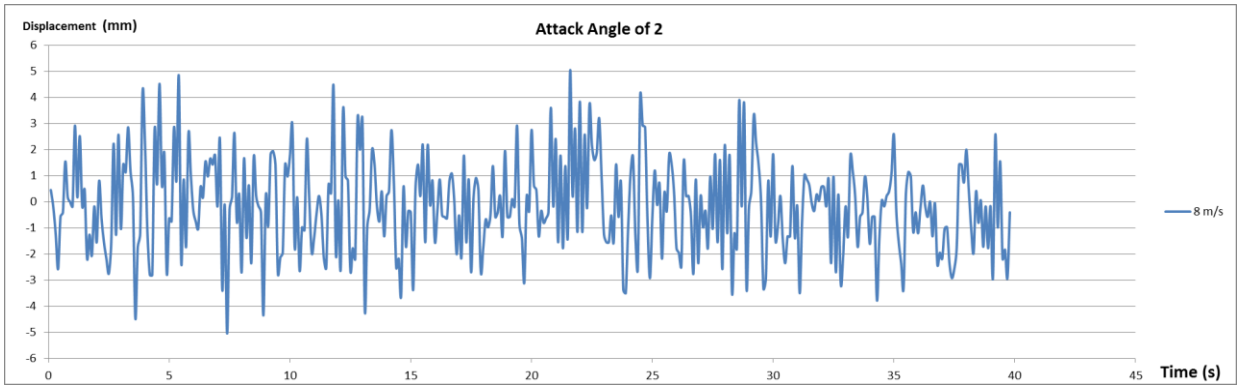
Displacement (mm)
Attack Angle of 2
8 m/s
Time (s)

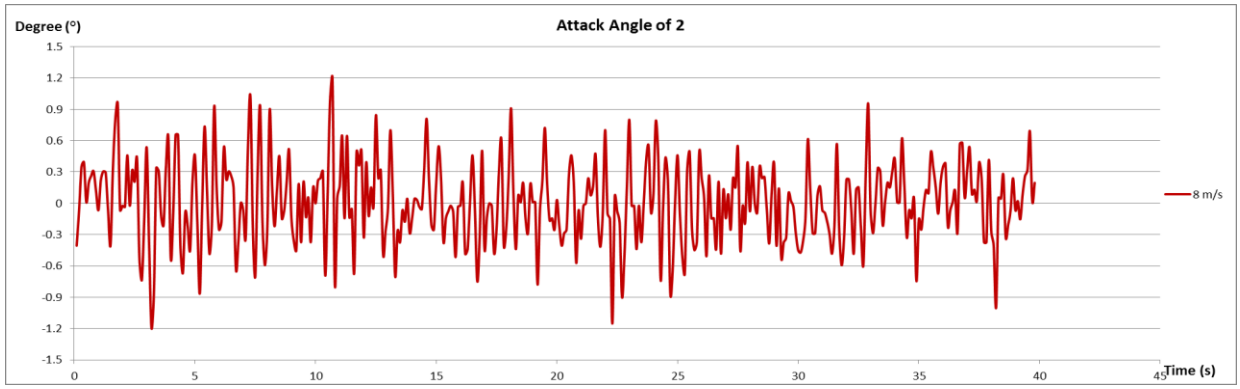
Degree (°)
Attack Angle of 2
8 m/s
Time (s)

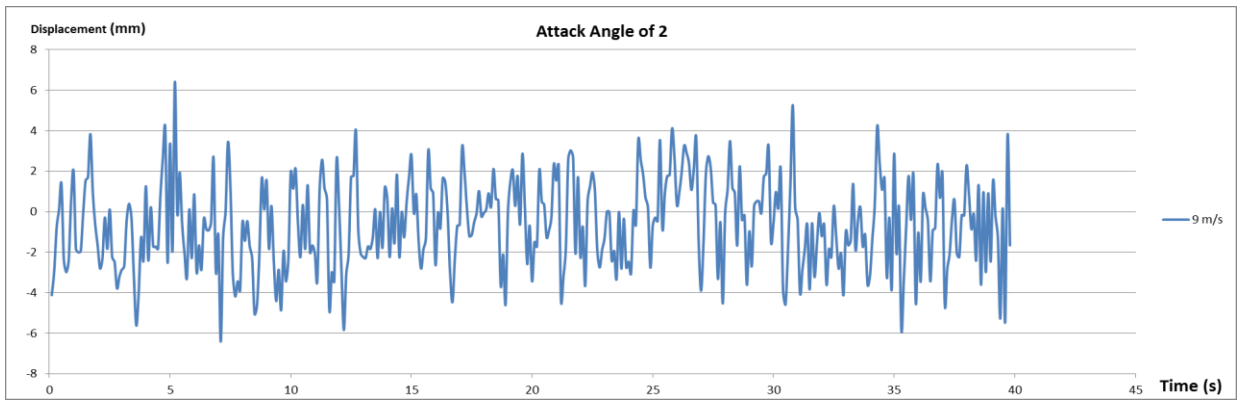
Displacement (mm)
Attack Angle of 2
9 m/s
Time (s)

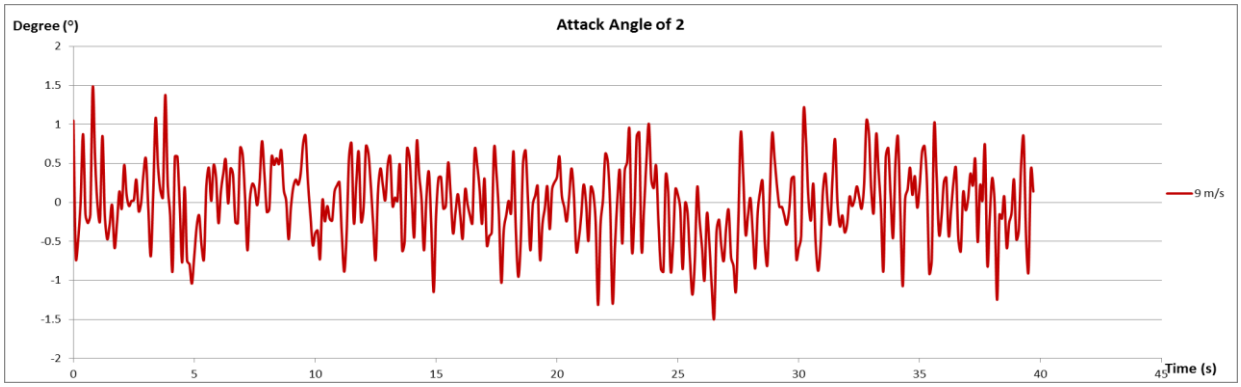
Degree (°)
Attack Angle of 2
9 m/s
Time (s)

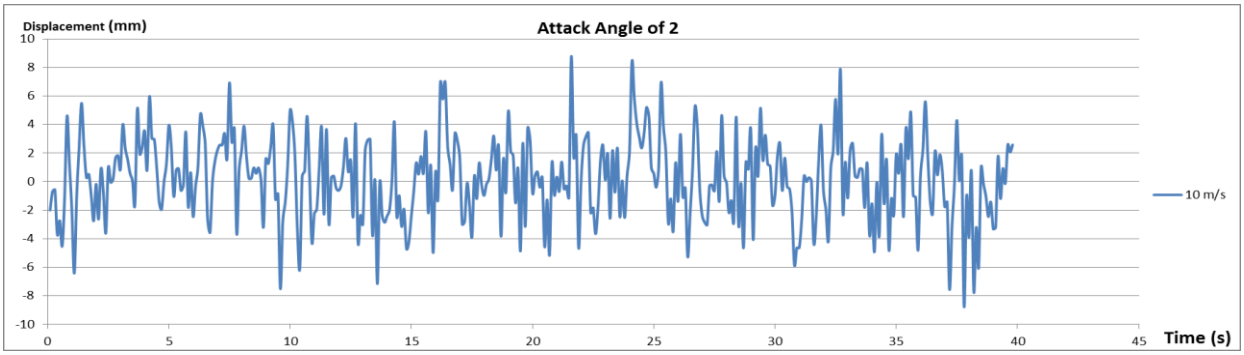

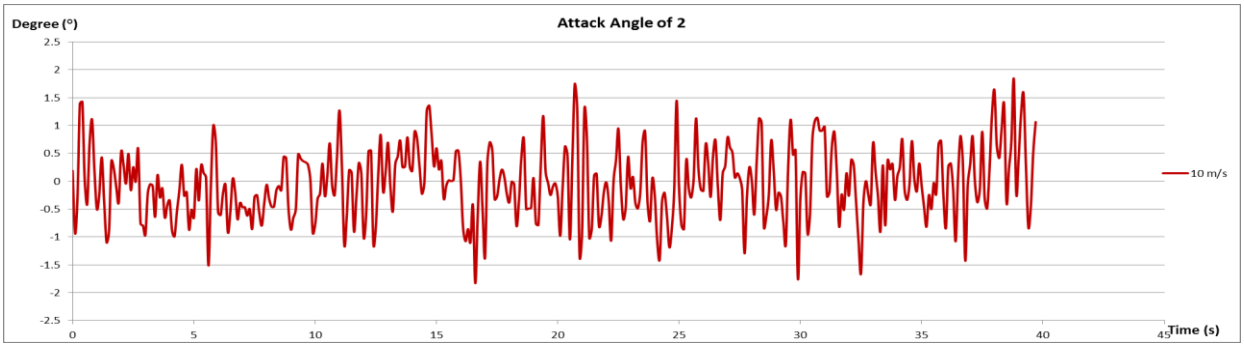

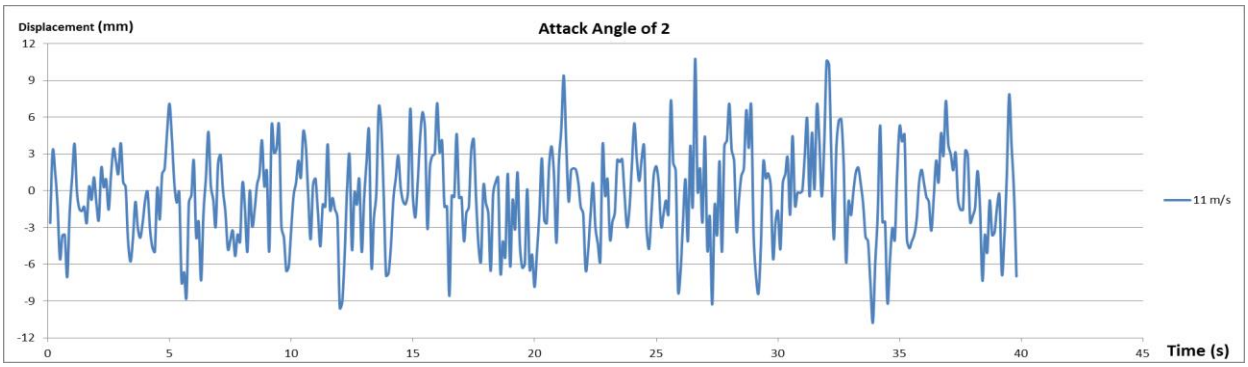

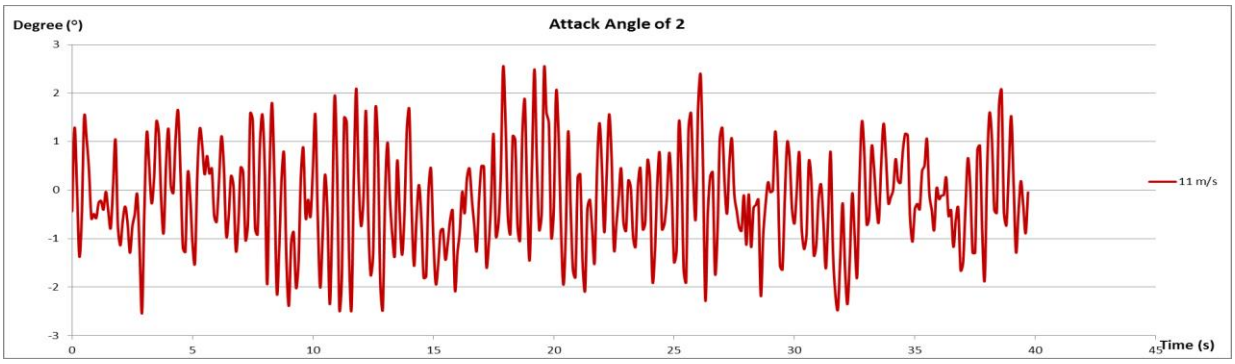

Time displacement histories for the vertical and torsional modes at 4 m/s and 11 m/s wind speed under 2 °attack angle

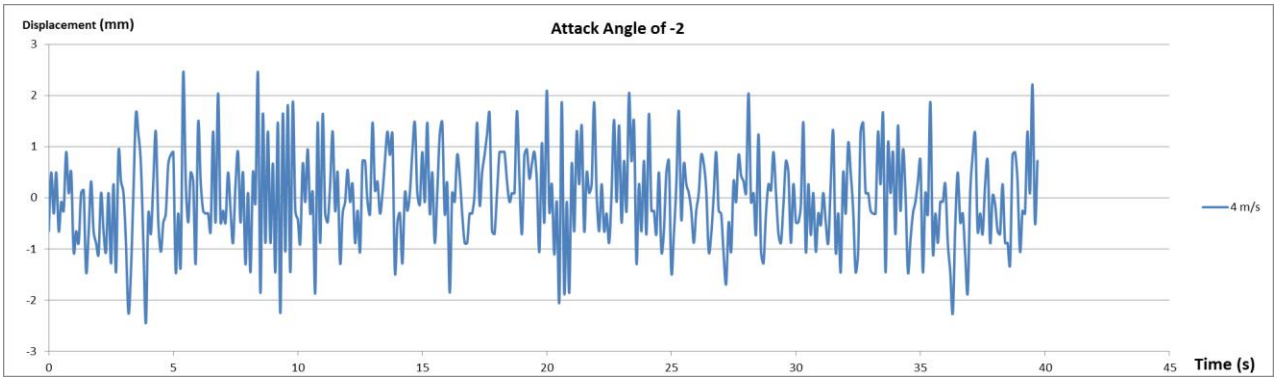
Displacement (mm)
Attack Angle of -2
3
2
1
0
-1
-2
-3
0
5
10
15
20
25
30
35
40
45
Time (s)
4 m/s

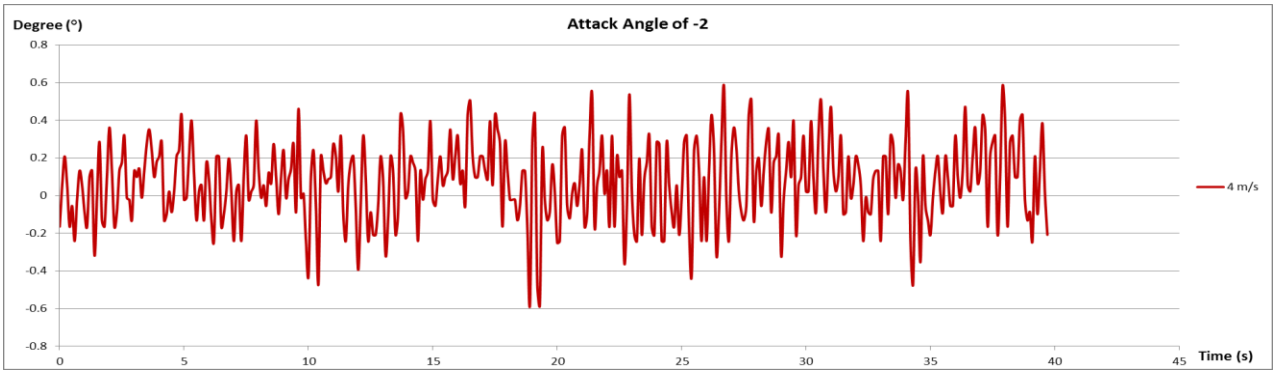
Degree (°)
Attack Angle of -2
0.8
0.6
0.4
0.2
0
-0.2
-0.4
-0.6
-0.8
0
5
10
15
20
25
30
35
40
45
Time (s)
4 m/s

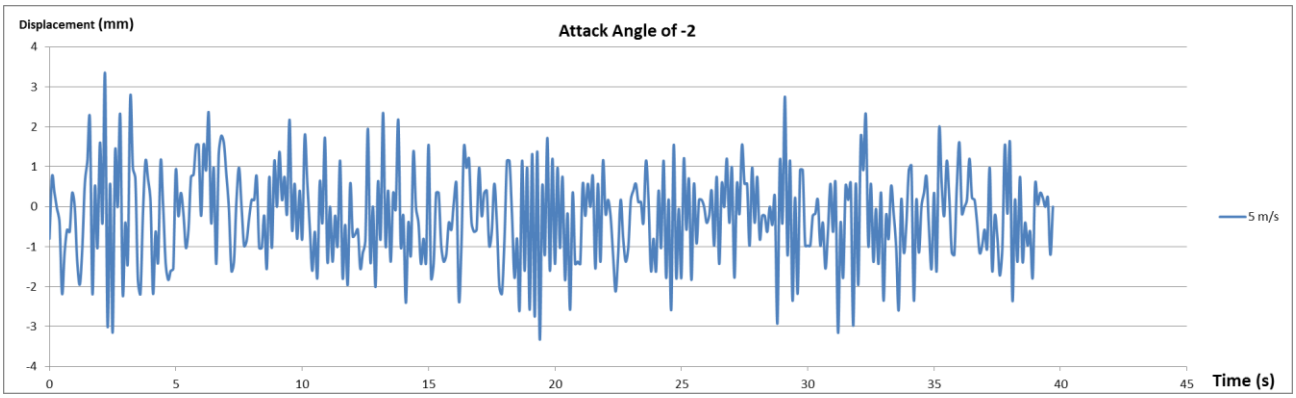
Displacement (mm)
Attack Angle of -2
4
3
2
1
0
-1
-2
-3
-4
0
5
10
15
20
25
30
35
40
45
Time (s)
5 m/s

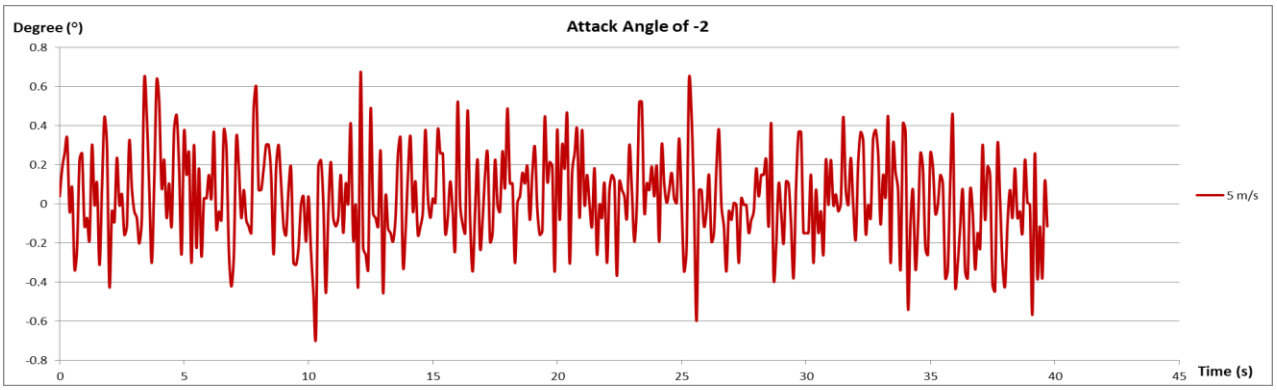
Degree (°)
Attack Angle of -2
0.8
0.6
0.4
0.2
0
-0.2
-0.4
-0.6
-0.8
0
5
10
15
20
25
30
35
40
45
Time (s)
5 m/s

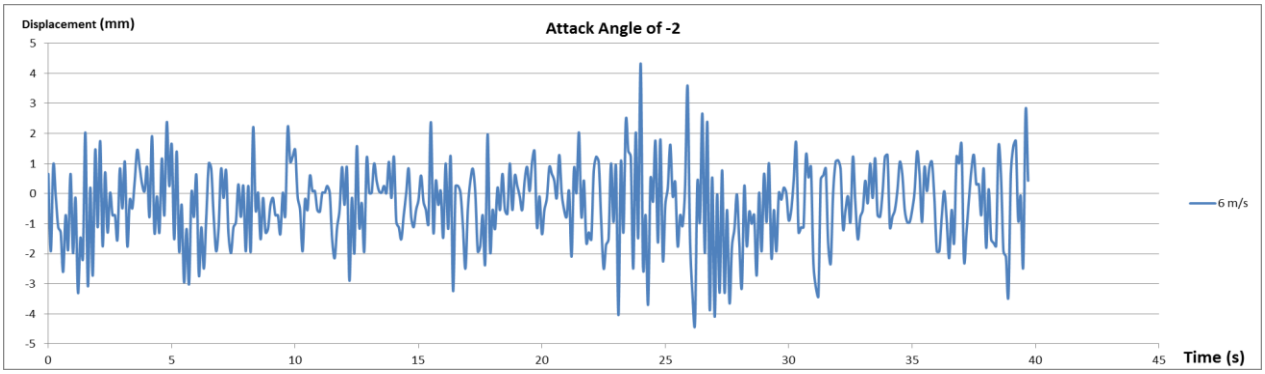
Displacement (mm)
Attack Angle of -2
5
4
3
2
1
0
-1
-2
-3
-4
-5
0
5
10
15
20
25
30
35
40
45
Time (s)
6 m/s

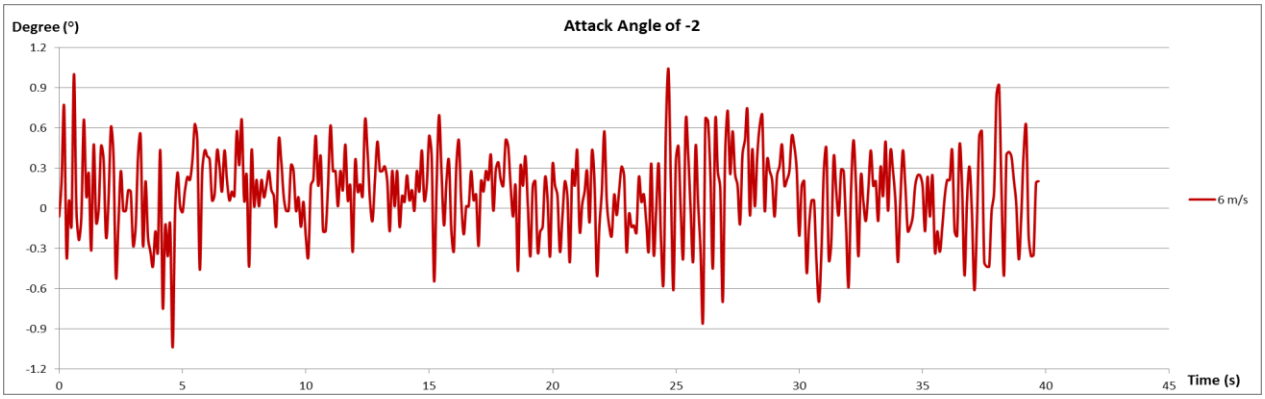
Degree (°)
Attack Angle of -2
1.2
0.9
0.6
0.3
0
-0.3
-0.6
-0.9
-1.2
0
5
10
15
20
25
30
35
40
45
Time (s)
6 m/s

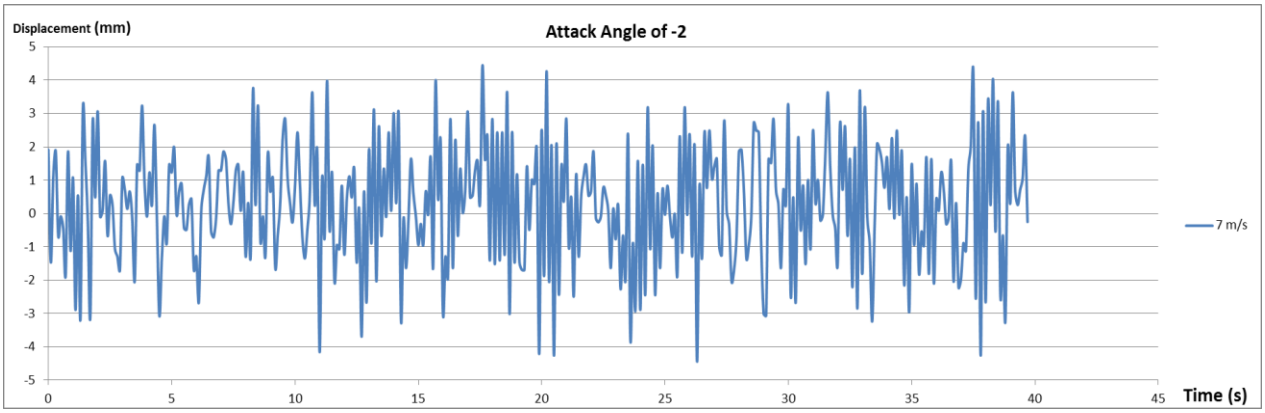
Displacement (mm)
Attack Angle of -2
5
4
3
2
1
0
-1
-2
-3
-4
-5
0
5
10
15
20
25
30
35
40
45
Time (s)
7 m/s

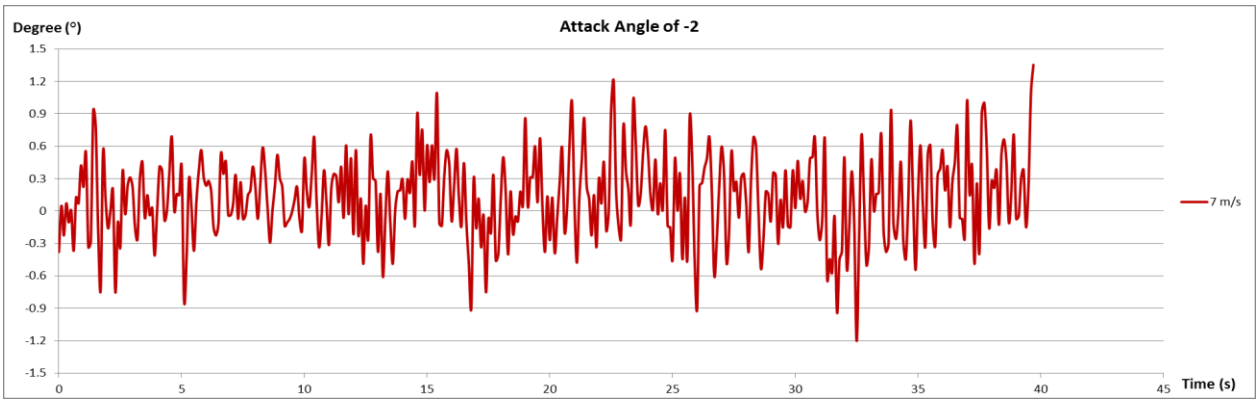
Degree (°)
Attack Angle of -2
1.5
1.2
0.9
0.6
0.3
0
-0.3
-0.6
-0.9
-1.2
-1.5
0
5
10
15
20
25
30
35
40
45
Time (s)
7 m/s

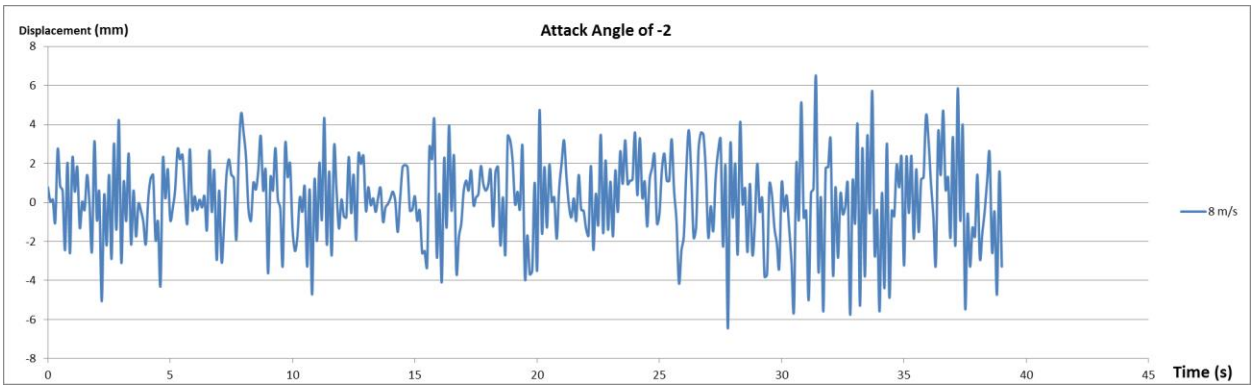
Displacement (mm)
Attack Angle of -2
8
6
4
2
0
-2
-4
-6
-8
0
5
10
15
20
25
30
35
40
45
Time (s)
8 m/s

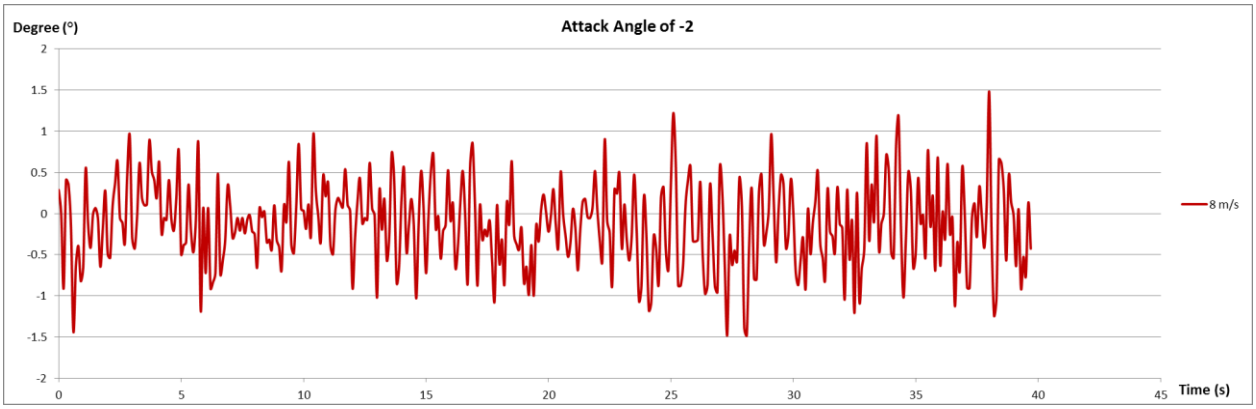
Degree (°)
Attack Angle of -2
2
1.5
1
0.5
0
-0.5
-1
-1.5
-2
0
5
10
15
20
25
30
35
40
45
Time (s)
8 m/s

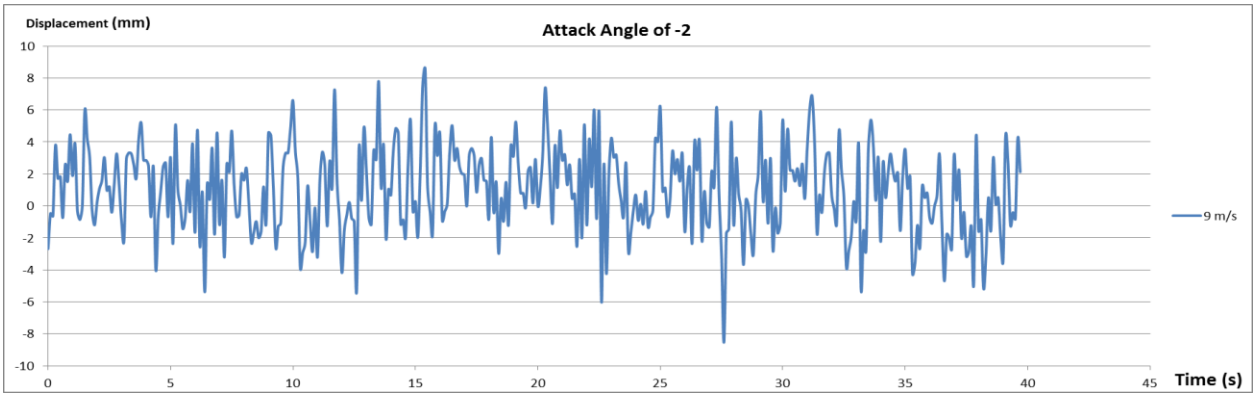
Displacement (mm)
Attack Angle of -2
10
8
6
4
2
0
-2
-4
-6
-8
-10
0
5
10
15
20
25
30
35
40
45
Time (s)
9 m/s

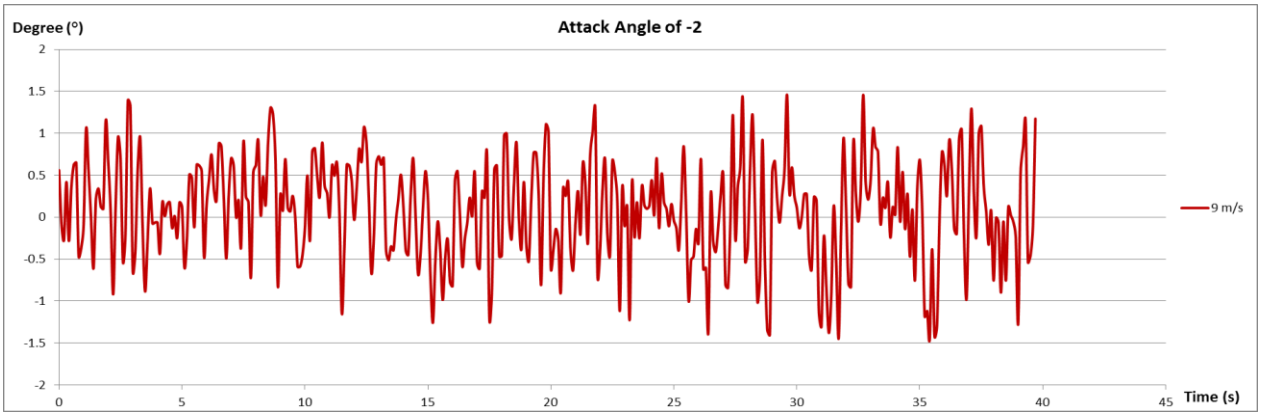
Degree (°)
Attack Angle of -2
2
1.5
1
0.5
0
-0.5
-1
-1.5
-2
0
5
10
15
20
25
30
35
40
45
Time (s)
9 m/s

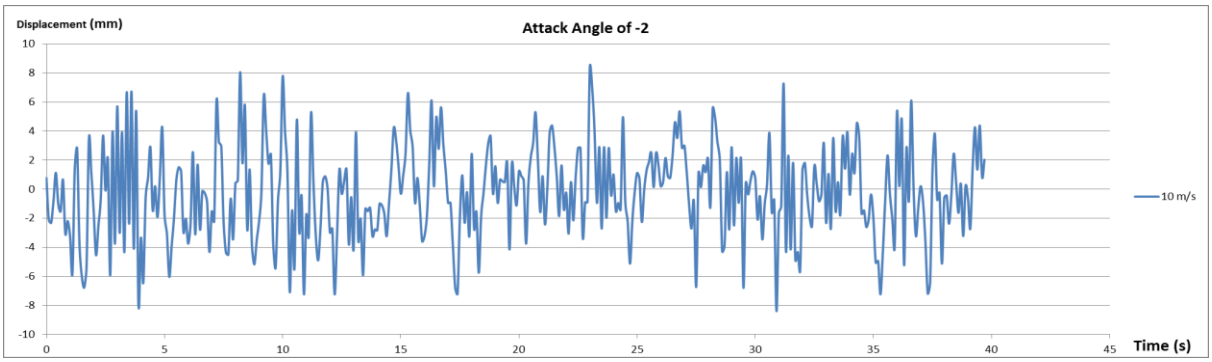

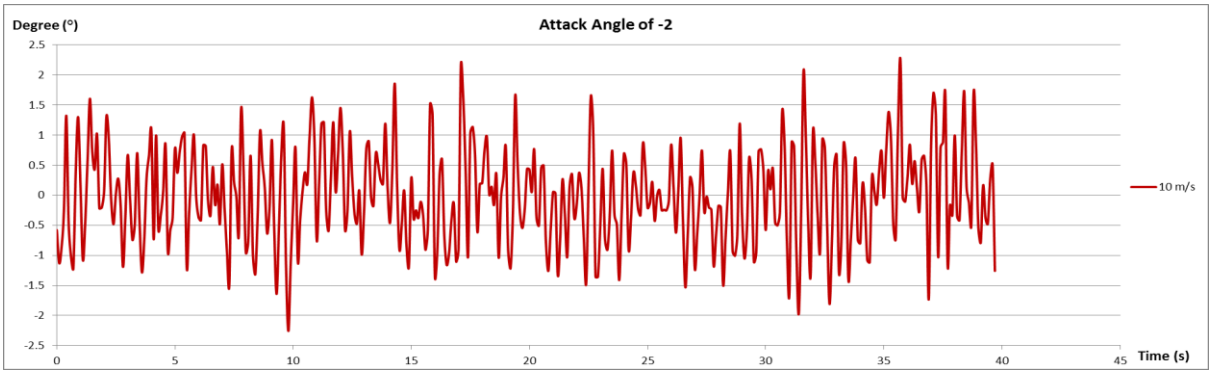

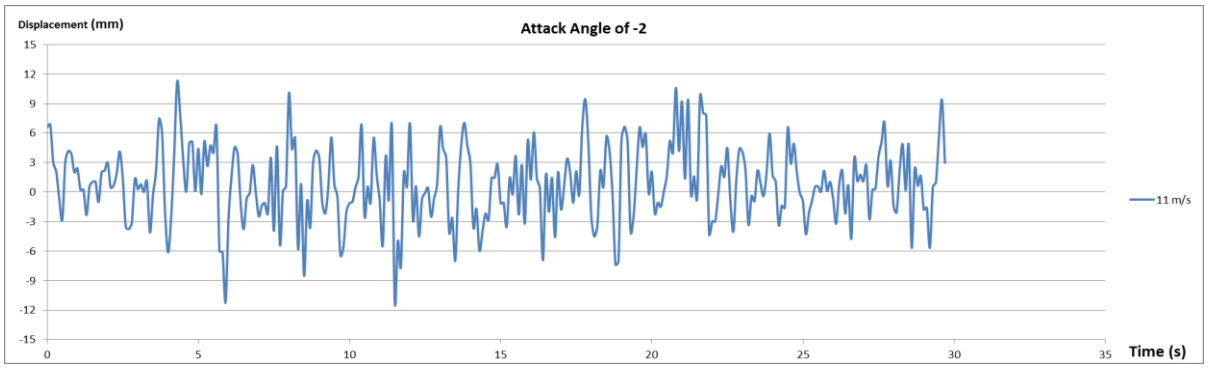

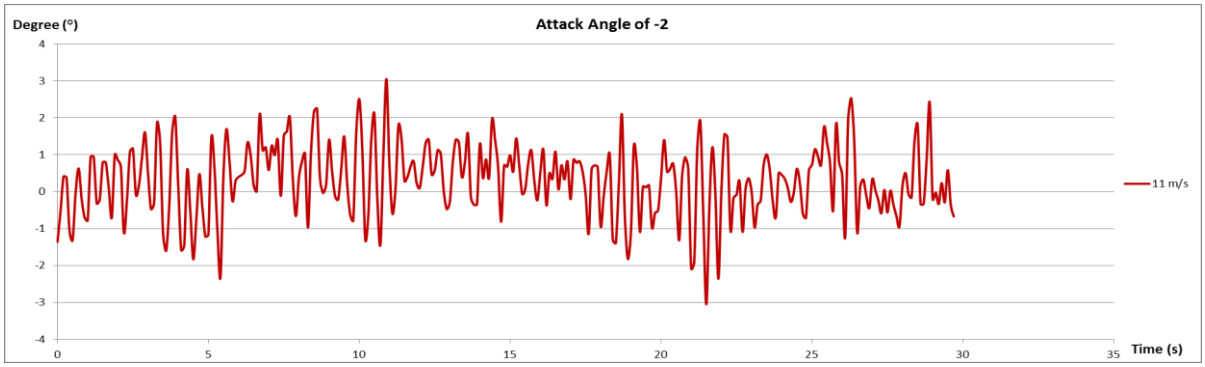

Time displacement histories for the vertical and torsional modes at 3 m/s and 11 m/s wind speed under -2 °attack angle

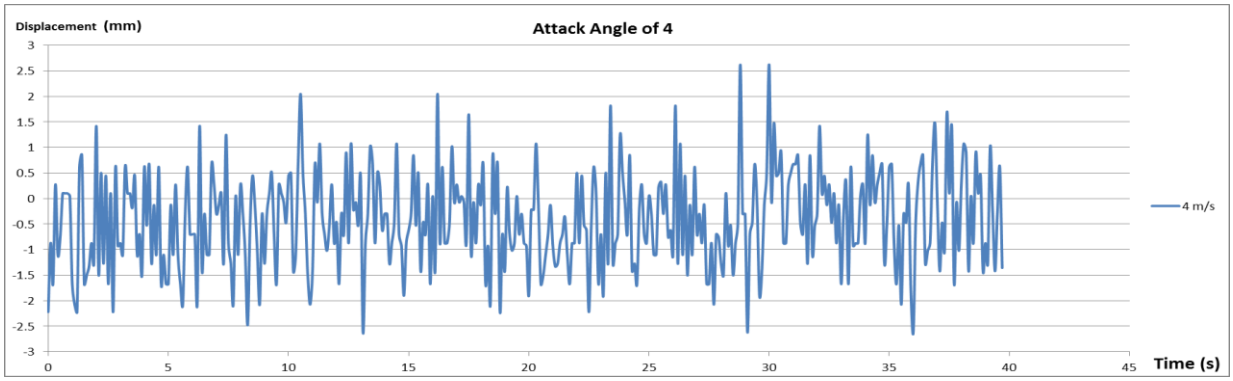
Displacement (mm)
Attack Angle of 4
3
2.5
2
1.5
1
0.5
0
-0.5
-1
-1.5
-2
-2.5
-3
0
5
10
15
20
25
30
35
40
45
Time (s)
4 m/s

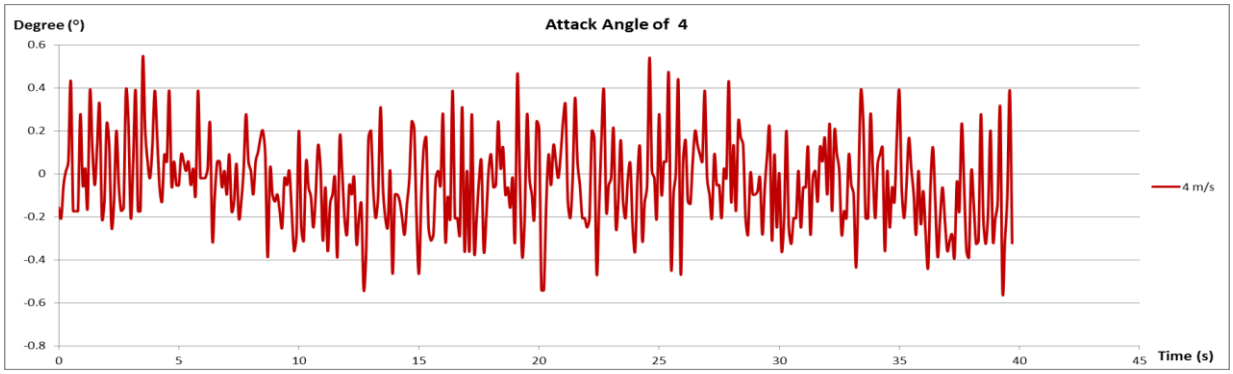
Degree (°)
Attack Angle of 4
0.6
0.4
0.2
0
-0.2
-0.4
-0.6
-0.8
0
5
10
15
20
25
30
35
40
45
Time (s)
4 m/s

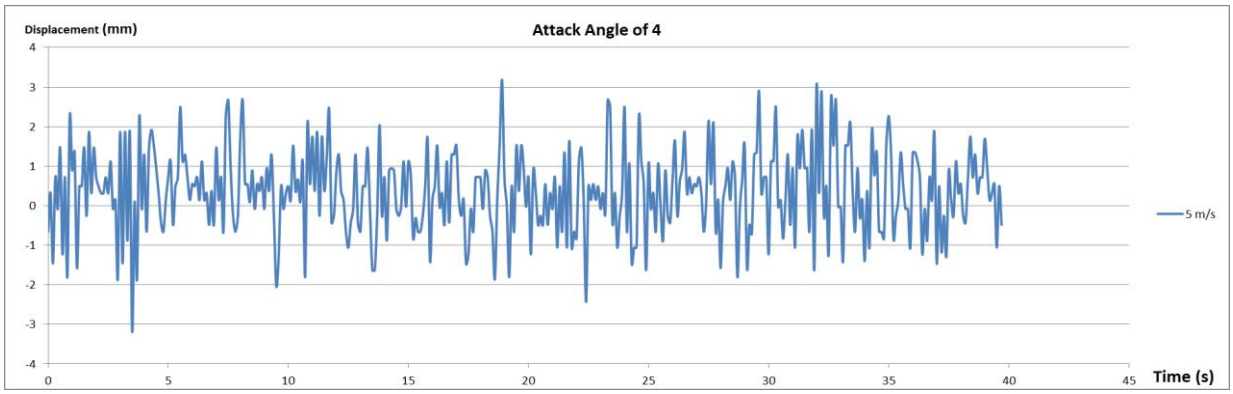
Displacement (mm)
Attack Angle of 4
4
3
2
1
0
-1
-2
-3
-4
0
5
10
15
20
25
30
35
40
45
Time (s)
5 m/s

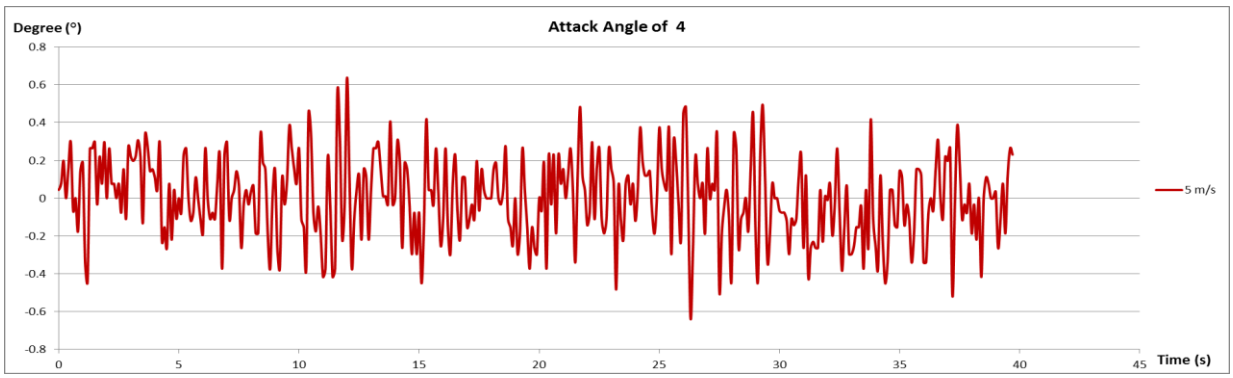
Degree (°)
Attack Angle of 4
0.8
0.6
0.4
0.2
0
-0.2
-0.4
-0.6
-0.8
0
5
10
15
20
25
30
35
40
45
Time (s)
5 m/s

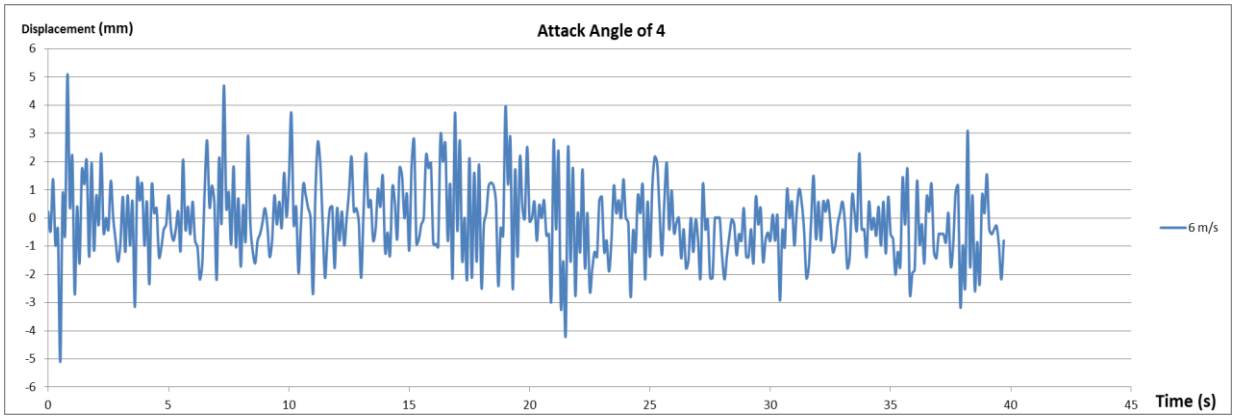
Displacement (mm)
Attack Angle of 4
6
5
4
3
2
1
0
-1
-2
-3
-4
-5
-6
0
5
10
15
20
25
30
35
40
45
Time (s)
6 m/s

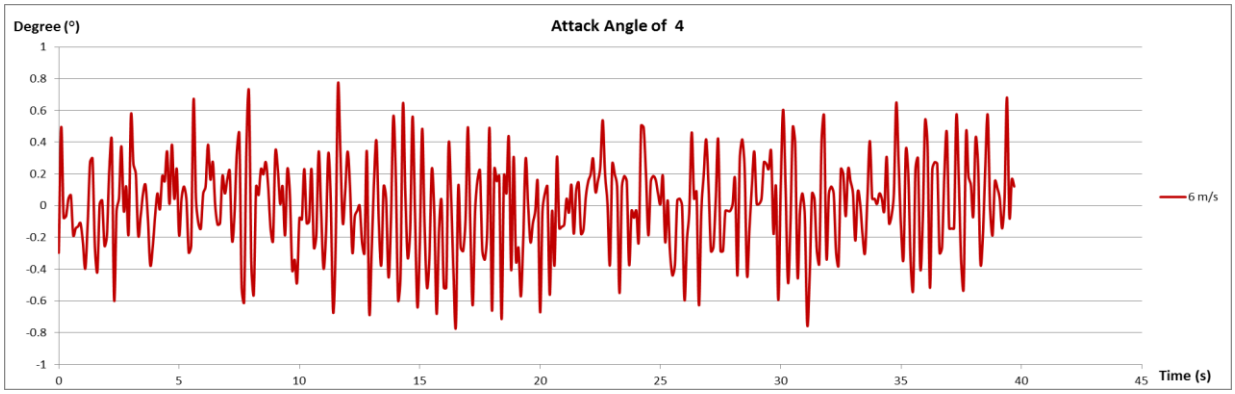
Degree (°)
Attack Angle of 4
1
0.8
0.6
0.4
0.2
0
-0.2
-0.4
-0.6
-0.8
-1
0
5
10
15
20
25
30
35
40
45
Time (s)
6 m/s

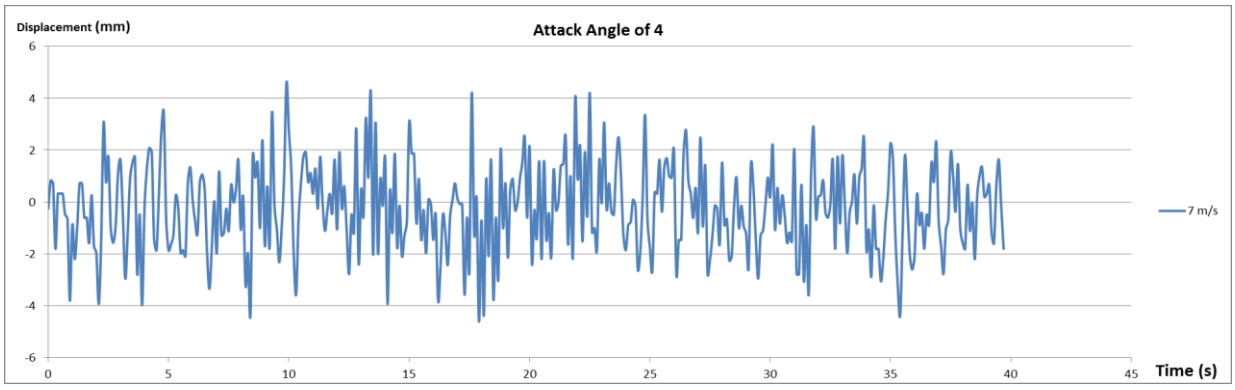
Displacement (mm)
Attack Angle of 4
6
4
2
0
-2
-4
-6
0
5
10
15
20
25
30
35
40
45
Time (s)
7 m/s

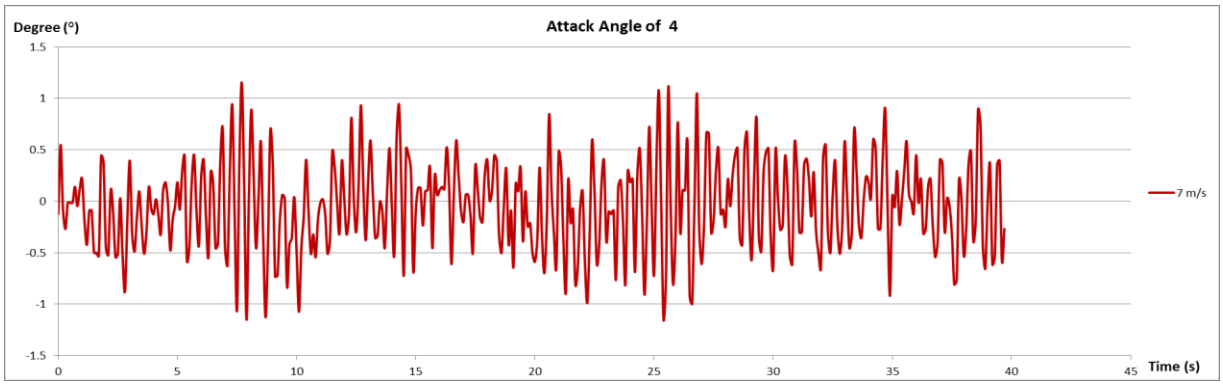
Degree (°)
Attack Angle of 4
1.5
1
0.5
0
-0.5
-1
-1.5
0
5
10
15
20
25
30
35
40
45
Time (s)
7 m/s

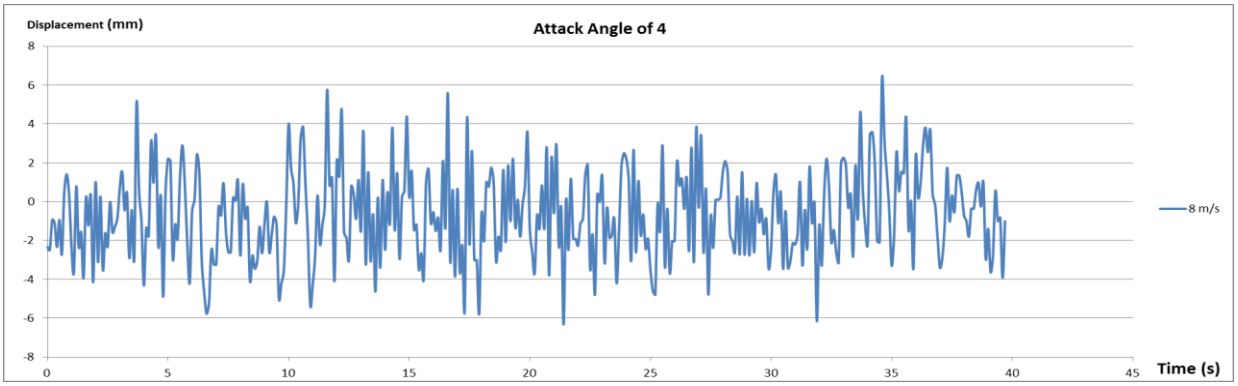

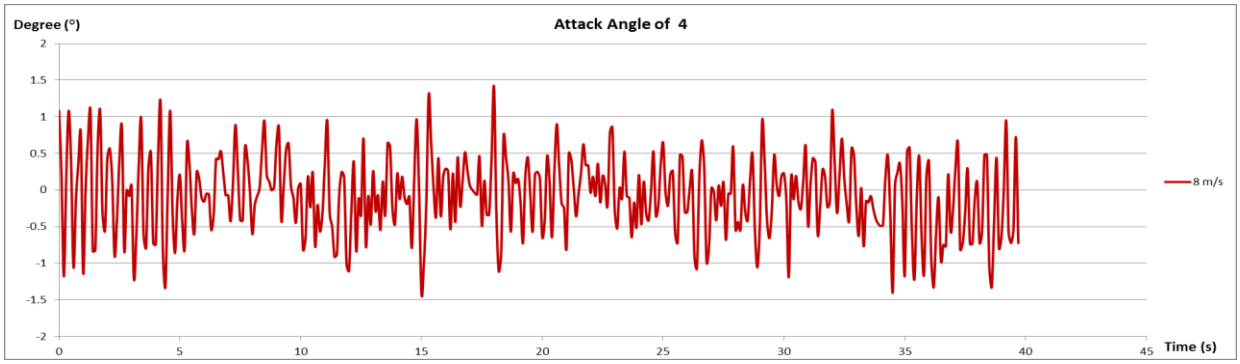

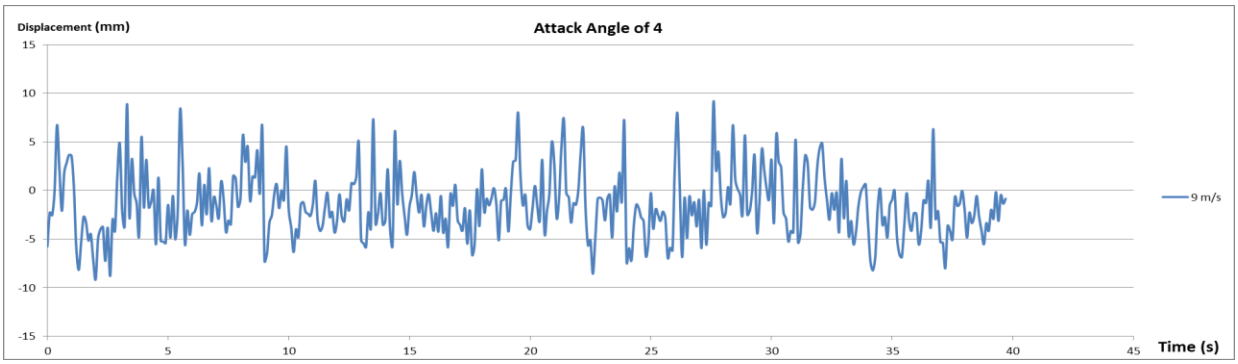

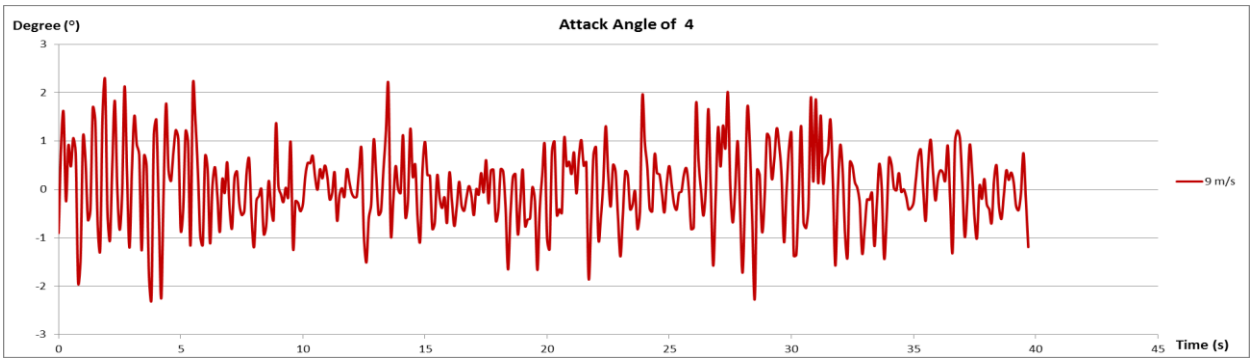

Time displacement histories for the vertical and torsional modes at 4 m/s and 9 m/s wind speed under 4 °attack angle

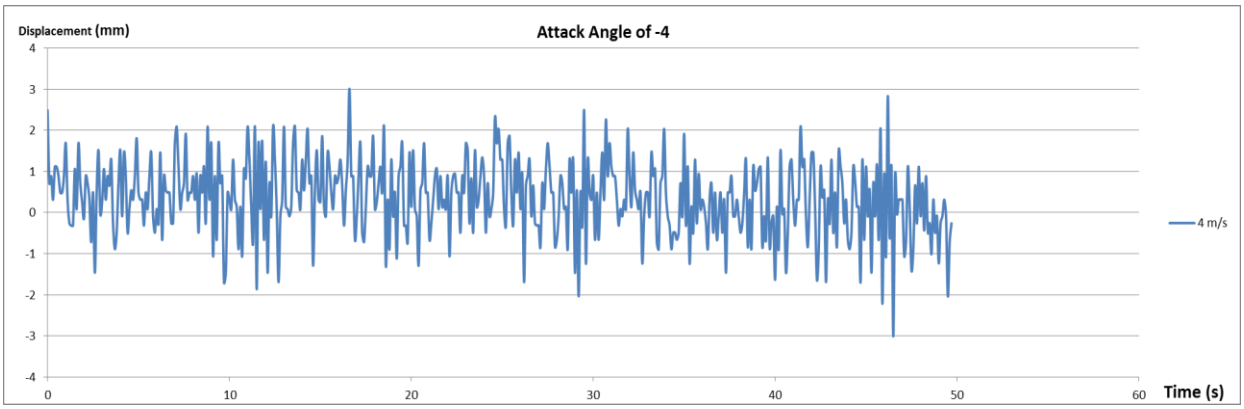
Displacement (mm)
Attack Angle of -4
4
3
2
1
0
-1
-2
-3
-4
0
10
20
30
40
50
60
Time (s)
4 m/s

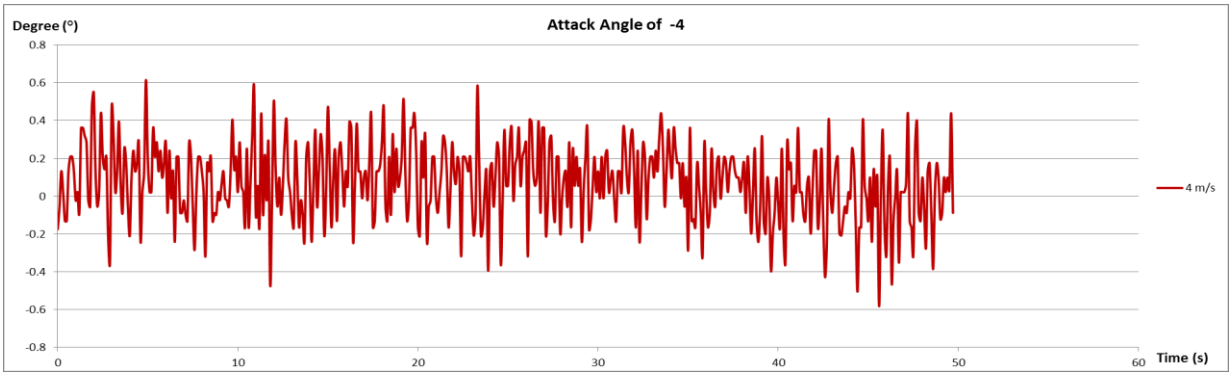
Degree (°)
Attack Angle of -4
0.8
0.6
0.4
0.2
0
-0.2
-0.4
-0.6
-0.8
0
10
20
30
40
50
60
Time (s)
4 m/s

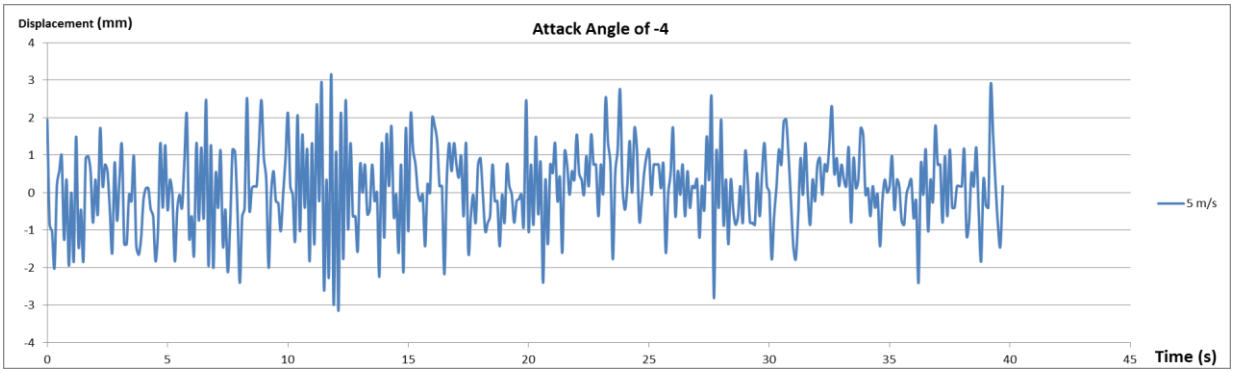
Displacement (mm)
Attack Angle of -4
4
3
2
1
0
-1
-2
-3
-4
0
5
10
15
20
25
30
35
40
45
Time (s)
5 m/s

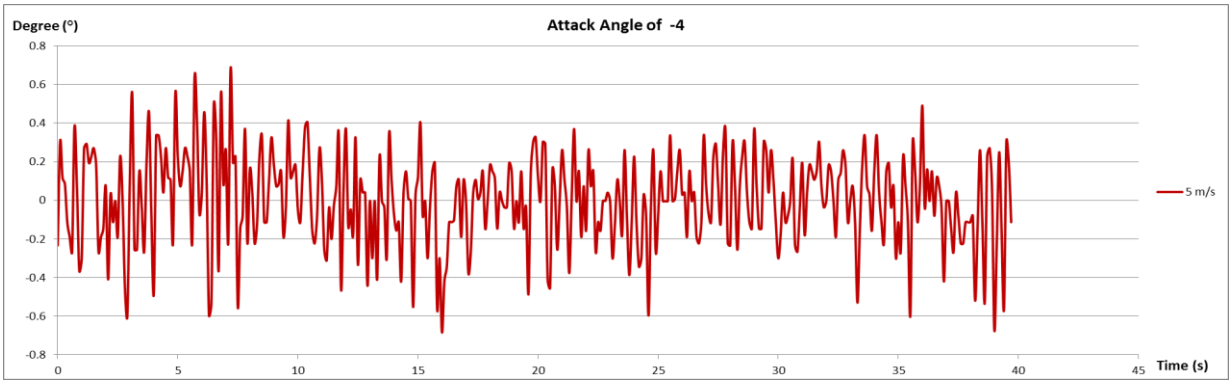
Degree (°)
Attack Angle of -4
0.8
0.6
0.4
0.2
0
-0.2
-0.4
-0.6
-0.8
0
5
10
15
20
25
30
35
40
45
Time (s)
5 m/s

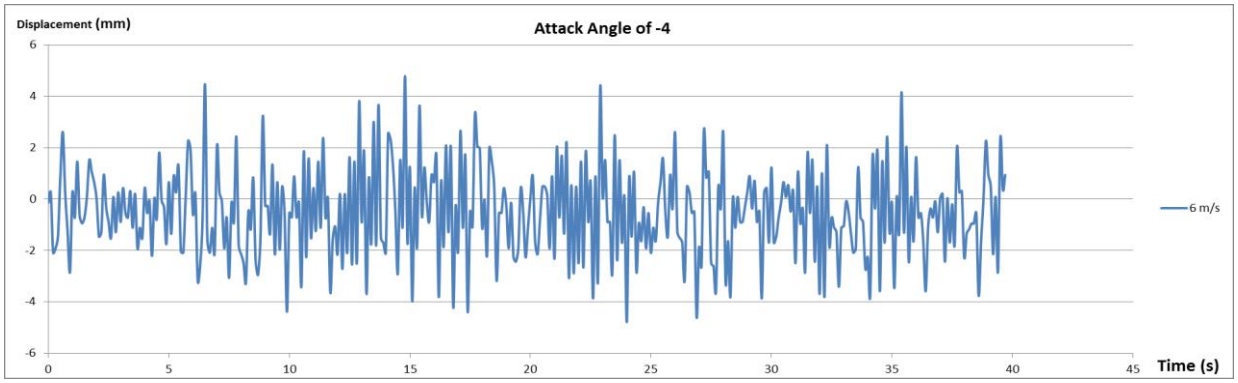
Displacement (mm)
Attack Angle of -4
6
4
2
0
-2
-4
-6
0
5
10
15
20
25
30
35
40
45
Time (s)
6 m/s

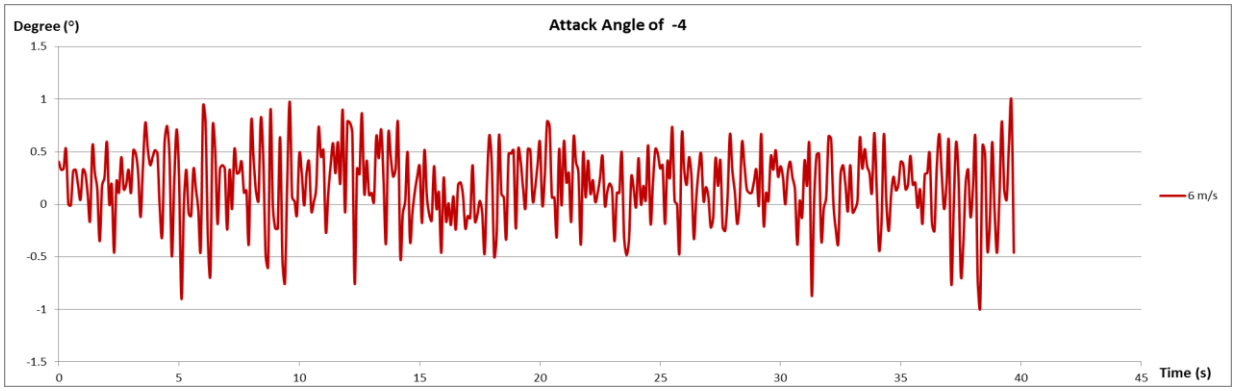
Degree (°)
Attack Angle of -4
1.5
1
0.5
0
-0.5
-1
-1.5
0
5
10
15
20
25
30
35
40
45
Time (s)
6 m/s

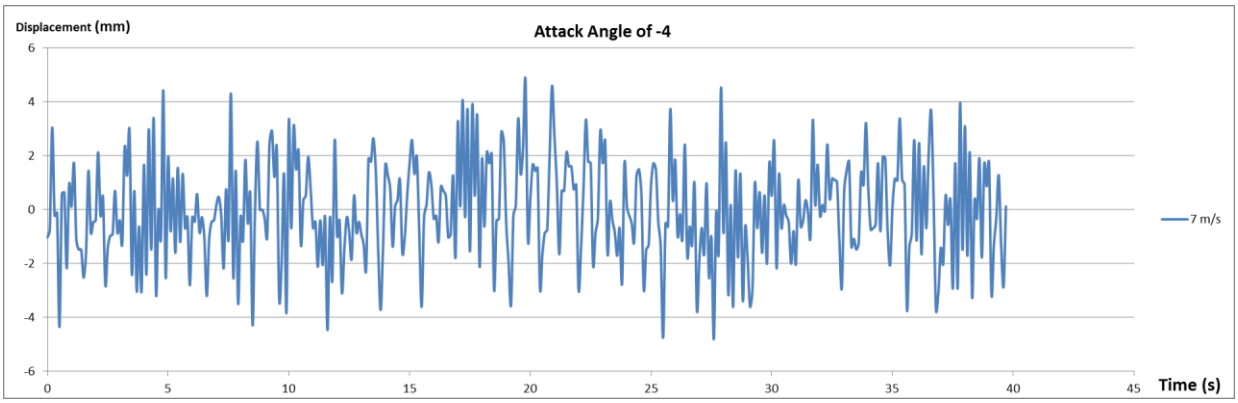
Displacement (mm)
Attack Angle of -4
6
4
2
0
-2
-4
-6
0
5
10
15
20
25
30
35
40
45
Time (s)
7 m/s

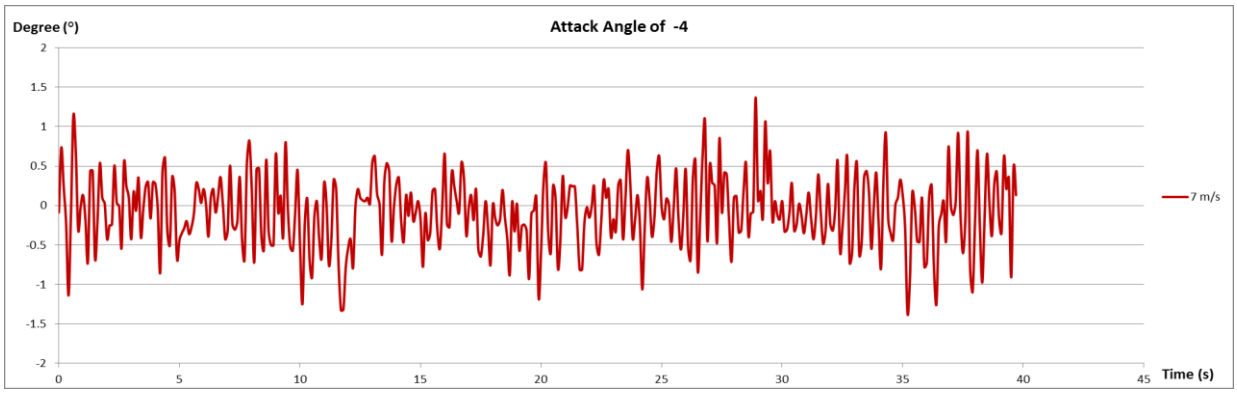
Degree (°)
Attack Angle of -4
2
1.5
1
0.5
0
-0.5
-1
-1.5
-2
0
5
10
15
20
25
30
35
40
45
Time (s)
7 m/s

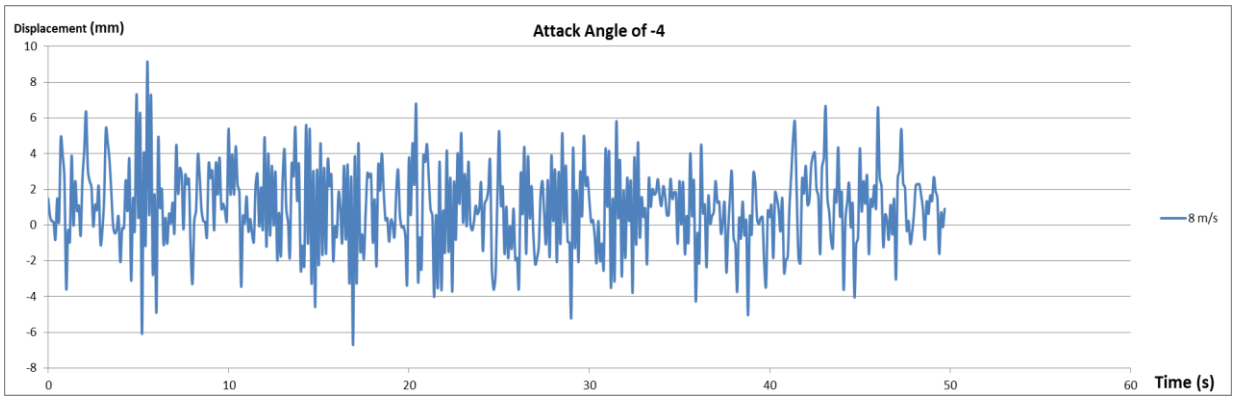
Displacement (mm)
Attack Angle of -4
10
8
6
4
2
0
-2
-4
-6
-8
0
10
20
30
40
50
60
Time (s)
8 m/s

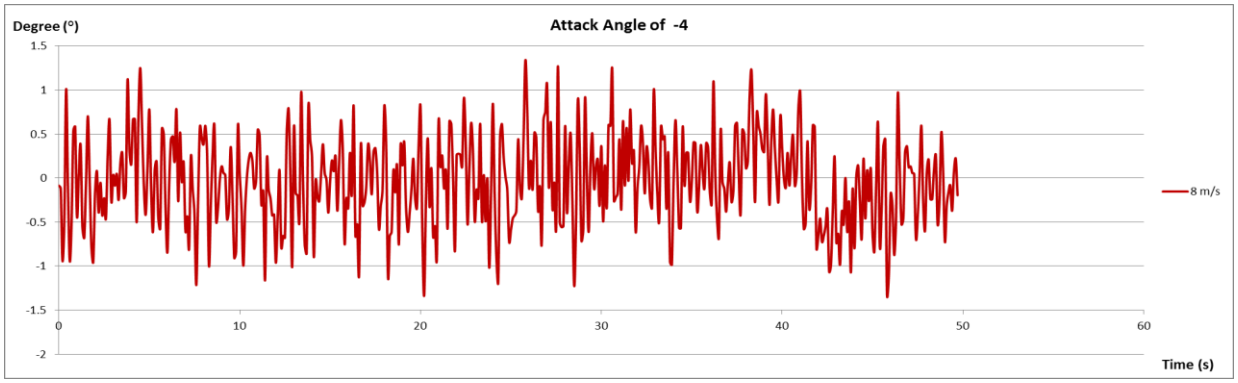
Degree (°)
Attack Angle of -4
1.5
1
0.5
0
-0.5
-1
-1.5
-2
0
10
20
30
40
50
60
Time (s)
8 m/s

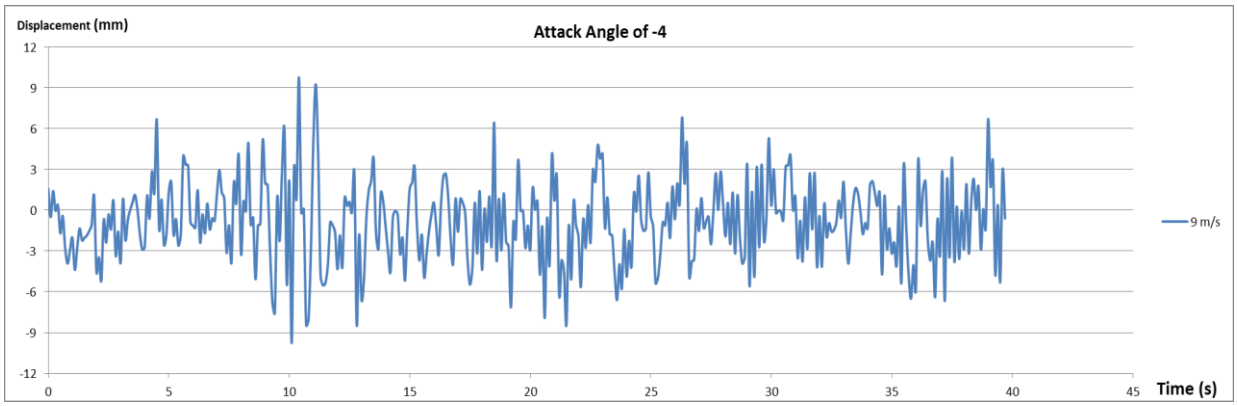
Displacement (mm)
Attack Angle of -4
12
9
6
3
0
-3
-6
-9
-12
0
5
10
15
20
25
30
35
40
45
Time (s)
9 m/s

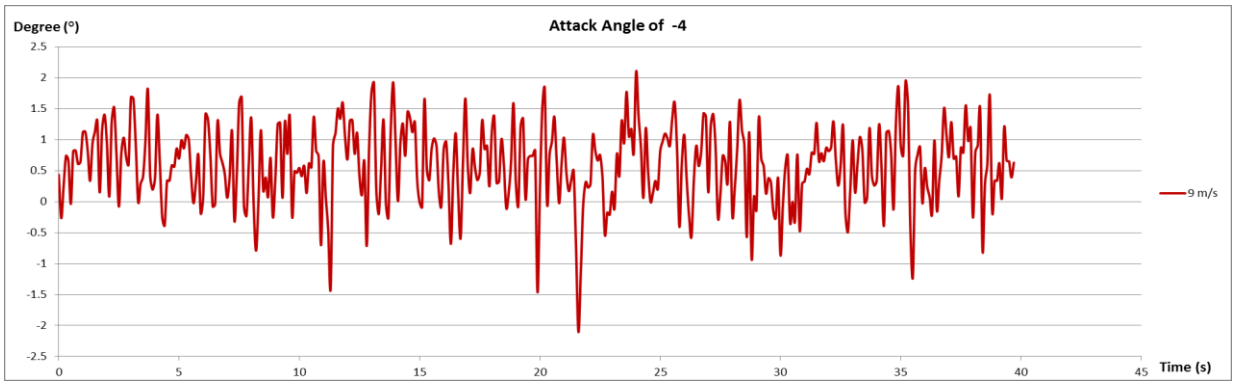
Degree (°)
Attack Angle of -4
2.5
2
1.5
1
0.5
0
-0.5
-1
-1.5
-2
-2.5
0
5
10
15
20
25
30
35
40
45
Time (s)
9 m/s

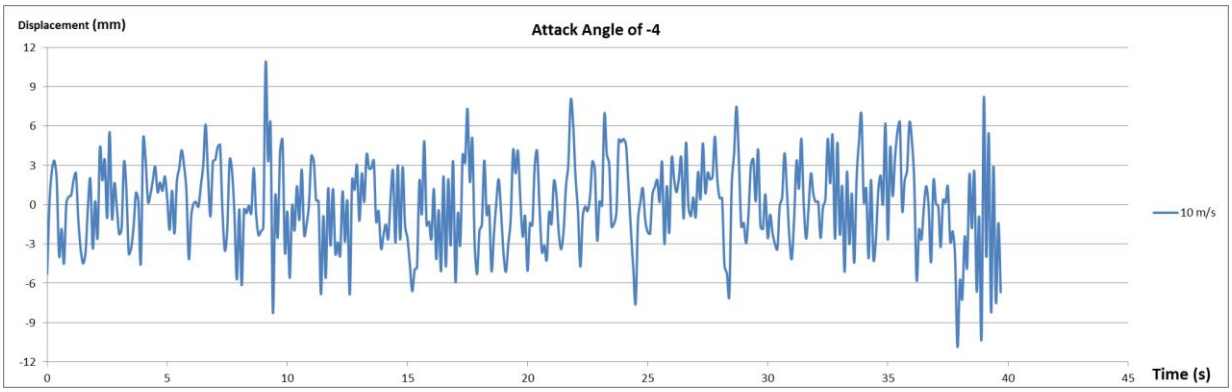

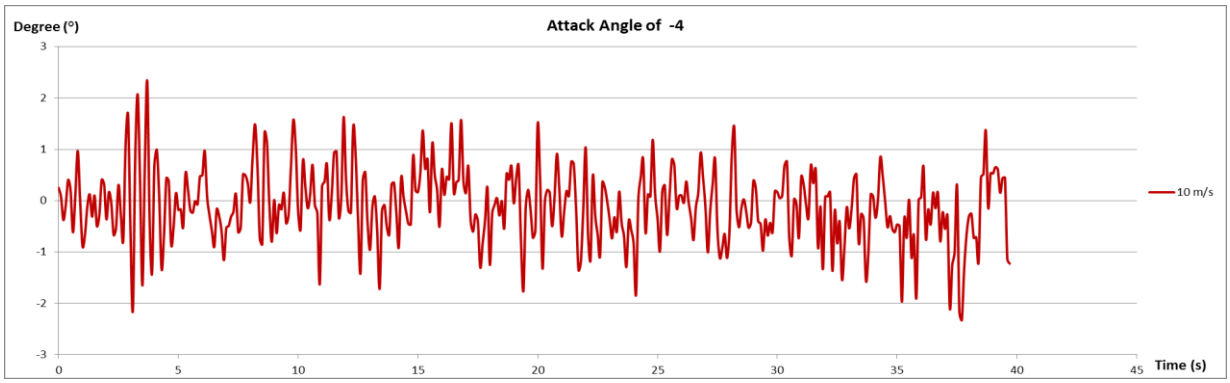

Time displacement histories for the vertical and torsional modes at 4 m/s and 10 m/s wind speed under -4 °attack angle

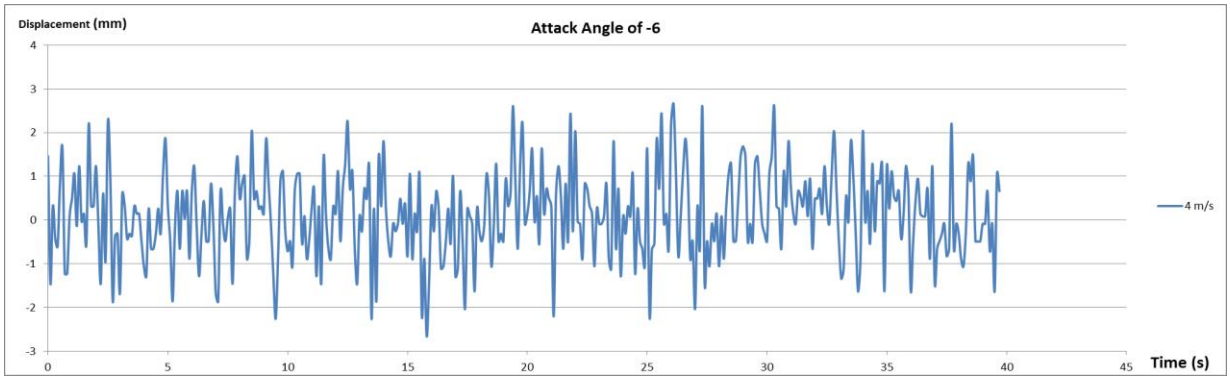

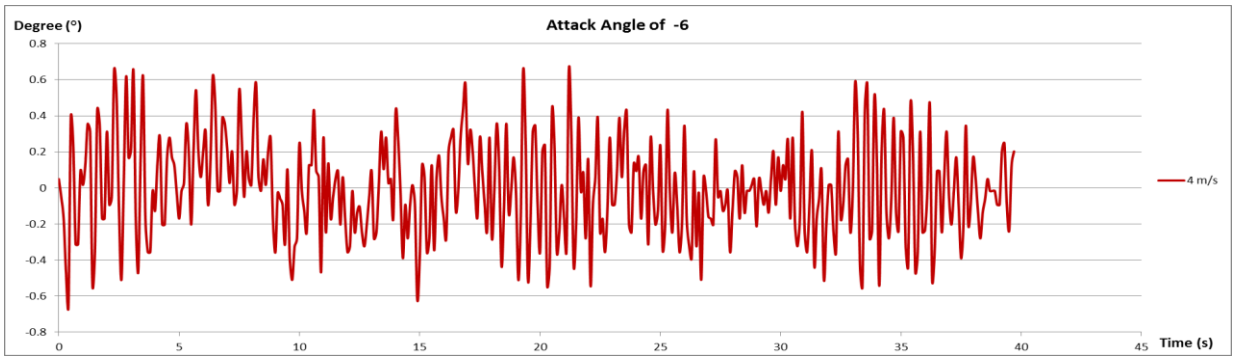
Degree (°)
Attack Angle of -6
0.8
0.6
0.4
0.2
0
-0.2
-0.4
-0.6
-0.8
0
5
10
15
20
25
30
35
40
45
Time (s)
4 m/s

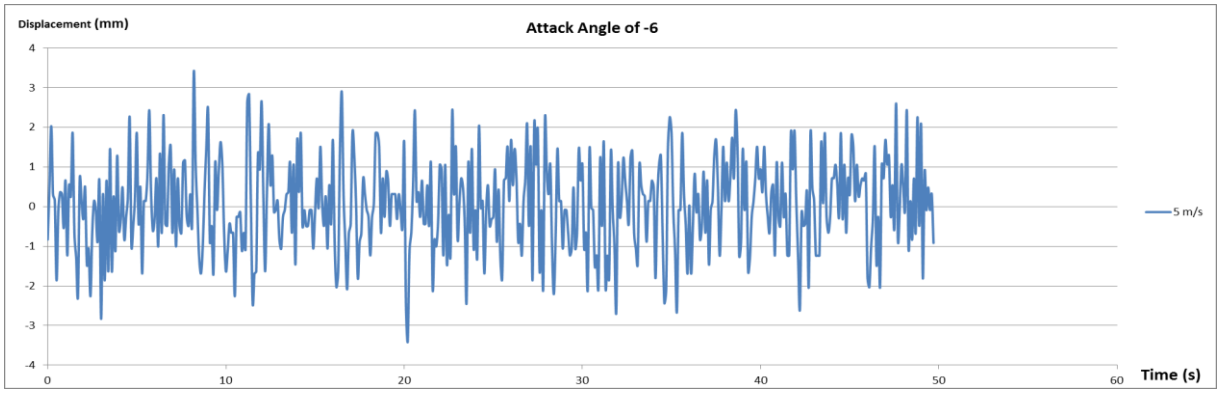
Displacement (mm)
Attack Angle of -6
4
3
2
1
0
-1
-2
-3
-4
0
10
20
30
40
50
60
Time (s)
5 m/s

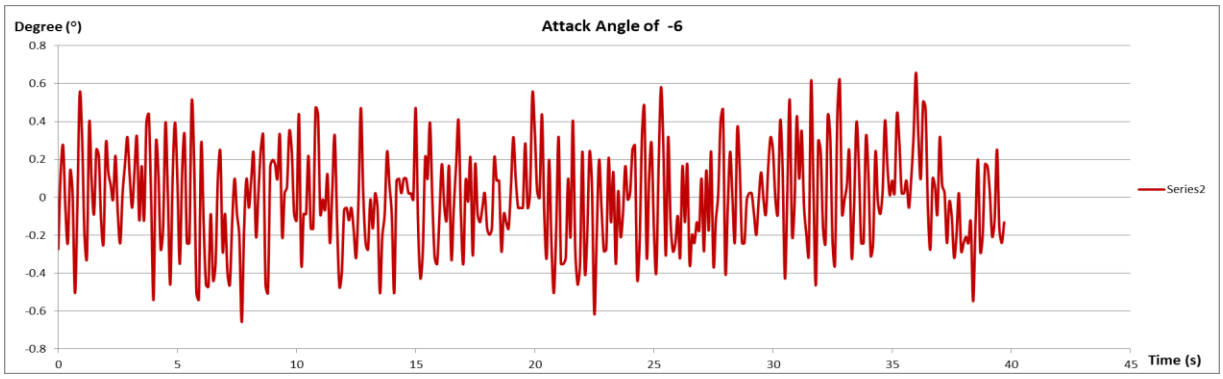
Degree (°)
Attack Angle of -6
0.8
0.6
0.4
0.2
0
-0.2
-0.4
-0.6
-0.8
0
5
10
15
20
25
30
35
40
45
Time (s)
Series2

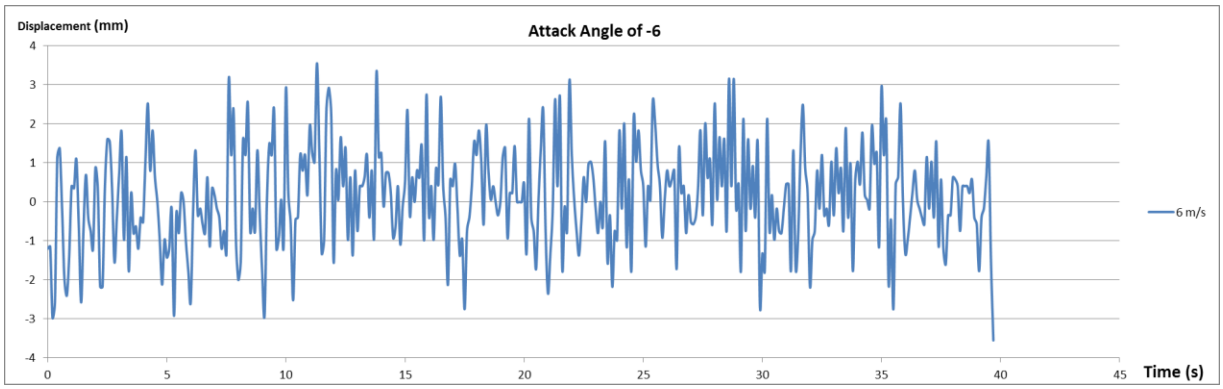
Displacement (mm)
Attack Angle of -6
4
3
2
1
0
-1
-2
-3
-4
0
5
10
15
20
25
30
35
40
45
Time (s)
6 m/s

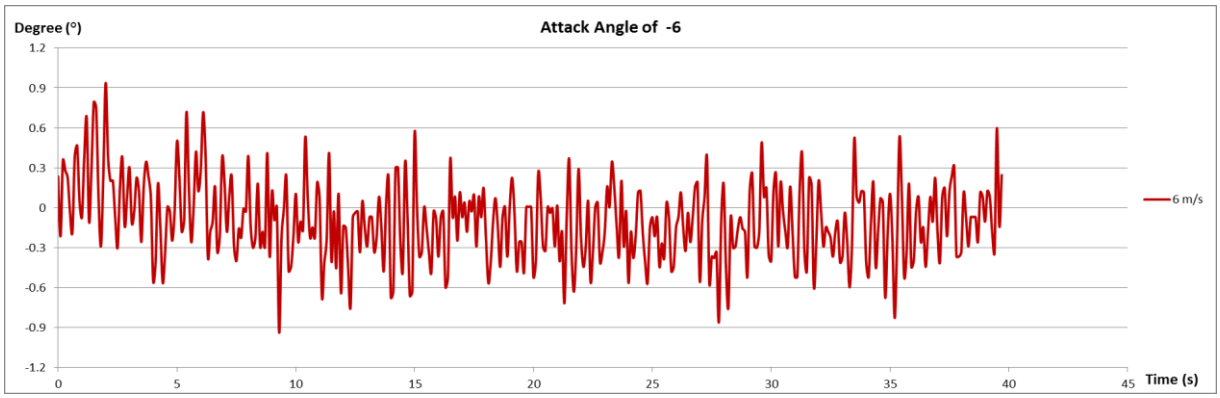
Degree (°)
Attack Angle of -6
1.2
0.9
0.6
0.3
0
-0.3
-0.6
-0.9
-1.2
0
5
10
15
20
25
30
35
40
45
Time (s)
6 m/s

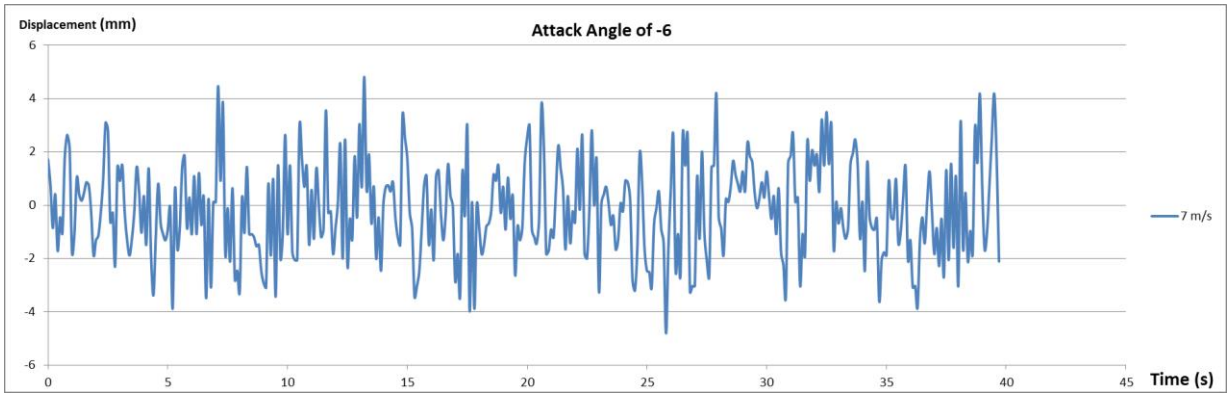
Displacement (mm)
Attack Angle of -6
6
4
2
0
-2
-4
-6
0
5
10
15
20
25
30
35
40
45
Time (s)
7 m/s

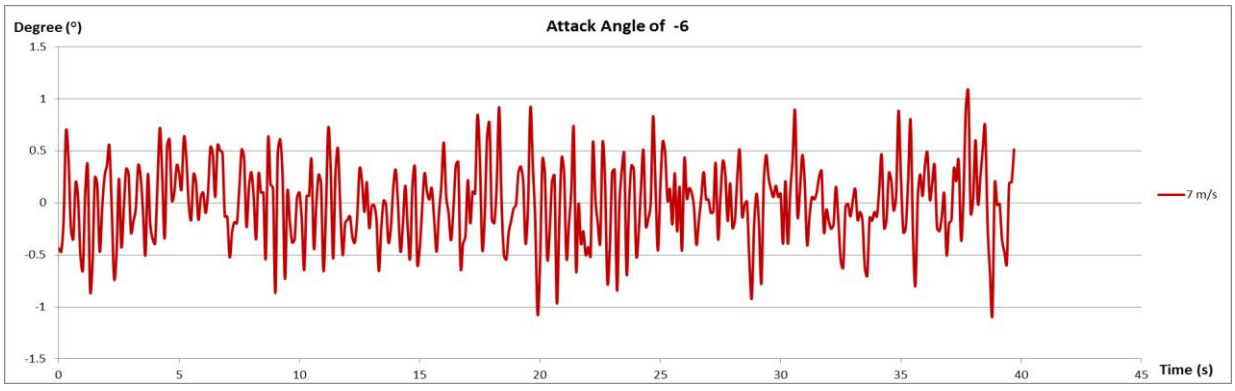
Degree (°)
Attack Angle of -6
1.5
1
0.5
0
-0.5
-1
-1.5
0
5
10
15
20
25
30
35
40
45
Time (s)
7 m/s

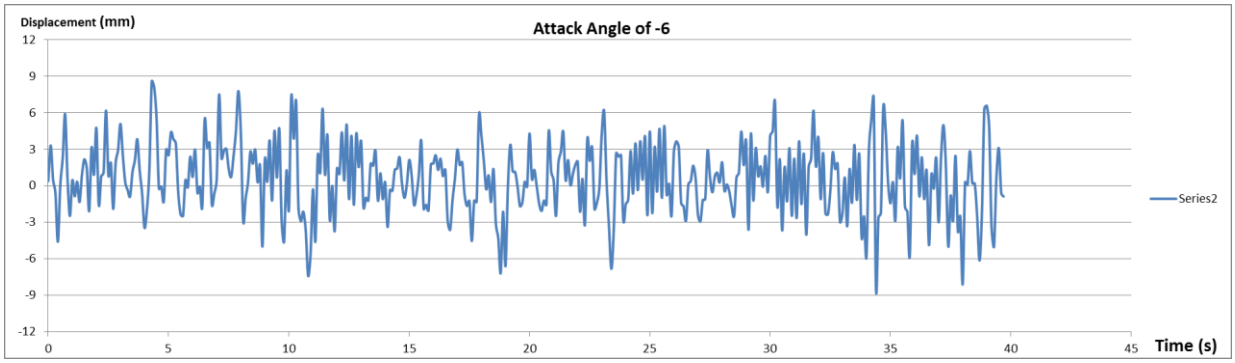

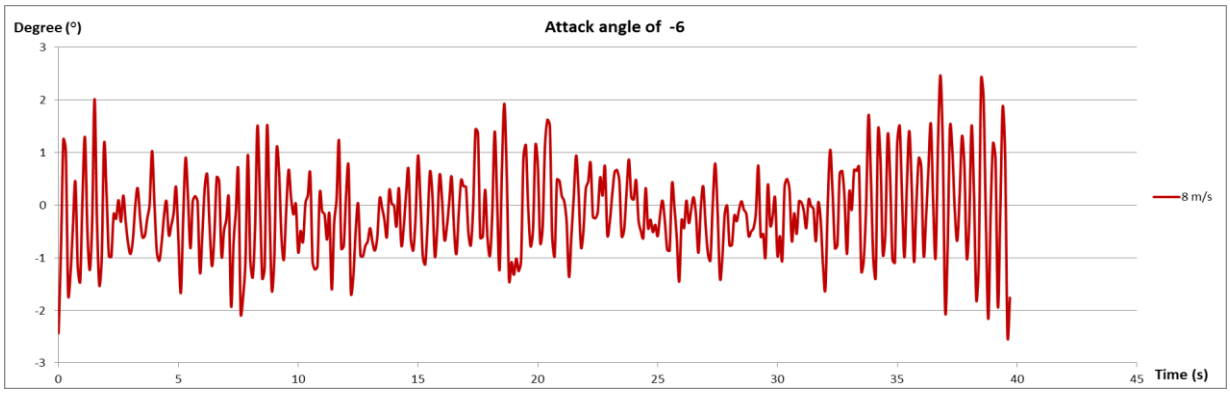

Time displacement histories for the vertical and torsional modes at 4 m/s and 8 m/s wind speed under -6 °attack angle

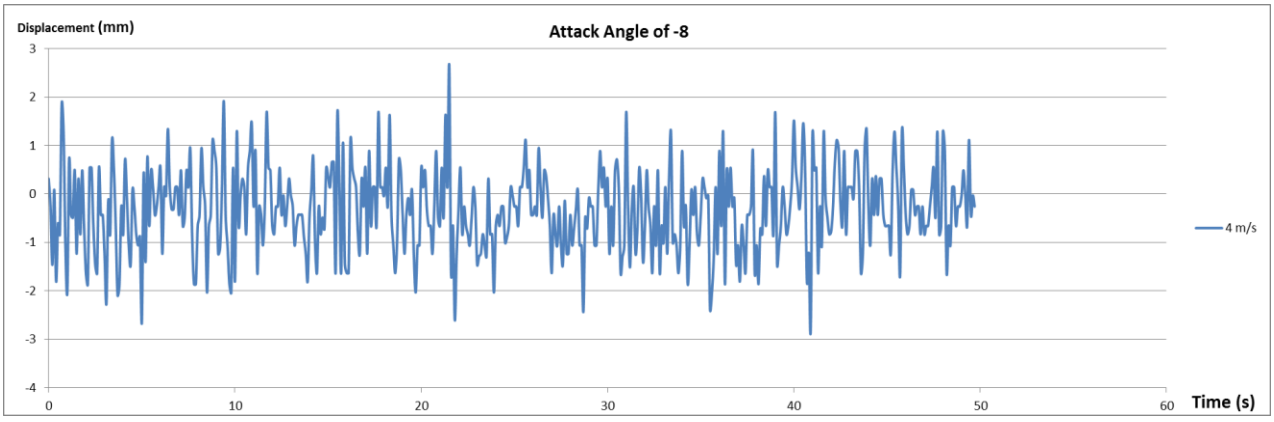

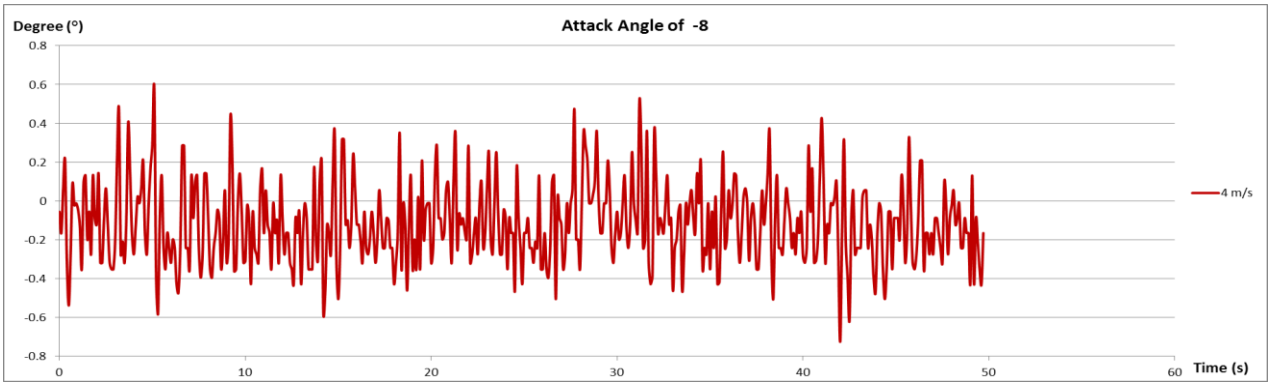
Degree (°)
Attack Angle of -8
0.8
0.6
0.4
0.2
0
-0.2
-0.4
-0.6
-0.8
0
10
20
30
40
50
60
Time (s)
4 m/s

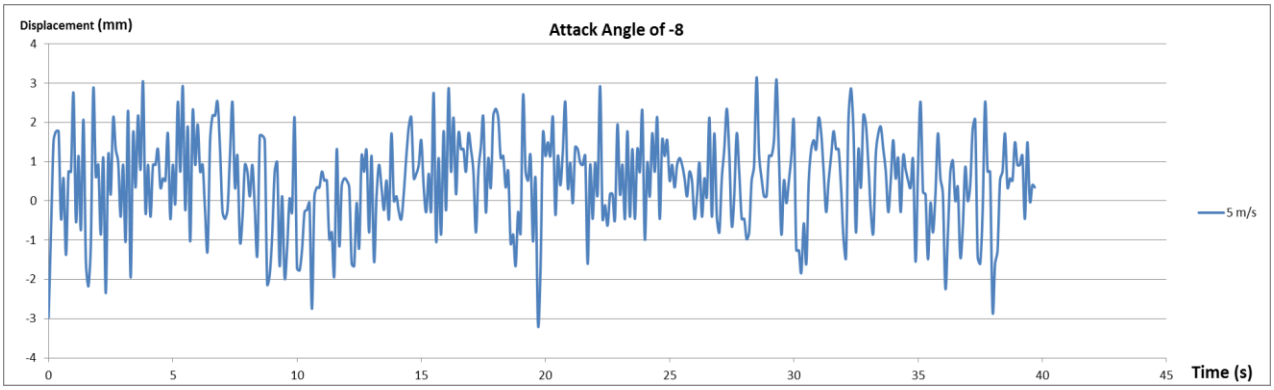
Displacement (mm)
Attack Angle of -8
4
3
2
1
0
-1
-2
-3
-4
0
5
10
15
20
25
30
35
40
45
Time (s)
5 m/s

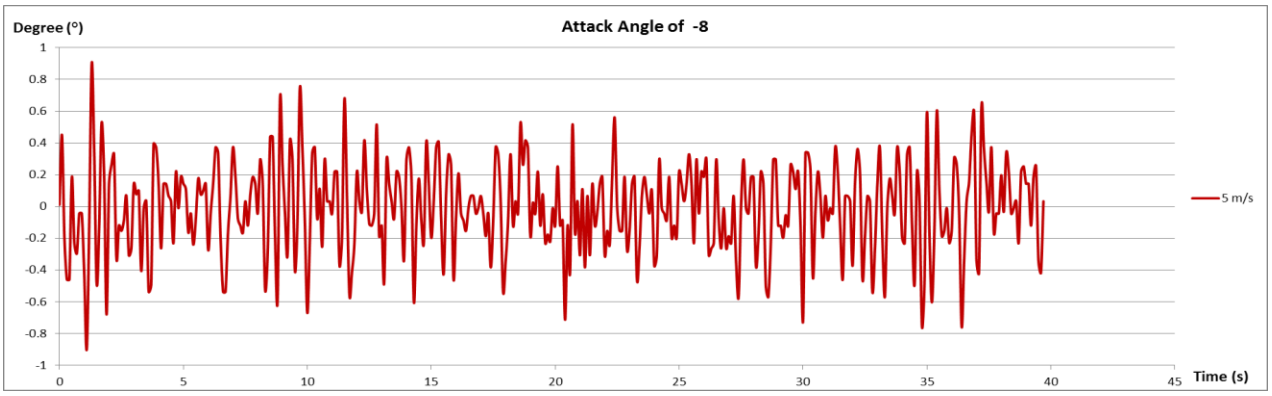
Degree (°)
Attack Angle of -8
1
0.8
0.6
0.4
0.2
0
-0.2
-0.4
-0.6
-0.8
-1
0
5
10
15
20
25
30
35
40
45
Time (s)
5 m/s

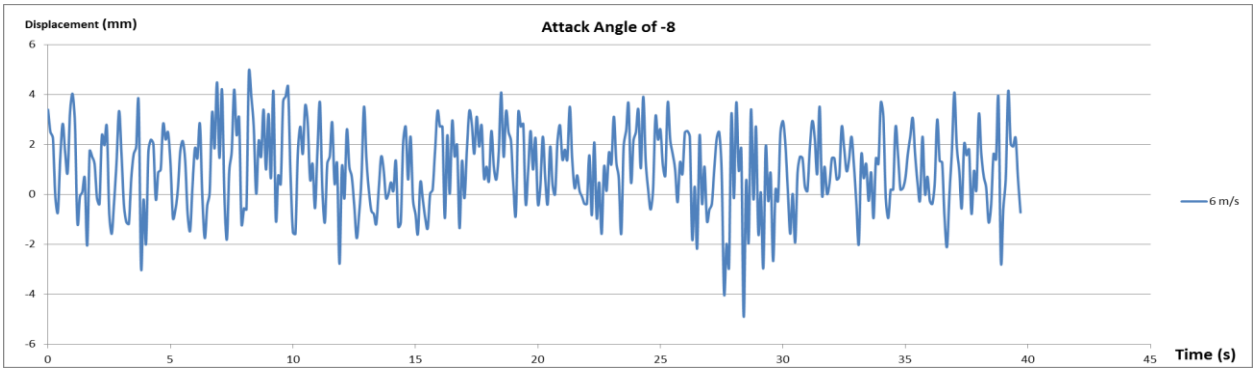
Displacement (mm)
Attack Angle of -8
6
4
2
0
-2
-4
-6
0
5
10
15
20
25
30
35
40
45
Time (s)
6 m/s

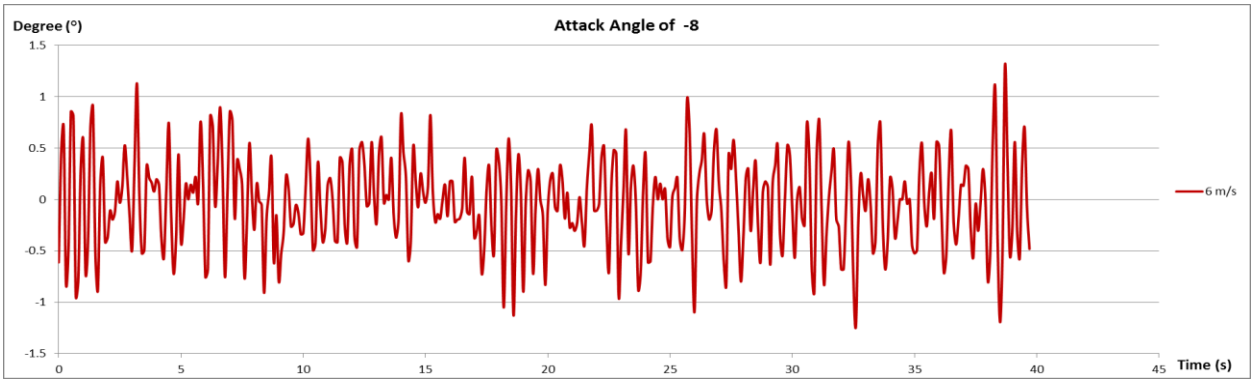

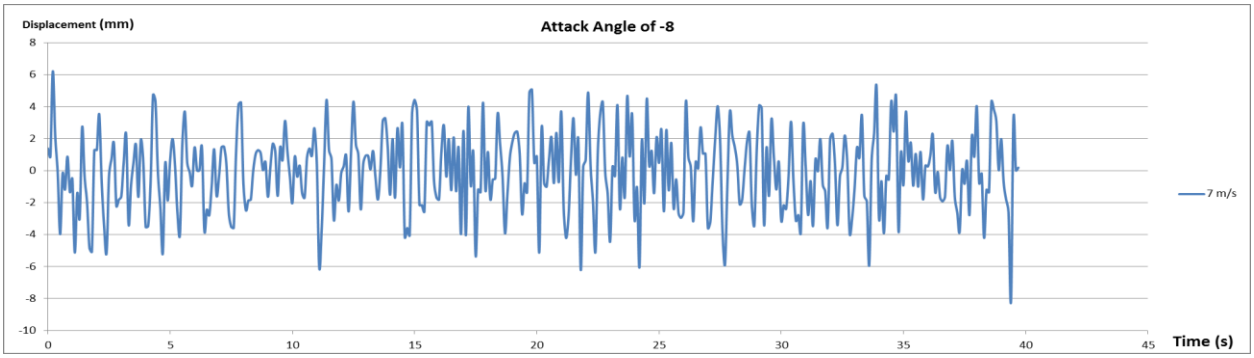

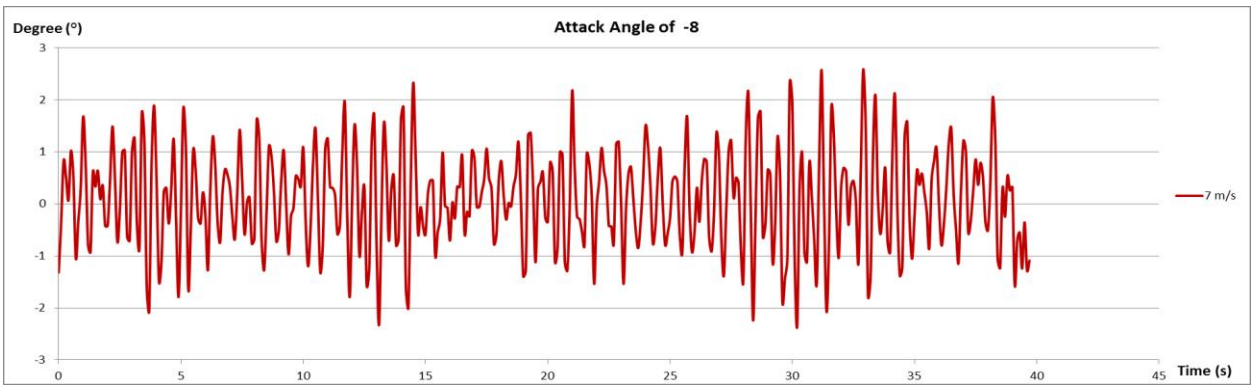

Time displacement histories for the vertical and torsional modes at 4 m/s and 7 m/s wind speed under -8 °attack angle

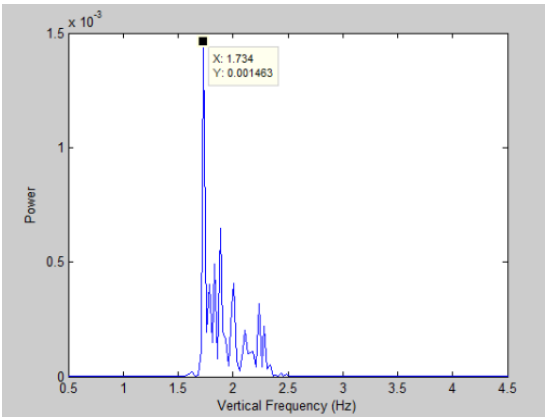
x 10^-3
X: 1.734
Y: 0.001463
Power
Vertical Frequency (Hz)

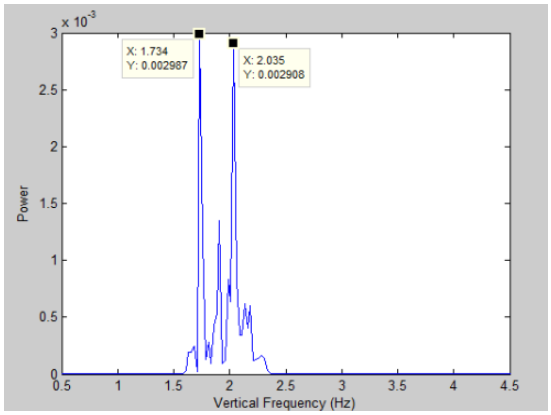
x 10^-3
X: 1.734
Y: 0.002987
X: 2.035
Y: 0.002908
Power
Vertical Frequency (Hz)

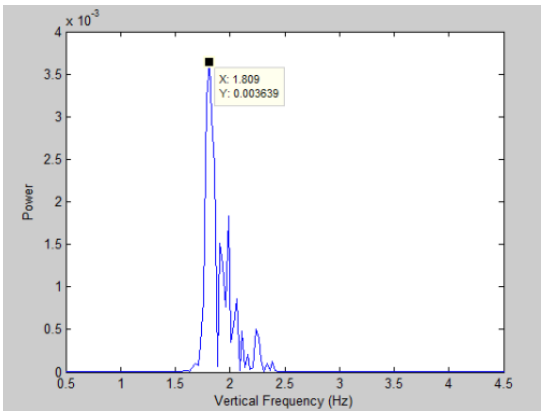
x 10^-3
X: 1.809
Y: 0.003639
Power
Vertical Frequency (Hz)

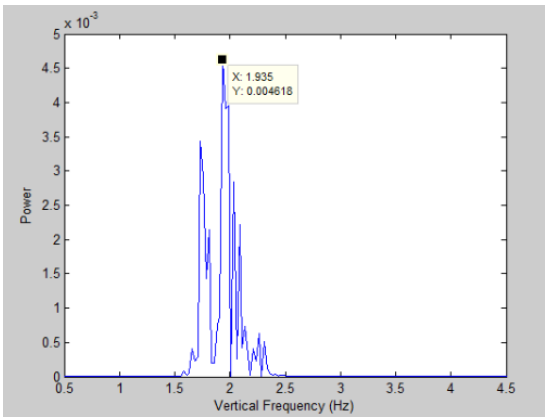
x 10^-3
X: 1.935
Y: 0.004618
Power
Vertical Frequency (Hz)

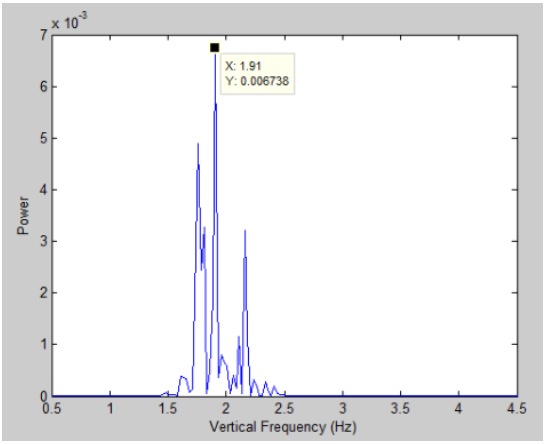
x 10^-3
X: 1.91
Y: 0.006738
Power
Vertical Frequency (Hz)

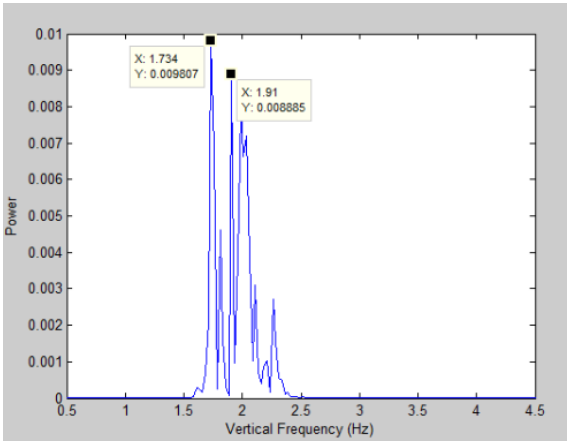
X: 1.734
Y: 0.009807
X: 1.91
Y: 0.008885
Power
Vertical Frequency (Hz)

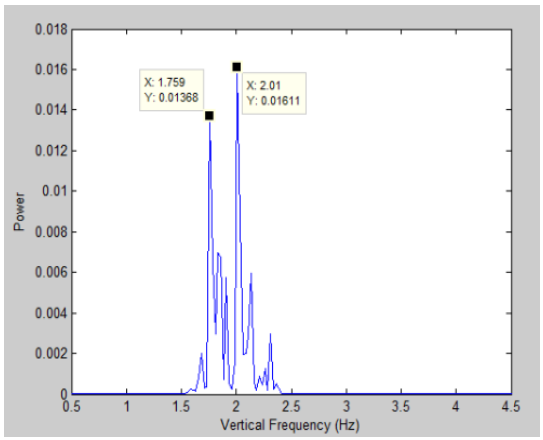

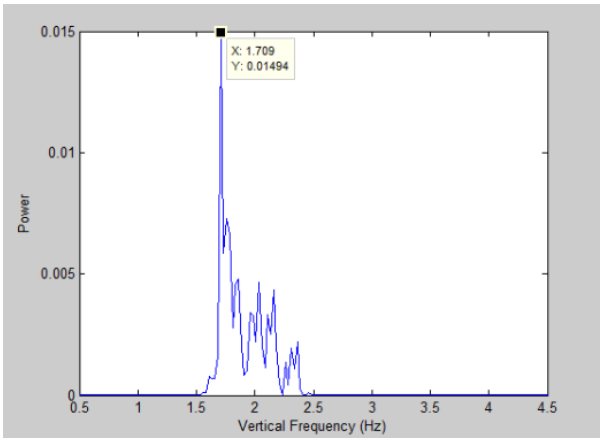

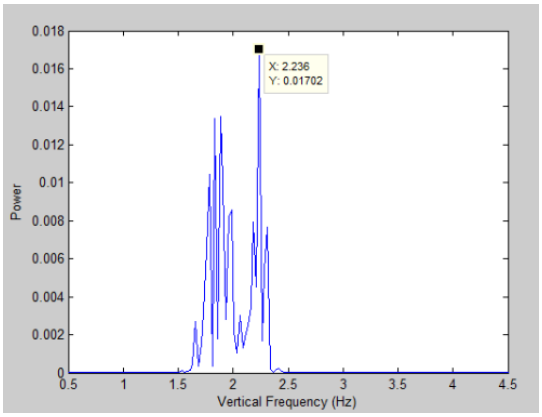

Frequency variation for vertical mode for attack angle of 0 °

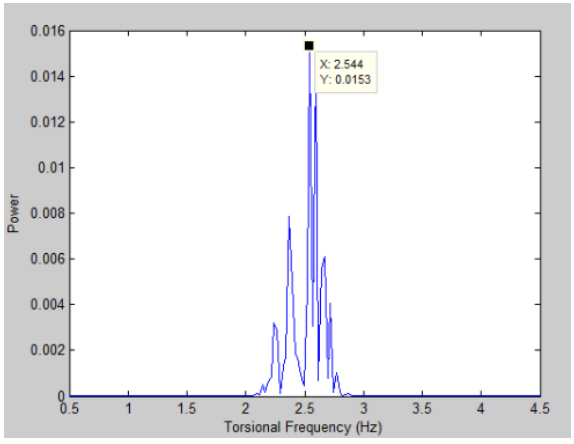

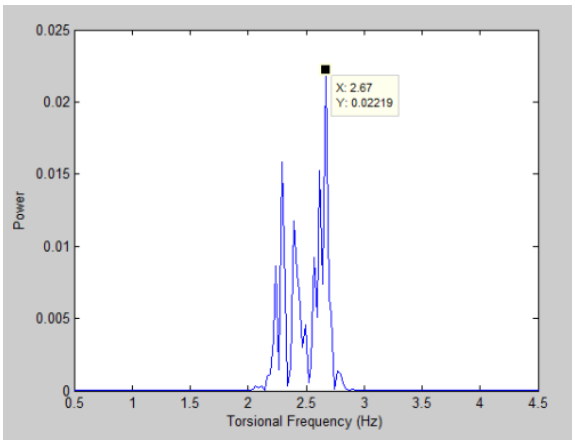

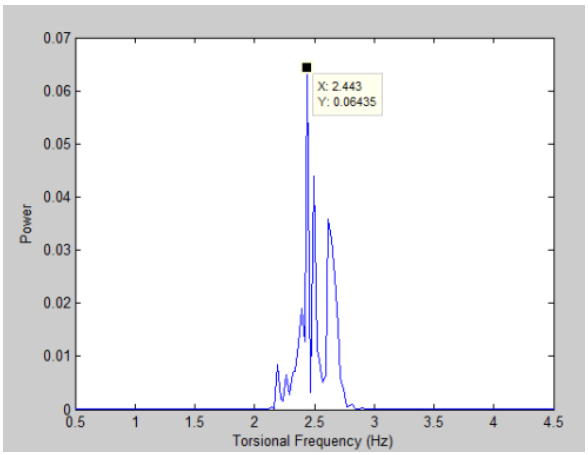
X: 2.443
Y: 0.06435
Power
Torsional Frequency (Hz)

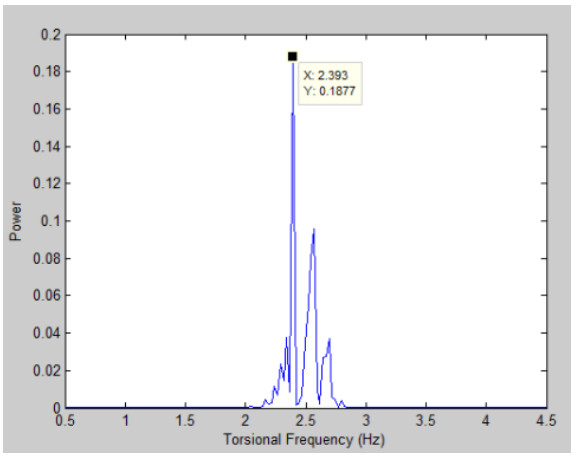
X: 2.393
Y: 0.1877
Power
Torsional Frequency (Hz)

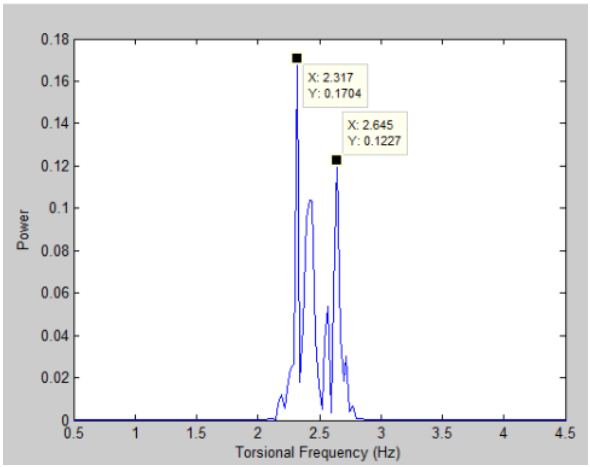
X: 2.317
Y: 0.1704
X: 2.645
Y: 0.1227
Power
Torsional Frequency (Hz)

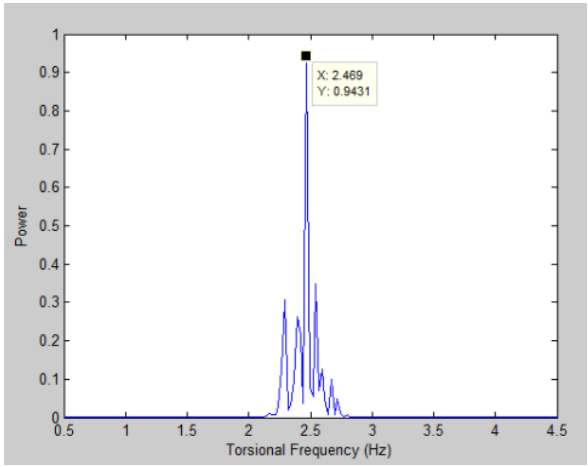
X: 2.469
Y: 0.9431
Power
Torsional Frequency (Hz)

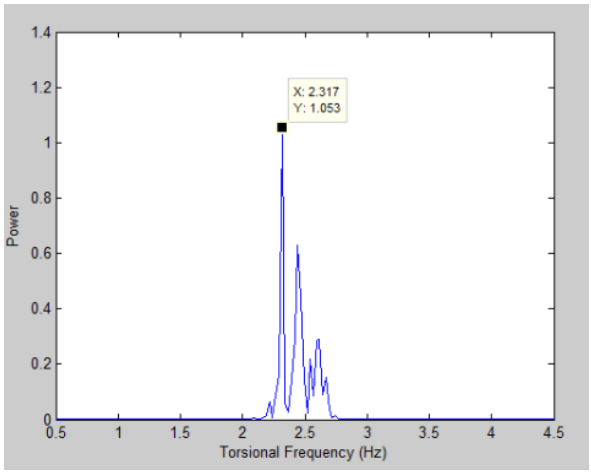
X: 2.317
Y: 1.053
Power
Torsional Frequency (Hz)

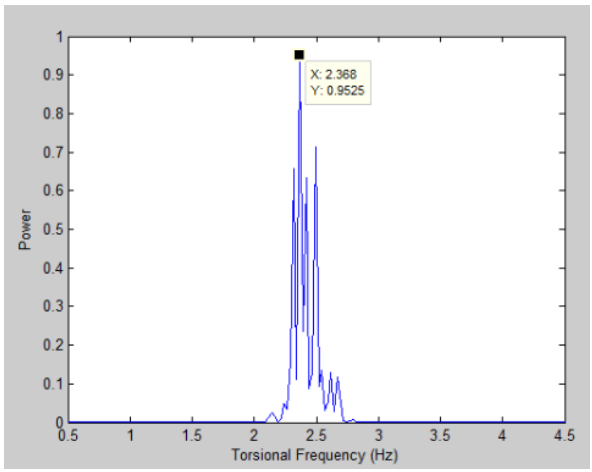
X: 2.368
Y: 0.9525
Power
Torsional Frequency (Hz)

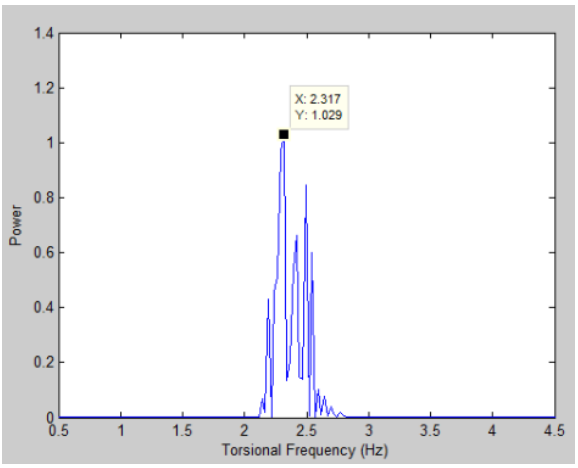

Frequency variation for torsional vibration mode for attack angle of 0 °

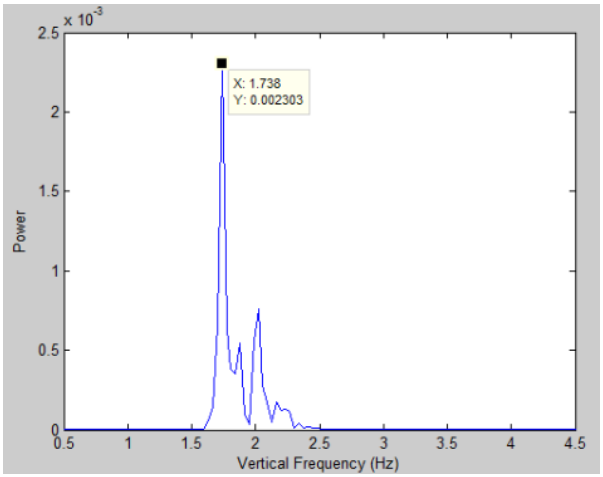

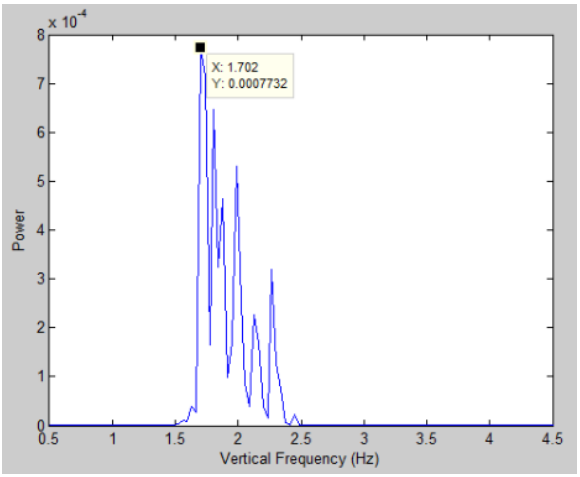

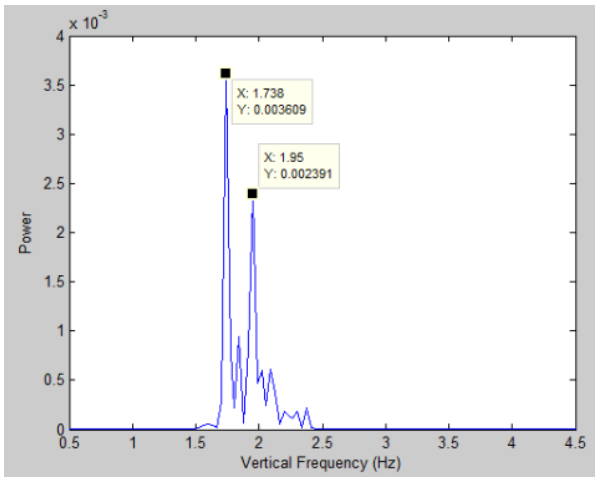
x 10^-3
X: 1.738
Y: 0.003609
X: 1.95
Y: 0.002391
Power
Vertical Frequency (Hz)

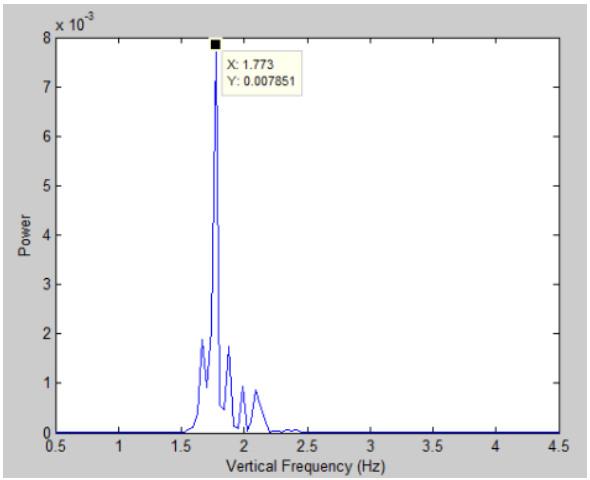
x 10^-3
X: 1.773
Y: 0.007851
Power
Vertical Frequency (Hz)

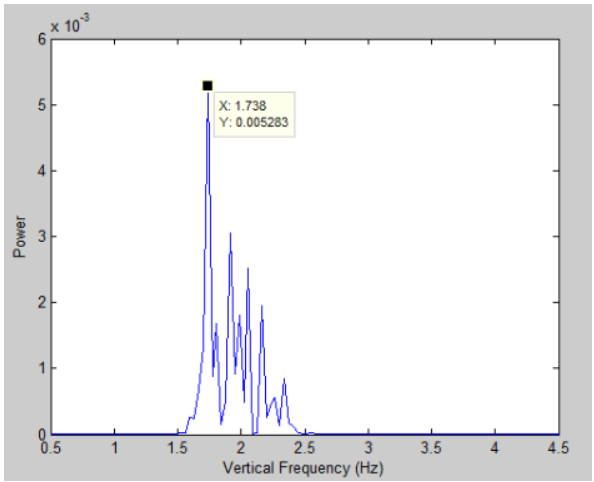
x 10^-3
X: 1.738
Y: 0.005283
Power
Vertical Frequency (Hz)

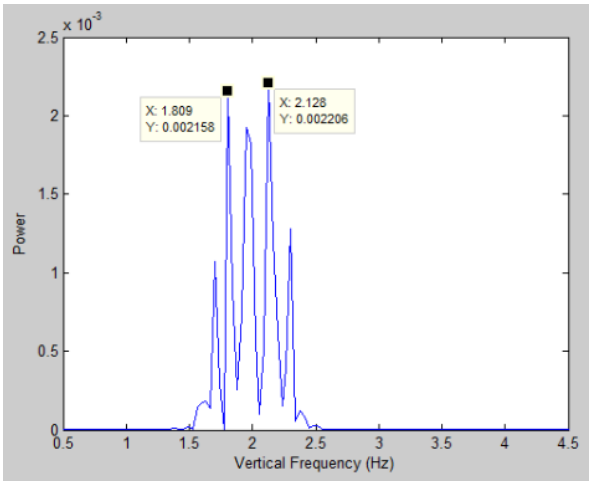
x 10^-3
X: 1.809
Y: 0.002158
X: 2.128
Y: 0.002206
Power
Vertical Frequency (Hz)

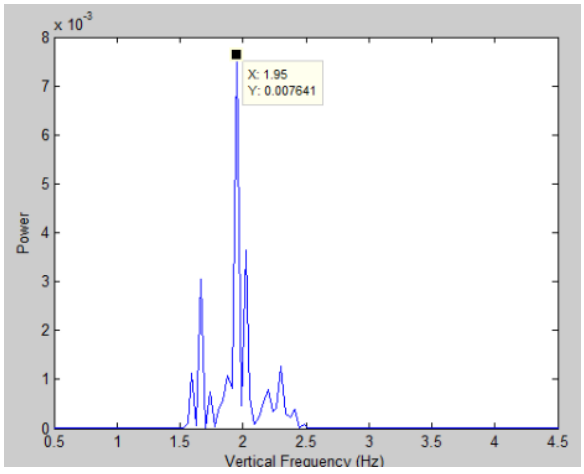
x 10^-3
X: 1.95
Y: 0.007641
Power
Vertical Frequency (Hz)

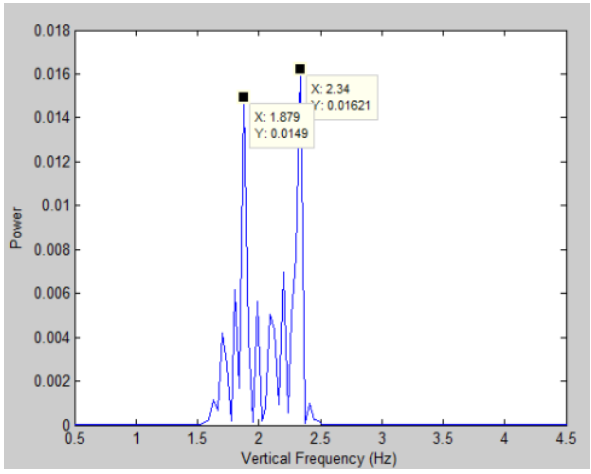
X: 2.34
Y: 0.01621
X: 1.879
Y: 0.0149
Power
Vertical Frequency (Hz)

Frequency variation for vertical vibration mode for attack angle of 2 °

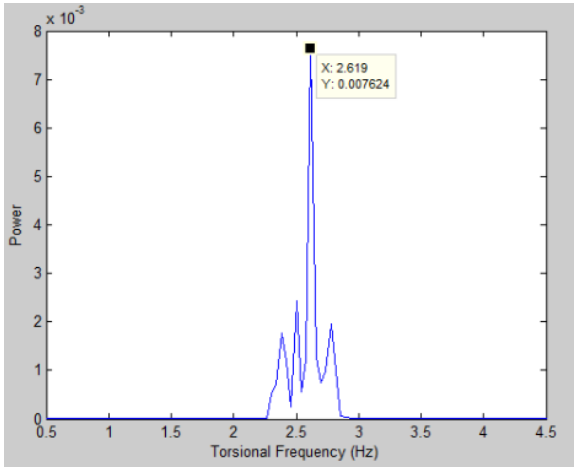

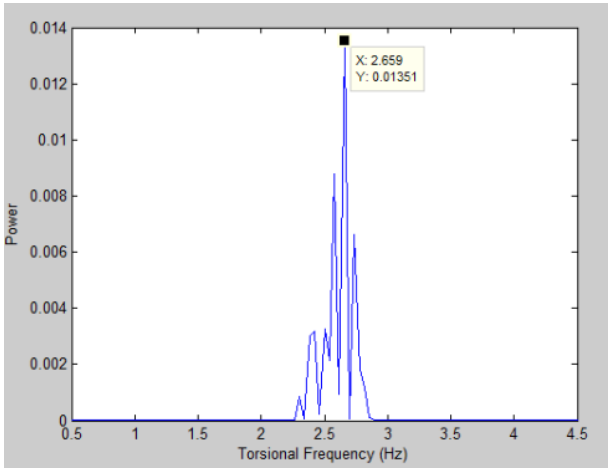

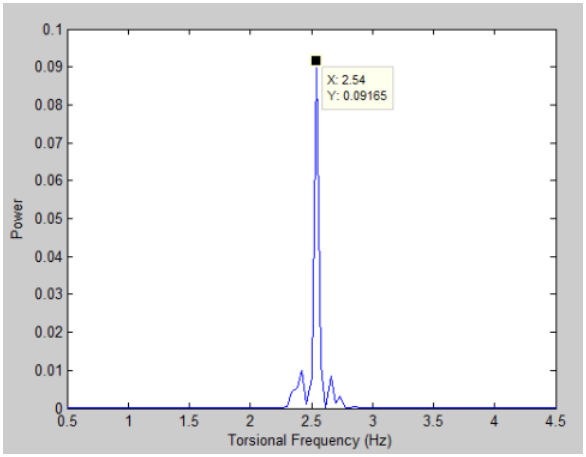

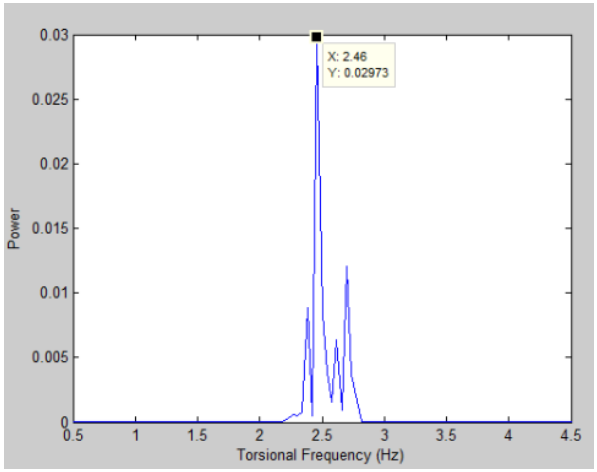

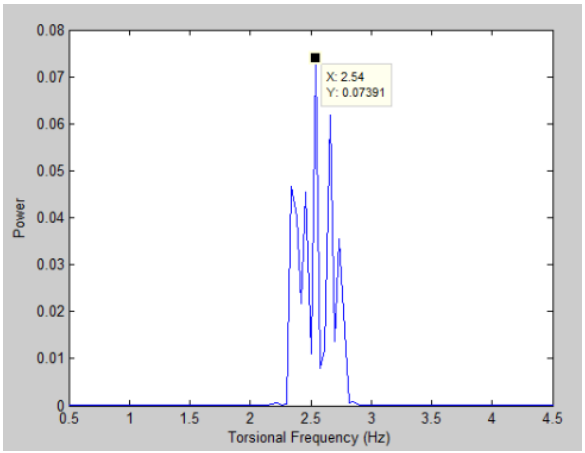

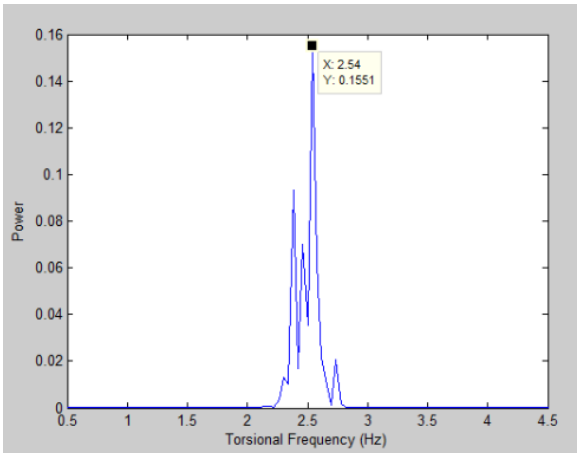

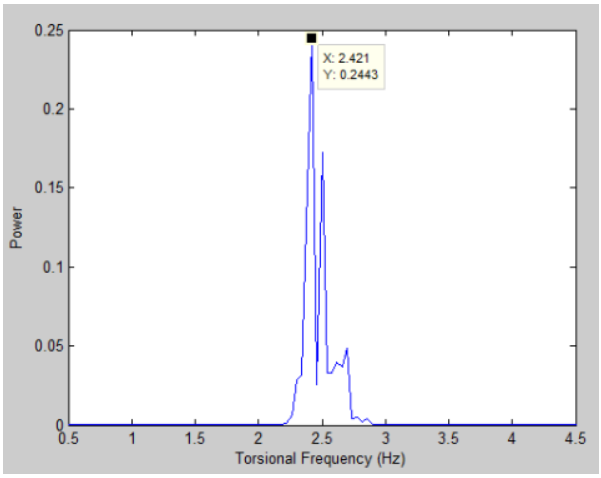

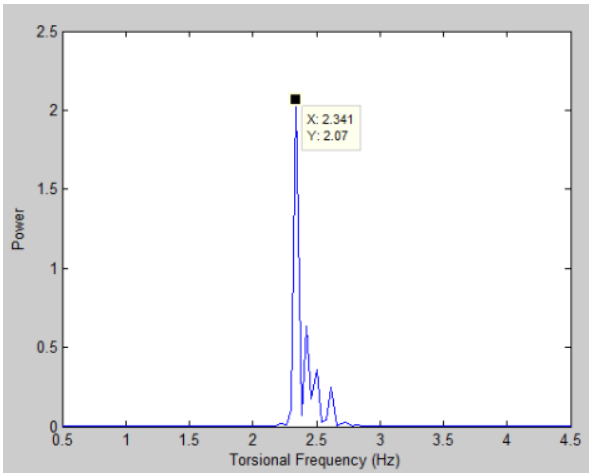

Frequency variation for torsional vibration mode for attack angle of 2 °

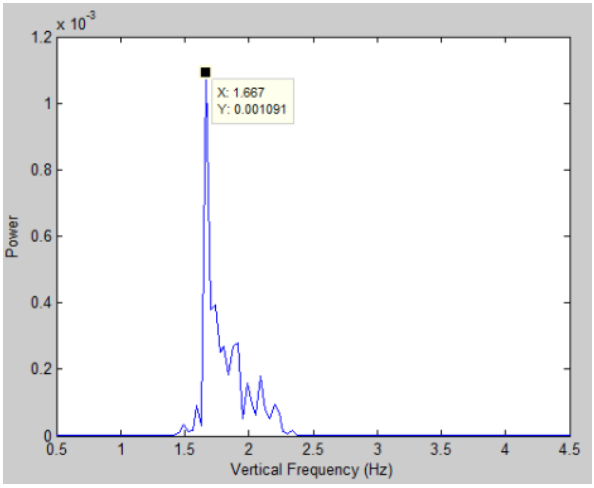

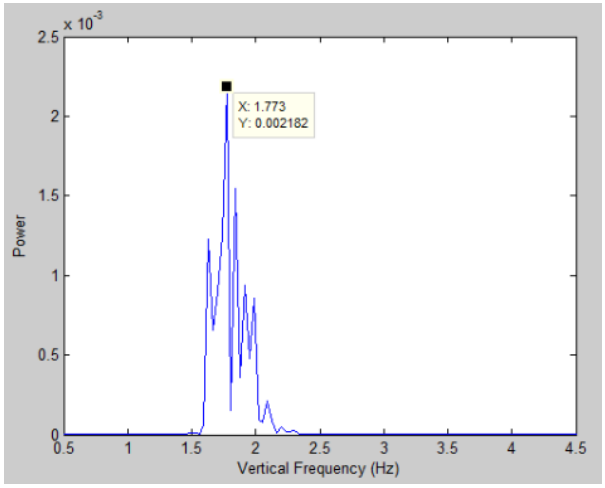

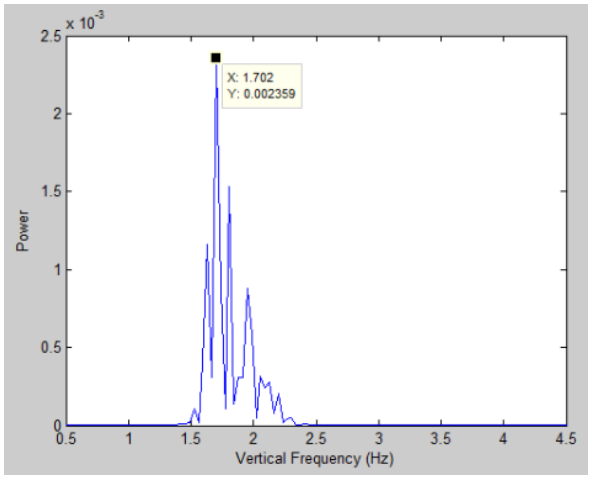

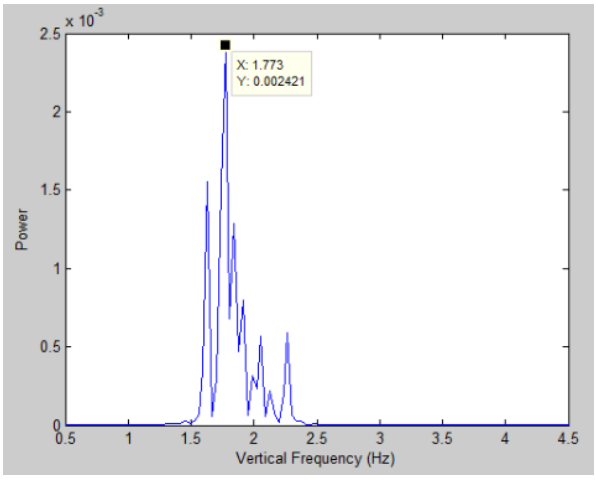

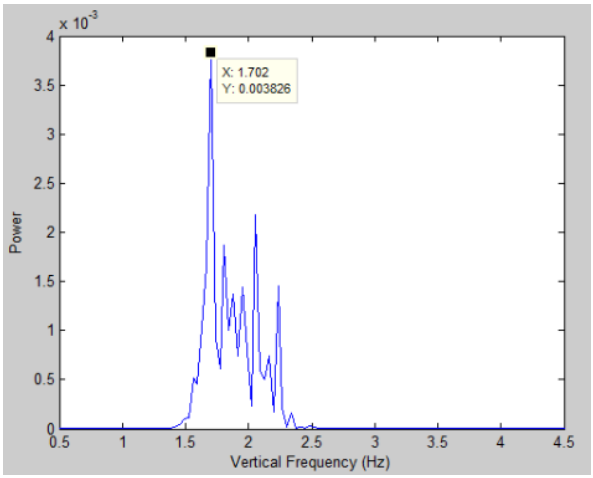

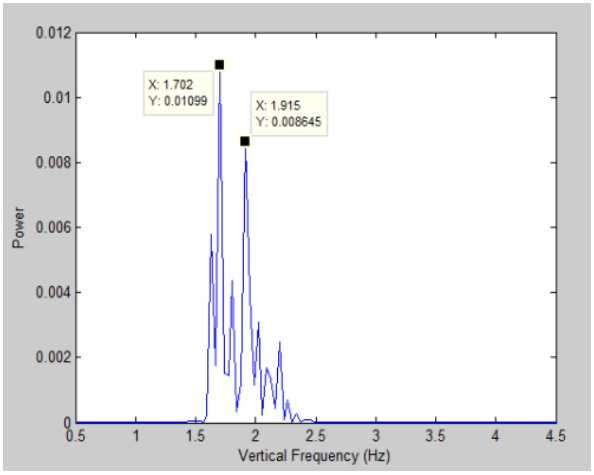

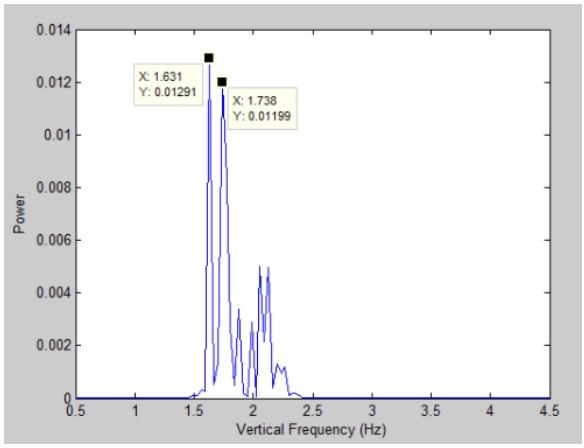

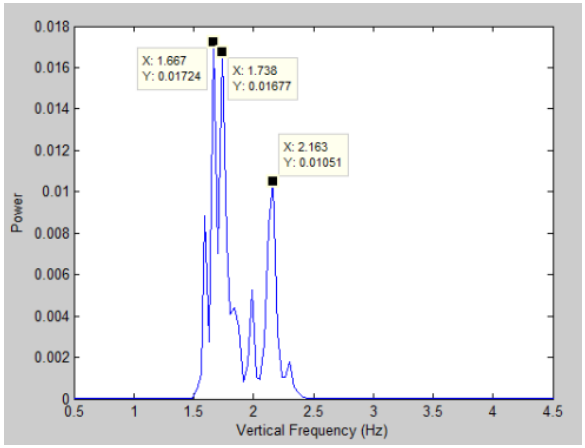

Frequency variation for vertical vibration mode for attack angle of -2 °

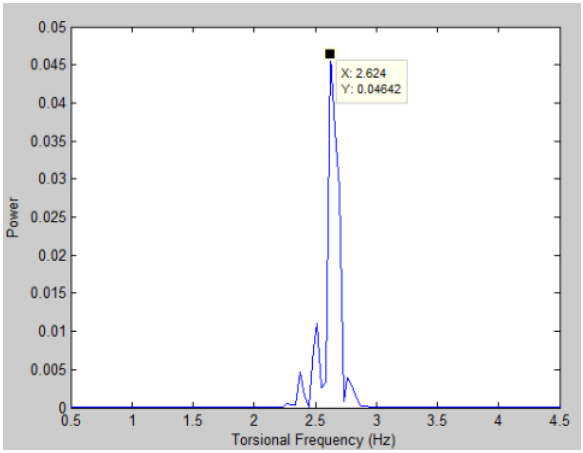

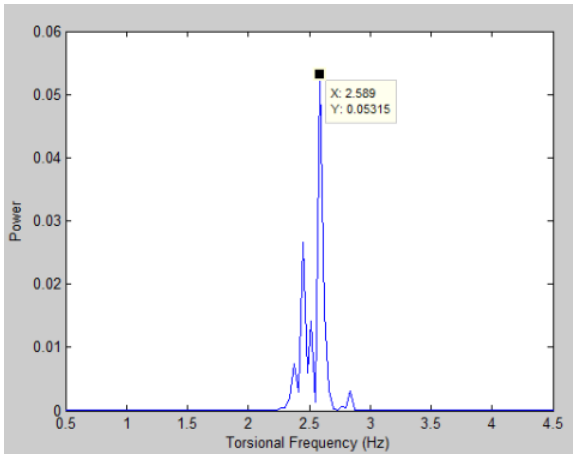

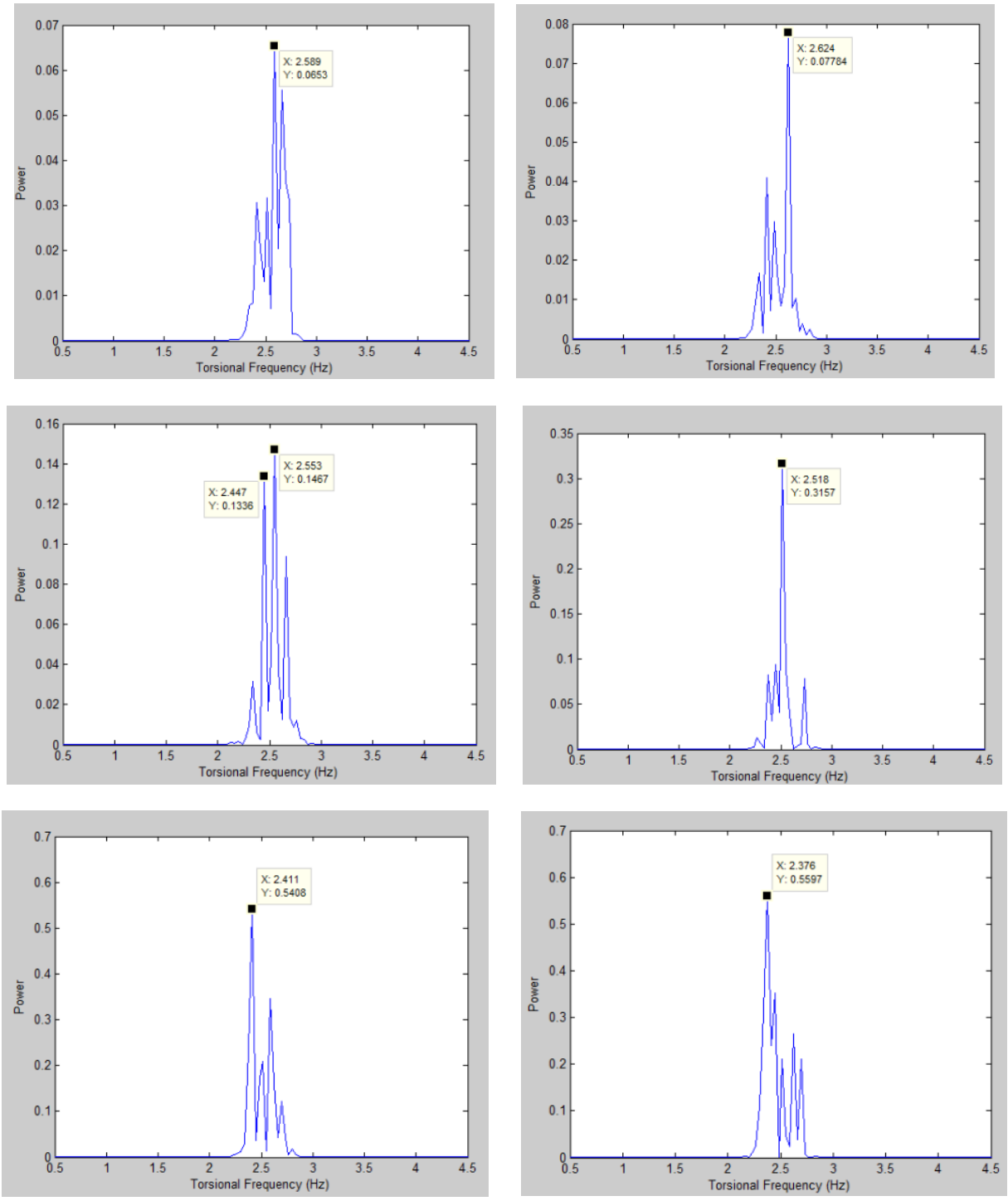

Frequency variation for torsional vibration mode for attack angle of -2 °

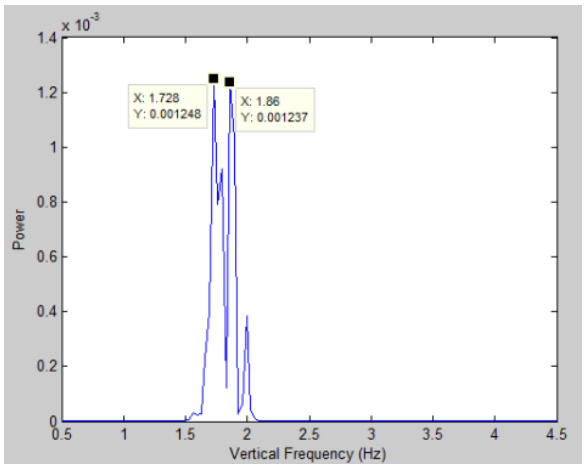
x 10^-3
X: 1.728
Y: 0.001248
X: 1.86
Y: 0.001237
Power
Vertical Frequency (Hz)

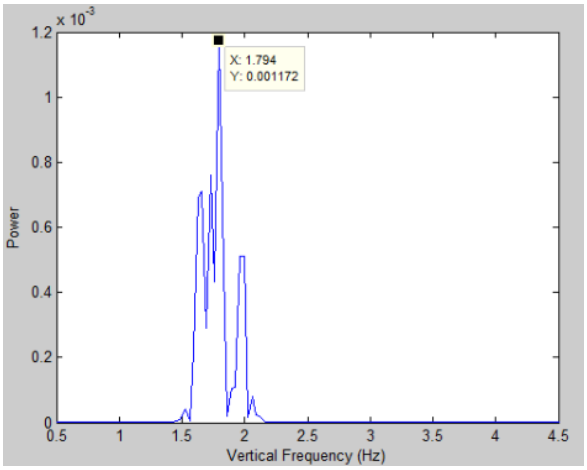
x 10^-3
X: 1.794
Y: 0.001172
Power
Vertical Frequency (Hz)

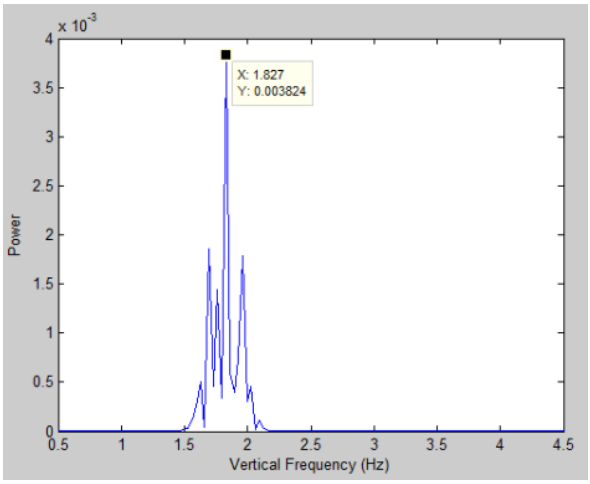
x 10^-3
X: 1.827
Y: 0.003824
Power
Vertical Frequency (Hz)

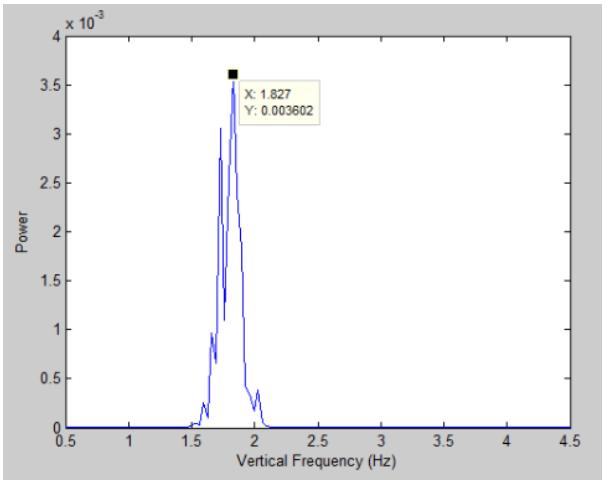
x 10^-3
X: 1.827
Y: 0.003602
Power
Vertical Frequency (Hz)

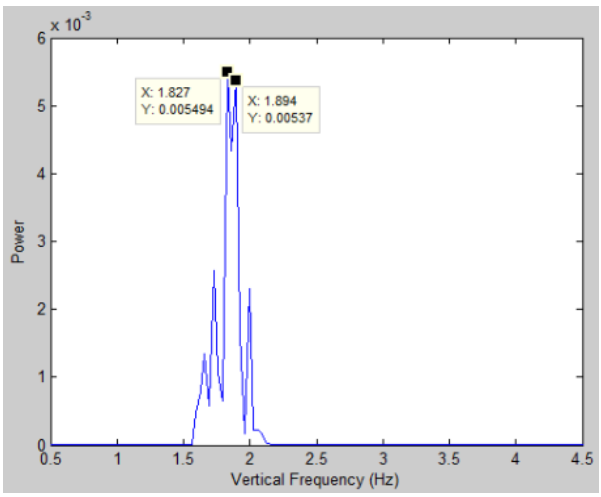
x 10^-3
X: 1.827
Y: 0.005494
X: 1.894
Y: 0.00537
Power
Vertical Frequency (Hz)

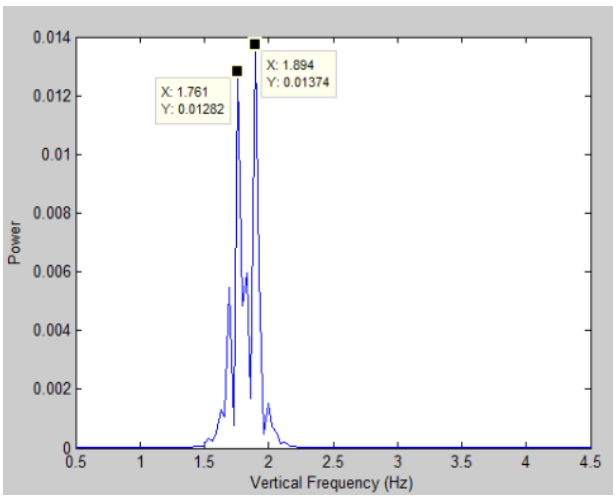
X: 1.894
Y: 0.01374
X: 1.761
Y: 0.01282
Power
Vertical Frequency (Hz)

Frequency variation for vertical vibration mode for attack angle of 4 °

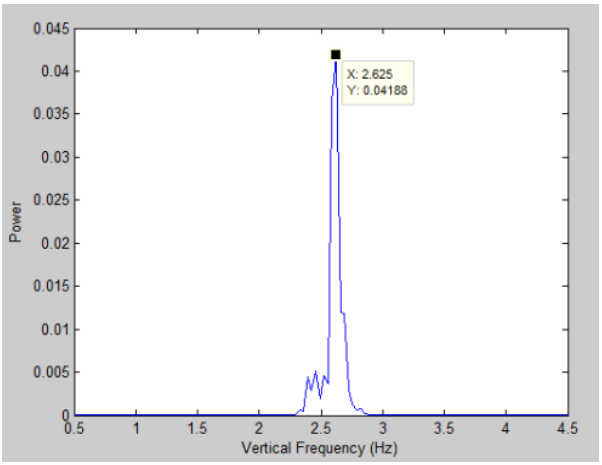

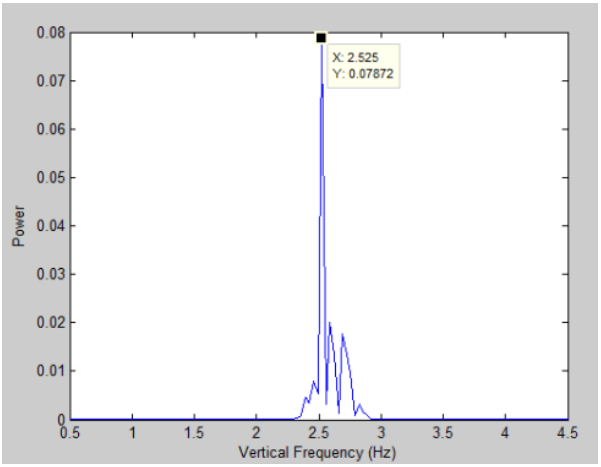

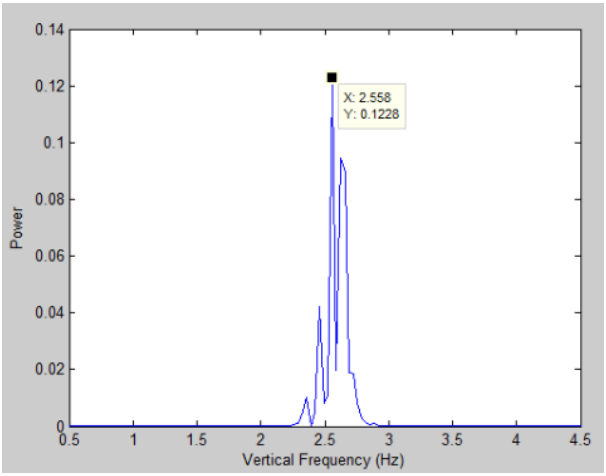

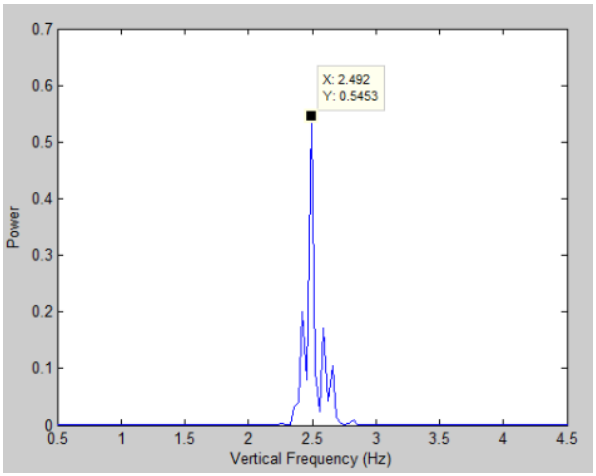

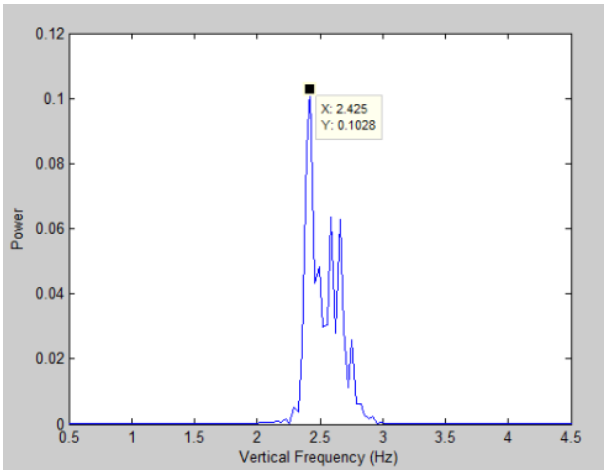

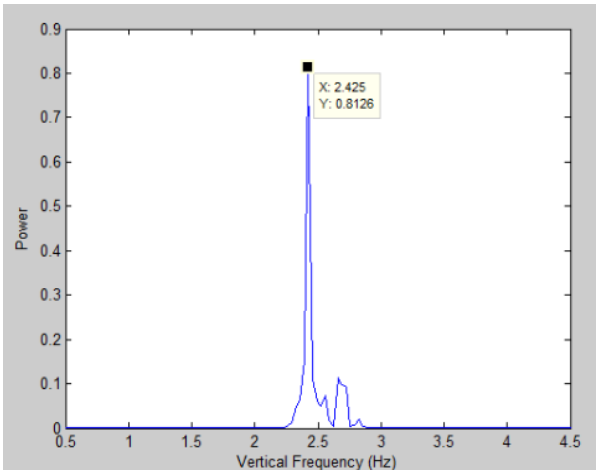

Frequency variation for torsional vibration mode for attack angle of 4 °

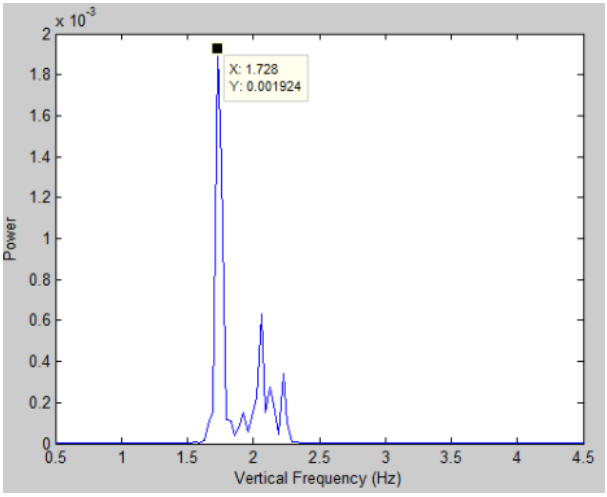

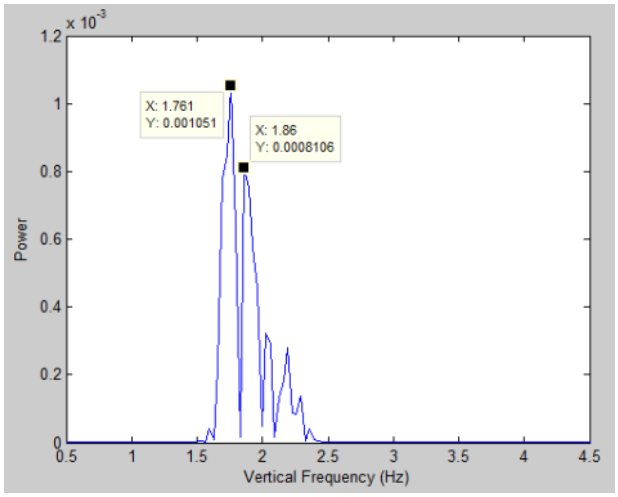

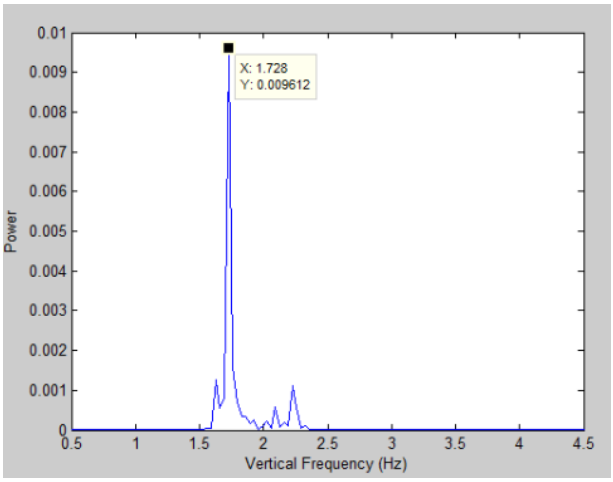

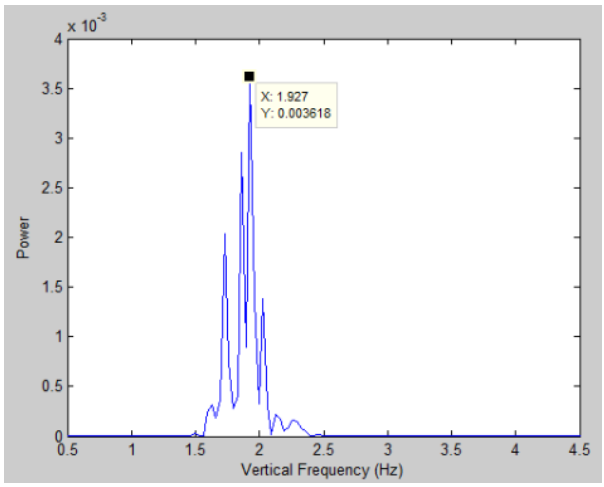

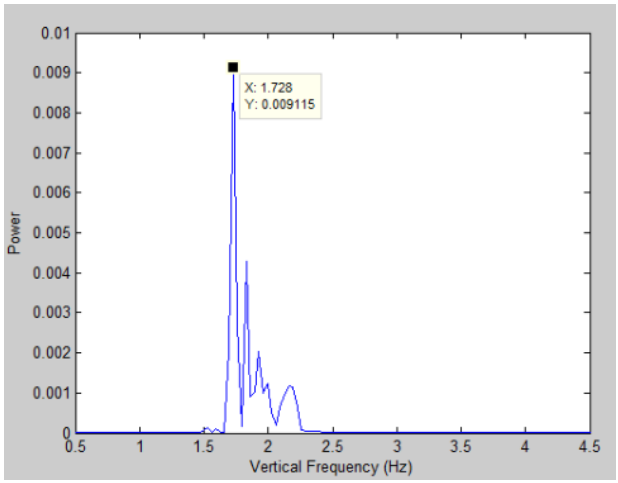

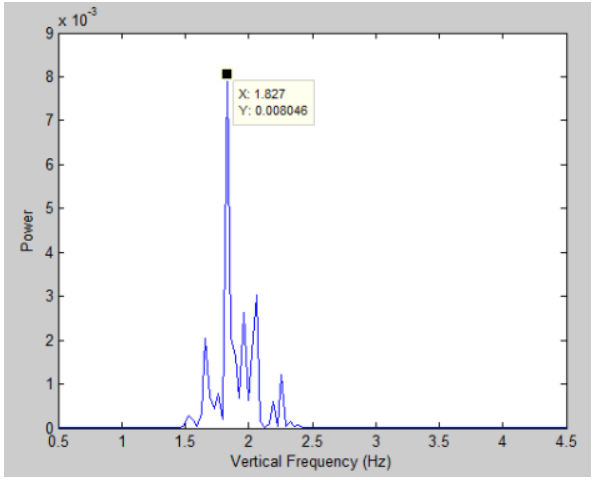

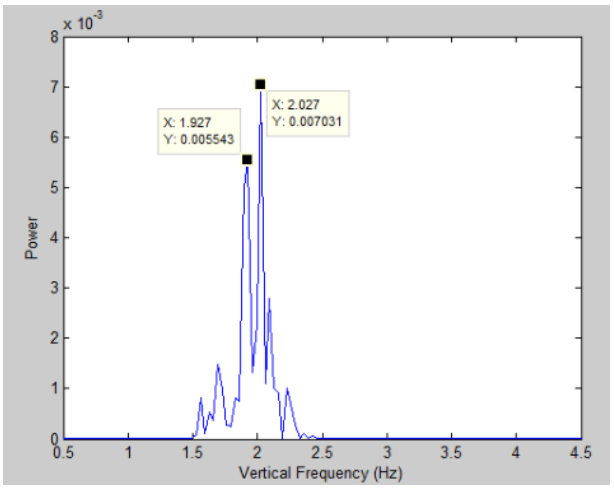

Frequency variation for vertical vibration mode for attack angle of -4 °

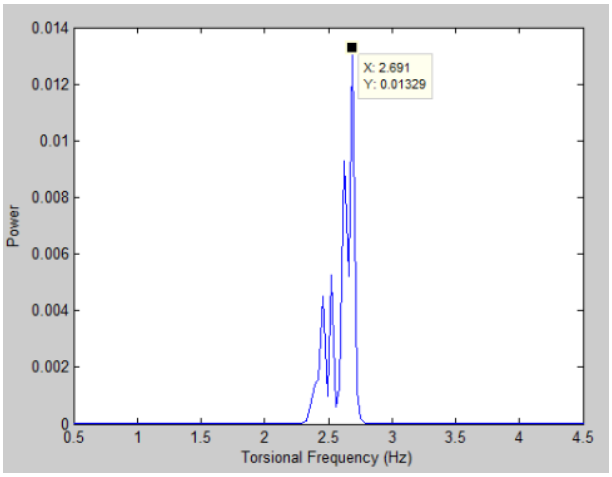

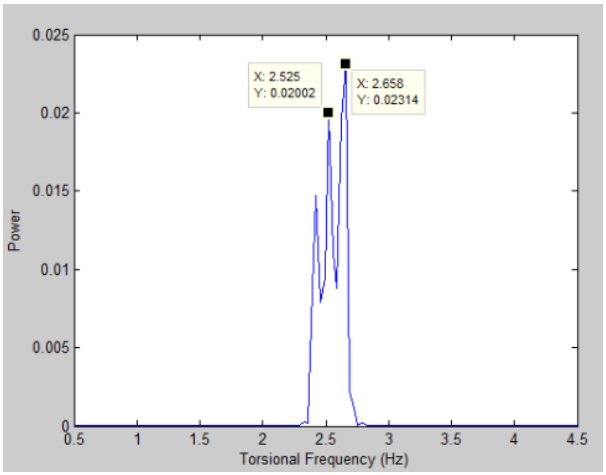

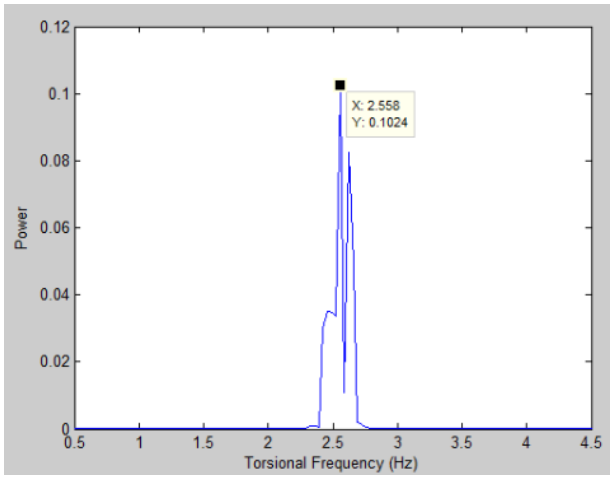

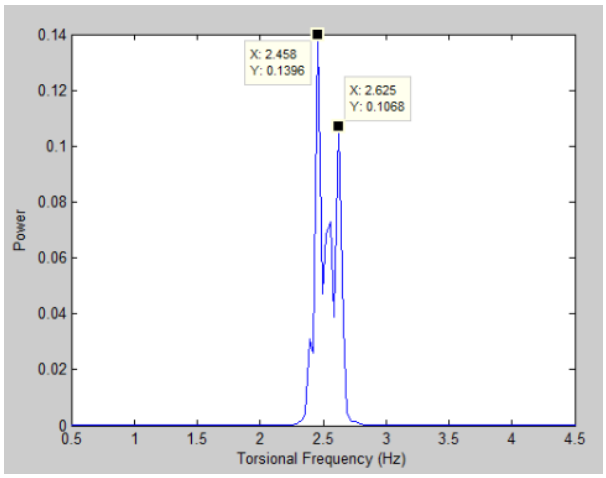

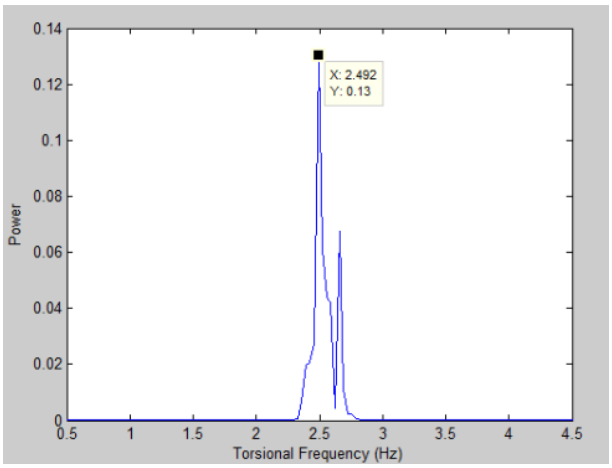

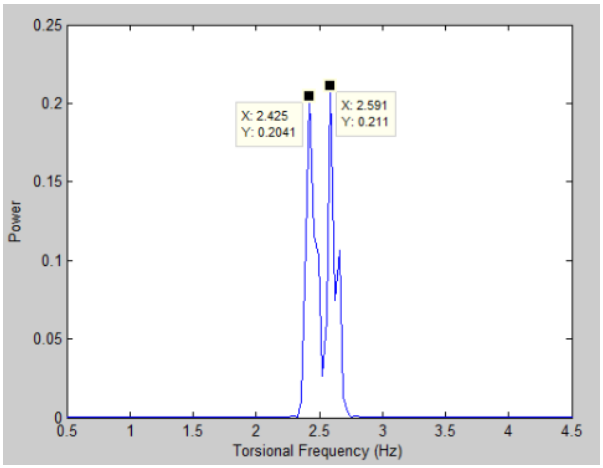

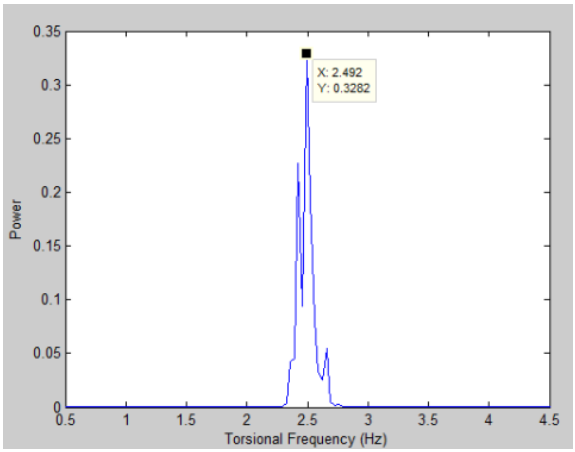

Frequency variation for torsional vibration mode for attack angle of -4 °

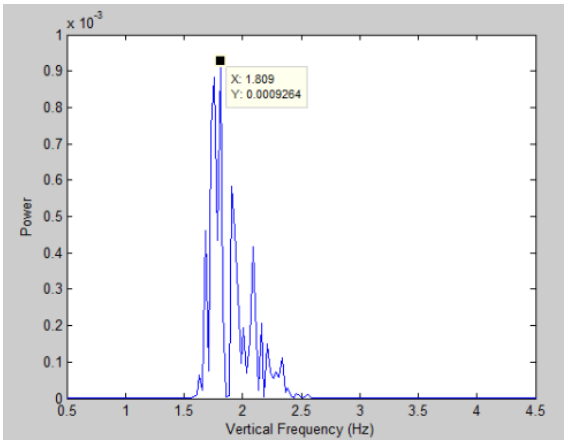

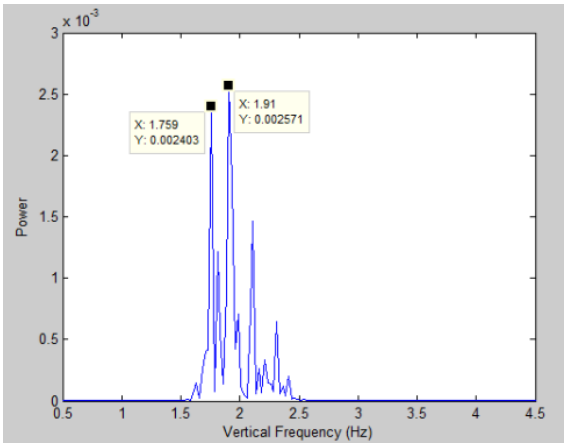

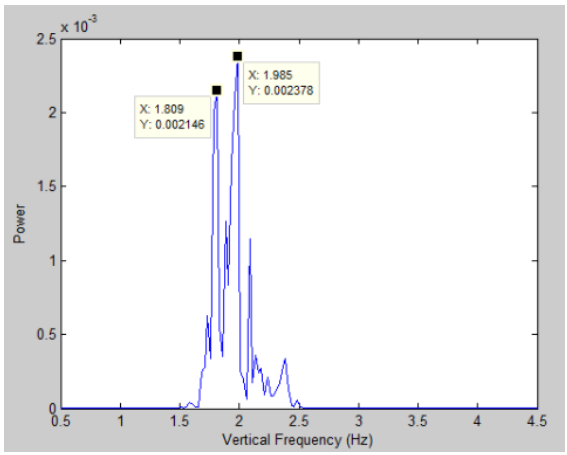

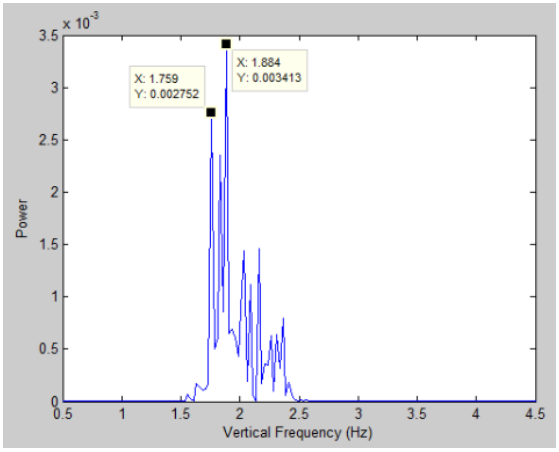

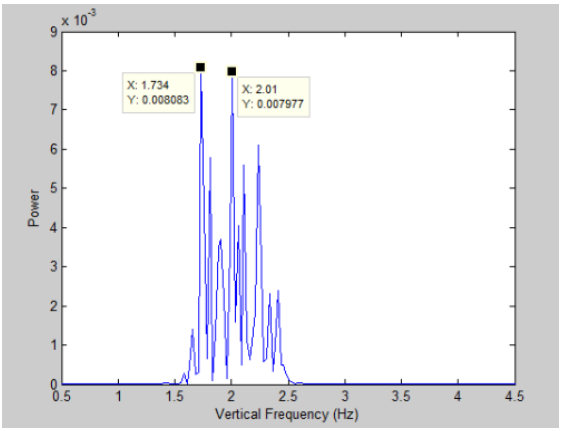

Frequency variation for vertical vibration mode for attack angle of -6 °

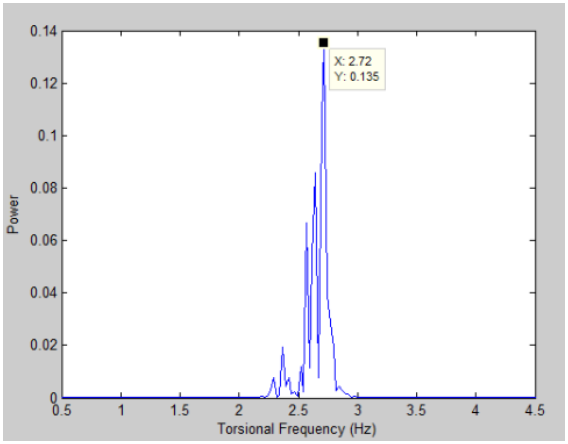

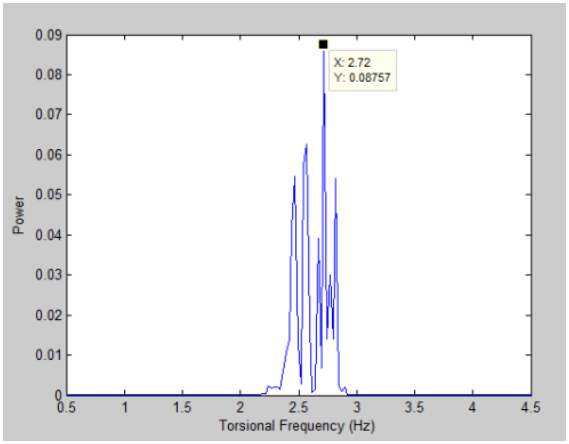

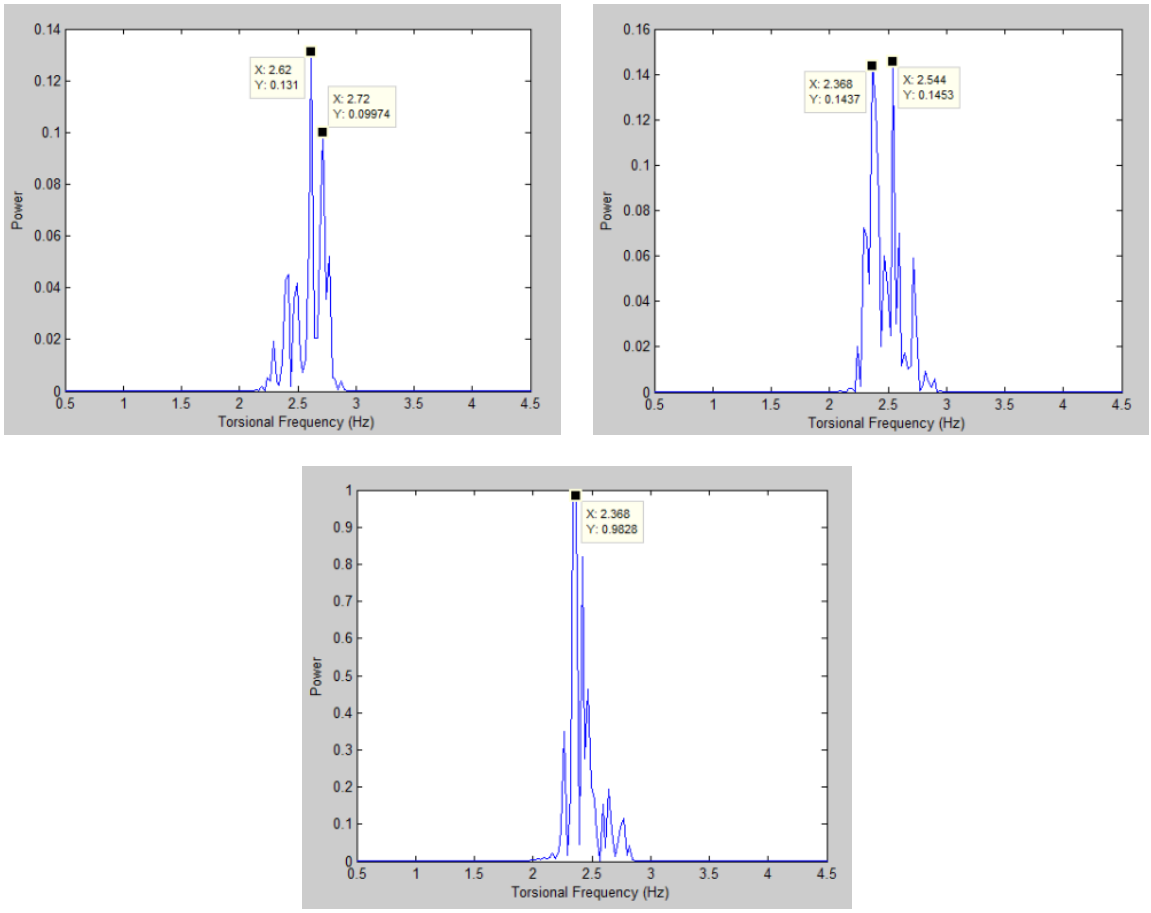

Frequency variation for torsional vibration mode for attack angle of -6 °

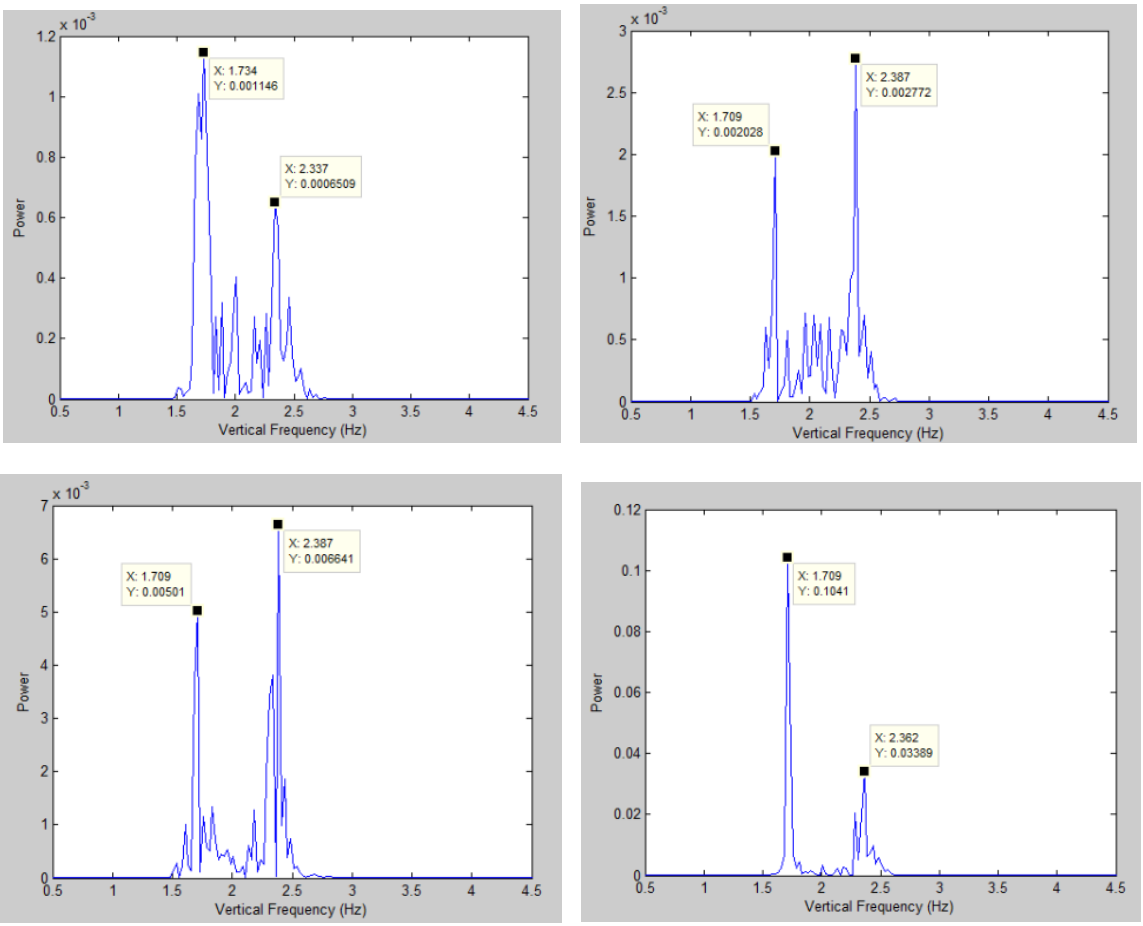

Frequency variation for vertical vibration mode for attack angle of -8 °

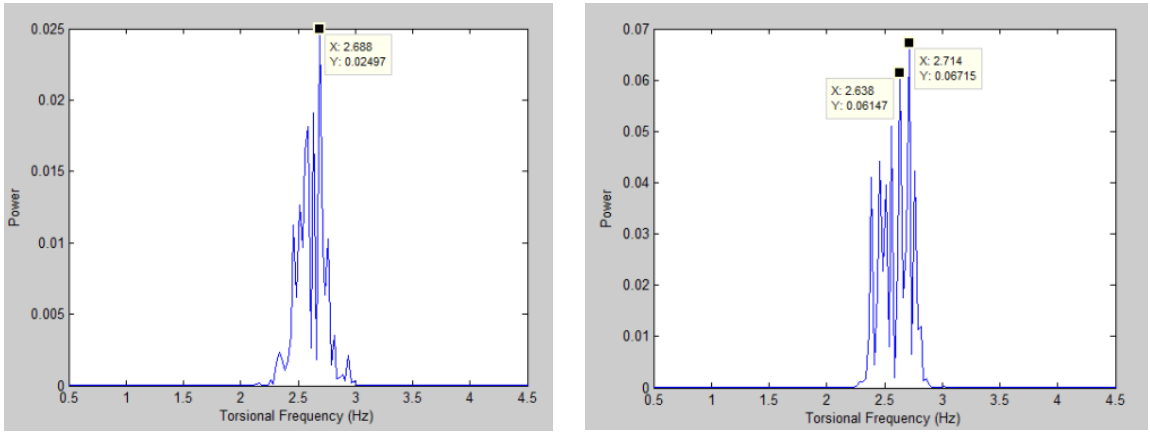

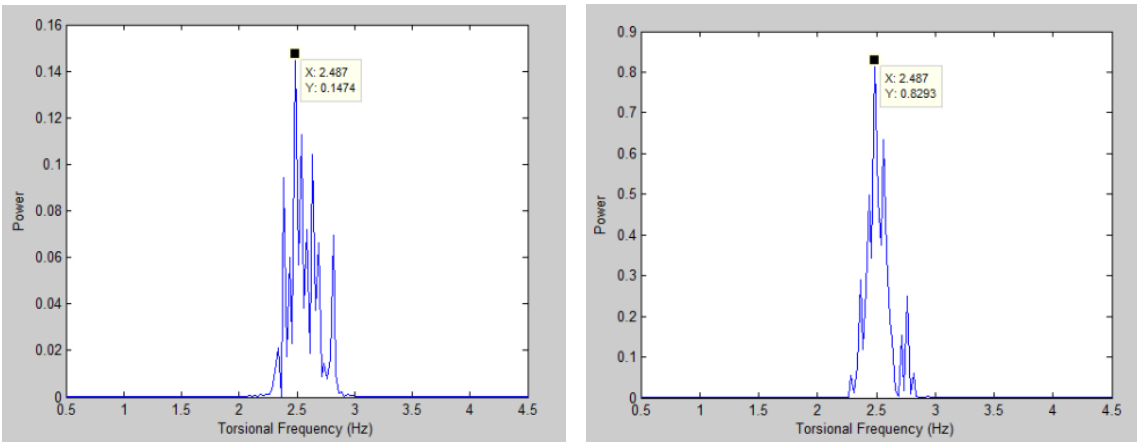

Frequency variation for torsional vibration mode for attack angle of -8 °